

# Development of a Low-cost Catalytic Membrane Reactor for Sulfur Recovery

Thesis

Submitted in Partial Fulfilment of the Requirements  
for the degree of

**DOCTOR OF PHILOSOPHY**

by

**SUJOY BOSE**



Department of Chemical Engineering

Indian Institute of Technology Guwahati

Guwahati-781039, India

November, 2015

# Development of a Low-cost Catalytic Membrane Reactor for Sulfur Recovery



***Sujoy Bose***

---

# **Development of a Low-cost Catalytic Membrane Reactor for Sulfur Recovery**

**Thesis**

*Submitted in Partial Fulfilment of the Requirements  
for the degree of*

**DOCTOR OF PHILOSOPHY**

by

**SUJOY BOSE**

**Roll No.: 11610709**



**Department of Chemical Engineering  
Indian Institute of Technology Guwahati  
Guwahati-781039, India**

**November, 2015**



*Dedicated to*

*Thakur shri shri Balak Bramhachari and My Parents  
for whom I have become what I am today*

---





**Department of Chemical Engineering  
Indian Institute of Technology Guwahati  
Guwahati, Assam-781039, India**

---

**CERTIFICATE**

It is certified that the work contained in the thesis entitled “**Development of a Low-cost Catalytic Membrane Reactor for Sulfur Recovery**”, by **Sujoy Bose**, has been carried out under my guidance and supervision. This work documented in this thesis has not been submitted to any other University or Institute for the award of any other degree or diploma.

Date:

---

**[Dr. Chandan Das]**

Associate Professor

Department of Chemical Engineering

Indian Institute of Technology Guwahati

Guwahati – 781039, India



## *Acknowledgements*

---

I would like to express my gratitude to all those who helped and guided me in different ways in completing this research work within the time span of four years directly or indirectly. First of all, I would like to express my sincere gratitude to my supervisor, **Dr. Chandan Das**, for providing me continuous inspiration, keeping faith on me and guiding me during the entire course of work. I am indebted to him for his useful suggestions and constant encouragement throughout the entire period.

I am grateful to **Dr. Chandan Das** for his continuous support and giving me liberty in choosing how to approach in different issues. I appreciate very much his expertise in the work field, flexibility and openness in dealing with the specific and general needs of this research work. His uncompromising approach to complete the experimental section, data analysis, writing manuscripts as well as thesis within specified time period helped me a lot in completing my research work. He taught me how to write and improve the quality of a journal paper and the thesis. I thank him for his patience and friendly nature and sharing his valuable time with me during the project tenure. The numerous brain storming sessions during the project meetings with him were very fruitful in enriching my analytical power and knowledge. It has been an amazing experience working with **Dr. Chandan Das**, which will help me a lot in my future to complete work within a specified time with maintaining the quality of work.

I must also thank to my doctoral committee members **Dr. Mihir Kumar Purkait**, **Dr. Tapas Kumar Mandal**, Department of Chemical Engineering, **Dr. Bulu Pradhan**, Department of Civil Engineering, for their valuable suggestions and contributions towards my research work.

## *Acknowledgements*

---

I am also thankful to **Prof. Ramgopal Uppaluri** and **Dr. S. S. Bag**, Department of Chemistry.

I must also thank the faculty members of the Department of Chemical Engineering for their kind cooperation during my project tenure in the department. I am also thankful to all staff members, Laboratory superintendents, especially **Dr. Lukumoni Borah**, **Mr. Kaustavmani Deka**, **Mr. Dipak Kumar Barman** and scientific officer of the Chemical engineering department for their genuine help during my entire research period.

I am also grateful to **Dr. Anil Verma**, Department of Chemical Engineering, and his research scholar **Mr. Avijit Ghosh** for allowing me to carry **Flexural Strength** analysis using **Universal Tensile Test Machine** in their laboratory, which has been very important in this research work.

I am also thankful to **Dr. K.S.R. Krishna Murthy** and **Dr. S. Kanagaraj**, Department of Mechanical Engineering for allowing me to use instruments in their laboratory. I should acknowledge the help provided by **Mr. Sanjib Sarma** and **Mr. Saifuddin Ahmed**, Junior Technical Superintendent, Strength of Materials Laboratory and Material Science Laboratory, Department of Mechanical Engineering, respectively.

I am also thankful to the **Central Instruments Facility** of IIT Guwahati for allowing me to carry out **Scanning Electron Microscopy** analysis, **Field Emission Scanning Electron Microscopy** analysis, **Electron Spin Resonance**, **Surface Area Analyzer** and **Raman Spectroscopy** analysis etc., which has been vital in this research work. In this regard, I should acknowledge the assistance provided by **Dr. Kula Kamala Senapati**, **Mr. Chandan**

## *Acknowledgements*

---

**Borgohain**, Scientific officer, and **Mr. Madhurjya Borah**, Junior Technical Superintendent, Central Instruments Facility, IIT Guwahati and all the operators allotted for these instruments.

I am also thankful to the **Central Workshop** of IIT Guwahati for helping me in the fabrication of my experimental setup which was the most essential part of my research work.

I was fortunate enough to get excellent batch mates like **Mr. Manish Kumar Sinha**, **Mr. Rajeev Parmar** and **Mr. Sankar Chakma** for their friendly support and assistance. I am also thankful to my seniors, **Dr. Mahesh Kumar Gagrai**, **Dr. Vijay Singh**, **Mr. Arijit Das** and juniors, **Mr. Suman Saha**, **Mr. Kibrom Alebel Gebru**, **Mr. Amit Baran Das**, **Mr. Abhisek Shukla**, **Mr. Abhradip Pal**, **Mr. Chelli V. Rao** and **Mr. Raj Kumar Das** for their friendly behaviour and assistance. Special thanks to **Mr. Rishiket Kundu**, **Mr. Vishesh Dhaliwal**, **Mr. Rahul Dohare**, **Mr. Vineet Kumar** and **Ms. Shubhangi Parde** for their help and co-operation in my research work.

Most of all, I would like to express my deepest sense of gratitude to all my family members, my parents and all the well-wishers. Their love, care, sacrifices and encouragement have made it possible for me to come so far.

**Sujoy Bose**





## Abstract

---

The work reported in this thesis is the development of catalytic membrane and membrane reactor for the recovery of sulfur. The problem associated with high manufacturing cost of the conventional catalytic membrane and membrane reactors encourage us to develop a novel scheme for the fabrication of catalytic membrane and membrane reactor. The purpose of fabricating catalytic membrane reactor is to minimize complications of the conventional sulfur recovery process using three catalytic bed reactors in the refineries. On the basis of the aforesaid problem statement, this entire study is divided into three segments along with the application of the fabricated catalytic membrane.

In the first study, the fabrication of ceramic support membrane using sawdust, an inexpensive pore-former is discussed. The extensive uses of pore-formers are considered to be a major factor for determining morphology in ceramic membrane fabrication. Hence, five different size ranges of sawdust (as pore-former) screened through 30, 44, 60, 72 and 100 B.S.S. meshes (500, 355, 250, 212, and 150  $\mu\text{m}$ ) are utilized and are believed to influence on membrane porosity, pore size and surface texture. Two series of experiments have been conducted; the first set of experiment is utilized to determine thermal behavior and particle size of sawdust as well as the change in physical properties of sawdust when burnt in the presence of air and the sustainability of raw and burnt-sawdust in acid and alkali media is also determined. The second set of experiment is the selection of appropriate sized sawdust particle for the fabrication of ceramic membrane based on first set of experiments for understanding the behavior of sawdust during membrane fabrication. After the selection of suitable sawdust particle, a low-cost ceramic tubular support membrane is fabricated via dry compaction method using cheap materials, namely, sawdust along with kaolin and feldspar. Thermogravimetric analysis, particle size distribution, image analysis, volumetric porosity and gas permeation experiments, acid-alkali test and three-point bend test are studied to characterize the fabricated

membrane, systematically. The fabricated membrane is then optimized in terms of morphology, thermal, mechanical and chemical stability. The sintering temperature amongst 550, 700 and 850°C for support membrane fabrication is also optimized. The manufacturing cost of the membrane is estimated. An empirical model using response surface methodology (RSM) is proposed to investigate the role of parameters, such as, preparation pressure and binder contents on the porosity and flexural strength of the fabricated membrane based on central compact design (CCD). A comparative study on manufacturing cost and mechanical strength of the membrane prepared with and without binder is also discussed.

Secondly, a series of activated  $\gamma$ -alumina (high surface area) supported Mo/Co catalysts with different Mo loadings (8, 12, 16 and 20 wt.%) have been prepared through the impregnation by soaking metal precursors over the alumina support followed by drying and calcination. A comparative study on  $\gamma$ -Al<sub>2</sub>O<sub>3</sub> with high and low surface area has been performed to understand the metal-support interaction and to select the suitable support in terms of metallic dispersion and metallic surface area for better catalytic activity. Conventional instruments, such as, BET analyser, X-ray diffractometer, Fourier transform infrared spectroscopy, field emission scanning electron microscopy, electro spin resonance, laser Raman spectroscopy, transmission electron microscopy and CO chemisorb are used to characterize the synthesized catalyst. The metal content on alumina and calcination temperature are optimized as 16 wt. % and 400°C, respectively on the basis of maximum metal dispersion and metallic surface area.

Furthermore, a complete experimentation involving fabrication and characterization of the CMR by coating of catalyst on the exterior surface of the low-cost tubular ceramic support membrane is reported. The fabrication procedure includes coating of catalyst over the membrane surface with a solid lubricant i.e. molybdenum disulfide (MoS<sub>2</sub>) by paint coating

## Abstract

---

technique, which can provide long life, no contamination and can sustain in harsh environment. The coating procedure is adopted for the simplicity, ease of methodology and minimization of cost. The viability and economic feasibility of the coating method have been discussed along with the morphological (porosity) and structural behaviour of the coated ceramic surface when lubricated with catalyst to assess the influence of lubricant on such coatings. The manufacturing cost of the catalytic membrane is also evaluated.

Finally, the application of the fabricated CMR i.e., the removal or recovery of elemental sulfur using catalytic membrane reactor as a function of catalytic activity (conversion, yield and selectivity) and mass transport study is described. An experimental set up made of stainless steel is designed and fabricated to carry out a batch experiment at room temperature ( $28 \pm 2^\circ\text{C}$ ) to collect elemental sulfur in solid form. The multi-reactant mass transfer behaviour of the CMR is studied on the basis of reaction equilibrium constant, membrane area and reactor volume which claims that the fabricated reactor behaves like an ideal CMR by means of 87% yield and 80% conversion of reactant.



## Research Publications

---

### Published journals from this work

- [1] S. Bose, C. Das, “Preparation and characterization of Low-cost tubular ceramic support membranes using sawdust as a pore-former”, **Materials Letters**, 110 (2013) 152-155.
- [2] S. Bose, C. Das, “Sawdust: From wood waste to pore-former in the fabrication of ceramic membrane”, **Ceramics International**, 41 (2015) 4070-4079.
- [3] S. Bose, C. Das, “Role of binder and preparation pressure in tubular ceramic membrane processing: Design and optimization study using response surface methodology (RSM)”, **Industrial & Engineering Chemistry Research**, 53 (31) (2014) 12319-12329.
- [4] S. Bose, C. Das, “Preparation, characterization, and activity of activated  $\gamma$ -alumina-supported molybdenum/cobalt catalyst for the removal of elemental sulfur”, **Applied Catalysis A: General**. (Under review)
- [5] S. Bose, C. Das, “Solid Lubricant-based Coating of Catalyst on the Surface of Tubular Ceramic Support for Catalytic Membrane Fabrication”, **International Journal of Applied Ceramic Technology**. (Under review)
- [6] S. Bose, R. Kundu, C. Das, “Mass transfer in a novel tubular catalytic membrane reactor (CMR) for the recovery of elemental sulfur”, **Chemical Engineering and Processing: Process Intensification**. (Revision submitted)
- [7] S. Bose, C. Das, “Fabrication of Catalytic Membrane and Membrane reactor: an Economic and Innovative Route”, **Materials Today: Proceedings** (Under review)

### International Conferences

- **S. Bose, C. Das**, "Catalytic membranes and membrane reactors to achieve a green environment: A review", 12th International Conference on Inorganic Membranes (**ICIM 2012**), 9-13th July 2012, University of Twente, Enschede, The Netherlands.
- **S. Bose, C. Das**, "Fabrication of low cost ceramic membrane from organo-polymeric wood precursors", Processing and fabrication of Advanced Materials XXI (**PFAM 21**), 10-13 December 2012, Indian Institute of Technology, Guwahati, Assam, India.
- **S. Bose, C. Das**, "Study of microstructures of ceramic-wood composites", Fourth International Conference on Recent Advances in Composite Materials (**ICRACM 2013**), 18-21 February, 2013, IIT BHU, Goa, India.
- **S. Bose, C. Das**, "Influence of Porosity on Flexural Strength and Flexural Modulus of an Eco-ceramic Membrane", International Conference on Mechanical, Industrial and Materials Engineering 2013 (**ICMIME 2013**), 1-3 November, 2013, RUET, Rajshahi, Bangladesh.
- **S. Bose, C. Das**, "Investigation of morphological and mechanical behaviour of a ceramic membrane based on different parameters", International Conference on "Membranes and Applications" (**ICMA 2013**), 22-23 November, 2013, CSIR-CGCRI, Kolkata, India.

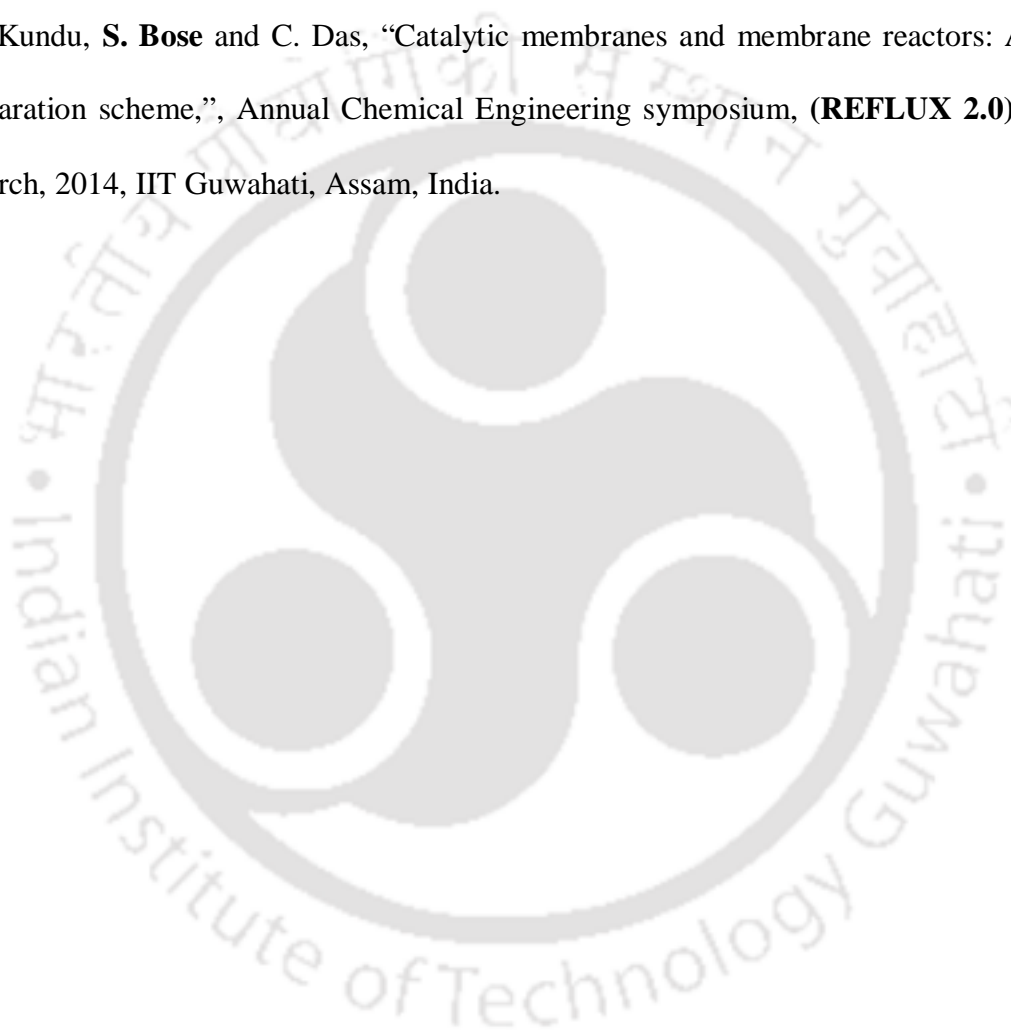
### National Conferences

- **S. Bose, C. Das**, "Utilities and basic functions of ceramic membranes in catalytic membrane and membrane reactors", International conference on Sustainable Technologies for Energy and Environment in Process Industries, 65th Annual Session of Indian Institute of Chemical Engineers, (**CHEMCON 2012**), 27-30 December, 2012, NIT Jalandhar , India.

## Research Publications

---

- **S. Bose**, C. Das, "A morphological and mechanical study of an eco-ceramic membrane influenced by parameters", Innovative approaches for food security and health care for better tomorrow, 66th Annual Session of Indian Institute of Chemical Engineers (**CHEMCON 2013**), 27-30 December, 2013, Institute of Chemical Technology, Mumbai, India.
- R. Kundu, **S. Bose** and C. Das, "Catalytic membranes and membrane reactors: A novel separation scheme," Annual Chemical Engineering symposium, (**REFLUX 2.0**), 29-30 March, 2014, IIT Guwahati, Assam, India.





# Contents

---

	Page No.
Dedication	I
Certificate	III
Acknowledgement	V-VII
Abstract	IX-XI
Research publications	XIII-XV
Contents	XVII-XXII
Nomenclature	XXIII-XXVI
List of Tables	XXVII-XXVIII
List of Figures	XXIX-XXXIV
<b>Chapter 1 Introduction and Objectives</b>	<b>1-44</b>
<b>1.1 Introduction</b>	<b>1-42</b>
1.1.1 Air pollutants, their sources and effects on human health	2
1.1.2 Industrial sources and separation techniques	2-11
1.1.3 Membrane separation processes	12
1.1.4 Membrane reactors	12-21
1.1.4.1 <i>Classification of MRs based on their configuration</i>	16-21
1.1.5 Catalytic membrane reactor (CMR)	21-40
1.1.5.1 <i>Synergistic effect of separation and reaction</i>	24-25
1.1.5.2 <i>Membrane functions in CMR and applications</i>	25-28
1.1.5.3 <i>Opposite flow mode catalytic membrane reactors</i>	28-35
<i>Hydrogen sulphide (H<sub>2</sub>S) laden gas treatment</i>	29-31
<i>Catalytic combustion of propane</i>	31-32
<i>Oxi-dehydrogenation (ODH) of Propane to Propylene</i>	33-34
<i>Other catalytic reactions</i>	34-35
1.1.5.4 Fabrication of CMR	35-40
1.1.6 Catalytic membrane reactors vs. traditional reactors	40-41
1.1.7 Possible scopes for further research	41-42

<b>1.2 Aim and Objective of the present research</b>	<b>42-44</b>
<b>Chapter 2 Fabrication and Characterization of Low-cost Ceramic Support Membrane</b>	<b>45-83</b>
<b>2.1 Experimental</b>	<b>46-55</b>
2.1.1 Raw materials	46
2.1.2 Selection and treatment of sawdust particle	46-47
2.1.3 Membrane fabrication	47-49
2.1.4 Characterization techniques	49-54
2.1.4.1 Physical characterizations	49-51
<i>Thermogravimetric analysis (TGA)</i>	49
<i>Particle size distribution</i>	49
<i>X-ray diffraction (XRD)</i>	50
<i>Fourier transform infrared spectroscopy (FTIR)</i>	50
<i>Surface morphology</i>	50-51
<i>Volumetric porosity</i>	51
2.1.4.2 Permeation characterization	52-54
<i>Experimental set up</i>	52
<i>Gas permeation</i>	53-54
2.1.4.3 Three-point bend test	54
2.1.4.4 Acid-alkali test	54
2.1.5 Statistical analysis	55
<b>2.2 Results and discussions</b>	<b>55-83</b>
2.2.1 Characterization of sawdust	56-68
2.2.1.1 <i>Effect of particle size of sawdust on the porosity and pore size of the membrane</i>	56-61
2.2.1.2 <i>Thermogravimetric (TGA) analysis</i>	61-62
2.2.1.3 <i>Functional group identification</i>	62-66
2.2.1.4 <i>Compositional analysis and study of microstructures of modified sawdust</i>	66-68
2.2.2 Physical characterization of membranes screened through 44 B.S.S. mesh	69-76

## Contents

---

2.2.2.1 TGA analysis	69
2.2.2.2 Effect of raw materials content on particle size distribution	70-71
2.2.2.3 Determination of porosity using Archimedes' principle	71-72
2.2.2.4 Surface morphological analysis	72-73
2.2.2.5 Pore size analysis built on FESEM images	74-75
2.2.2.6 Phase identification by XRD analysis	75-76
2.2.3 Permeation characterization of membrane screened through 44 B.S.S. mesh	77-78
2.2.3.1 Determination of porosity and pore diameter via gas permeation	77-78
2.2.4 Mechanical stability	78
2.2.5 Chemical stability	78-80
2.2.6 Cost evaluation of the membrane sieved through 44 B.S.S. mesh screen	80-82
<b>2.3 Summary</b>	<b>82-83</b>
<b>Chapter 3 Membrane Parameter Optimization using Response Surface Methodology (RSM)</b>	<b>85-112</b>
<b>3.1 Materials and methods</b>	<b>86-90</b>
3.1.1 Membrane fabrication	86
3.1.2 Membrane characterization	86-90
3.1.2.1 Three-point bend test	86
3.1.2.2 Membrane porosity	87
3.1.2.3 Surface morphology	87
3.1.2.4 Average pore diameter and porosity	87
3.1.2.5 Acid-alkali test	87-88
3.1.3 Response surface methodology via design of expert	88-90
3.1.4 Cost estimation	90
<b>3.2 Results and discussion</b>	<b>91-112</b>
3.2.1 Analysis of variance (ANOVA) and response surface	91-96
3.2.1.1 Membrane flexural strength	91-94
3.2.1.2 Membrane porosity	94-96
3.2.2 Model verification on the basis of statistical analysis	96-101

3.2.3 Optimization study	101-104
3.2.4 Study of phase transformation and microstructure of the optimized membrane	104-106
3.2.5 Gas permeation test of the optimized membrane	106-108
3.2.6 Chemical stability test of the optimized membrane	108-109
3.2.7 Cost of the fabricated support membrane	109-110
<b>3.3 Comparison with formerly published work</b>	<b>110-111</b>
<b>3.4 Summary</b>	<b>112</b>
<b>Chapter 4 Synthesis and Characterization of Catalyst</b>	<b>113-140</b>
<b>4.1 Materials and methods</b>	<b>114-115</b>
4.1.1 Chemicals for catalyst preparation	114
4.1.2 Catalyst synthesis	114-115
<b>4.2 Characterization techniques</b>	<b>115-119</b>
4.2.1 BET surface area analysis	115-116
4.2.2 Particle size analysis	116
4.2.3 Fourier Transform Infrared Spectroscopy (FTIR)	116
4.2.4 X-ray diffraction (XRD)	116-117
4.2.5 Field-emission scanning electron microscopy (FESEM)	117
4.2.6 Electro spin resonance (ESR)	117
4.2.7 H <sub>2</sub> Temperature Programmed Reduction (TPR)	117
4.2.8 CO chemisorption	118
4.2.9 Laser Raman spectroscopy (LRS)	119
4.2.10 Transmission electron microscope (TEM)	119
<b>4.3 Results and discussion</b>	<b>119-138</b>
4.3.1 Effect of support, Mo content and calcination temperature on metal dispersion and metallic surface area	120-122
4.3.2 Identification of bimetallic oxide catalyst	123-132
4.3.3 ESR-TPR of bimetallic oxide catalyst	132-136
4.3.4 Verification of the presence of optimized crystalline catalyst	136-138

## **Contents**

---

<b>4.4 Summary</b>	<b>139</b>
--------------------	------------

### **Chapter 5 Fabrication and Characterization of Low-cost Catalytic**

<b>Membrane</b>	<b>141-157</b>
-----------------	----------------

<b>5.1 Materials and methods</b>	<b>142-144</b>
----------------------------------	----------------

5.1.1 Materials used	142-144
----------------------	---------

5.1.2 Catalytic membrane fabrication method	144
---	-----

<b>5.2 Characterization techniques</b>	<b>145-147</b>
--	----------------

5.2.1 Membrane surface morphology	145
-----------------------------------	-----

5.2.2 Film thickness measurement	145-146
----------------------------------	---------

5.2.3 Phase transformation study	146
----------------------------------	-----

5.2.4 Spectrophotometric analysis	146
-----------------------------------	-----

5.2.5 Cost estimation	147
-----------------------	-----

<b>5.3 Results and discussion</b>	<b>147-156</b>
-----------------------------------	----------------

5.3.1 Determination of porosity of the coated membrane and thickness of the coated layer	147-148
--	---------

5.3.2 Surface morphology of coated membrane using FESEM image analysis	148-149
--	---------

5.3.3 XRD analysis	149-151
--------------------	---------

5.3.4 FTIR analysis of coated membranes	151-153
---	---------

5.3.5 EDX mapping analysis	153-154
----------------------------	---------

5.3.6 Manufacturing cost evaluation	155-156
-------------------------------------	---------

<b>5.4 Summary</b>	<b>156-157</b>
--------------------	----------------

### **Chapter 6 Performance of Catalytic Membrane and**

<b>Membrane Reactor</b>	<b>159-188</b>
-------------------------	----------------

<b>6.1 Materials and methods</b>	<b>160-161</b>
----------------------------------	----------------

6.1.1 Chemicals and catalyst synthesis	160
--	-----

6.1.2 Reactor configuration	160-161
-----------------------------	---------

<b>6.2 Characterization techniques</b>	<b>162-165</b>
--	----------------

6.2.1 Catalytic test	162-164
6.2.2 Analytical instruments used	164-165
6.2.2.1 <i>Gas chromatography</i>	164-165
6.2.2.2 <i>Identification of the desired product</i>	165
<b>6.3 Theory</b>	<b>166-173</b>
6.3.1 Motivation for batch reactors	166
6.3.2 Assumptions considered	167
6.3.3 Reaction kinetics and mass balance equation	167-174
<b>6.4 Results and discussion</b>	<b>174-187</b>
6.4.1 Catalytic activity	174-149
6.4.1.1 <i>Material balance</i>	174
6.4.1.2 <i>Conversion of H<sub>2</sub>S into elemental sulfur</i>	175-179
6.4.1.3 <i>Mass transfer limitation</i>	179
6.4.2 IR transmittance spectra of elemental sulfur	179-181
6.4.3 Influence of fixed pressure difference over the membrane on the flux and mole fraction of H <sub>2</sub> S and SO <sub>2</sub> changing with time	181-183
6.4.4 Reaction rate, equilibrium reaction constant ( $K_{eq}$ ) and mass transport coefficient at boundary layer of the membrane ( $k_{ij}$ )	183-186
6.4.5 Comparison with formerly published work	187
6.4.6 Experimental versus Theoretical data	188-191
<b>6.5 Summary</b>	<b>191-192</b>
<b>Chapter 7 Overall Conclusions and Scope of Future Work</b>	<b>193-195</b>
<b>Appendix</b>	<b>197-198</b>
<b>References</b>	<b>199-216</b>
<b>Curriculum vitae</b>	

## Nomenclature

---

$A$	Model terms for preparation pressure
$A_{eff}$	Effective membrane area ( $m^2$ )
$A_i$	Area of peak I ( $m^2$ )
$B$	Model terms for sodium metasilicate (SM) content
$B_0$	A specific membrane parameter ( $m^2$ )
$C$	Model terms for boric acid (BA) content
$C_A$	Concentration of reactant gas after time $t$ ( $mol.m^{-3}$ )
$C_{A_0}$	Initial concentration of reactant gas ( $mol.m^{-3}$ )
$C_{overall_0}$	Overall initial concentration of both the reactants ( $mol.m^{-3}$ )
$C_{R_{outlet}}$	Concentration of feed gases present in the permeate ( $mol.m^{-3}$ )
$C_s$	Reactant concentration at the external surface of catalyst ( $mol.m^{-3}$ )
$C_{R_{inlet}}$	Initial concentration of reactant gases in the inlet of the reactor ( $mol.m^{-3}$ )
$c_t$	Total concentration of the reactant gases ( $mol.m^{-3}$ )
$d_{sl}$	Density of solid-lubricant solution ( $g.m^{-3}$ )
$d$	Active particle diameter (m)
$d_i$	Partial desirability function for specific responses
$d_p$	Pore diameter (m)
$d_i$	Pore diameter of the $i$ -th pore ( $\mu m$ )
$d_s$	Area average pore diameters
$dX_{overall}$	Change in rate of disappearance of the reactant gases with time ( $mol.m^{-3}.min^{-1}$ )
$D$	Metal dispersion (%)
$D_{ij}$	Effective diffusivity of the reactant gases ( $m^2.min^{-1}$ )
$D_{inert,k}$	Knudsen diffusion coefficient ( $m^2.min^{-1}$ )
$h$	Height of the membrane (m)
$J_i$	Flux of $i$ -th component gases ( $mol.m^{-2}.min^{-1}$ )
$J_j$	Flux of $j$ -th component gases ( $mol.m^{-2}.min^{-1}$ )
$J_{membrane,i}$	Flux of the reactant gases through the membrane wall ( $mol.m^{-2}.min^{-1}$ )

## Nomenclature

$J_{visc}$	Flux considering transport mechanism, viscous flow ( $\text{mol.m}^{-2}.\text{min}^{-1}$ )
$k$	Effective permeability factor ( $\text{m.min}^{-1}$ )
$k_b$	Backward rate constant ( $\text{mol. L}^{-1}.\text{min}^{-1}$ )
$K_{eq}$	Equilibrium constant
$k_f$	Forward reaction rate constant ( $\text{mol. L}^{-1}.\text{min}^{-1}$ )
$k_{ij}$	Mass transfer coefficient for components $i$ and $j$ ( $\text{m.min}^{-1}$ )
$l$	Pore length (m)
$l_d$	Distance between the reactor wall and the membrane surface where the diffusion occurs (m)
$L$	Thickness of the membrane (m)
$m$	Mass of the coating over the exterior surface of the membrane (g)
$m_s$	Mass of the sample (g)
$m.w$	Molecular weight of the metal ( $\text{g.mol}^{-1}$ )
$M_A, M_B$	Molar mass of the reactant gases ( $\text{g. mol}^{-1}$ )
$M_{N_2}$	Molecular weight of the inert gas ( $\text{g.mol}^{-1}$ )
$\%M$	% metal
$n$	Number of pores (%)
$N_A$	Avogadro's number
$p$	Pressure at which reactant gases are entered into the reactor (MPa)
$p_i$	Partial pressure of the species $i$ (MPa)
$P_i$	The permeance ( $\text{mol.m}^{-2}.\text{min}^{-1}.\text{MPa}$ )
$P_{tot}$	Total pressure (MPa)
$P_2$	Membrane pressure at permeate side (MPa)
$\Delta P$	Trans-membrane pressure drop (MPa)
$P_{amb}$	Ambient pressure (MPa)
$P_{std}$	Standard pressure (MPa)
$Q$	Volumetric flow rate ( $\text{m}^3.\text{min}^{-1}$ )
$r$	Diameter of the particle (m)
$r_a$	Reaction rate per volume of the catalyst ( $\text{mol.m}^{-3}.\text{min}^{-1}$ )
$r_o$	Outer radius of the membrane coated with catalyst (m)

## Nomenclature

---

$r_{overall}$	Rate of disappearance of the reactant gases ( $\text{mol.m}^{-3}.\text{min}^{-1}$ )
$R$	The universal gas constant ( $\text{m}^3.\text{MPa.K}^{-1}.\text{mol}^{-1}$ )
$R_b$	Rate of the reaction in the bulk ( $\text{mol.m}^{-3}.\text{min}^{-1}$ )
$R_{int}$	Rate of the reaction at the interface ( $\text{mol.m}^{-3}.\text{min}^{-1}$ )
$R1$	Model response for membrane flexural strength
$R2$	Model response for membrane porosity
$R^2$	Coefficient of multiple determination
$R_{Adj}^2$	Adjusted statistic coefficient
$R_{Pred}^2$	Predicted statistic coefficient
$S$	Permeable area of the membrane ( $\text{m}^2$ )
$S_f$	Stoichiometric factor
$t$	Time required to covert reactant gases into products (min)
$T$	Temperature (K, °C)
$T_{amb}$	Ambient temperature (K, °C)
$T_c$	The thickness of the coated layer (m)
$T_{std}$	Standard temperature (K, °C)
$v$	Molecular mean velocity of the operating gas ( $\text{m}.\text{min}^{-1}$ )
$v_A, v_B$	Diffusion volumes of the reactant gases ( $\text{m}^3$ )
$v_\phi$	Volumetric flow rate ( $\text{m}^3.\text{min}^{-1}$ )
$v_i$	The stoichiometric coefficient of component $i$
$v_j$	The stoichiometric coefficient of component $j$
$V_c$	Volume of the coated surface ( $\text{m}^3$ )
$V$	The reactor volume ( $\text{m}^3$ )
$V_m$	Volume of the fabricated membrane ( $\text{m}^3$ )
$V_{syr}$	Syringe volume injected (mL)
$V_g$	Molar volume of the gas at STP (mL)
$W_1$	Weight of the dry membrane (m)
$W_2$	Weight of the wet membrane (m)
$x_j, x_j^{int}$	The molar fractions at the bulk and the interface
$x_i$	The molar fraction of the species $i$

## Nomenclature

$x_{S_8}, x_{H_2O}, x_{H_2S}$ and $x_{SO_2}$	The mole fractions of products and reactants
$X$	Conversion of the reactants into product (%)
$\bar{x}$	The average mole fraction between the bulk and the catalyst-membrane surface interface
$\Delta x$	The difference in mole fraction between the bulk and the catalyst-membrane surface interface

## Greek letters

$\eta$	The viscosity of the gas (MPa.min)
$\alpha$	Axial points in CCD
$\varepsilon$	The porosity
$\tau$	The tortuosity factor
$\varepsilon/\tau^2$	Effective porosity
$\rho_{H_2O}$	Density of water ( $\text{g.m}^{-3}$ )
$\phi_{W-P}$	Weisz-Prater criterion
$\delta_m$	Cross-sectional area of active metal atom ( $\text{m}^2$ )

## Abbreviations

ANOVA	Analysis of variances
APD	Active particle diameter (m)
CCD	Central composite design
MD	Metal dispersion (%)
MSA	Metallic surface area ( $\text{m}^2.\text{g}^{-1}$ )
Prob>F	Probability value greater than F-value
RSM	Response surface methodology
Sqrt	Square root (a mathematical term)
TF	Turnover frequency ( $\text{cm}^{-1}$ )

## List of Tables

Table No.	Title	Page No.
<b>Table 1.1</b>	Chemical properties of sulfur	4
<b>Table 1.2</b>	Classification of membrane reactors [8]	14
<b>Table 1.3</b>	Use of different catalysts for catalytic membrane reactors	36
<b>Table 2.1</b>	Composition of raw materials used for the preparation of ceramic support membrane	48
<b>Table 2.2</b>	Particle size characteristics of sawdust materials	58
<b>Table 2.3</b>	Determination of particle size and pore diameter for the membrane sintered at 850°C	59
<b>Table 2.4</b>	Porosity determined using Archimedes' principle and gas permeation study for the membrane sintered at 850°C	60
<b>Table 2.5</b>	Membrane porosity (made of sawdust screened through 44 B.S.S. mesh)	71
<b>Table 2.6</b>	Weight losses of the ceramic membrane after sintering using 44 B.S.S. mesh screened sawdust along with different weight ratios of raw materials	73
<b>Table 2.7</b>	Parameters determined from the study of graph between nitrogen gas permeability and average pressure obtained from gas permeability data	78
<b>Table 2.8</b>	Cost evaluation of fabricated membrane from the unit cost of raw materials	81
<b>Table 3.1</b>	Design arrangement and experimental responses for central composite design (CCD)	89
<b>Table 3.2</b>	Design summary: Input variables and their coded and actual values used in the response surface study	90
<b>Table 3.3</b>	Analysis of variance (ANOVA) for respective response surface quadratic models	93
<b>Table 3.4</b>	ANOVA and regression analysis for Flexural strength and porosity	96
<b>Table 3.5</b>	Optimized input variables calculated from CCD	99
<b>Table 3.6</b>	Error analysis between predicted and experimental value	104
<b>Table 3.7</b>	Change in porosity of the optimized membrane in acid and alkali media as a function of temperature	109

<b>Table 3.8</b>	EDX analysis of the optimized membrane materials sintered at 850°C temperature before and after acid-alkali test	109
<b>Table 3.9</b>	Cost assessment of the optimized membrane	110
<b>Table 4.1</b>	Catalyst compositions and surface area of support	115
<b>Table 4.2</b>	Chemisorption analysis data	122
<b>Table 4.3</b>	BET surface area, pore volume and maximum reduction temperature of catalysts	130
<b>Table 5.1</b>	Different combinations used to prepare and characterize the coated membranes	143
<b>Table 5.2</b>	Weight of the lubricant, binder and additive used in preparing lubricant solution for coating over support membranes	144
<b>Table 5.3</b>	Estimated cost of the catalytic membranes	155
<b>Table 6.1</b>	Sulfur formation steps for the oxidation of H <sub>2</sub> S by SO <sub>2</sub> (Claus reaction) [151]	170
<b>Table 6.2</b>	Parameters (feed, reactor conditions) used to solve the equations in the study	174
<b>Table 6.3</b>	Catalytic activity of the sample catalysts calcined at 400 and 600°C	176
<b>Table 6.4</b>	Polynomial fitting of the catalytic activity (experimental data) of the CMR with the theoretical data	188
<b>Table 6.5</b>	Determination of catalytic activity of the CMR on the basis of polynomial fitting	188
<b>Table 6.6</b>	Statistical analysis of the predicted catalytic activity of the CMR	189
<b>Table 6.7</b>	Summary of predicted catalytic activity based on statistical analysis	189
<b>Table 6.8</b>	ANOVA analysis for overall conversion, selectivity and yield	189

## List of Figures

Figure No.	Title	Page No.
<b>Figure 1.1</b>	Sources and effects of different air pollutants on human beings	3
<b>Figure 1.2</b>	Schematic diagram of sulfur recovery unit	9
<b>Figure 1.3</b>	Membrane reactors based on the principle of configurations A to H	20
<b>Figure 1.4</b>	A conventional membrane reactor system	22
<b>Figure 1.5</b>	Schematic of an integrated membrane reactor system that combines reactor and separator into a single unit	23
<b>Figure 1.6</b>	The three main membrane functions in a membrane reactor	25
<b>Figure 1.7</b>	Membrane reactor with separate feed of reactants	29
<b>Figure 2.1</b>	Fabrication of support membrane: (a) fabricated mould made of mild steel; (b) schematic diagram of the prepared tubular membrane support; (c) muffle furnace; (d) top view of the fabricated tubular ceramic membrane	48
<b>Figure 2.2</b>	Experimental set up for gas permeability test	52
<b>Figure 2.3</b>	Volume weighed particle size distribution of (a) raw sawdust particles and sample mixtures sieved through mesh sizes of (b) 30 B.S.S., (c) 44 B.S.S., (d) 60 B.S.S., (e) 72 B.S.S. and (f) 100 B.S.S.	57
<b>Figure 2.4</b>	TGA/DTA plot of four individual raw materials and SM6 decomposed in presence of nitrogen atmosphere at 10°C/min	62
<b>Figure 2.5</b>	FTIR patterns of 44 B.S.S. mesh screened raw sawdust	63
<b>Figure 2.6</b>	FTIR patterns of 44 B.S.S. mesh screened chemically modified sawdust without thermal modification	64
<b>Figure 2.7</b>	FTIR patterns of 44 B.S.S. mesh screened thermally modified sawdust at 550, 700 and 850 °C	65
<b>Figure 2.8</b>	FTIR patterns of 44 B.S.S. mesh thermally treated sawdust after alkali test	66
<b>Figure 2.9</b>	SEM images of (a) raw and (b,c) alkali-acid treated sawdust, burnt-sawdust sintered at (d) 550, (e) 700, (f) 850 °C and chemical (alkali treated) modification of burnt-sawdust at (g) 550, (h) 700, (i) 850 °C	67
<b>Figure 2.10</b>	EDX patterns of (a) raw and (b,c) alkali-acid treated sawdust, burnt-sawdust sintered at (d) 550, (e) 700, (f) 850 °C and chemical (under alkali treatment) modification of burnt-sawdust at (g) 550, (h) 700, (i) 850 °C	68

<b>Figure 2.11</b>	FESEM micrographs of SM6 sintered at (a) 550°C (b) 700°C and (c) 850°C	72
<b>Figure 2.12</b>	Pore size distribution of the fabricated SM6 membrane sintered at three different temperatures (550, 700 and 850°C) as determined from FESEM images	75
<b>Figure 2.13</b>	X-ray diffraction patterns of (a) the sample mixture sintered at different temperatures 1: kaolinite; 2: feldspar; 3: graphite 4: cellulose 5: xylitol; and (b) kaolinite powder 1: kaolinite (PDF-00-001-0527)	76
<b>Figure 2.14</b>	Effect of pressure on gas permeability for membranes sintered at different temperatures	77
<b>Figure 2.15</b>	EDX analysis of the fabricated tubular ceramic membrane (SM6) before acid-alkali test sintered at (a) 550, (b) 700 and (c) 850°C	79
<b>Figure 2.16</b>	EDX spectrum and data of SM6 membranes after acid (a, b, c) and alkali (a*, b*, c*) test	80
<b>Figure 3.1</b>	Response surface plotted on (a) sodium metasilicate (SM) content and preparation pressure, (b) boric acid (BA) content and preparation pressure, and (c) sodium metasilicate (SM) content and boric acid (BA) content for membrane flexural strength	92
<b>Figure 3.2</b>	Response surface plotted on (a) sodium metasilicate (SM) content and preparation pressure, (b) boric acid (BA) content and preparation pressure, and (c) sodium metasilicate (SM) content and boric acid (BA) content for membrane porosity	95
<b>Figure 3.3</b>	Interaction via (a) sodium metasilicate (SM) content and preparation pressure, (b) boric acid (BA) content and preparation pressure, and (c) sodium metasilicate (SM) content and boric acid (BA) content for membrane flexural strength (circular dots (●) in figures represent design points)	97
<b>Figure 3.4</b>	Interaction via (a) sodium metasilicate (SM) content and preparation pressure, (b) boric acid (BA) content and preparation pressure, and (c) sodium metasilicate (SM) content and boric acid (BA) content for membrane porosity (circular dots (●) in figures represent design points)	98
<b>Figure 3.5</b>	Normal probability plot of residual for (a) membrane flexural strength and (b) porosity	99

<b>Figure 3.6</b>	Plot between residual and predicted response for (a) membrane flexural strength and (b) porosity	100
<b>Figure 3.7</b>	Plot of predicted versus actual values for membrane (a) flexural strength ( $R^2 = 0.98$ ); (b) porosity ( $R^2 = 0.98$ )	101
<b>Figure 3.8</b>	Response surface plot of desirability operating region over SM:BA at preparation pressure set at 9.81 MPa	103
<b>Figure 3.9</b>	XRD patterns of the ceramic membrane (C1: optimized composition, C2: composition for validation) sintered at 550, 750 and 850°C with the formation of inoyite (PDF-00-006-0361) and nephiline (00-019-1176)	105
<b>Figure 3.10</b>	FESEM images of the ceramic membrane surface sintered at (a) 550, (b) 700 and (c) 850°C using optimized composition from CCD analysis	106
<b>Figure 3.11</b>	Effective permeability factor vs. average pressure for the optimized membranes sintered at 550, 700 and 850°C temperatures	107
<b>Figure 4.1</b>	FTIR spectra of the Co-Mo catalysts over $\gamma$ -Al <sub>2</sub> O <sub>3</sub> with low surface area in the range of (a) 300-900 cm <sup>-1</sup> & (b) 3000 to 4000 cm <sup>-1</sup> calcined at 400°C	123
<b>Figure 4.2</b>	FTIR spectra of the Co-Mo catalysts formed on $\gamma$ -Al <sub>2</sub> O <sub>3</sub> (low surface area) at 600°C in the range of (a) 300-900 cm <sup>-1</sup> and (b) 3000-4000 cm <sup>-1</sup>	124
<b>Figure 4.3</b>	FTIR spectra after impregnating Mo-Co precursor over $\gamma$ -Al <sub>2</sub> O <sub>3</sub> (high surface area) calcined at (a-b) 400 °C and (c-d) 600 °C. (e) Comparison of IR spectra between $\gamma$ -Al <sub>2</sub> O <sub>3</sub> with low and high surface area at room temperature	125
<b>Figure 4.4</b>	Comparisons of the XRD spectra of Co-Mo/ $\gamma$ -Al <sub>2</sub> O <sub>3</sub> catalysts of different Mo and Co loadings calcined at (a) 400°C and (b) 600°C for 5 h using $\gamma$ -Al <sub>2</sub> O <sub>3</sub> with low surface area and calcined at (c) 400°C and (d) 600°C for 5 h using $\gamma$ -Al <sub>2</sub> O <sub>3</sub> with high surface area as support	127
<b>Figure 4.5</b>	N <sub>2</sub> adsorption/desorption isotherms for $\gamma$ -alumina (low surface area) based catalysts calcined at (a) 400°C and (b) 600°C with pore volume distribution (inset); (c-d) pore size distribution	128
<b>Figure 4.6</b>	N <sub>2</sub> adsorption/desorption isotherms for $\gamma$ -alumina (high surface area) supported catalysts calcined at (a) 400°C and (b) 600°C with pore volume distribution (inset); (c-d) pore size distribution	129
<b>Figure 4.7</b>	FESEM micrographs of Mo-Co over $\gamma$ -Al <sub>2</sub> O <sub>3</sub> (low surface area) containing (a) 8% Mo, SC1, (b) 12% Mo, SC2, (c) 16% Mo, SC3 calcined	131

at 400°C and (d) 8% Mo, SC1, (e) 12% Mo, SC2, (f) 16% Mo, SC3 calcined at 600°C. FESEM micrographs of Co-Mo over  $\gamma$ -Al<sub>2</sub>O<sub>3</sub> (high surface area) containing (g) 8% Mo, SC1, (h) 12% Mo, SC2, (i) 16% Mo, SC3 calcined at 400°C and (j) 8% Mo, SC1, (k) 12% Mo, SC2, (l) 16% Mo, SC3 calcined at 600°C

- Figure 4.8** ESR spectra of the Mo-Co catalysts of different Mo and Co loadings (SC1 – 8% Mo & 12.67% Co, SC2 – 12% Mo & 4% Co and SC3 – 16% Mo & 5.33% Co) calcined at (a) 400°C and (b) 600°C with  $\gamma$ -Al<sub>2</sub>O<sub>3</sub> having low surface area and (c)  $\gamma$ -Al<sub>2</sub>O<sub>3</sub> (high surface area) 133
- Figure 4.9** H<sub>2</sub> temperature-programmed reduction profile of the Mo-Co/ $\gamma$ -Al<sub>2</sub>O<sub>3</sub> catalysts. Catalysts prepared with (a) alumina having low surface area and (b) alumina (high surface area) maintaining different calcination temperatures 134-135
- Figure 4.10** Particle size distribution of the catalysts having high MD and MSA 136
- Figure 4.11** Raman Spectra of MoO<sub>3</sub> and CoMoO<sub>4</sub> for alumina (high surface area) supported catalyst (SC3) calcined at 350, 400 and 600°C 137
- Figure 4.12** (a) Transmission electron micrograph, (b) EDX study, (c) SAED analysis and (d) pore size distribution of the optimized catalyst with high MD and MSA 138
- Figure 5.1** (a) Eco-ceramic low-cost ceramic tubular membrane; height – 45 mm, diameter – 50 mm and thickness – 10 mm. (b) catalytic membrane after coating of catalyst using solid lubricant. (c) schematic diagram of the novel scheme 143
- Figure 5.2** Porosity of four different membranes coated with MoS<sub>2</sub>, namely, M1 (binder & additive); M2 (binder & without additive); M3 (additive & without binder); M4 (without binder & additive) 148
- Figure 5.3** FESEM images of the MoS<sub>2</sub> coated membrane: (a) binder & additive, M1; (b) binder & without additive, M2; (c) additive & without binder, M3; (d) without binder & additive, M4 149
- Figure 5.4** XRD patterns of (A) commercial MoS<sub>2</sub> powder (B) MoS<sub>2</sub> coated membrane with four different compositions, namely, (a) M1, (b) M2, (c) M3 and (d) M4 150-151

<b>Figure 5.5</b>	FTIR spectra of MoS <sub>2</sub> coated membrane prepared with binder & additive (curve a), M1; binder & without additive (curve b), M2; additive & without binder (curve c), M3; and without binder & additive (curve d), M4	152
<b>Figure 5.6</b>	EDX mapping micrographs: (a) Distribution and deposition of alumina, molybdenum and cobalt along with sulfur particles on (a) M1 (b) M2 (c) M3 (d) M4	154
<b>Figure 6.1</b>	CMR configuration for multi-component mass transport	160
<b>Figure 6.2</b>	Figure 6.2 Schematic diagram of the experimental set up [N.B. – (a) the study is under batch mode; (b) the purpose of showing inlet and outlet features is to assist audiences to better understand the process	163
<b>Figure 6.3</b>	Conversion of H <sub>2</sub> S into elemental sulfur as a function of time with the optimized catalyst: (a) SC3_400°C having maximum MD (93.69%) and MSA (480.51 m <sup>2</sup> g <sup>-1</sup> ), (b) SC4_600°C having minimum MD (1.15%) and MSA (5.94 m <sup>2</sup> g <sup>-1</sup> ), (c) relation between product concentration and overall conversion of reactant with time. (d) Variation of turnover frequency (TF) with time	177
<b>Figure 6.4</b>	Determination of rate constants by plotting $\ln (C_{A0}/C_A)/(C_{A0}-C_A)$ vs $t/(C_{A0}-C_A)$	178
<b>Figure 6.5</b>	FTIR spectra of (a) elemental sulfur (S <sub>8</sub> ) deposited on the catalytic membrane surface, (b) unreacted reactants and gaseous sulfur collected from permeate	180
<b>Figure 6.6</b>	(a) Molar flux of reactant into the membrane as a function of time; (b) change in mole fraction of the reactants with time	182
<b>Figure 6.7</b>	Variation of equilibrium constant with time (curve a), Reaction rate as a function of disappearance of H <sub>2</sub> S evaluated using Eq. (6.12) (curve b) and overall reaction rate calculated on the basis of mass balance using Eq. (6.11) (curve c)	184
<b>Figure 6.8</b>	(a) Overall rate of disappearance of H <sub>2</sub> S by means of material balance inside the reactor obtained from Eq. 6.8. (b) Change in concentration of both H <sub>2</sub> S and SO <sub>2</sub> with time	186

**Figure 6.9** (a) Plot of experimental and theoretical values for overall conversion, selectivity and yield, and (b) plot of regular residual for overall conversion, selectivity and yield

190



# Chapter 1

---

## Introduction and Objectives

# Chapter 1

## Introduction and Objectives

*This chapter presents a brief summary on various air pollutants; their sources and the effect on human health and our environment. Several conventional techniques to separate most damaging industrial pollutant to our society like elemental sulfur are also discussed. Fundamental idea of membrane reactor is also outlined in brief. The necessity of introduction of membrane reactor and catalytic membrane reactor system over the conventional sulfur recovery schemes or systems are also mentioned. The basic functions of catalytic membrane reactors based on different configurations, mode of operations (extractor, distributor, and active contactor), different flow patterns, advantages and various applications along with the research problems are presented precisely. Detailed literature review related to the fabrication of catalytic membrane and their applications are also discussed. A comparison between catalytic membrane reactor and conventional reactors is also mentioned. Possible scopes for further improvement in the fabrication of catalytic membranes and membrane reactors are also specified. Objectives on the fabrication of catalytic membrane reactors including ceramic support preparation, synthesis and deposition of catalyst on the support membrane have been elaborately discussed. The aim of implementing the manufactured catalytic membrane reactor for a novel purpose is also pointed out.*

## 1.1 Introduction

### 1.1.1 Air pollutants, their sources and effects on human health

Air pollution introduces different particulates, biological molecules, or harmful gases on the Earth's atmosphere, such as, ozone, carbon dioxide, nitrogen dioxide, sulfur dioxide and greenhouse gases etc. These air pollutants including particulate matter, lead, toxic air pollutants, chlorofluorocarbons can affect the health, survival, or activities of many living organisms including humans. Air pollutants can be solid particles, liquid droplets, or gases, it can be of natural origin or man-made. These air pollutants are categorised as primary and secondary. Generally, primary pollutants are produced from a process, such as, ash from a volcanic eruption, carbon monoxide gas from motor vehicle exhaust, or the sulfur dioxide released from factories. Secondary pollutants are not released in the ecosystem directly. Rather, secondary pollutants are formed when primary pollutants react or interact with air [1,2].

Several human and industrial activities are the reasons behind the production of major primary pollutants, like, ozone, carbon monoxide, nitrogen dioxide, particulate matter, sulfur dioxide, lead, toxic air pollutants, stratospheric ozone depleters and greenhouse gases [3,4]. Their sources and effects on the environment are presented schematically (see **Figure 1.1**).

### 1.1.2 Industrial sources and separation techniques

Nowadays, it is a great challenge to keep the environment clean and free from toxic and hazardous materials, mainly coming out from chemical and petrochemical industries. These not only hold an important position in the world of economy but also, are the main users of energy resources and a major source of industrial pollution. These industries mainly deal with chemical reactions and separations. The significant step to ease environmental problems related to the process industries is the improvement in efficiency of reaction and separation processes.

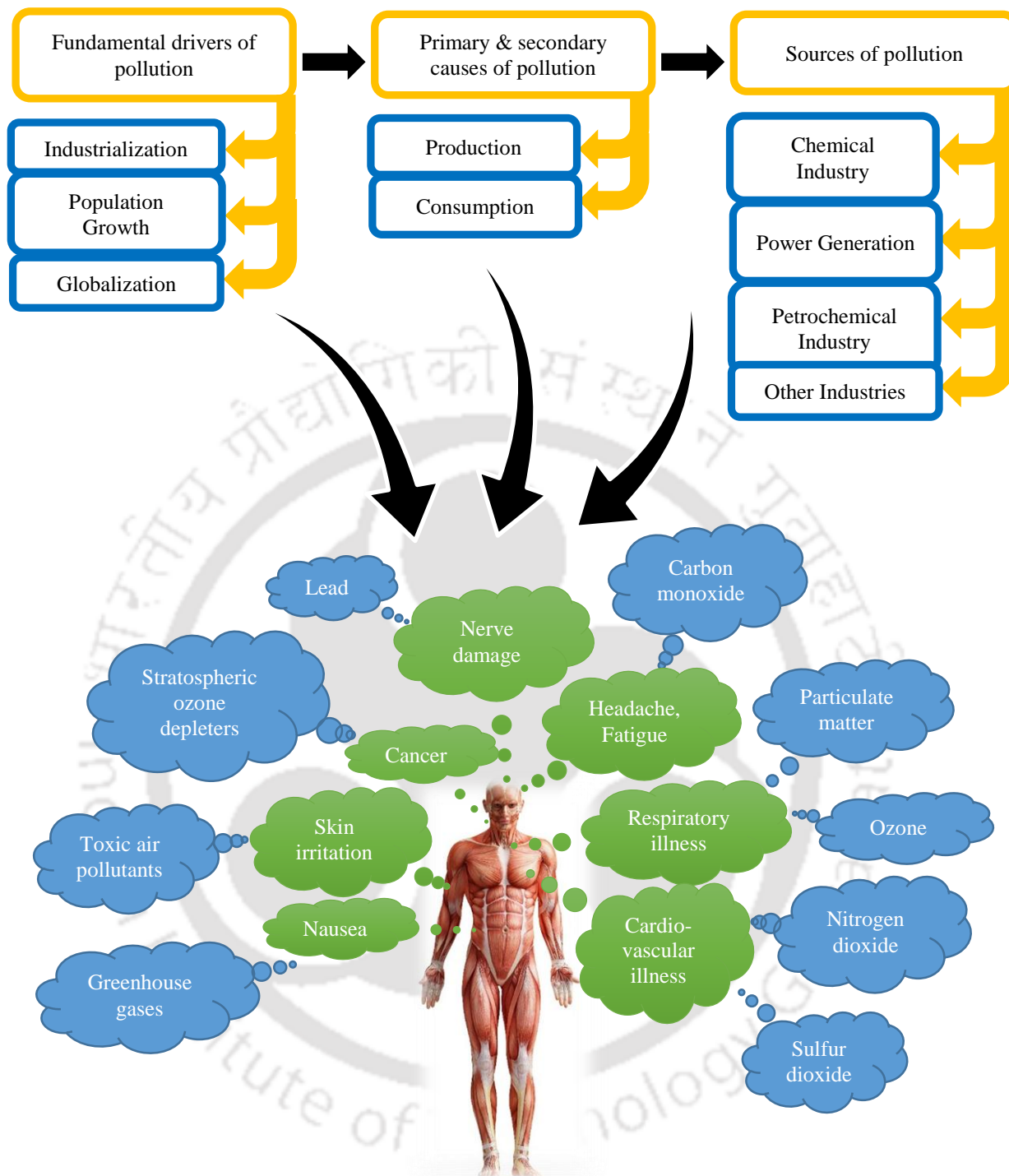


**Figure 1.1** Sources and effects of different air pollutants on human beings

These industries are the main sources of the air pollutants mentioned above, specially, sulfur dioxide gas which produces from fuels. Elemental sulfur is the reason of emission of sulfur dioxide gas when the fuel is burnt. The increasing environmental awareness in the last

few decades has prompted the emergence of stricter regulations covering the threshold limit of sulfur in fuels and effluents to much lower values. The chemical properties of sulfur, are shown in **Table 1.1**. It can causes irritation of the eyes and throat, due to inhalation of sulfur in the gaseous phase. The expected regulation of the sulfur content in the years to come in petroleum liquid fuels is less than 50 ppm by weight. Usually, petroleum products are regarded to constitute four types of sulfur compounds namely alkylbenzothiophenes (~39%), dibenzothiophenes (DBT), alkyl DBT's (~20%) without substitutions at 4 and 6 positions, alkyl DBT's with substitutions at 4 or 6 positions (~26%) [4].

**Table 1.1** Chemical properties of sulfur

Atomic number	16
Atomic mass	32.06 g.mol <sup>-1</sup>
Electronegativity according to Pauling	2.5
Density	2.07 g.cm <sup>-3</sup> at 20 °C
Melting point	388.36 K (for rhombic); 392.6 K (for monoclinic)
Boiling point	717.8 K
vander Waals radius	0.127 nm
Ionic radius	0.184 (-2) nm ; 0.029 (+6) nm
Isotopes	5
Electronic shell	[Ne] 3s <sup>2</sup> 3p <sup>4</sup>
Energy of first ionisation	999.3 kJ.mol <sup>-1</sup>
Energy of second ionisation	2252 kJ.mol <sup>-1</sup>
Energy of third ionisation	3357 kJ.mol <sup>-1</sup>
Crystal structure	Rhombic, monoclinic
Oxidation states	-2, +4 and +6

The reason of removing sulfur from the intermediate product naphtha streams within a petroleum refinery is that sulfur, even in extremely low concentrations, poisons the noble metal catalysts platinum and rhenium in the catalytic reforming units that are subsequently used to upgrade the naphtha streams. Thus, the purpose of removing sulfur is to reduce the sulfur dioxide emissions resulting from using those fuels in automotive vehicles, aircraft, railroad locomotives, ships, or oil burning power plants, residential and industrial furnaces, and other forms of fuel combustion.

### ***Separation of sulfur: Conventional technologies***

Conventional technologies for the removal of organic sulfur are (i) selective adsorption, (ii) sweetening, (iii) oxidative desulfurization (ODS), (iv) bio desulfurization and (v) hydrodesulphurization process utilizing cobalt/molybdenum catalysts using Claus reactor, thereby producing the undesired H<sub>2</sub>S gas as a by-product [5].

### ***Selective adsorption***

Selective adsorption technology involves either the selective removal of sulfur molecules using reduced metals thereby forming sulfides or selective removal of sulfur molecules by adsorbents in the absence of hydrogen under ambient or mild conditions. However, drawbacks of using adsorption technology includes the requirement of sophisticated and complex design structure, high operation and maintenance cost. Furthermore, the cost of solvents used in these process is quite high and the regeneration of adsorbent due to heating becomes an environment concern leading to the formation of SO<sub>2</sub>.

### ***Sweetening***

This process comprises sweetening of sour gas with regenerative solvent like ethanolamine, a liquid absorbent that acts much like the glycol solution in dehydration. After bubbling through the liquid, the gas emerges almost entirely stripped of sulfur. The ethanolamine is processed for removal of the absorbed sulfur and is reused. The main problems that can be encountered in the operation of sour gas treating facilities using chemical solvents are: failure to meet H<sub>2</sub>S specification for product gas; solution foaming in the contactor or regenerator; corrosion in pipes and vessels; solvent losses. Another disadvantage of this process is the corrosive nature of amines which damages plants and rises the operating and maintenance cost.

### ***Oxidative desulfurization***

The oxidative desulfurization of diesel fuel using hydrogen peroxide as an oxidant involves an aqueous/organic bi-phase catalytic system, in which the sulfur-containing compounds are present in the diesel phase while the hydrogen peroxide and the catalyst are present in the aqueous phase. Oxidation reaction rates in biphasic systems are low because of mass transfer limitations across the interface. The reaction may take place at the interface or in the bulk of one of the phases. The rate of the process will be determined either by the rate of the chemical reaction or by the rate of diffusion.

### ***Bio desulfurization***

Bio desulfurization involves removal of sulfur from fossil fuels through a series of enzyme catalysed reactions. However, due to lack of theoretical knowledge about various bacteria and their behaviour at industrial conditions the use of this process is not widespread.

Also the cost of the reactors used to carry out these process is quite high making use of this process infeasible.

### *Claus process*

Hydrodesulphurization, also known as HDS, is a process in which sulfur is removed from crude oil, and oil-derived feedstock for the petrochemical industry, by combining it with hydrogen to form hydrogen sulfide ( $\text{H}_2\text{S}$ ). Since 19<sup>th</sup> century in India, the most significant gas desulfurizing process used for recovering elemental sulfur from gaseous hydrogen sulfide is Claus process. First patented in 1883 by the scientist Carl Friedrich Claus, the Claus process has become the industry standard. A schematic process flow diagram of a basic 3-bed Claus unit is shown in **Figure 1.2**(Redrawn from reference 6). As shown in the **Figure 1.2**, the feed gas to a Claus process unit is burned in a reaction furnace using sufficient combustion air to burn only one-third of the  $\text{H}_2\text{S}$  it contains. That is accomplished by using a flow ratio controller to provide the required ratio of combustion air to feed gas. The reaction furnace pressure and temperature are maintained at about 1.5 bar gauge (barg) and  $1000^\circ\text{C}$ , respectively. At those conditions, the Claus reaction occurs thermally in the reaction furnace (i.e., without requiring any catalyst). About 70% of the  $\text{H}_2\text{S}$  in the feed gas is thermally converted into elemental sulfur in the reaction furnace. The hot reaction product gas, containing gaseous sulfur, is used to produce steam in a boiler (called a waste heat boiler) which results in cooling the gases. The gas is then further cooled and condensed in a heat exchanger while producing additional steam. The condensed liquid sulfur is separated from the remaining unreacted gas in the outlet end of the condenser and sent to product storage.

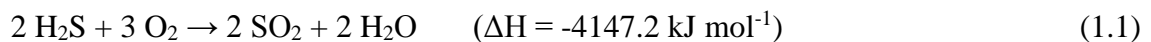
The separated gas is then reheated and enters the first catalytic reactor maintained at an average temperature of about  $305^\circ\text{C}$  where about 20% of the  $\text{H}_2\text{S}$  in the feed gas is converted into elemental sulfur. The outlet product gas from the first reactor is cooled in another condenser

while also producing steam. Again, the condensed liquid sulfur is separated from the residual unreacted gas in the outlet end of the condenser and directed to product storage.

The separated gas from the second condenser is sent to another reheater and the sequence of gas reheat, catalytic reaction, condensation and separation of liquid sulfur from unreacted gas is repeated for the second and third reactors at successively lower reactor temperatures. About 5% and 3% of the H<sub>2</sub>S in the feed gas is thermally converted into elemental sulfur in the second reactor and third reactors, respectively. For a well-designed sulfur recovery plant having three catalytic reactors (as shown in the flow diagram), an overall conversion of at least 98% can be achieved. In fact, the latest modern designs can achieve up to 99.8% conversion. The remaining gas separated from the last condenser is referred to as "tail gas" and is either burned in an incinerator or further desulfurized in a "tail gas treatment unit" (TGTU) [6].

The process mainly consists of three stages, are thermal, catalytic and incineration step. In the thermal step, hydrogen sulfide-laden gas reacts in a sub-stoichiometric combustion at temperatures above 850 °C such that elemental sulfur precipitates in the downstream process gas cooler. The hydrogen sulfide (H<sub>2</sub>S) content and the concentration of other combustible components (hydrocarbons or ammonia) determine the location where the feed gas is burned.

Claus gases (acid gas) with no further combustible contents apart from H<sub>2</sub>S are burned in lances surrounding a central muffle by the following chemical reaction:



This is a strong exothermic reaction generating sulfur dioxide that reacts away in subsequent reactions.

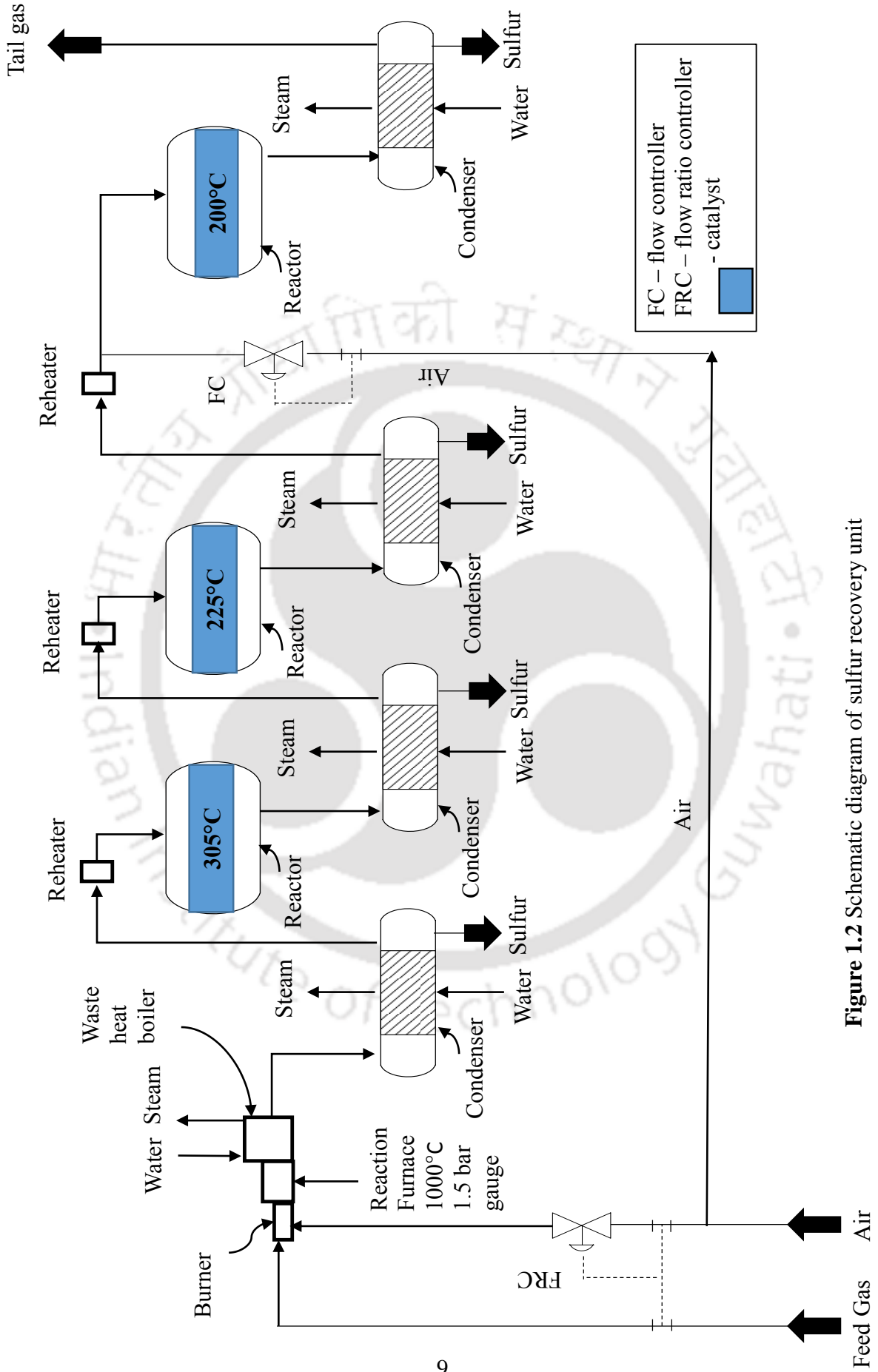
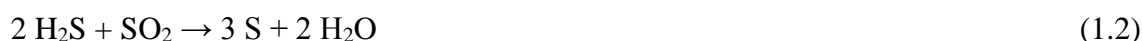
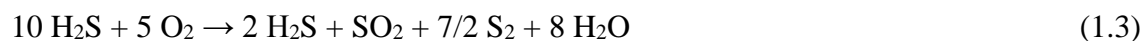


Figure 1.2 Schematic diagram of sulfur recovery unit

The most important one is the Claus reaction:

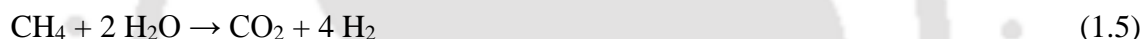


The overall equation is:

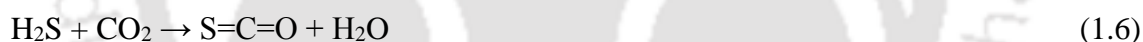


Usually, 60 to 70% of the total amount of elemental sulfur produced in the process is obtained in the thermal process step. Other chemical processes taking place in the thermal step of the Claus reaction are:

- The formation of hydrogen gas:



- The formation of carbonyl sulfide:



- The formation of carbon sulfide:



A catalytic reactor contains a bed of catalyst with a depth of about 90 to 120 cm. In the refineries, the most widely used Claus reaction catalyst is porous aluminum oxide ( $\text{Al}_2\text{O}_3$ ), commonly referred to as alumina. The alumina catalyst owes its activity to a very high surface area of  $300 \text{ m}^2 \cdot \text{g}^{-1}$  or higher. About 95% of that surface area is provided by pores having diameters of less than 8 nm (80 angstroms). The catalyst not only increases the kinetics (i.e., the rate of reaction) of the Claus reaction [Eq. (1.1)], but it also hydrolyses the carbonyl sulfide (COS) and carbon disulfide ( $\text{CS}_2$ ) that are formed in the reaction furnace. Other Claus catalysts based on titanium dioxide ( $\text{TiO}_2$ ) are also used due to higher activity for the hydrolysis of COS

and CS<sub>2</sub> which allows the first Claus reactor to operate at lower temperatures compared to alumina catalysts. But, they are significantly more expensive than the alumina catalysts.

The catalytic recovery of sulfur consists of three sub steps: heating, catalytic reaction and cooling plus condensation. These three steps are normally repeated a maximum of three times. Where an incineration or tail-gas treatment unit (TGTU) is added downstream of the Claus plant, only two catalytic stages are usually installed. Using two catalytic stages, the process will typically yield over 97% of the sulfur in the input stream [6].

Though the process is well established, it has some drawbacks in terms of financial aspects. To recover 99% sulfur, not only three catalytic bed reactors are required in catalytic step but also often requires subsequent Tail gas treating unit or SUPERCLAUS<sup>®</sup> step which is very time consuming as well as not healthy for financial aspect in refineries making the existing system costlier. Even, catalytic reaction and separation occur in two different units, another reasons to make the process costlier in industries. However, this technology is being identified to economically competitive to remove many classes of compounds containing sulfur other than aromatic dibenzothiophene (DBT) and 4,6-alkyl substituted DBTs.

To circumvent the above problem, an alternative scheme has to be introduced which will be economic as well as provide high separation performance.

A membrane-based reactive separation process (also known as membrane reactor process), which is a combination of two distinct functions, i.e. reaction and separation, has been around as a concept since the early stages of the membrane field, but have only attracted considerable technical interest during the last decade or so. These processes have some significant industrial interests as these are promised to be compact and less capital intensive, and because of their promise for probable extensive savings in the processing costs.

### 1.1.3 Membrane separation processes

Nowadays membrane-based separation processes using membrane reactors (MRs) are finding extensive, and ever increasing use in the petrochemical, food and pharmaceutical industries, in biotechnology, and in a variety of environmental applications, including the treatment of contaminated water streams and air. The advantages of the membrane separation processes over the conventional methods (adsorption, absorption, distillation etc.) are minimal energy consumption and nominal initial capital investment.

Membranes are classified either by the nature of the membrane (porous or dense) or by the type of material (organic, polymer, inorganic, metal, etc.). Even membranes are also classified by their structure i.e., symmetric or asymmetric. Membranes are manufactured in a diverse range of geometries which include flat, tubular, and multi-tubular, hollow-fiber, and spiral-wound membranes. The type of membrane geometry depends on the material made from ceramic membranes, usually, come in tubular, flat and multi-tubular geometries, whereas spiral-wound and hollow-fibre membranes are made of polymers. In recent past, the global demand for membrane modules is estimated at approximately 15.6 billion USD in 2012. Driven by new developments and innovations in material science and process technologies, global increasing demands, new applications, and others, the market has grown around 8% annually in 2013-14. It is forecast to increase to 21.22 billion USD in 2016 and reach 25 billion in 2018 [7].

### 1.1.4 Membrane reactors

A membrane reactor is a plug-flow reactor that contains an additional cylinder of some porous material within it, kind of like the tube within the shell of a shell-and-tube heat exchanger. This porous inner cylinder is the membrane that gives the membrane reactor its name. With respect to conventional reactors, a membrane reactor (MR) permits the improvement of the

performances in terms of reaction conversion, products selectivity, and so on. In fact, by means of the so-called “shift effect”, the thermodynamic equilibrium restrictions can be overcome. At least, MRs behaviour could be the same of a conventional reactor working at the same MRs operating conditions. There are variety of reactor configurations in the classification of membrane reactors according to the design and application of membrane reactor to the particular reaction, are listed in **Table 1.2**.

In catalytic membrane reactor (CMR), the membrane exhibits catalytic activity, causing the location of reaction and separation to coincide. The catalytic activity of the membrane can be inherent to the membrane material or can be achieved by coating the membrane with a catalytically active material. Catalytic non-permselective membrane reactor (CNMR) has catalytic property but only distribute the reactant for the enhancement of yield and selectivity of the product. It is only used to provide a well-defined reactive interface. In recent past, the mostly used reactor configuration in research study is packed bed membrane reactor (PBMR), in which the membrane provides only the separation function. The membrane might separate the desired product from the mixture products at the downstream, or simply distribute the reactant for the purpose of increasing reaction site, respectively. In order to provide an additional catalytic function in the PBMR configuration, Packed-bed catalytic membrane reactor (PBCMR) is introduced. For better control of process temperature packed-bed should be replaced by a fluidized-bed (FBMR or FBCMR)

Biotechnology is another area in which membrane-based reactive separations are attracting great interest. There, membrane processes are coupled with industrially important biological reactions.

**Table 1.2** Classification of membrane reactors [8]

Description	Features
<b>CMR:</b> Catalytic membrane reactor	<ul style="list-style-type: none"> <li>• A membrane with intrinsically catalytic layer or a membrane prepared by catalytic material</li> <li>• Both separation and reaction occur at the membrane surface</li> </ul>
<b>CNMR:</b> Catalytic non-permselective membrane reactor	<ul style="list-style-type: none"> <li>• A membrane providing catalyst site but could not separate every substances</li> <li>• CMR, mostly acts as reactant distributor than separator</li> </ul>
<b>PBMR:</b> Packed-bed membrane reactor	<ul style="list-style-type: none"> <li>• Catalyst packed either in the interior or exterior the membrane volume</li> <li>• Membrane acts as reactant distributor</li> </ul>
<b>PBCMR:</b> Packed-bed catalytic membrane reactor	<ul style="list-style-type: none"> <li>• Catalyst packed either in the interior or exterior the membrane volume</li> <li>• Membrane prepared by catalytic material and functions to separate certain substances</li> </ul>
<b>FBMR:</b> Fluidized-bed membrane reactor	<ul style="list-style-type: none"> <li>• Similar as PBMR but catalyst is not packed within the reactor</li> <li>• Has better temperature control than PBMR especially for exothermic process</li> </ul>
<b>FBCMR:</b> Fluidized-bed catalytic membrane reactor	<ul style="list-style-type: none"> <li>• Similar as FBMR but membrane with catalytic properties</li> </ul>

These include the broad class of fermentation-type processes, widely used in the biotechnology industry for the production of amino acids, antibiotics, and other fine chemicals. Membrane-based reactive separation processes are of interest for the continuous elimination of metabolites, the immobilization of bacteria, enzymes, or animal cells in the production of many high-value added chemicals.

Membrane bioreactors (MBR) have been extensively studied in the food and pharmaceutical industries. The dairy industry, in particular, has been a pioneer in the use of microfiltration (MF), ultrafiltration (UF), nanofiltration (NF), and reverse osmosis (RO) membranes. Applications include the processing of various natural fluids (milk, blood, fruit juices, etc.), the concentration of proteins from milk, and the separation of whey fractions, including lactose, proteins, minerals and fats. These processes are typically performed at low temperature and pressure conditions making use of commercial membranes [8].

MBR are finding fertile ground for application in biochemical synthesis for the production of a broad spectrum of products. These ranges from food, liquid fuels (e.g., ethanol), and plant metabolites, to fine chemicals, including medical products, flavouring agents, food colours, fragrances, etc. For the synthesis of high purity pharmaceutical and food products membranes may offer advantages over the more conventional separation techniques like distillation, evaporation, crystallization etc. This is because they are simpler, less energy intensive, and can operate under the mild conditions required to maintain biological, or enzymatic activity for the synthesis of biochemical, which are sensitive to heat.

The way membranes (in various forms, i.e., cylindrical, coaxial, flat-sheet, spiral-wound, and hollow-fibre, etc.) couple with the bioreactor depends on the role of the membrane performance. The simplest configuration consists of two separate but coupled units, one being the bioreactor the other the membrane module. The alternate configuration involves coupling of membrane and bioreactor into the same unit [9].

A growing application of MBR is in wastewater treatment. Conventionally, wastewater treatment is carried out either by physicochemical techniques or by biological processes. The physicochemical techniques often simply transfer the contaminants in the waste water streams into a different medium that must, itself, be disposed of, or, when they destroy them, they often

also generate toxic by-products, which are difficult to eliminate. The biological processes have an advantage, in that they transform the complex organic contaminants into simple, harmless gaseous or water-soluble compounds, together with residual sludge. On the other hand, the conventional biological treatment at the same point have the disadvantage that one must physically separate the biocatalyst from the treated water. However, for heavily polluted wastewaters, fast growing biomass clogs the beds, and results in bed shutdowns, and the need for frequent regeneration.

Though MBR offer advantages over the conventional bioreactors, they, themselves are not completely free of problems. One such key problem relates to changes in biocatalyst activity. This is a serious concern for whole-cell MBR, when the cells are immobilized in the membrane's pore structure. For enzymatic MBR, an important problem is the intrinsic decrease in activity as a result of the enzyme's immobilization on the membrane support or the grafting onto various macromolecules in order to increase its molecular size and improve its retention by the membrane. One of the most serious problems encountered with MBR is biofouling, which typically manifests itself by a dramatic decrease over time in permeate flow. It may be caused by adsorption on the membrane surface and in its internal porous structure of the various metabolites cells produce, and of the coagulated proteins from lysed cells. These accumulate in the reactor over time, and also tend to increase the solution viscosity. Another cause of biofouling is pore plugging when cells are fixed in the membrane, thus, considerably decreasing mass transfer [10].

#### **1.1.4.1 Classification of MRs based on their configuration**

Catalytic reactors based on ceramic membrane are classified into three categories and these are (a) Inert membrane reactors (IMR), used to add or remove certain species from the

reactor without direct participation of membrane in the reaction, (b) Catalytic membrane reactors (CMR), itself a catalyst or become catalytically active during preparation by addition of catalyst precursors, and (c) Combination of CMR and IMR, catalytically active both by inside and outside of the membrane. These categories are explained by different configurations and these are labelled as Configuration A, B, C, D, E, F, G and H as shown in **Figure 1.3**. Inert membrane reactors (IMR) are explained by configuration A, used to add or remove particular species from reactor without direct participation of the membrane in reaction. The removal of at least one reaction product involves equilibrium displacement and offers higher reaction yield, e.g., Removal of hydrogen in dehydrogenation reactions is the most widely used application for this type of configuration. This configuration is also been fit to other processes such as decomposition of  $H_2S$  and  $H_2O$  and production of synthesis gas [11,12].

**Configuration A** provides both selective (e.g. Pd or Ag-based alloys on ceramic substrates) and preferential (removal of product silica, alumina, titania, glass, zeolite membranes etc.) separation as it is confirmed by several scientists. In this case, the membrane does not participate in the reaction directly, but it is used to add or remove certain species from the reactor. The most widely used application involves equilibrium displacement by removal of at least one reaction product [13,14].

**Configuration B** offers higher yield through reaction coupling. In this case, on both sides of the membrane, complementary processes are run that use either the permeated species (chemical coupling, e.g., dehydrogenation/hydrogenation, or dehydrogenation/combustion reactions), or the heat generated in the reaction (thermal coupling, exothermic/endergonic processes). The reactions often use different catalysts, which would be packed on opposite sides of the membrane tube [15,16].

**Configuration C** describes the distribution of a reactant to a fixed bed of catalyst packed in the opposite side of the membrane. IMRs of this configuration (may be meso- or microporous membranes) have already been used successfully as oxygen distributors in methane oxidative coupling [17,18] and the production of olefins and oxygenates [19,20] from the oxidation of alkanes. The membrane used for the distribution of oxygen in oxidation processes is safer as it reduces formation of hot spots, runaway reactions and gives greater selectivity through control of the concentration of the selected species along the reactor with respect to the conventional feed arrangements. Porous membranes with a dense layer can also be applied for reactant distribution but have some difficulties in attaining high permeation fluxes related to oxidation reactions.

Reactant distribution can also be achieved using porous membranes with a thin but dense permselective layer. In the case of oxidation reactions, this would have the important advantage of using air instead of oxygen in the oxygen-supply side. However, there are few results reported to date, which is mainly due to the difficulties in attaining sufficiently high permeation fluxes (which is usually achieved by reducing the thickness of the dense layer), while at the same time maintaining the membrane properties during prolonged exposure at operating conditions. The only clear advantage with respect to reactant distribution using porous membranes would be available from **Configuration D** where at least in principle, the oxygen species transported through the membrane could react before recombination and desorption takes place. This would completely avoid the presence of gas phase oxygen, and could certainly represent a valuable alternative provided that a membrane with sufficiently high reaction selectivity and permeability to oxygen can be developed. In this case the reaction on one side of the membrane acts as an efficient oxygen sink resulting in an enhanced oxygen transport across the membrane.

*Configuration E* defines the separation of reactants on both sides of a porous catalytic membrane in which the reaction takes place in a small zone or a plane inside the porous structure as the reaction rate is higher than the mass transport, avoiding the slip of reactants to the opposite side and also helps to reduce the unwanted side reactions. By changing the reactant concentrations outside the membrane, the position of the reaction plane can be shifted to a new location where transport rates to the reaction zone are again matched by the reaction stoichiometry, which gives a lower residence time in the reaction zone, and also reduces further reaction of partial oxidation products [21]. The same principle has been demonstrated with experiments and model calculation by CO [22] and H<sub>2</sub>S oxidation [23]. The performance of a membrane reactor with separate feeding of reactant for the catalytic combustion of methane based on this concept has been reported recently [24].

*Configuration F* is a modified version of configuration C. The objective of this configuration is to minimize the concentration of oxygen in the reacting environment and to deliver a sharp distribution of the active component across the entire membrane [25-27]. In this case, the goal is the same (reduce the concentration of oxygen in the reacting environment), although the oxygen partial pressure is now lowered by feeding it through a diffusion layer of sufficient resistance. Oxygen diffusion can take place by itself or in the presence of a stagnant fluid filling the pores of the membrane. This can be achieved by feeding an inert species at approximately the same partial pressure to both sides of the membrane. The diffusion zone is followed by a catalytic layer, where the reaction of oxygen and the reactant permeated from the opposite side takes place.

The purpose of using *Configuration G* is to improve the contact in gas-liquid-solid systems by providing a distinct contact zone, as shown in **Figure 1.3**.

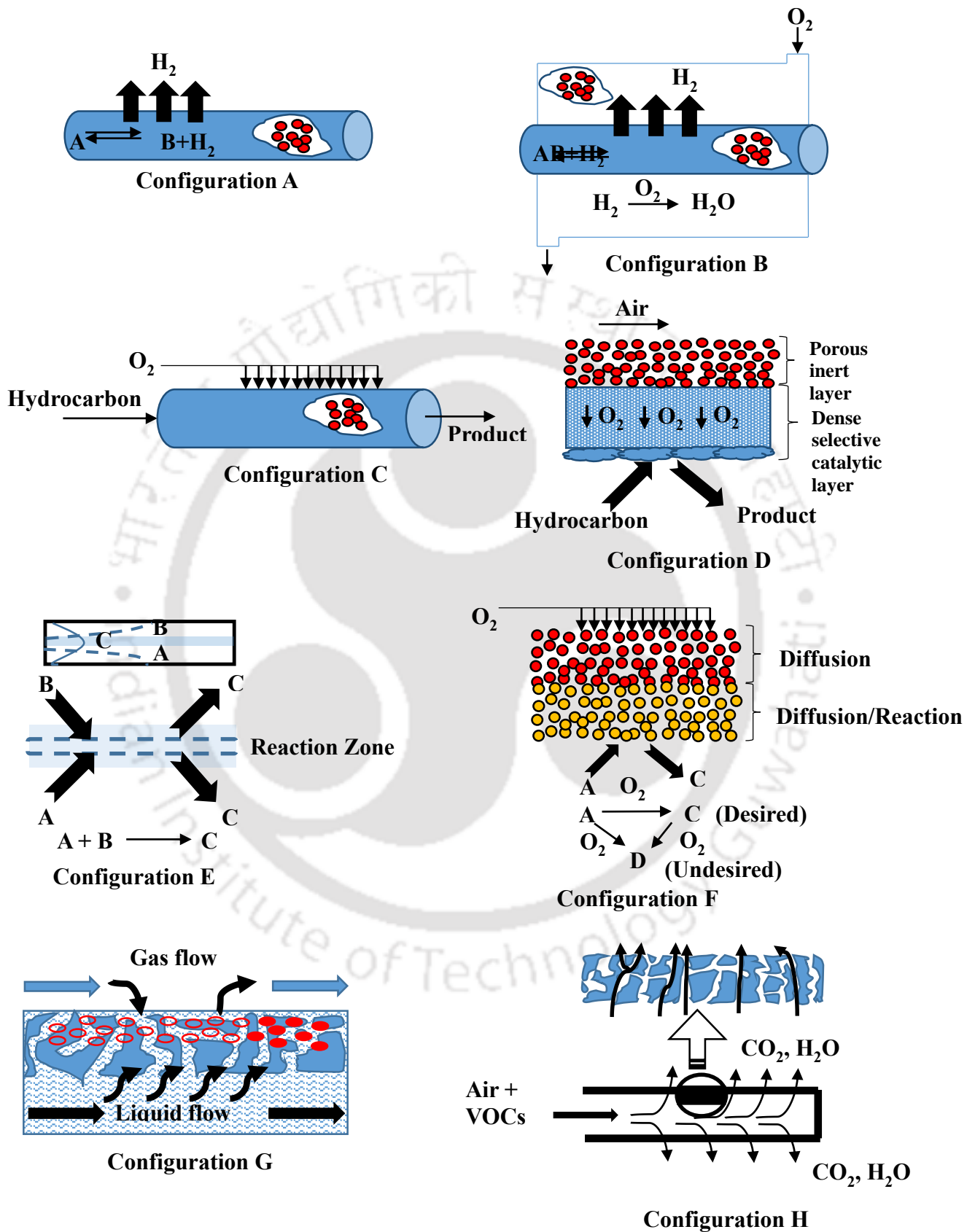


Figure 1.3 Membrane reactors based on the principle of configurations A to H

This configuration has the potential to overcome the difficulty of catalyst recovery that appears in slurry reactors. The concept has already been popular in the case of hydrogenation reactions over Pt/Al<sub>2</sub>O<sub>3</sub> catalysts [28,29].

*Configuration H* delivers the same idea like configuration G. The last two configurations aim to improve contact efficiency as well as conversion by decreasing mass transfer resistance. This approach has been employed to prepare a catalytically modified fly ash filters for alcohol dehydration and for the reduction of the nitrogen oxides with NH<sub>3</sub> [30,31].

### 1.1.5 Catalytic membrane reactor (CMR)

A large number of research works in the field of membrane reactors (MRs) have been published since 1960 when MRs had been introduced only as a concept in the field of membrane technology. In such an integrated process, the membrane is used as an active participant in a chemical transformation for increasing the reaction rate, selectivity and yield. Thus membrane-based reactive separation processes have been introduced, i.e., combination of both separation and reaction in a single unit, is generally termed as catalytic membrane reactor (CMR). The significant benefit of using CMR is the capacity to maintain the synergistic effect between reaction and separation [7]. Two important parameters are always in considerations at the time of preparation of catalytic membrane i.e. selectivity and permeability. Selectivity means the ability of a membrane to allow only some substances to enter the cell of the membrane not the other substances which is related to purity of the substance which is being separated. Permeability is expressed as flux, rate of diffusion of molecules per unit area per unit time which is related to the amount of substance removal, is being separated.

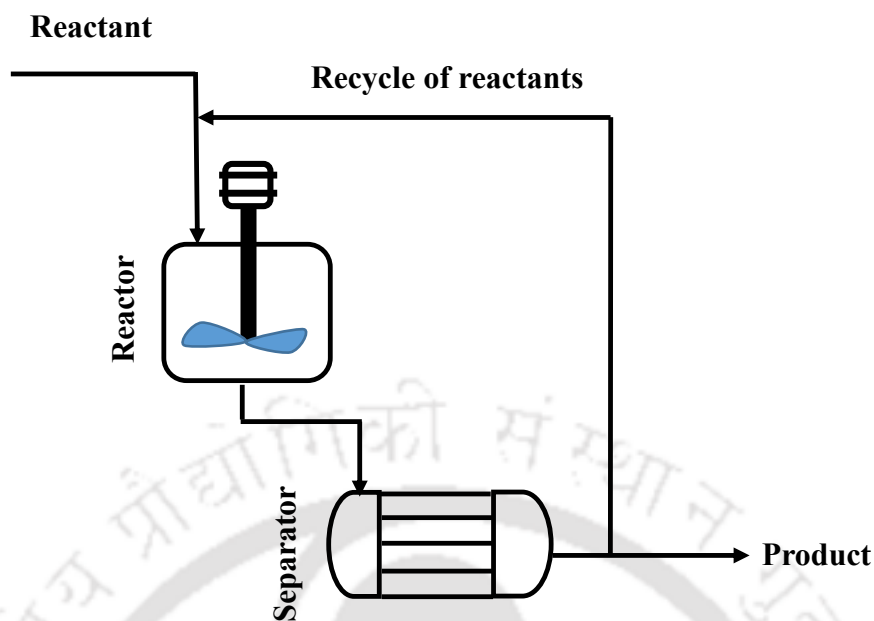


**Figure 1.4A** conventional membrane reactor system

The conventional membrane reactor system used before 1980s is shown in **Figure 1.4**. **Figure 1.5** displays the new concept of having reaction and separation together in a single unit. Other advantages of catalytic membrane reactors are less energy consumption, simple design and ability of achieving high yield or selectivity which make this concept popular [8].

Several investigations have discussed catalytic membrane reactors (CMRs) concept and their various potential benefits, such as, increased reaction rate, enhanced selectivity and yield for a variety of reactions involving basic functions of membrane as extractor, distributor or contactor [32] and different configurations [33,34]. Numerous review articles related to the applications of CMR have already been published in recent pasts [35]. But there is tons of scope for further improvement of CMRs in different applications, especially in petroleum industries.

In the petrochemical industry, olefins such as ethylene and propylene are the most important chemicals used for the production of polyolefins, namely, polyethylene, polypropylene, styrene, ethyl benzene, ethylene dichloride, acrylonitrile, and isopropanol. An

important step in the manufacture of olefins is large-scale separation of the olefin from the corresponding paraffin [36].

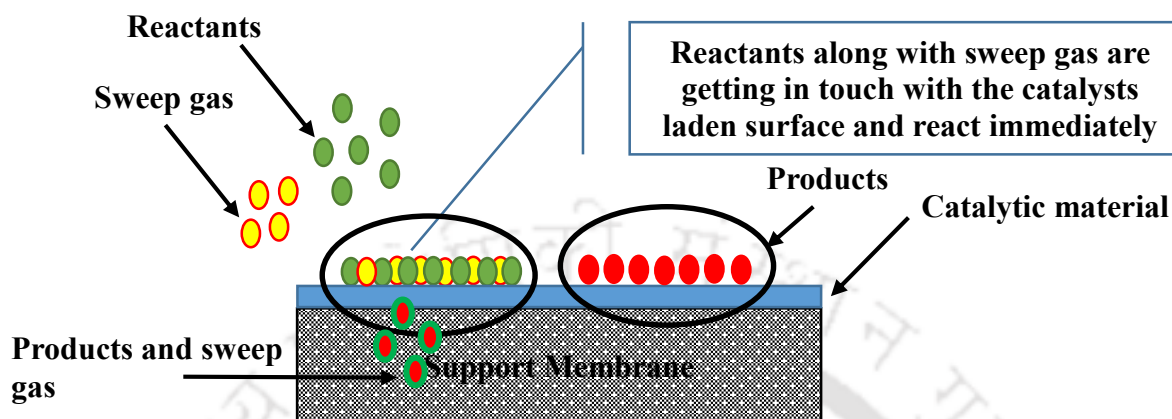


**Figure 1.5** Schematic of an integrated membrane reactor system that combines reactor and separator into a single unit

Furthermore, dehydrogenation, oxidative coupling of methane, steam reforming of methane, removal of sulfur (Claus reaction) and water gas shift reaction are some important reactions in the petrochemical industry. Membrane gas separation is attractive because of its simplicity and low energy cost, but it has one major drawback which is the reverse relationship between selectivity and permeability. Petrochemical waste streams may contain phenolic compounds or aromatic amines. These are highly toxic and at high concentrations inhibits biological treatment. Membrane aromatic recovery system (MARS) is a relatively new process for recovery of aromatic acids and bases. Wastewater in petrochemical industry is currently treated by activated sludge process with pre-treatment of oil/water separation [8]. Tightening effluent regulations and increasing need for reuse of treated water have generated interest in the treatment of petrochemical wastewater with the advanced membrane bio-reactor (MBR) process. Strict environmental rules and guidelines for pollutants have caused attention in the separation of pollutants like sulfur compounds with the advanced Claus process. In refineries,

presently, almost 99% sulphur is separated from sulfur-laden by-product gases (contain hydrogen cyanide, hydrocarbons and sulfur dioxide etc.) using three Claus reactors (converter) by thermal and catalytic step.

#### 1.1.5.1 Synergistic effect of separation and reaction

The conventional packed bed reactor has limitation of the reaction equilibrium. In packed bed reactor the reactants are premixed and brought into contact with the reaction products, inducing the uncontrollable reaction between products and intermediate or reactant to the undesirable one. The synergistic effect of separation and reaction occur simultaneously within a single unit is particularly apparent for reactions limited by thermodynamic equilibrium considerations, for example, the catalytic hydrocarbon dehydrogenation or esterification reactions [32].

The membrane functions as the separator of the desired product from the mixture stream, encouraging the reaction to proceed on the right side of reaction and producing more products; in other words, shifting the equilibrium of the reaction “to the right” (according to Le Chatelier’s Principle) for higher conversion. Meanwhile, this will enhance the selectivity and yield of the product by preventing the further conversion of desired product to the undesired one for certain reactions.

Some of the porous inert membranes, however, are used as the distributor of the reactants in order to elongate the reaction site along the membrane, providing more reaction site but mitigating the hot spot of reaction zone as compared to the catalyst bed in the packed bed reactor.

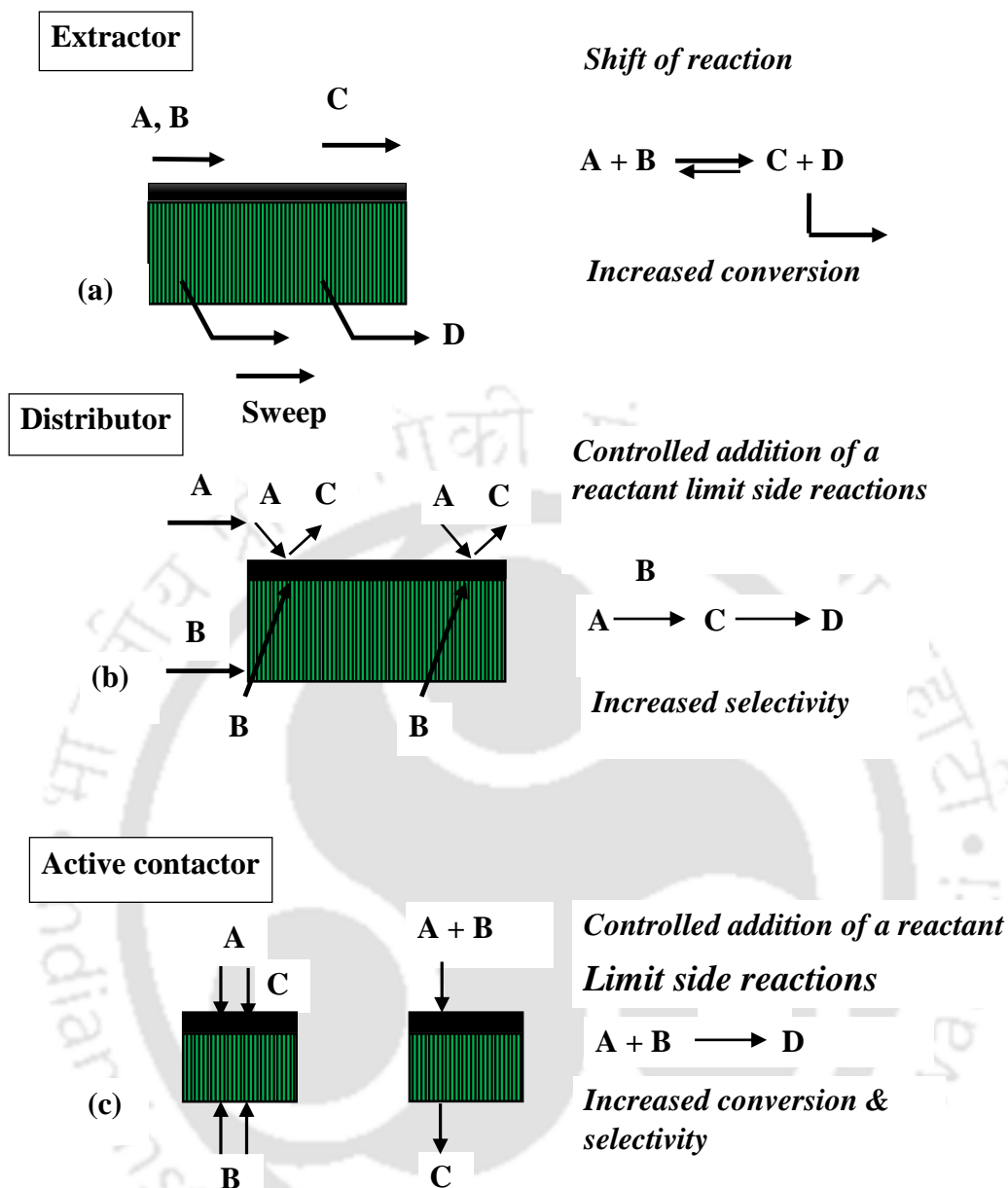


**Figure 1.6** The three main membrane functions in a membrane reactor

### 1.1.5.2 Membrane functions in CMR and applications

The basic functions of porous ceramic membranes in membrane reactors are divided into three primary categories and these are, as shown in **Figure 1.6** [33]:

**(i) An extractor:** the removal of product(s) increases the reaction conversion by shifting the reaction equilibrium;

**(ii) A distributor:** the controlled addition of reactant(s) limits side reactions and increases the selectivity;

**(iii) An active contactor:** the controlled diffusion of reactants to the catalyst can lead to a catalytic reaction zone and offers higher conversion and selectivity.

The MR extractor mode has been successfully investigated to increase the conversion of a number of equilibrium limited hydrogen producing reactions, such as, alkane dehydrogenation, by selectively extracting the hydrogen produced [8], the water gas shift, the steam reforming of methane and the decomposition of  $\text{H}_2\text{S}$  and  $\text{HI}$ , etc. The two important factors controlling the efficiency of the process are  $\text{H}_2$  permselectivity of the membrane and its permeability. Except  $\text{H}_2$  removal, some decomposition reactions in which  $\text{O}_2$  is removed have also been studied in extractor mode [36]. Reactive separations for light alkane dehydrogenation reactions to produce olefins have also been effectively executed using inorganic porous membranes.

Propane dehydrogenation reaction has been studied in a packed bed membrane reactor using a microporous  $\text{Si}/\text{Al}_2\text{O}_3$  membrane made by chemical vapor deposition or chemical vapor infiltration (CVD/CVI) with a  $\text{H}_2$  permeance of around  $1.4 \times 10^{-9} \text{ mol.m}^{-2}.\text{Pa}^{-1}.\text{s}^{-1}$ , and a  $\text{H}_2/\text{C}_3\text{H}_8$  permselectivity in the range of 70-90 at  $500^\circ\text{C}$ . Authors reported conversion had twice as high as the equilibrium value in the PBMR at  $500^\circ\text{C}$  [37,38].

The parallel reactions like oxy-dehydrogenation of hydrocarbons, oxidative coupling of methane are the typical examples of the distributor mode MR. Membranes are generally used to control the supply of  $\text{O}_2$  in a fixed bed of catalyst in order to by-pass the flammability area

and to separate the alkane from  $O_2$  in oxidative coupling of methane. Membranes are applied in MRs to optimize the  $O_2$  profile concentration along the reactor and to maximize the selectivity in the desired oxygenate product. This concept has also a beneficial role for the high temperature in exothermic reactions [39]. The first study of oxy-dehydrogenation of hydrocarbons using porous membranes was in the CMR configuration [40].

In the active contactor mode, the membrane acts as a diffusion barrier and is not permselective but catalytically active. The concept is used with a forced flow-mode or with an opposing reactant mode i.e., the transportation of one reactant through the membrane is in the opposite direction of another reactant. The forced flow contactor mode is studied for enzyme-catalysed reactions [8], total oxidation of volatile organic compounds [41], oxidative coupling of methane [42], selective hydrogenations [43], photocatalytic oxidation of carbonyl compounds and bio aerosols [44]. The selectivity of alkene hydrogenation triphasic reactions can also be enhanced when both the alkene and hydrogen are forced to pass through a microporous catalytic membrane [45].

The opposing reactant contactor mode applies to both equilibrium and irreversible reactions [46]. In this reactor, the different reactants are fed separately at the two sides of a catalytically active membrane. In such case, a small reaction zone forms in the membrane in which reactants are in stoichiometric ratio. In this arrangement a permselective membrane is not essential, the membrane only supplies the reaction zone. The partial pressure difference is the force which help the reactants to diffuse towards each other in catalytic zone.

The aim behind this concept is to attain full conversion of the pollutant, and to avoid its slippage out of the reactor. If the reaction kinetics is faster than the mass transport in the membrane, a reaction zone is formed which prevents the side reactions. This concept have been demonstrated for the selective catalytic reduction (SCR) of nitric oxide with ammonia to

nitrogen and water [47]. The Claus reaction between hydrogen sulfide and sulfur dioxide in a CMR using this concept are studied earlier [21]. Hydrogen sulfide ( $H_2S$ ) and sulfur dioxide ( $SO_2$ ) have been fed on the opposite sides of the membrane and the reaction take place within the membrane itself. It is reported that using this kind of system, undesired side reactions can be avoided by properly adjusting the operating conditions. Triphasic (gas/liquid/solid) reactions (e.g. olefin hydrogenation) can also be improved by using this concept, which are limited by the diffusion of the volatile reactant [28,48]. The other applications using this concept are in the area of oxidation of carbon monoxide, catalytic combustion of propane, oxidative dehydrogenation of propane, catalytic combustion of methane and catalytic combustion of natural gas etc.

### 1.1.5.3 Opposite flow mode catalytic membrane reactors

The basic principles and applications of opposite reactant mode CMR concept along with various alternative membrane reactor concepts are briefly discussed below. The concept is shown pictorially in **Figure 1.7**. The literatures dealing with catalytic membrane reactors in opposite-flow mode are limited. However, the concept is highly appreciable performing several catalytic reactions in gas phase.

Catalytic membrane reactors with separate feed of reactants resulting in excellent mass transfer between fluid and membrane, avoid slip (the reaction takes place entirely inside the membrane). Using this kind of membrane reactors can minimize thermal runaways and can assist to avoid undesired side reactions by properly adjusting the operating conditions. This type of reactors are easily controllable and exclusively applied for combustion processes as no explosive mixture will build up and safety will increase. Claus reactions are studied to realize

the effect of reversibility of the reaction and pressure difference on the flux of the gaseous mixture.

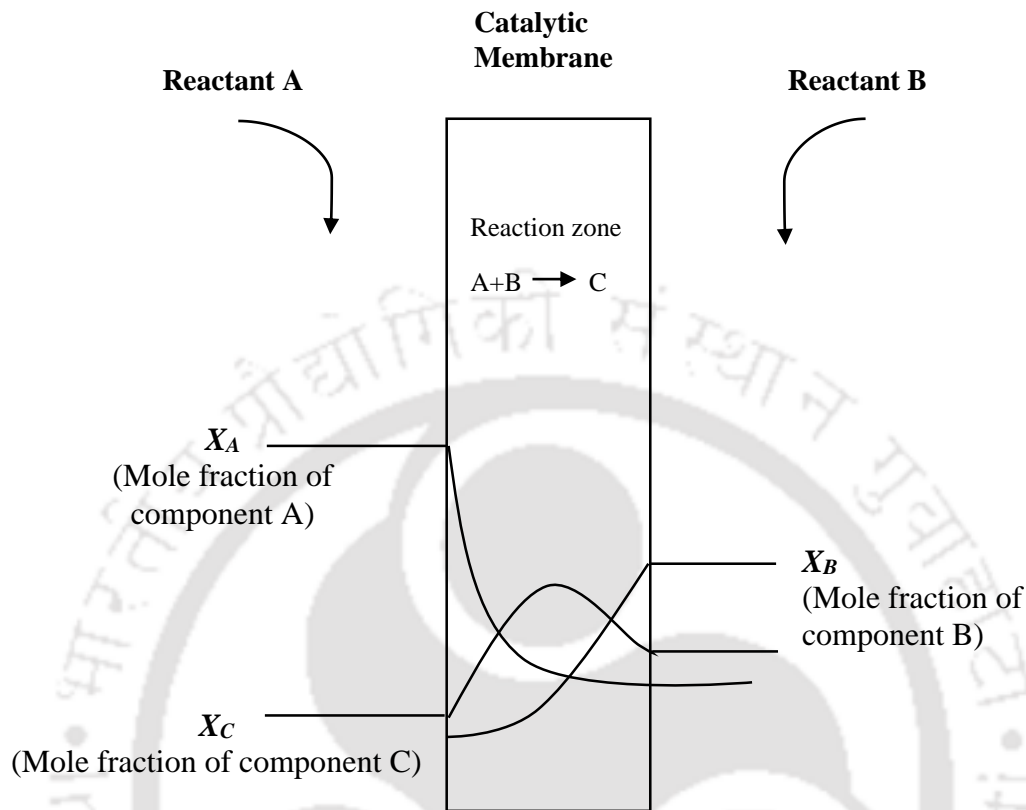


**Figure 1.7** Membrane reactor with separate feed of reactants

### ***Hydrogen sulphide ( $H_2S$ ) laden gas***

The first application of a catalytic membrane reactor is reported using simplified model with separate feed of reactant [49]. By means of mathematical modelling of molecular diffusion and viscous flow of an instantaneous and reversible Claus reaction [50] inside the membrane, catalytic membranes are prepared with  $\alpha\text{-Al}_2\text{O}_3$  with a mean pore diameter of 350nm, a porosity of 41% and a thickness of 4.5mm, impregnated with  $\gamma\text{-Al}_2\text{O}_3$ . In this study, a mathematical model has been developed to understand the effect of reversibility of the reaction and pressure difference on the flux of the gaseous mixture in the membrane reactor consisted of two well mixed chambers.

The influence of reversibility has been investigated by means of a simulation which is carried out at temperatures of 200°C and 300°C in absence of a pressure difference. The simulated results refers reversibility of the reaction mainly arises for a lower equilibrium constant of the Claus reaction. According to the concept of this reactor, reaction zones can be shifted from one place to another by varying the ratio between the driving forces for diffusion of the reactants. In this reactor setup, the mass transfer resistances in the gas phase is important, especially, when a pressure difference over the membrane is vital but a moderate pressure difference does not affect the basic principle of this reactor.

In another work, a mathematical model based on dusty gas model (DGM) using Claus reaction have been proposed which describes mass transport due to molecular diffusion and viscous flow combined with an instantaneous reversible reaction in a membrane reactor with opposite feed of reactants [51]. It is concluded from a comparative study that the previously presented simplified model qualitatively predicts correct molar fluxes including the slip of reactants to the opposite sides of the membrane both in absence and presence of a moderate pressure difference over the membrane. The mathematically predicted conversion of sulphur at temperatures of 220°C and 268°C are presented to be 10 to 20% lower than the molar fluxes predicted by theoretical model. Conversions based on pressure difference demonstrate that the transport mechanism follows surface diffusion. No slip of reactant is observed until the pressure difference is up to 0.7 bar. A stainless steel membrane (pore diameter  $>1\mu\text{m}$ ) have been designed instead of using ceramic membrane due to the difficulty of impregnation of catalyst which would not be reproducible and controllable by means of homogeneity and activity for the iron catalysed oxidation of  $\text{H}_2\text{S}$  with separate feed of reactants [23]. In order to study the influence of diffusion and convection on the overall mass transfer, DGM is implemented which predicts the conversion in the presence of a pressure difference. This model predicts a

substantial increase in conversion with the pressure difference. It is concluded that sintered metal membrane reactor can also be operated as equal as a ceramic membrane reactors can do with separate feed of reactants.

### *Catalytic combustion of propane*

For catalytic combustion of propane, a tubular support membrane made of  $\alpha$ -alumina (nominal pore diameter, 0.7  $\mu\text{m}$ , mean pore radius of 0.31  $\mu\text{m}$  and porosity of 34.6%) have been prepared which is catalytically activated by applying a layer of Pt/ $\gamma$ -Al<sub>2</sub>O<sub>3</sub> catalyst [52]. The behaviour of the reactor in the absence of trans-membrane pressure gradients is also studied. The reaction rate inside the membrane is fast compared to the transport rate of the reaction takes place in a small zone inside the membrane and no slip of propane and oxygen to their respective opposite sides occurs, attributing to the transport-controlled regime. The higher conversion is observed, when propane is fed at the shell-side with low concentrations and any slip of propane is prevented for concentrations lower than 35%, its stoichiometric excess shifts the reaction region towards the more active tube-side of the membrane, thus enabling higher conversions than with a tube-side feed of propane.

In 1995, the same group [53] have studied the behaviour of the reactor in the transport-controlled regime when pressure differences are applied over the membrane. A tubular catalytic membrane reactor is fabricated consisting of a porous  $\alpha$ -alumina with a  $\gamma$ -Al<sub>2</sub>O<sub>3</sub> separation layer, deposited on the pore walls of the membrane via “urea method” [54]. Further 1 wt. % of platinum is deposited by vacuum impregnation method. A propane-nitrogen mixture and air containing stream are forced to permeate through a Pt/  $\gamma$ -Al<sub>2</sub>O<sub>3</sub> catalytic membrane operating in transport-controlled regime to provide close contact between the gas molecules and combustion sites, reducing the slip of reactants and provided high kinetics. The maximum conversion is achieved when propane is fed in stoichiometric excess i.e. 7%, the reaction zone

shifts towards the air side. On contrary, when propane is fed at a lower concentration (4%) the reaction zone tends to stand closer to the feed-side, provide minimum conversion.

While the previous investigation [53] is limited to the high-temperature operating conditions, the next study verifies the transport of reactants and the conversion, the influence of catalyst loading over the membrane on the reactor performance [55]. It has been concluded that maximum conversion can be achievable in the kinetics controlled regime when more catalyst is deposited in the membrane pores. Maximum propane conversions with minor slip of reactants through the membrane is possible when propane feed concentration and the trans-membrane pressure gradient are not too high.

The concept of an opposite flow catalytic membrane reactor operating in transport-controlled regime on the basis of non-isothermal modelling for catalytic combustion of propane is reported in literature [56]. A tubular catalytic membrane reactor (length: 100 mm) is made of  $\gamma$ -Al<sub>2</sub>O<sub>3</sub> with platinum (Pt), is enclosed in a cylindrical stainless steel module and separated by two chambers i.e., shell side and tube side. The platinum content of the catalyst is maintained as 1 wt. % to the weight of  $\gamma$ -Al<sub>2</sub>O<sub>3</sub>, whereas the  $\gamma$ -Al<sub>2</sub>O<sub>3</sub> content of the membrane is kept 4 wt. % on the basis of entire membrane weight. The influence of reaction kinetics on the reactor performance is observed only in the low-temperature and kinetics-controlled regime. The mono-dispersed model results an unsatisfactory model performance owing to position of the reaction zone due to uniform catalyst distribution. The bi-dispersed model is selected for the uneven catalyst distribution over the membrane. The isothermal model gives exact assessments of the achieved conversion only when the reactor is operating in transport-controlled regime, but fails to predict the steady-state multiplicity that occurs at low temperatures.

### *Oxi-dehydrogenation (ODH) of Propane to Propylene*

AV/ $\gamma$ -Al<sub>2</sub>O<sub>3</sub> catalyst based conventional packed-bed reactor is used for oxi-dehydrogenation of propane and is compared with other reactors, like, monolith-like reactor and catalytic membrane reactor [57]. A catalyst is prepared on the support of  $\gamma$ -Al<sub>2</sub>O<sub>3</sub> powder in the form of a thin layer (0.2 wt. %, thickness of the skin 2  $\mu$ m) and spread over on the internal side of a tubular porous ceramic membrane (height - 150 mm). The reactants are fed in co-current mode at the core side of the monolith-like reactor. In packed bed reactor, maximum conversion of propane is attained at the temperature of 450°C using 9.2 mol% isobutane, 1.6 mol% oxygen and balanced helium as feedstock with propylene and carbon dioxide as products. The selectivity to propylene is obtained more than 60% at low residence time. It is reported that the selectivity is decreased with increasing propane conversion whereas the conversion of propane and oxygen are increased when the residence time increases. The maximum selectivity of propylene, high turnover number and maximum conversion of propane are achieved for monolith-like structure compared to the packed-bed reactor. But, catalytic membrane reactor shows an improvement in selectivity compared to both packed-bed reactor and monolith-like structure. But no improvement in selectivity is obtained with respect to the monolith-like configuration when a reverse CMR configuration is introduced and is due to the fact of quicker oxygen diffusion through the membrane from the shell to the core side.

The effect of different type of catalytic membranes and their feed arrangement are verified on the yield (propene) [58]. The influence of the back permeation of the reactant hydrocarbon and its prevention is mainly focused. The conversion and selectivity of reactants are also measured where there is no trans-membrane pressure gradient and no convective flow. Three types of tubular membranes of 200 nm in separation layer pore diameters with segregated feed mode are introduced. The membranes are (a) thin V/ $\gamma$ -Al<sub>2</sub>O<sub>3</sub> layer on the inside of a  $\alpha$ -

Al<sub>2</sub>O<sub>3</sub> support, (b) thin V/γ-Al<sub>2</sub>O<sub>3</sub> layer on top of a SiO<sub>2</sub>/α-Al<sub>2</sub>O<sub>3</sub> support for better resistance to permeation, (c) thin V/γ-Al<sub>2</sub>O<sub>3</sub> layer on the tube side of a zeolite/α-Al<sub>2</sub>O<sub>3</sub> support. Maximum selectivity is observed for the configuration in which oxygen (and helium) fed from the shell side due to lower partial pressure of oxygen in the active layer. It is noted that the segregated feed mode membrane offers high selectivity with respect to premixed feed membrane even if the diffusion resistance is low in the support layer at 550°C. However, high conversion values with decrease in selectivity is observed for the membranes having no zeolite crystals or silica within the support layer. The membrane made of silica with a higher diffusion resistance in the support layer provides higher conversion at both temperatures. Selectivity increases with increasing temperature owing to strong reduction in back diffusion and the distribution of oxygen within the support layer with significant diffusion resistance.

#### ***Other catalytic reactions***

Two Pt/γ-Al<sub>2</sub>O<sub>3</sub>-activated porous membrane reactor (M1 and M2) with separate feed of reactants for the combustion of methane are prepared by the incipient wetness impregnation method by depositing platinum (1 wt. % and 7 wt. %) over the tubular α-alumina porous membrane [24]. The conversion is measured by means of different operating parameters such as operating temperature, feed (methane) concentration, type and amount of catalyst deposited, pressure difference applied over the membrane, time of operation etc. In this study, the maximum specific heat power (15 kWm<sup>-2</sup>) is obtained with negligible slip of methane to the air-feed side (an undesired occurrence which reduces the advantages of this membrane reactor), is close to M2 which is the most active and permeable membrane.

In another study, a Pd and Pt/SiO<sub>2</sub>/α-Al<sub>2</sub>O<sub>3</sub> membrane are prepared by depositing colloidal SiO<sub>2</sub> and by impregnating both Pd and Pt overnight followed by calcination at 600°C

for 2 h on a  $\alpha$ -Al<sub>2</sub>O<sub>3</sub> membrane supports (ID-7 cm and OD-10 cm) for catalytic combustion of methane [59]. Methane and oxygen are fed separately to the tube and shell sides. Platinum membranes revealed lower CO production at above 580°C but H<sub>2</sub> has never been detected in the outlet gases whereas no CO and H<sub>2</sub> are observed for palladium membranes.

The behaviour of methanol conversion, influence of the membrane characteristics, sweep gas flow rate, effect of the operating temperature and the different flux configurations for hydrogen production using methanol steam reforming (MSR) reaction in membrane reactor are verified by three different membranes (MR1, MR2 and MR3) [60]. Both co-current and counter-current mode are applied. A comparative study between the fabricated membrane with a traditional membrane reactor (length: 250 mm; ID: 6.7 mm) consists of stainless steel tube is also reported. MR1 is a Pd-Ag/TiO<sub>2</sub>-Al<sub>2</sub>O<sub>3</sub> asymmetric porous commercial membrane whereas MR2 is an asymmetric porous membrane with a Pd-Ag deposit. MR3 is a dense thin wall membrane tube with a Pd-Ag deposit. It is concluded that high methanol conversion, high hydrogen production and low carbon monoxide selectivity are provided by MR3 in opposite-flow mode at high temperature and high sweep gas flow rate which is superior to the other two membranes.

#### 1.1.5.4 Fabrication of CMR

In recent years, interests in the development of ceramic membranes for different catalytic reactions have been increased due to their thermal and mechanical resistivity. Several types of support membranes such as disc shape, hollow fibre, tubular are well accepted in research fields. Nowadays, tubular membranes are favouring towards researchers because of their ability to handle process streams with high solids and high viscosity properties. Membrane area of tubular membrane per unit volume is small and can easily be reduced fouling by mechanical cleaning.

Usually ceramic membrane supports are formed by shaping mixture of inorganic compounds with organic additives or inorganic binders followed by sintering. Several methods are used to prepare porous membranes from inorganic materials such as phase separation, leaching, anodic oxidation, pyrolysis, particle dispersion, slip casting and sol-gel process [61]. A Pd-based tubular porous inorganic catalytic membrane reactor has been prepared and applied for water remediation by catalytic hydrogenation and H<sub>2</sub>O<sub>2</sub> synthesis [60]. An MFI based membrane presenting a nanocomposite structure within a 15 cm long porous alumina tube, is prepared by hydrothermal synthesis of silica (Aerosil 380) and tetra-propylammonium hydroxide) [63]. The incorporation of catalysts into membranes not only offers the opportunity to perform selective catalytic synthesis but also separate reactants and/ or products simultaneously. This review identifies the effect of use of different catalysts on different chemical process applications, given in **Table 1.3**.

**Table 1.3** Use of different catalysts for catalytic membrane reactors

Catalyst	Application	Reference
Pd-Ru metal alloy	Selective and continuous methods of hydrogenation	[64]
Pd alloy	cyclopentadiene to cyclopentene naphthalene to tetralin furan to tetrahydrofuran furfural to furfuryl alcohol	[65]
Pd/Ru/W	Dehydrogenation of 2-methyl-1-butene to isoprene	[66]
Pt/Si, Pt/Mo	Adsorption of ethene in the absence and presence of CO	[67]
Ga <sub>2</sub> O <sub>3</sub> /MoO <sub>3</sub>	Oxidative dehydrogenation of propane	[68]
NiO/MgO	Catalytic partial oxidation of coke oven gas to syngas	[69]
Ni/Pd/Ag	H <sub>2</sub> production by low pressure methane steam reforming	[70]
Ni-Nb-O	Oxidative dehydrogenation of ethane to ethylene	[71]
CuO/ZnO/Al <sub>2</sub> O <sub>3</sub>	Steam reforming of methanol	[72]
CoMo/Al <sub>2</sub> O <sub>3</sub>	Reaction of thiophene hydrodesulfurization	[73]

During the recent years, there have been a number of investigations dealing with the coating techniques for the deposition of active catalysts on the surface of the inorganic support membrane for catalytic membrane reactors such as physical vapour deposition (PVD) [74-77], chemical vapour deposition (CVD) [78], and modified chemical vapour deposition [79], sol-gel coating [80-82], electroless plating and electroplating [83-85], co-condensation technique and magnetic sputtering technique [86], spray pyrolysis [87] etc.

CVD is a key technology in the field of catalytic membrane reactors to deposit active catalysts over the support membrane. CVD process can be applied to modify membrane pore size as this process generally provide good control of pore size. Though the process is quite time consuming, even undesired compounds and impurities may be formed, causing reduction in the performance of the membrane [88], this process is widely used in the fabrication of products, such as, semiconductors, optoelectronics, optics, refractory fibres, filters, etc. [89].

In addition, the advantages of using CVD for membrane preparation are the simple, relatively inexpensive equipment and precursor materials for metal deposition [90, 91]. In spite of using the CVD for hydrocarbons, other membranes reformed by CVD techniques include palladium [92], SiC [93], and silica [94], are mostly used for separating gaseous mixtures. Theoretical analyses of CVD application to modify pore size are studied earlier by using the population balance theory [95]. Another researcher has done the same study using percolation theory [96] and numerical analysis [97]. These studies has suggested that the pore size distribution of the membrane, the kinetics of the CVD reactions and the transient kinetics of the modification process play important role in the modification of pore size. A new technique chemical-vapour infiltration (CVI) has been used by several groups. They prepared SiC membranes by the CVI using  $\text{SiH}_2\text{Cl}_2$  and  $\text{C}_2\text{H}_2$ , diluted with  $\text{H}_2$ , and  $\gamma\text{-Al}_2\text{O}_3$  tubes as supports

[98] and a SiC membrane using an  $\alpha$ -alumina tube as the support, and used CVD of  $(C_3H_7)_3SiH$  at 700-800°C [93].

The modified CVD co-deposition is another newly developed technique having several advantages compared to alternative techniques [99-101]. This process is also quite interesting in the application of platinum aluminide coatings for gas turbine hardware by CVD, co-deposition of aluminium, hafnium, zirconium and silicon [102].

The electroless plating looks to be an attractive method as it requires very simple processing equipment and is able to coat a complex shaped component with a layer of uniform thickness. It is a very prolonged process like CVD but controlling thickness of a film is not easy by the electroless plating. A significant advantage of electroless plating is that it is well-matched to applications on available commercial membranes [103]. The catalytic dehydrogenation of isopropanol using a  $Cu/SiO_2$  catalyst is performed in a Pd-Cu alloy membrane reactor. The membrane is prepared by electroless plating of alumina supports followed by heat treatment after electroplating [104]. Two types of Ni-P alloy/ceramic membranes are prepared by both the conventional electroless Ni-plating technique and re-crystallization technique for dehydrogenation of ethanol to acetaldehyde. Ethanol conversion is considerably higher in the former than in the membrane reactor using the recrystallized membrane [105]. In a recent study, a new amorphous Ni-B alloy membrane by electroless plating method has been employed for ethanol dehydrogenation. A Pd/Ag dense membrane on a mesoporous  $\gamma-Al_2O_3$  membrane by electroless plating has been utilized for the catalytic dehydrogenation of methanol [106]. A combination of electroplating with the electroless chemical reduction using the patterned mask is a newly developed method. The advantages of this fabrication method are the initial compositing between the polymer and platinum particles that can be assured by the chemical reduction method and the thickness of each electrode, can be controlled easily and rapidly by

electroplating [107]. Controlled thickness and porosity of a thin film can be accurately achieved by sol-gel process. Composite membranes resulting from this process are generally microporous and mesoporous, on which permeation of gases is mainly controlled by surface transport and/or the Knudsen diffusion mechanism [88]. The preparation of microporous membranes by sol-gel modification of mesoporous  $\gamma$ -Al<sub>2</sub>O<sub>3</sub> membranes is discussed earlier in 1995 [108]. This approach is successfully employed to vary the position of a narrow step distribution of Pt across the membrane radius [109]. The possibility of placing consecutive ceramic layers of different materials via sol-gel has also been discussed, where each layer could be loaded with a different catalyst [110]. A V-P-O catalytic membrane is prepared for the partial oxidation of butane via sol-gel process shows the flexibility of this method to allow the synthesis of thin porous catalytic films that are difficult to achieve by other processes [111].

PVD is a less strenuous technique, offers faster deposition rates and controls the film thickness but not the uniformity. To maintain the uniformity, rotation may be necessary which depends on the shape of the component to be coated. In this process, the solid material to be deposited is first evaporated in a vacuum system, followed by condensation and deposition as a thin film on a cooler substrate. The magnetron sputtering technique contains a vacuum chamber comprising a target (a plate of the material to be deposited) and a substrate (the material). A high energy ion strikes the conductive target imparting momentum to atoms of the target and deposited on the target. Argon is generally used as sputtering gas. A combination of PVD and sputtering technique for the deposition of palladium on the outer surface of commercial ceramic tubular membranes is investigated to conduct water gas shift reaction but failed. A new economical and less time consuming process, i.e. co-condensation is then proposed, looks to be more interesting for their purpose. By using this process, an apparently uniform palladium (Pd) thin film (thickness 0.1  $\mu\text{m}$ ) which gives higher hydrogen flux through the layer have been obtained [88].

Another well-known method is spray pyrolysis which is much simpler than other methods, in which a solution of metal salts is sprayed into a heated gas stream and pyrolysed. This method has been applied for the formation of composite Pd membranes for hydrogen separation. The outer surface of the porous alumina alloy fibre is coated using  $\text{Pd}(\text{NO}_3)_2$  and a  $\text{AgNO}_3$  solution on a  $\text{H}_2\text{-O}_2$  flame, to obtain a Pd-Ag alloy film [87]. In a recent work, synthesis of the  $\gamma\text{-Ga}_2\text{O}_3\text{-Al}_2\text{O}_3$  solid solutions by spray pyrolysis has been examined to obtain spherical particles using an aqueous solution of  $\text{Ga}(\text{NO}_3)_3$  and  $\text{Al}(\text{NO}_3)_3$  in the presence of  $\text{HNO}_3$ . It is reported that spray pyrolysis give amorphous products unless a sufficient thermal energy is supplied during the technique. Physical properties of the solid solutions are affected by the spray pyrolysis conditions is also confirmed [112]. In another recent work, a new technique is introduced, i.e., ultrasonic spray analysis, is a combination of spray analysis and aerosol assisted CVD (AACVD) to prepare Nitrogen-doped carbon nanotubes from mixtures of acetonitrile and imidazole, which prove to be quite interesting [113].

### 1.1.6 Catalytic membrane reactors vs. traditional reactors

Nowadays scientists and engineers are more attracted towards catalytic membrane reactors (CMR) compared to conventional reactors (PFR, CSTR, etc.) to remove/recover products involving both catalytic reaction and separation. There are a number of technical issues that make CMR more interesting and are as follows:

- Membrane reactors combine both reaction and separation simultaneously to increase conversion. One of the products of a given reaction is removed from the reactor through the membrane, forcing the equilibrium of the reaction "to the right" (according to Le Chatelier's Principle), so that more product is produced.
- Enhanced conversion, making the process more economical.
- Increased reaction rates

- Reduced by-product formation
- The possibility of separating molecules in a customized but cheap manner
- Minimization of thermal damage
- The possibility for recycling and lower exhausts
- The moderate energy consumption

Though the use of CMR is advantageous and is involved in different applications, issues regarding manufacturing cost need to be taken care of.

### 1.1.7 Possible scopes for further research

Though the concept of CMR is well established and involved in different applications, numerous issues are pointed in further development of CMRs, listed below:

- (a) Selection of suitable materials for membrane fabrication.
- (b) Parametric optimization (sintering temperature, applied pressure) of membrane preparation methods using trial and error approach in experimentation.
- (c) Evaluation of the best membrane module (tubular, hollow fibre, flat) and mode of application (dead-end, cross-flow etc.)
- (d) Selection of suitable catalysts for different purposes.
- (e) Evaluation of optimal operating conditions (preparation technique, calcination temperature) that enable to offer higher yield.
- (f) Choosing of simple coating techniques instead of using conventional processes like PVD, CVD, vacuum coating etc.

- (g) Evaluation of the best membrane reactor configurations and mode of applications (extractor, distributor and contactor).

A critical review from significant research findings convey the following scopes for improvement in the fabrication of catalytic membrane reactors. Firstly, use of low-cost ceramic support rather than using alumina based costly support shall be stimulated to reduce the manufacturing cost of the catalytic membrane reactor for various industrial applications. Secondly, membrane fabrication including catalyst preparation and coating techniques need to be simple and inexpensive with least possible use of costly instruments. For this reason, conventional coating techniques are not be a better choice as these techniques are very costly and do not draw attention towards industry peoples. Hence, research in this direction must not be encouraged and a new manufacturing and coating technique have to find out for the fabrication of catalytic membranes.

## 1.2 Aim and objectives of the present research

The main objective of the research is to fabricate a catalytic membrane and membrane reactor which will be cost effective and efficient in separation performance. Hence, we have divided the entire manufacturing process of catalytic membrane reactor (CMR) into three different steps which include (i) fabrication of ceramic support membrane, (ii) catalyst preparation and (iii) coating of catalyst over the exterior membrane surface.

### **Fabrication, characterization and optimization of ceramic tubular support membrane**

1. **Fabrication** of low-cost tubular ceramic membrane using cheap raw materials.
2. **Utilization** of sawdust as pore-former in ceramic membrane manufacturing.

3. **Verification** of membrane performance capability on the basis of morphology, mechanical and chemical stability.
4. **Optimization** study of membrane parameters using response surface methodology (RSM) for predicting the effect of different parameters, such as, binder and preparation pressure on the membrane morphology and mechanical (flexural) strength.
5. **Evaluation** of production cost of the fabricated tubular ceramic membrane support.

#### **Synthesis and characterization of catalyst**

1. **Synthesis** of a catalyst via impregnation by soaking of metal precursors on a support matrix for the fabrication of a catalytic membrane and membrane reactors to recover elemental sulfur from H<sub>2</sub>S-laden gas source.
2. **Characterization** of catalyst on the basis of significant parameters, such as, metal dispersion and metallic surface etc.
3. **Verification** of catalyst performance based on catalytic activity i.e., conversion, yield and selectivity by means of Claus reaction.

#### **Fabrication and characterization of catalytic membrane reactor (CMR)**

1. **Development** of a new catalytic membrane by assembling ceramic support membrane and catalyst applying a new technique, namely, paint coating.
2. **Characterization** of the catalytic membrane reactor to identify its feasibility in terms of morphology.
3. **Verification** of the prepared membrane reactor's performance on the basis of conversion, yield and selectivity.

4. **Estimation** of manufacturing cost of the catalytic membrane reactor in terms of support membrane cost, catalyst development charge and the fee of the reactor mold.

#### **Removal or recovery of elemental sulfur by CMR**

1. **Recovery** of elemental sulfur from the mixture of hydrogen sulfide and sulfur dioxide gas.
2. **Validation** of the newly developed CMR's performance by understanding the multi-reactant mass transfer behaviour and kinetics using a theoretical approach.



# Chapter 2

---

## Fabrication and Characterization of Low-cost Ceramic Support Membrane

## Chapter 2

# Fabrication and Characterization of Low-cost Ceramic Support Membrane

*As a part of the concentrated research effort pursued by our laboratory for the development of low-cost catalytic membrane and membrane reactor from individual unit operation step, the present work aims at development of a feasible scheme for the fabrication of catalytic membrane. Hence, the purpose of this work is to fabricate a low-cost membrane as a support of a catalytic membrane. The selection of raw materials, specially, pore-former for the membrane fabrication is discussed elaborately. The sintering temperature for the fabrication of membrane is optimized on the basis of thermogravimetric analysis. The influence of pore-former on the membrane morphology, mechanical and chemical stability of the ceramic support membrane are observed. A study based on the behavior of the pore-former is attempted to account for the changes in thermal and chemical properties during sintering. The manufacturing cost of the membrane is evaluated in terms of raw material cost, energy consumption fee and mold preparation price. The membrane is finally optimized on the basis of sintering temperature, membrane morphology, like, porosity, pore size and manufacturing cost.*

---

This work is published in the following journals:

S. Bose, C. Das, "Preparation and characterization of low cost tubular ceramic support membranes using sawdust as a pore-former", *Materials Letters*, 110 (2013) 152-155.

S. Bose, C. Das, "Sawdust: From wood waste to pore-former in the fabrication of ceramic membrane", *Ceramics International*, 41 (2015) 4070-4079.

## 2.1 Experimental

### 2.1.1 Raw materials

The chemicals used in this study are kaolin (Loba Chemie Pvt. Ltd., Mumbai, India), quartz (HiMedia Laboratories Pvt. Ltd., Mumbai, India), sawdust (mixture of teak, coco and sal wood, taken from local sawmill), and feldspar (National Chemicals, Gujarat, India) for the fabrication of eco-ceramic membrane support served for different functional aspects.

Kaolin is used to provide low plasticity and high refractory properties to the membrane support. Mechanical and thermal stability are contributed to the membrane by the addition of quartz. Sawdust, a ligno-cellulosic material contains cellulose, hemicellulose and lignin compounds. Sawdust is unique as a pore-former for the fabrication of ceramic membrane because it easily forms pore by removing cellulose, hemicellulose and lignin compounds during heating and is cheap. The released ligno-cellulosic material emits via some uneven paths which makes the membrane porous and contributes to the membrane porosity. Feldspar is utilized to obtain a glassy matrix in the early stage of the firing process. Concentrated HCl (1N) and NaOH pellets for acid-alkali test are purchased from M/s Merck India Pvt. Ltd.

### 2.1.2 Selection and treatment of sawdust particle

Selection of pore-former with an appropriate particle size is the heart of a porous ceramic membrane. The pore size and porosity are important aspects in this regard. A high particle size of pore-former is necessary for a highly porous ceramic body. Selection of sawdust as a pore-former is attempted for ceramic membrane fabrication to achieve a better efficiency with a lower economy as those obtained by other standard pore-formers.

Five different size ranges of sawdust screened through 30, 44, 60, 72 and 100 B.S.S. are considered to select the appropriate size of sawdust particle suitable for ceramic support membrane fabrication. Thermal modification of sawdust has been performed to realise the change in physical properties of sawdust which is the significant factor for understanding the pathway of making pores in ceramic membranes. The raw sawdust particles undergo three heat treatment steps. Firstly, the raw sawdust is dried at room temperature ( $28 \pm 2^\circ\text{C}$ ) for 24 h. After that, it is dehydrated at  $100^\circ\text{C}$  (373 K) for 12 h using  $\alpha$ -alumina crucible in a muffle furnace followed by heating at  $250^\circ\text{C}$  (523 K) for 24 h. Secondly, it is sintered from  $250^\circ\text{C}$  to desired sintering temperatures i.e.,  $550^\circ\text{C}$  (823 K),  $700^\circ\text{C}$  (973 K) and  $850^\circ\text{C}$  (1123 K) at a heating rate of  $2^\circ\text{C}/\text{min}$  for 5 h. Then the thermally modified sawdust is cooled by an atmospheric cooling process implemented by switching off the muffle furnace. The raw sawdust and burnt samples are separately dipped into acid (concentrated hydrochloric acid, pH 2) and alkali (NaOH, pH 12) solutions for seven days separately to confirm any change in composition and surface structure.

### 2.1.3 Membrane fabrication

The support membrane is prepared by thorough mixing and grinding of sawdust (sieved through gyratory sieve shaker) along with dry inorganic raw materials, such as, kaolin, feldspar and quartz of different weight ratios (**Table 2.1**) using mixer machine and ceramic mortar, namely, SM1 to SM6. The compositions are selected on trial basis to get the best results in terms of morphological properties, chemical and mechanical stability and preparation cost. The grinded mixture is placed into a cylindrical mould (O.D.: 50 mm and 50 mm height; 10 mm thickness) (**Figure 2.1**) and applied 9.81 MPa pressure by hydraulic press (Velan Engineering,

Tamilnadu, India) for 1 min to prevent the propagation deformation and keep homogeneity in the raw material mixture.

**Table 2.1** Composition of raw materials used for the preparation of ceramic support membrane

Name of membrane support	Composition dry basis (wt. %)				Operating Pressure (MPa)
	Kaolin	Quartz	Saw dust	Feldspar	
SM1	40	20	30	10	9.81
SM2	40	30	10	20	
SM3	30	10	20	40	
SM4	40	25	10	25	
SM5	50	25	25	0	
SM6	50	0	25	25	

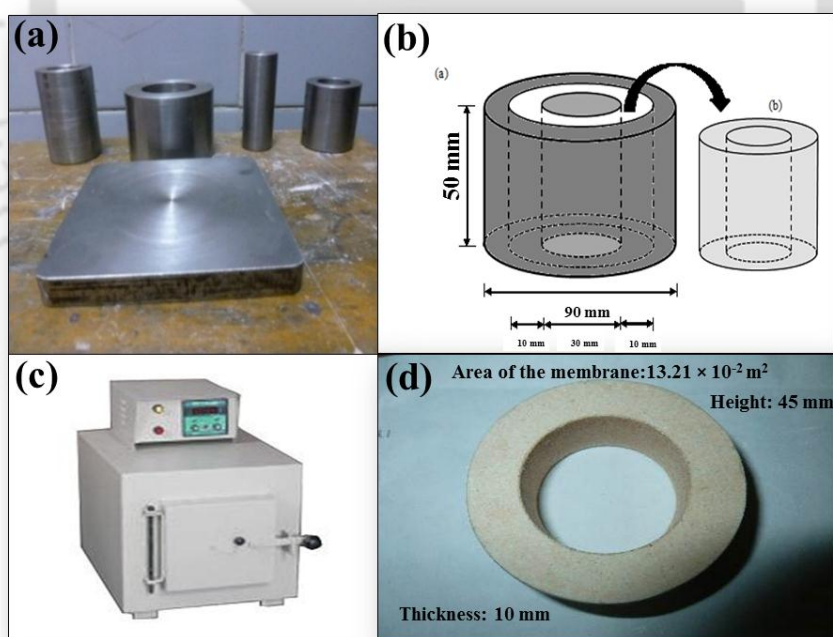


**Figure 2.1** Fabrication of support membrane: (a) fabricated mould made of mild steel; (b) schematic diagram of the prepared tubular membrane support; (c) muffle furnace; (d) top view of the fabricated tubular ceramic membrane

The fabricated membrane is then removed cautiously from the mould and subjected to three heat treatment steps. The entire heating step is considered as it is carried out for the thermal modification of raw sawdust to understand the behaviour of sawdust inside the ceramic body during sintering of membrane in a better way. After sintering, the membrane is cooled by an atmospheric cooling process implemented by switching off the muffle furnace. The membranes achieved a hard, rigid and porous texture after sintering.

## 2.1.4 Characterization techniques

### 2.1.4.1 Physical characterizations

#### *Thermogravimetric analysis (TGA)*

The purpose of TGA-STA (TGA/SDTA 851<sup>®</sup>, Mettler Toledo, Switzerland) is to measure the changes in physical properties of raw materials with change in temperature. The optimum sintering temperature regime where the sawdust completely burns out is also determined. The sample analysis is done in a  $\alpha$ -alumina crucible from 25°C to 900°C at a heating rate of 10°C/min in nitrogen atmosphere to prevent damage of sawdust particles due to oxidation.

#### *Particle size distribution*

Particle size distribution analysis of sawdust and the sample mixtures are carried out in a laser particle size analyser (LPSA) (Malvern Mastersizer 2000 APA 5005<sup>®</sup> hydro MU, Malvern Instruments, Worcestershire, U.K.). All sawdust samples and sample mixtures are mixed and distributed in distilled water during sample preparation stage. The sample is then sonicated using an ultrasonic bath (JEIOTECH UC-02) and ready for the experimentation.

### ***X-ray diffraction (XRD)***

The phase composition of the sintered ceramic membrane is analysed by XRD studies using Bruker™ D8 Advanced series powder diffractometer with Cu K $\alpha$  radiation of 40kV and 40mA in the 2 $\theta$  range of 5-80° with 0.05° steps at a rate of 1s per step. A small portion is cut from the fabricated ceramic membrane and is then grinded in a ceramic mortar for the analysis. The sample is placed on a circular fibre plate and then mounted on the sample holder inside the instrument.

### ***Fourier transform infrared spectroscopy (FTIR)***

The change in functional group of raw, chemically modified and thermally modified sawdust is verified using FTIR (Shimadzu IR Affinity-1, Japan) in the range of 400-4000 cm<sup>-1</sup>. Potassium bromide (M/s Merck India Pvt. Ltd) is used for background study. Potassium bromide (KBr) is first kept in hot air oven (Universal Hot Air Oven, Navyug India, Kolkata, India) and dried at 100°C for overnight to remove moisture present in it. Sawdust samples of 1-2 mg are grinded and mixed with dried KBr using ceramic porcelain mortar and loaded into a sample holder mounted in the instrument.

### ***Surface morphology***

Microstructural images and chemical composition of the sawdust are verified before and after sintering steps and acid-alkali treatment to analyse the effect of sintering steps on sawdust particles as well as the sustainability of sawdust in acid-alkali media. The morphology and the chemical compositions of the raw and resulting samples (thermally and chemically modified) are investigated using SEM and EDX (LEO 1430VP®, Oxford). A small amount of sawdust sample is taken as specimen. Sawdust is first coated with gold particle under vacuum

as sawdust particles are non-conducting in nature. The sample is then evacuated and placed on an aluminium stab using carbon tape. The aluminium stab along with the sample is then mounted on the sample holder inside the instrument.

Field emission scanning electron microscopy (FESEM) (Zeiss) with energy dispersive X-ray (EDX) (LEO 1430VP®) is used to estimate the pore size, surface topography and chemical element present in the fabricated membrane, respectively. Average membrane pore size of the fabricated tubular ceramic support membrane and their distribution are determined by ImageJ software (Version 1.37). A small portion of the membrane is cut off for analysis. Similar procedure is applied for the analysis as stated above for sawdust sample.

### ***Volumetric porosity***

Volumetric porosities of all fabricated membranes are determined based on gravimetric analysis of water entrapped in the pores of the membrane walls. The sintered membranes are first measured in dry condition and then immersed in deionized water for 24 h. The water soaked membranes are dried with the help of tissue paper and weighed. The volumetric porosity is calculated from the following equation:

$$\varepsilon_v = \frac{\text{void volume}}{\text{bulk volume}} = \frac{(W_2 - W_1) / \rho_{H_2O}}{V_m} = \frac{(W_2 - W_1)}{\rho_{H_2O} \cdot V_m} \quad (2.1)$$

where  $W_2$  and  $W_1$  are the weights of the wet and dry membrane samples,  $\rho_{H_2O}$  is the density of the deionized water and  $V_m$  is the volume of the fabricated membrane respectively.

### 2.1.4.2 Permeation characterization

#### *Experimental set up*

An experimental set-up is fabricated for gas permeation study. As shown in **Figure 2.2**, the set-up used for this experiment consists of a tubular cell mounted on a flat rectangular base plate, made of perspex. The bottom end of the tubular cell is fixed with a flat rectangular plate and the top end is coupled with two rectangular flat plates by four flanges (black sticks). The fabricated membrane is fitted into the hollow sector inside the tubular cell by opening two top flat plates. Pressure gauges are attached with the membrane housing to maintain the gas flow rate at different trans-membrane pressures. The gas is purged into the membrane unit through a pipe from the top plate. The gas is then permeated through the outer wall of the tubular cell unit, connected to the bubble flow meter for measuring the gas flow rate at different trans-membrane pressures. A rubber balloon is attached at the one end of the bubble flow meter which contains soap solution. The gas permeation experiment is conducted at room temperature ( $28 \pm 2^\circ\text{C}$ ).

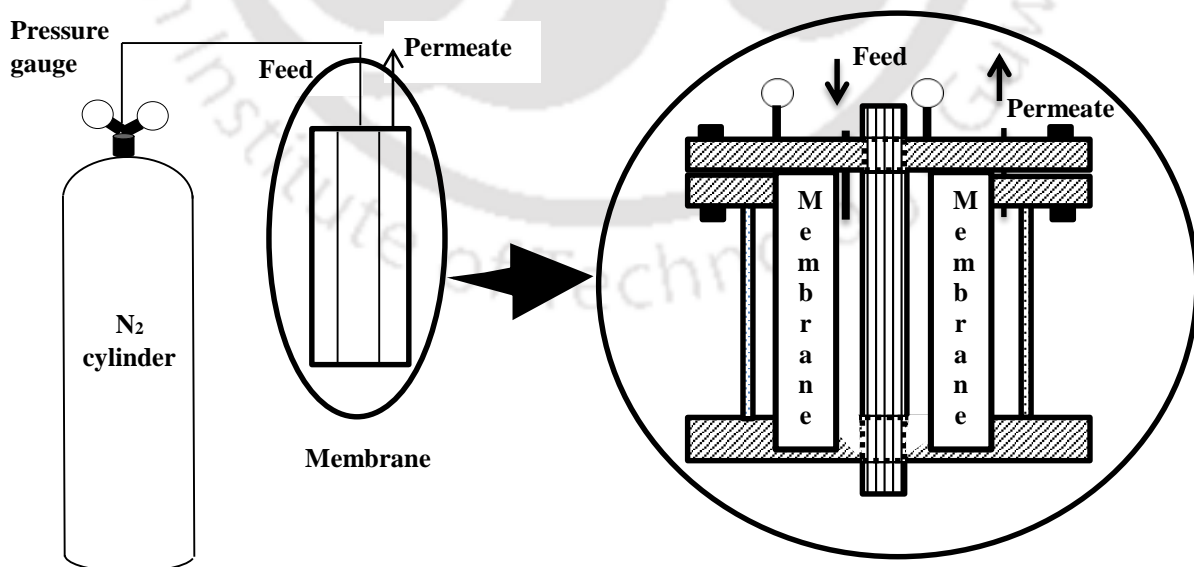


**Figure 2.2** Experimental set up for gas permeability test

### Gas permeation

The gas permeation data is utilized to estimate two vital membrane characteristics namely, average pore radius ( $r_g$ ) and effective porosity ( $\varepsilon/\tau^2$ ) according to the following expression [114]

$$k = 2.133 \left( \frac{r_g}{l} \right) v \frac{\varepsilon}{\tau^2} + 1.6 \left( \frac{r_g^2}{l} \right) \frac{1}{\eta} \left( \frac{\varepsilon}{\tau^2} \right) P \quad (2.2)$$

where,  $P$  is the average pressure on the membrane in MPa,  $v$  is the molecular mean velocity of the operating gas ( $\text{m}\cdot\text{min}^{-1}$ ),  $l$  is the pore length in m,  $\tau$  is the tortuosity factor of the membrane,  $\eta$  is the viscosity of the gas in Pa.s,  $k$  is the effective permeability factor in  $\text{m}\cdot\text{min}^{-1}$ . Eq. 2.2 simply characterised as a straight line in a graph drawn between  $k$  and  $P$ . In Eq. 2.2, the first term (intercept) and the second term (slope) resemble to Knudsen and viscous permeance, respectively. The values of the slope and intercept obtained from the graph are used to evaluate the pore diameter and porosity of the membrane.

The effective permeability factor  $k$  is calculated as

$$k = \frac{QP_2}{S\Delta P} \quad (2.3)$$

Where,  $S$  is the permeable area of the membrane ( $\text{m}^2$ ),  $Q$  is the volumetric flow rate ( $\text{m}^3\cdot\text{min}^{-1}$ ),  $P_2$  is the membrane pressure at permeate side and  $\Delta P$  is the trans-membrane pressure drop. The average pore radius ( $r_g$ ) of the membrane is evaluated using the slope,  $1.6 \left( \frac{r_g^2}{l} \right) \frac{1}{\eta} \left( \frac{\varepsilon}{\tau^2} \right)$  and intercept,

$2.133 \left( \frac{r_g}{l} \right) v \frac{\varepsilon}{\tau^2}$  of the created graph expressed as

$$r_g = 1.333 \frac{B}{A} v \eta \quad (2.4)$$

The gas permeance ( $p$ ) is calculated as

$$p = \frac{Q}{S \Delta P} \quad (2.5)$$

where,  $S$  is the permeable area of the membrane ( $m^2$ ),  $Q$  is the volumetric flow rate ( $m^3 \cdot min^{-1}$ ).

### 2.1.4.3 Three-point bend test

Three-point bend test (ASTM D790) has been performed to measure the strength of the fabricated ceramic membrane using a Universal Tensile Test Machine (Deepak polyplast Pvt. Ltd., India) maintaining 20 MPa load and 85 mm support span at room temperature ( $28 \pm 2^\circ C$ ) at a stroke rate of  $0.5 \text{ mm} \cdot \text{min}^{-1}$ . Rectangular bar-shaped specimens are prepared by maintaining thickness/length ratio as 1:16 for determining the flexural strength.

### 2.1.4.4 Acid-alkali test

The raw sawdust and burnt samples are separately dipped into acid (concentrated hydrochloric acid, pH 2) and alkali (NaOH, pH 12) solutions for 7 days separately to confirm any change in composition and surface structure. Chemical stability of the fabricated ceramic membrane is also verified by immersing the membrane into the acid (Conc. HCl, pH 2) and alkali (NaOH, pH 12) solution for seven days. Firstly, the membrane is weighed in dry condition and dipped into the solution of acid and alkali for one week at atmospheric conditions. Secondly, the membrane is weighed and estimated the porosity following the volumetric porosity determination technique. EDX (LEO 1430VP<sup>®</sup>, Oxford) analysis of the membranes before and after corrosion test is performed to verify the change in elemental composition.

### **2.1.5 Statistical analysis**

A study based on statistics (t-Test: Two-Sample Assuming Unequal Variances) using Excel built-in statistical software is performed to verify the difference between the porosity obtained from volumetric porosity and gas permeation study. Five specimens (porosity values) of each method (volumetric porosity and gas permeation) have been taken for the statistical analysis. Standard deviation of the porosity values obtained from the two methods is also calculated using Excel to confirm the preferable method for calculating porosity.

## **2.2 Results and discussions**

In this section, significant facts over the usefulness of sawdust as a pore-former in ceramic membrane fabrication have been pointed out systematically. Firstly, the effect of particle size of sawdust and sintering temperature on the porosity, pore size and microstructure of the ceramic membrane along with the thermogravimetric analysis of sawdust particles have been discussed elaborately. Secondly, a comparative study related to the identification of ligno-cellulosic material of raw and acid-alkali treated sawdust through FTIR analysis has been performed. Even, the identification of peak associated with ligno-cellulosic material of burnt-sawdust and acid-alkali treated burnt-sawdust are also verified. Finally, fabrication of membrane using selected screened sawdust and verification of their morphological properties, mechanical strength and chemical stability are studied.

## 2.2.1 Characterization of sawdust

### 2.2.1.1 Effect of particle size of sawdust on the porosity and pore size of the membrane

Particle size distribution of both raw sawdust (screened through B.S.S. 30, 44, 60, 72 and 100 mesh) and the sample mixtures for membrane fabrication are shown in **Figure 2.3 (a-f)**, respectively. It is observed that particle size of sawdust sieved through 30 B.S.S. (**Figure 2.3b**) and 44 B.S.S. mesh screen (**Figure 2.3c**) leads to wide range of distribution. This is due to the presence of wide variety of particle size of sawdust (combination of both fine and coarse particles) whereas the combinations which are prepared using sawdust screened through 60 and 72 B.S.S. mesh shows single mode distribution (**Figures 2.3d and e**). This nature of particle distribution attributes to a narrow range of particles which provides narrow range of pores. **Figure 2.3f** shows bimodal nature of particle size distribution of six different compositions using sawdust separated through 100 B.S.S. mesh which infers the presence of wide range of particles causes wide range of pores. Particle size of sawdust involving statistical parameters such as mode and average size is summarized in **Table 2.2**. Interestingly, it is found that the median particle sizes of sawdust screened through 60 and 72 B.S.S. are small due to the presence of fine particles of sawdust only (refer **Figure 2.3d and e** – narrow particle size distribution), provides completely dense membranes, and is not suitable for fabrication of membrane support of a catalytic membrane reactor. Hence, the other sawdust samples (30, 44 and 100 B.S.S.) are considered for further study.

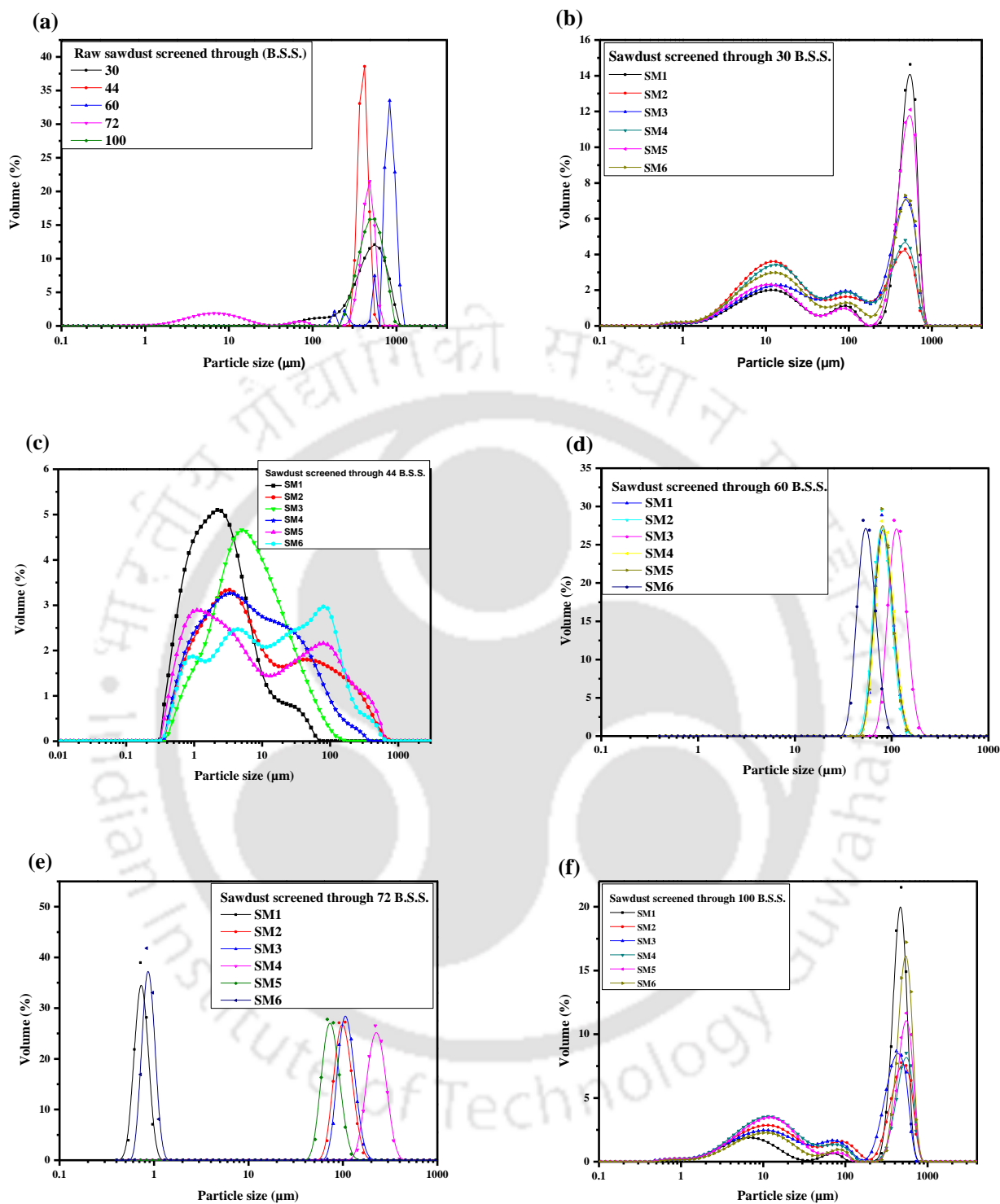


**Figure 2.3** Volume weighed particle size distribution of (a) raw sawdust particles and sample mixtures sieved through mesh sizes of (b) 30 B.S.S., (c) 44 B.S.S., (d) 60 B.S.S., (e) 72 B.S.S. and (f) 100 B.S.S.

The average pore diameter of the fabricated membrane from different sample mixtures having different weight ratios of raw materials with three different particle size ranges of sawdust of 500, 355 and 150  $\mu\text{m}$ , sieved through 30, 44 and 100 B.S.S. screen, respectively, are also shown in **Table 2.3**. **Table 2.3** shows median particle size and average pore size of the membrane.

**Table 2.2** Particle size characteristics of sawdust materials

	Sawdust				
Mode ( $\mu\text{m}$ )	150	212	250	355	500
Average particle size ( $\mu\text{m}$ )	298.95	1.836	1.253	205.143	153.43

For the sample mixtures containing sawdust of different sized particles sieved through 100 B.S.S. mesh, the average pore diameter varies between 0.05 to 0.10  $\mu\text{m}$ . Similarly, for membranes made of using sawdust of different sized particles sieved through 30 and 44 B.S.S. mesh, the average pore diameter varies between 0.04 to 0.10  $\mu\text{m}$  and 0.06 to 0.13 $\mu\text{m}$ , respectively, is in good agreement with literatures [115, 116]. It is observed that the average pore diameter of all the fired membranes are very close to each other unlike the particle size of sample mixtures together with different size of sawdust and its distribution. Even, it is quite interesting to note that SM5 membrane containing sawdust screened through 100 and 30 B.S.S. mesh become cracked and damaged during sintering owing to large particle size and absence of feldspar. This result enlightened the fact of choosing 44 B.S.S. screened sawdust as pore-former for the fabrication of ceramic membrane throughout the study.

**Table 2.3** Determination of particle size and pore diameter for the membrane sintered at 850°C

Membrane	Median particle size $D_{50}$ ( $\mu\text{m}$ ) of sample mixture					Average pore diameter ( $\mu\text{m}$ ) of the fired membrane obtained from gas permeation analysis		
	Sawdust sieved through 30 BSS	Sawdust sieved through 44 BSS	Sawdust sieved through 60 BSS	Sawdust sieved through 72 BSS	Sawdust sieved through 100 BSS	Membrane 30 BSS	Membrane 44 BSS	Membrane 100 BSS
SM1	383.64	17.15	0.094	0.152	444.39	0.04	0.06	0.05
SM2	23.84	10.92	0.096	0.137	54.34	0.09	0.10	0.09
SM3	104.39	11.20	0.131	0.097	101.73	0.07	0.08	0.07
SM4	30.34	22.85	0.106	0.242	22.72	0.10	0.11	0.10
SM5	326.09	6.493	0.087	0.090	19.44	-	0.13	-
SM6	42.61	13.248	0.072	0.708	401.84	0.07	0.13	0.07

**Table 2.4** Porosity determined using Archimedes' principle and gas permeation study for the membrane sintered at 850°C

Membrane	Volumetric porosity in % based on Eq. (2.1)			Porosity (%) from gas permeation study based on Eq. (2.2)		
	Membrane 30 BSS	Membrane 44 BSS	Membrane 100 BSS	Membrane 30 BSS	Membrane 44 BSS	Membrane 100 BSS
SM1	52	48	55	45	43	46
SM2	36	38	36	30	34	29
SM3	46	41	48	40	37	39
SM4	34	38	35	28	34	29
SM5	-	38	-	-	36	-
SM6	46	36	47	39	34	40

**Table 2.4** shows a comparative result of porosities of the fired samples using volumetric porosity determination technique (Archimedes' principle) and gas permeation study. Results obtained from gas permeation study is considered to be better than volumetric porosity method as the later technique has a tendency to keep water intact into the pores of ceramic body (called capillarity), thus showing higher porosity [115, 116]. But statistically (t-test), it is stated that the obtained porosities of the membranes (made of sawdust screened through 44 B.S.S. sieve) using volumetric porosity and gas permeation differ marginally as the t-Stat value (1.543) is not  $< -t$  Critical two-tail (-2.228) or  $> t$  Critical two-tail (2.228). However, the variation between the results is prominent from the standard deviation (dispersion) values which confirm that the gas permeation study provides better result. The standard deviation value of the porosities obtained from the gas permeation study is 3.50 which is less than that of the porosity values found from the volumetric porosity, is 4.30, indicates the data points tend to be very close to the mean or expected value for a low standard deviation whereas a high standard deviation

indicates that the data points are spread out over a large range of values (refer **Tables A1 and A2** in **Appendix.1**). It is true that porosity decreases with increase in average pore diameter and vice-versa but porosity also depends on raw materials present in the sample mixture. On the contrary, it is observed that the porosity of SM5 made of sawdust screened through 44 B.S.S. (**Tables 2.3 and 2.4**) increases with increase in average pore diameter as SM5 contains no feldspar which has the ability to reduce porosity of ceramic by forming glassy matrix during sintering.

### 2.2.1.2 Thermogravimetric (TGA) analysis

The major weight loss of saw dust is noted in the figure due to the removal of moisture and vaporization of organic matter (cellulose, hemicellulose and lignin) which involves both exothermic as well as endothermic reaction. This process of decomposition of sawdust consists of four major stages i.e., (i) moisture removal, (ii) hemicellulose decomposition, (iii) cellulose decomposition and (iv) lignin decomposition, shown in **Figure 2.4**. The first downward slope at 25°C in the TGA curve of sawdust indicates 9% weight loss due to the removal of moisture. The second and third major weight loss (~ 55%) is noted from 210°C to 350°C due to decomposition of hemicellulose, cellulose and pre-dehydration process of kaolin. The fourth stage i.e., lignin vaporization (weight loss ~ 16%) also starts from 210°C and ends at 825°C, is the main region of vaporization of ligno-cellulosic material [117]. This phenomenon is confirmed by a small exothermic peak at 825°C displayed in the DTA curve. The TGA curve of kaolin exhibits almost 10% weight loss due to the loss of the structural hydroxyl group from 425°C to 550°C is due to the transformation of kaolinite to metakaolinite [115]. This study confirms the temperature zones where moisture, cellulose, hemicellulose and lignin burns completely. Based on this study, heating temperature of raw sawdust as well as optimum sintering temperature for membrane fabrication have been decided.

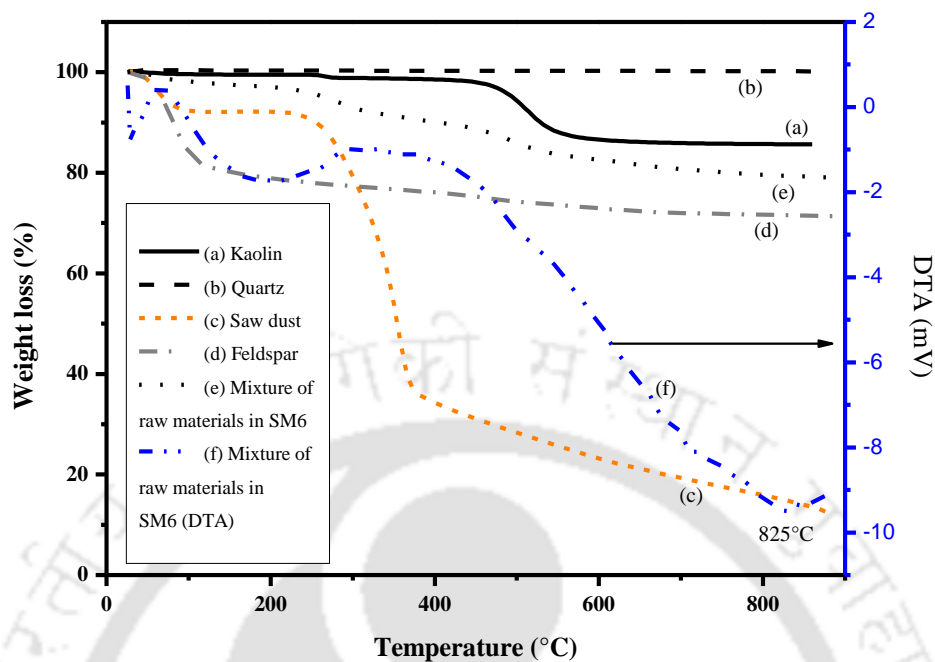


**Figure 2.4** TGA/DTA plot of four individual raw materials and SM6 decomposed in presence of nitrogen atmosphere at 10°C/min

### 2.2.1.3 Functional group identification

The alteration in physical characteristics of the thermally and chemically modified samples has been observed through Fourier transform infrared (FTIR) spectra in **Figure 2.5-2.8**. The peaks associated to the presence of hemicellulose, cellulose and lignin in the raw sawdust are clearly visible in the finger print region between 1100 and 1800  $\text{cm}^{-1}$  (**Figure 2.5**). Peaks at 1363  $\text{cm}^{-1}$  and at 1458  $\text{cm}^{-1}$  attributes to the C-H stretching vibration of cellulose and hemicellulose and the H-C-H bending of the cellulose and lignin, respectively. The C-O stretch band at 1244  $\text{cm}^{-1}$  and C=O stretch carbonyl at 1734  $\text{cm}^{-1}$  confirm the presence of non-conjugated ketones, carbonyls, ester groups and hardwood having higher xylan content

[118,119]. A broad and intense peak of C-H stretching in methyl and methylene groups at  $2916\text{ cm}^{-1}$  establish that the used sawdust is basically hardwood in nature [118].

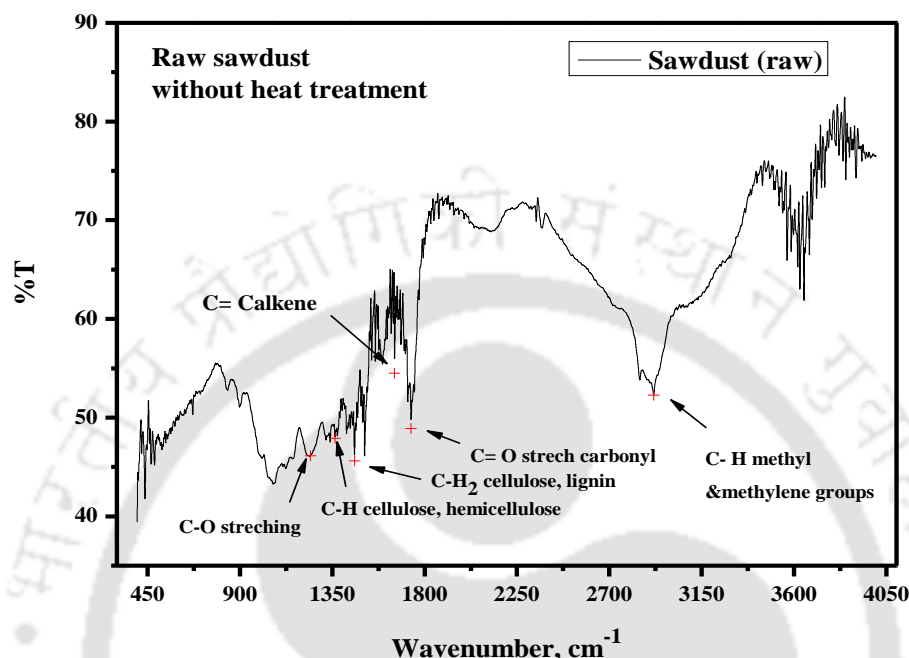


**Figure 2.5** FTIR patterns of 44 B.S.S. mesh screened raw sawdust

**Figure 2.6** indicates a little change in composition after keeping raw sawdust in contact with acid and alkali media for seven days. A decrease in band intensity is observed for all chemically modified sawdust samples indicating a change in composition of raw sawdust after reacting with hydrochloric acid and NaOH solution. For acid treated sawdust, the C-H stretching vibration of cellulose, hemicellulose and C-H stretching in methyl and methylene groups are being shifted to higher wavenumbers ( $1371$  and  $2920\text{ cm}^{-1}$ ) confirming the formation of H-O-C bending and C-H stretch in asymmetric O-CH<sub>3</sub> bonds of cellulose and lignin, respectively. But, the H-C-H bending of the cellulose and lignin band is shifted to a lower wavenumber value at  $1454\text{ cm}^{-1}$ . Alkali treated sawdust shows no such significant compositional change during alkali test. The presence of xylan content (C=O stretch carbonyl),

C-O stretch, C-H stretching vibration of cellulose and hemicellulose, H-C-H bending of the cellulose and lignin, C=C aromatic and C-H stretching in methyl and methylene groups are observed to wavenumber value at  $1730\text{ cm}^{-1}$ ,  $1238\text{ cm}^{-1}$ ,  $1363\text{ cm}^{-1}$ ,  $1371\text{ cm}^{-1}$ ,  $1649\text{ cm}^{-1}$  and  $2920\text{ cm}^{-1}$ , respectively.

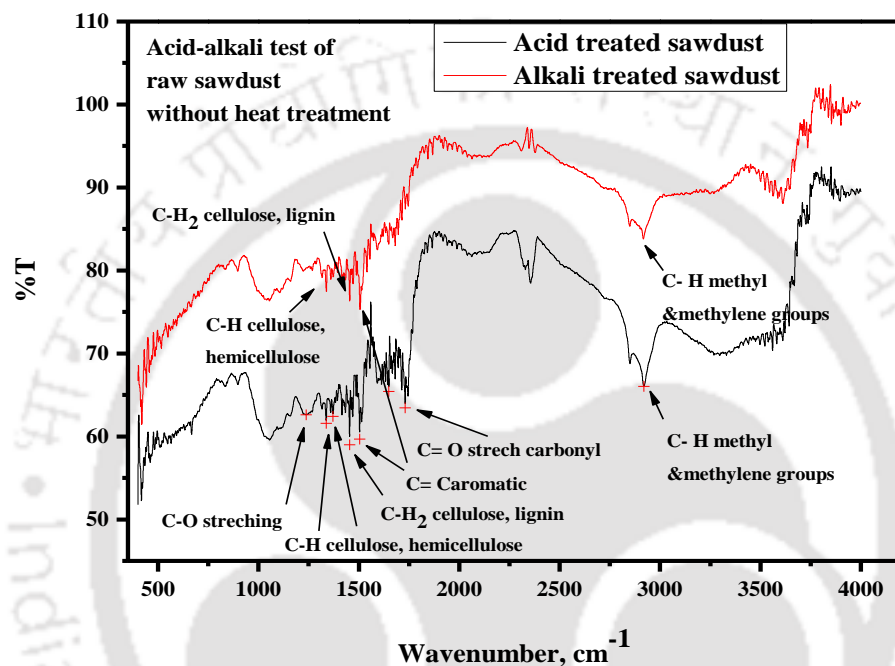


**Figure 2.6** FTIR patterns of 44 B.S.S. mesh screened chemically modified sawdust without thermal modification

**Figure 2.7** displays the infrared patterns of the sawdust introduced to three different temperatures at  $550$ ,  $700$  and  $850^{\circ}\text{C}$  in muffle furnace. The peaks in the finger print region related to the C=C aromatic rings, C=C alkenes and C=O carbonyls are clearly visible at  $1514\text{ cm}^{-1}$ ,  $1614\text{ cm}^{-1}$  and  $1633\text{ cm}^{-1}$ ,  $1730\text{ cm}^{-1}$ , respectively. **Figure 2.7** confirms that there is no such significant change in physical characteristics between raw and thermally modified sawdust in that region. The absence of any band associated to cellulose, hemicellulose, lignin and the presence of C-X group (X = Br, from  $500\text{-}700\text{ cm}^{-1}$ ) at  $503\text{ cm}^{-1}$  is observed due to complete

decomposition of cellulose, hemicellulose, lignin. The peaks at  $1047\text{ cm}^{-1}$  (asymmetric C-O stretching) and  $2351\text{ cm}^{-1}$  (asymmetric O=C=O stretch in the sp carbon region) confirms the formation of carbon dioxide gas during heating of sawdust. The presence of C-H stretching in methyl and methylene groups approves that the nature of the sawdust remain as hardwood after heat treatment.

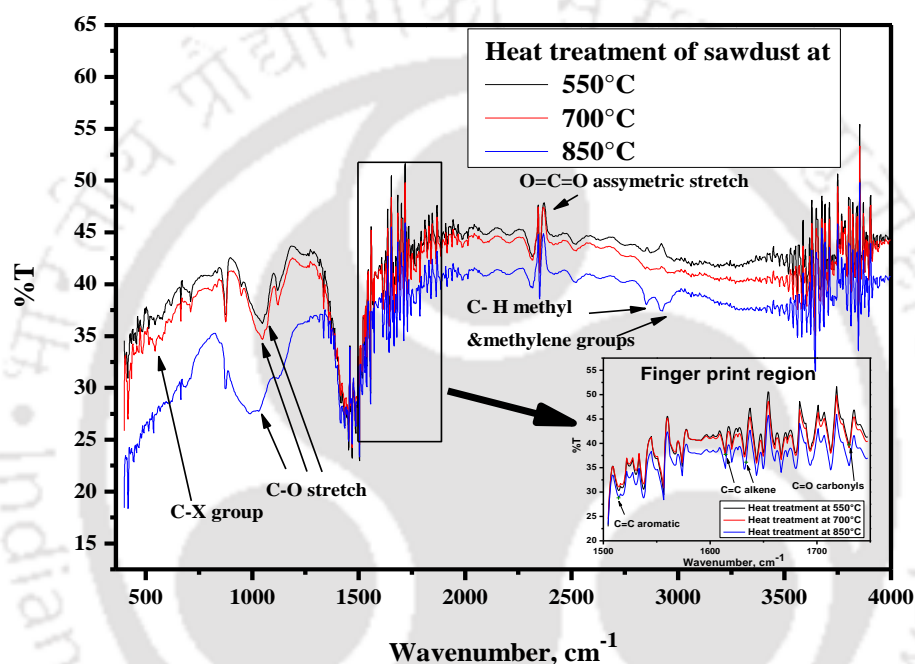


**Figure 2.7** FTIR patterns of 44 B.S.S. mesh screened thermally modified sawdust at 550, 700 and 850°C

After three different heat treatment steps, the thermally treated sawdust samples show absence of ligno-cellulosic bonds. Sawdust shows amorphous nature after heat treatment which can easily be penetrated by concentrated hydrochloric acid and water molecules to break hydrogen bonds. This causes no residue after acid treatment of all thermally modified sawdust samples. **Figure 2.8** shows similar peaks as it is found in **Figure 2.7** with tiny shifting of peak position of C-X group (only for the sample sintered at 550 and 700°C), asymmetric O=C=O

stretch and C-O stretching. No peaks are found at fingerprint region. Alkali test proves that no such significant change is observed while thermally treated sawdust sample is immersed into alkali media for seven days.

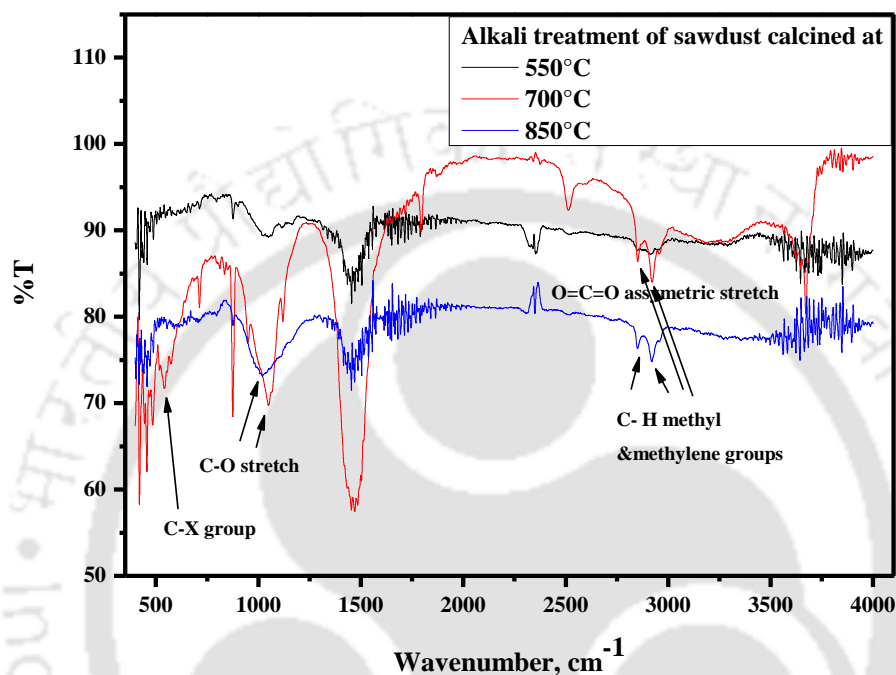


**Figure 2.8** FTIR patterns of 44 B.S.S. mesh thermally treated sawdust after alkali test

#### 2.2.1.4 Compositional analysis and study of microstructures of modified sawdust

The change in surface structures of raw and thermally-chemically modified sawdust by SEM are presented in **Figure 2.9**.

**Figure 2.9a** shows the scanning electron microscopy (SEM) images of raw sawdust without any thermal and chemical modification. The surface images of both alkali (**Figure 2.9b**) and acid (**Figure 2.9c**) treated sawdust display finger-like structure which is nearly similar to the image of raw sawdust.

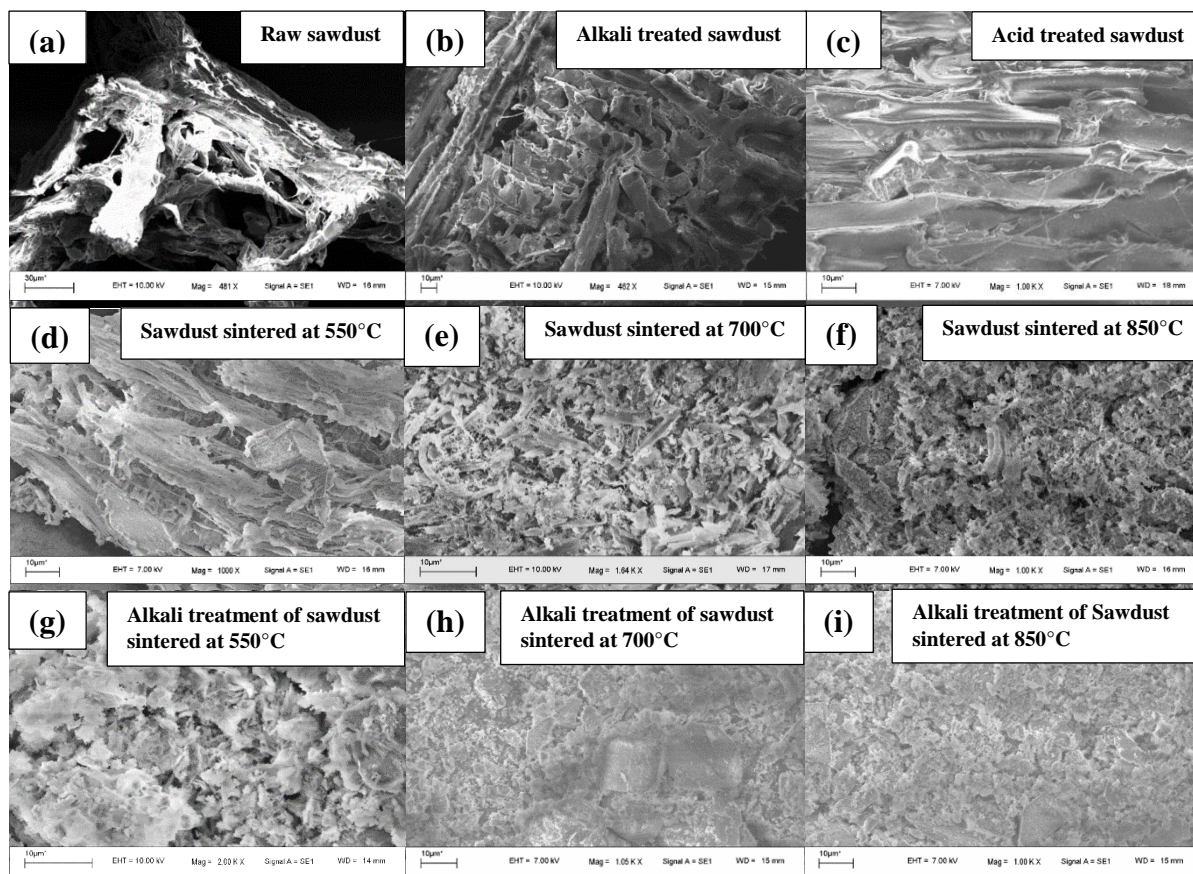


**Figure 2.9** SEM images of (a) raw and (b,c) alkali-acid treated sawdust, burnt-sawdust sintered at (d) 550, (e) 700, (f) 850°C and chemical (alkali treated) modification of burnt-sawdust at (g) 550, (h) 700, (i) 850°C

On the other hand, a clear change is observed in microstructure of thermally modified sawdust which clarifies the change in behaviour of sawdust during sintering. Remarkably, the thermally modified sawdust (sintered at 700 and 850°C) samples show micro-fibril structure (**Figure 2.9e-f**) whereas the sample sintered at 550°C exhibits a rod-like structure (**Figure 2.9d**) because the ligno-cellulosic material present in sawdust decomposes completely at higher temperature (850°C). **Figure 2.9g-i** also show micro-fibril like structures belong to alkali absorbed thermally-modified sawdust. No residues found for acid absorbed thermally-modified sawdust as burnt-sawdust dissolves completely in acid media.

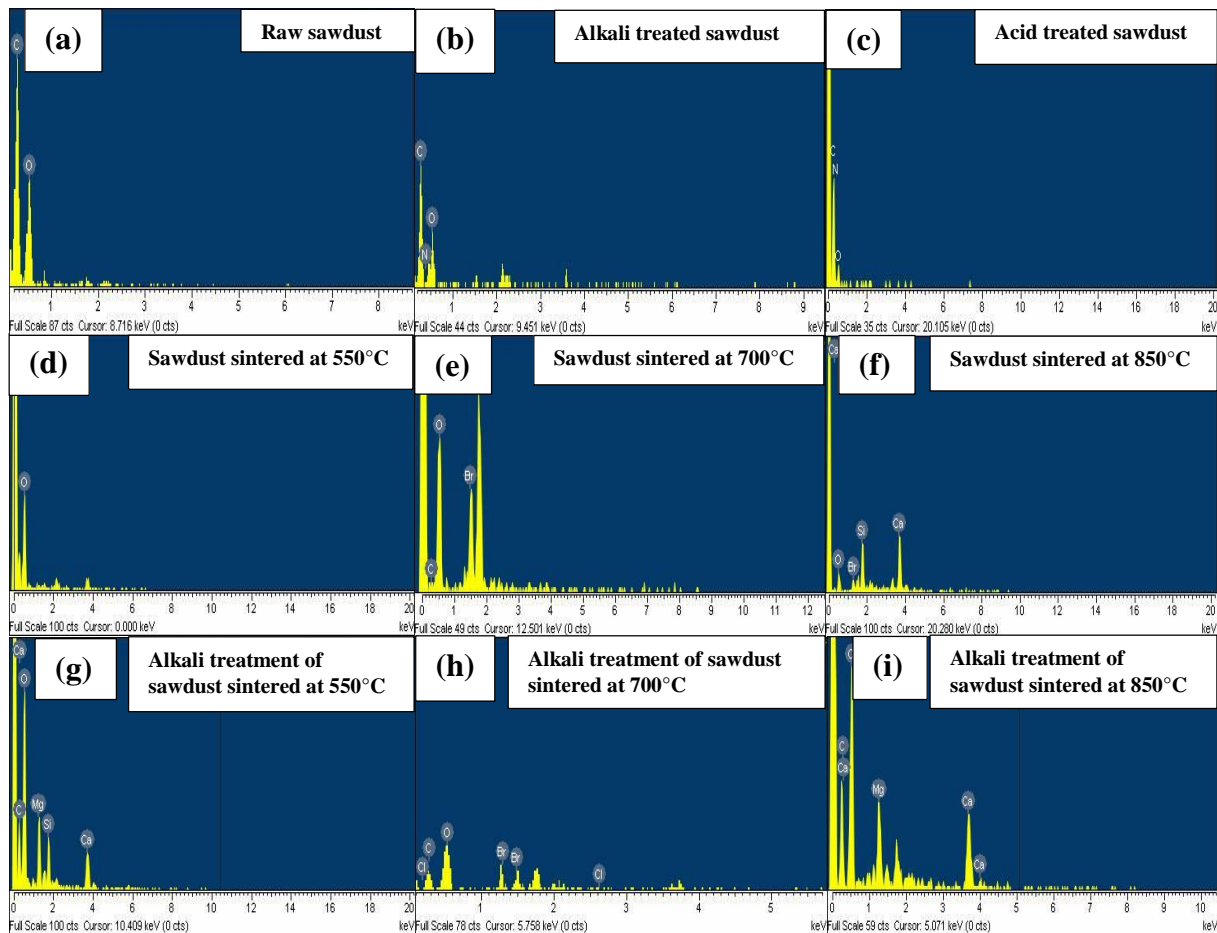


**Figure 2.10** EDX patterns of (a) raw and (b,c) alkali-acid treated sawdust, burnt-sawdust sintered at (d) 550, (e) 700, (f) 850°C and chemical (under alkali treatment) modification of burnt-sawdust at (g) 550, (h) 700, (i) 850°C

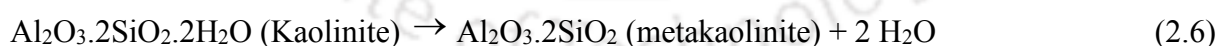
The variation in elemental composition of sawdust during the entire process is detected by EDX study (refer **Figure 2.10**). No such significant alterations in elemental composition of alkali and acid absorbed sawdust (**Figure 2.10b-c**) are observed compared to the elemental composition of the raw sawdust (**Figure 2.10a**). However, a slight change in elemental composition (presence of Cl, Br, Si, etc. as impurities) is observed in the thermally modified sawdust samples (**Figure 2.10d-f**) than that of the raw sawdust samples. However, no such major deviations in elemental composition of alkali absorbed thermally-modified sawdust samples are observed, as shown in **Figure 2.10g-i**.

## 2.2.2 Physical characterization of membranes screened through 44 B.S.S. mesh

As the discussion based on the characterization techniques, so far, has indicated sawdust screened through 44 B.S.S. mesh have an excellent impact on membrane formation compared to the other sawdust samples. On account of that, we will discuss fabrication and characterization of membrane using sawdust screened through 44 B.S.S. mesh in this section.

### 2.2.2.1 TGA analysis

**Figure 2.4** also shows the TGA/DTA curves of raw materials mixture (SM6) made of 44 B.S.S. mesh screened sawdust particle along with other raw materials like kaolin, quartz and feldspar. Total 81% weight loss of SM6 is observed up to 880°C whereas only 2 % is noted below 100°C due to the removal of loosely bonded water molecules present in the powder mixture. Weight loss of the sample from 210°C to 350°C is due to the pre-dehydration process of kaolin, confirmed from a small exothermic peak at 825°C displayed in the DTA curve of a mixture of raw materials in SM6. The TGA curve of kaolin exhibits almost 10% weight loss due to the loss of the structural hydroxyl group starts at 425°C and continues to 550°C, due to the transformation of kaolinite to metakaolinite [115] according to the following reaction:



No significant dissociation is observed for quartz particle in the curve b whereas feldspar shows almost 21% weight loss (curve d) due to the removal of moisture. Slight residue in form of ash is found for the sample mixture after 850°C which ensures that the pore-former is fully decomposed at this temperature regime.

### 2.2.2.2 Effect of raw materials content on particle size distribution

The effect of different weight ratios of kaolin, quartz, saw dust and feldspar on the particle size distribution of six different compositions are illustrated in **Figure 2.3c**. The majority of the particles of the sample mixtures are between 1 and 30  $\mu\text{m}$ . The multi-, bi- and mono- peak mode particle size distribution observes due to the effect of different weight ratios of all the raw materials (refer **Table 2.1**). SM1, SM3 and SM4 exhibits mono peak which implies smaller particle size of the raw materials. The average particle size of SM1, SM3 and SM4 are found as 2.05  $\mu\text{m}$ , 5.60  $\mu\text{m}$ , and 5.60  $\mu\text{m}$ , respectively. SM1 shows mono mode peak as the sample mixture contains higher amount of kaolin (average particle size of 2.34  $\mu\text{m}$ ) and sawdust which nullifies the effect of weight percentages of other raw materials. SM3 and SM4 are also exhibit mono peak curves with higher average particle sizes than SM1. An increase in average particle size of SM3 than SM1 is observed due to the higher weight percentage of feldspar (40 g) with average particle size of 8.56  $\mu\text{m}$ . On the other hand, the peak height is reduced in case of SM4 due to the presence of higher amount of kaolin and equal amounts of quartz (average particle size of 8.04  $\mu\text{m}$ ) and feldspar (average particle size of 8.56  $\mu\text{m}$ ). SM2 shows a bi-mode peak curve with an average particle size of 5.94  $\mu\text{m}$ . The nature of the particle size distribution curve as well as average particle size in SM2 is affected due to the higher weight percentage of quartz. The first peak in SM2 in the curve is due to the presence of kaolin, quartz and feldspar whereas the second peak is controlled by sawdust. SM5 and SM6 displays bi and tri-mode peak particle size distribution due to the presence of equal amounts of kaolin and sawdust in the composition. The average particle size of SM5 is found as 5.98  $\mu\text{m}$ . The tri mode peak curve of SM6 refers the same amount of sawdust and feldspar. The highest peak is contributed by sawdust followed by two small peaks due to kaolin and feldspar, respectively. The average particle size of SM6 is around 12.33  $\mu\text{m}$ , highest among the other combinations,

points to slightly dense structure with lower temperature which satisfies the porosity data obtained from volumetric technique and gas permeability test, discussed later in sub-section 2.2.3.1.

### 2.2.2.3 Determination of porosity using Archimedes' principle

The volumetric porosity of different membranes sintered at three different temperatures (550, 700 and 850°C) determined on the basis of Archimedes' principle (Eq. 2.1) are listed in **Table 2.5**.

**Table 2.5** Membrane porosity (made of sawdust screened through 44 B.S.S. mesh)

Membranes	Sintering temperature (°C)	Porosity (%) (Archimedes' principle)
SM1	550	40
	700	43
	850	48
SM2	550	33
	700	36
	850	38
SM3	550	38
	700	40
	850	41
SM4	550	34
	700	35
	850	38
SM5	550	31
	700	36
	850	38
SM6	550	19
	700	25
	850	36

The variation in porosity values of the fabricated membrane depends on four major factors and are particle size of raw materials, decomposition of sawdust contains cellulose, hemicellulose and lignin, sintering temperature and weight percentage of raw materials, especially, pore-former. Higher the amount of sawdust, higher is the porosity due to loose densification between particles which reflects in the porosity values of SM1 to SM5. The porosity of SM6 varies in the range between 19 to 36% which is less compared to other combinations due to lesser sawdust content. The porosity values increase with increase in temperature due to complete decomposition of sawdust and its high particle size. Based on the porosity values, SM6 is selected as the suitable composition for further characterization study.

#### 2.2.2.4 Surface morphological analysis

Microstructure of the membranes can be affected by the sintering profile. It has been seen that higher temperature provides much denser and smoother surface and also larger grain size and tiny pores.

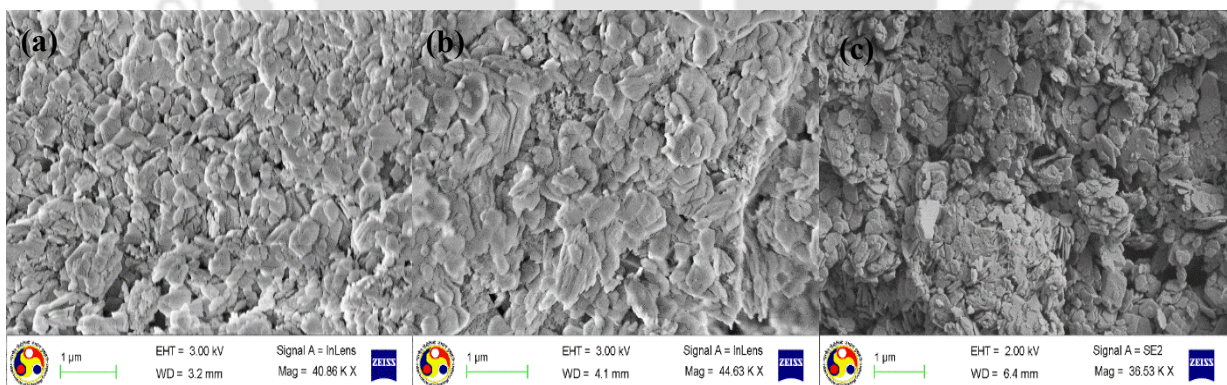


**Figure 2.11** FESEM micrographs of SM6 sintered at (a) 550°C (b) 700°C and (c) 850°C

FESEM has been used to observe the microstructure of the fabricated ceramic during the sintering process. **Figure 2.11** displays FESEM images and consistent grain size of sawdust-based tubular ceramic membrane after sintering at three different sintering temperatures. As

shown in **Figure 2.11a**, significant formation of grained structure is seen for the membrane sintered at 550°C. At 700°C, the grain boundaries start to form, but the grains do not merge together completely (**Figure 2.11b**). As the sintering temperature rises to 850°C, a compact surface is achieved. With increasing sintering temperature, the grain size is increased and the pores start to be eliminated. At sintering temperature of 850°C, most of the pores are vanished and form an uneven structure with complete disappearance of grain boundaries, as shown in **Figure 2.11c**.

FESEM images reveal that during sintering process, grains grow and merge together and form a compact structure. But, porosity (in terms of number of pores) is found to increase with increase in sintering temperature for all the membrane combinations except SM5 due to complete decomposition of sawdust with increasing temperature.

Percentage of weight loss of ceramic membranes with optimized sintering temperature is summarized in **Table 2.6**.

**Table 2.6** Weight losses of the ceramic membrane after sintering using 44 B.S.S. mesh screened sawdust along with different weight ratios of raw materials

Membrane composition	Sawdust (wt. %)*	Weight before sintering	Weight after sintering	Weight loss (%)
1	30	12.02	7.13	41
2	10	11.32	8.71	23
3	20	11.87	7.48	37
4	10	12.30	9.22	25
5	25	12.22	8.18	33
6	25	10.03	5.99	40

\*On the basis of weight percentages of other inorganic raw materials.

Loss in weight of the ceramic membranes depends upon weight ratios of sawdust and other raw materials. An increase in loss in weight due to the removal of ligno-cellulosic material with sintering temperature, is observed with increase in amount of sawdust, signifies the formation of high porous ceramic body. Therefore, higher the sawdust content, higher is the removal of ligno-cellulosic material and higher is the porosity in terms of the number of pores with the sintering temperature. Thus the effect of sawdust decomposition (elimination of cellulose, hemicellulose and lignin) is significant in ceramic morphology.

#### 2.2.2.5 Pore size analysis built on FESEM images

ImageJ software is used to measure the individual pore diameters of the different pores visible in the FESEM study. Pore size distribution is evaluated from the randomly selected sections of the five FESEM images of the membranes for about 450 pores using the software. The pore size distribution curve is evaluated by plotting different pore diameters with the values of number of pores, presented in **Figure 2.12**. An assumption has been made that the pores of the membranes are cylindrical in nature to calculate the area average pore diameters ( $d_s$ ).

$$d_s = \left[ \frac{\sum_{i=1}^n n_i d_i^2}{\sum_{i=1}^n n_i} \right]^{0.5} \quad (2.7)$$

where,  $n$  is the number of pores,  $d_i$  is the pore diameter in  $\mu\text{m}$  of the  $i$ -th pore. The average pore diameters of the SM6 membranes are calculated as 0.35, 0.25 and 0.19  $\mu\text{m}$  with increasing temperature. **Figure 2.12** also confirms the relation between pore size distribution and sintering temperature. The maximum number of pores (60%) for all sintering temperatures is in the range of 0.3 to 0.8  $\mu\text{m}$ .

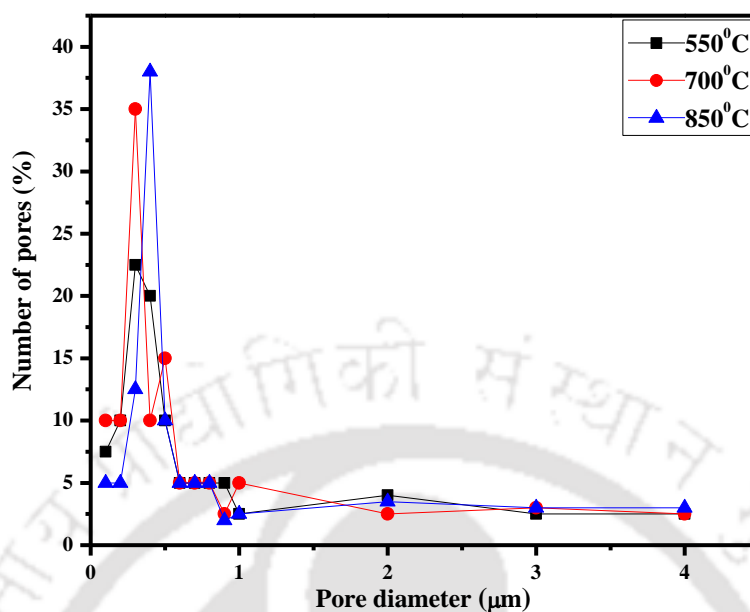


**Figure 2.12** Pore size distribution of the fabricated SM6 membrane sintered at three different temperatures (550, 700 and 850°C) as determined from FESEM images

#### 2.2.2.6 Phase identification by XRD analysis

**Figures 2.13a** summarizes XRD peaks for SM6 membranes sintered at 550°C, 700°C and 850°C and compares with the XRD patterns of raw kaolinite (**Figures 2.13b**). The peaks of raw sample mixture (air dried at room temperature,  $28 \pm 2^\circ\text{C}$ ) confirms the presence of kaolinite (PDF-00-001-0527), feldspar (PDF-00-031-0965) and graphite (PDF- 01-074-2330) with low intensity. The presence of cellulose (PDF-00-003-0192) and hemicellulose (PDF-00-032-1981) is confirmed by the peaks at  $19.936^\circ$  and  $21.290^\circ$  ( $2\theta$ ) for the air dried sample mixture. With increase in sintering temperature, no kaolinite peaks are observed as kaolinite converts into metakaolinite, already discussed by thermogravimetric analysis in the sub-section 2.2.1.2. Membrane sintered at 550°C indicates the presence of ligno-cellulosic material and graphite with low intensity. Calcination of SM6 at 850°C (Figure 2.16a) did not show any

strong peak as compared to the un-calcined sample mixture, indicating an amorphous texture with no phase change above 550°C and the presence of metakaolinite.

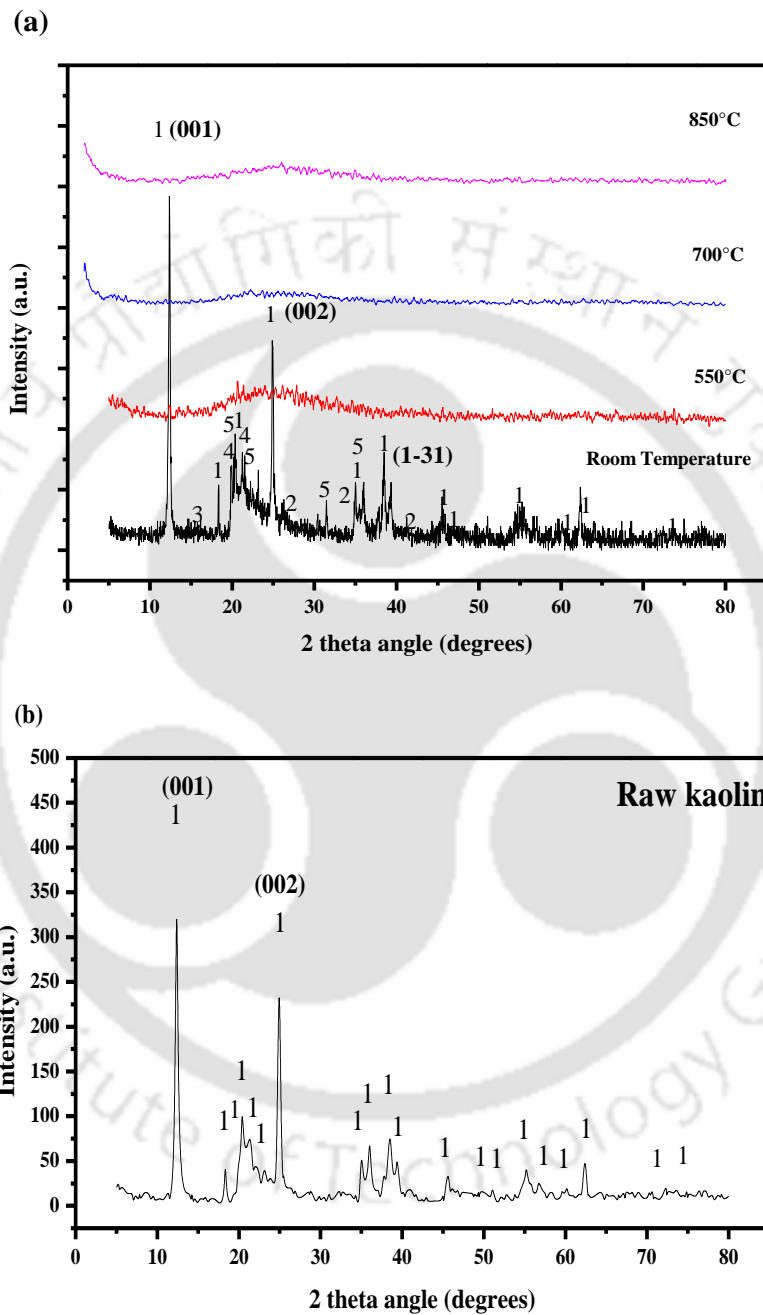


**Figure 2.13** X-ray diffraction patterns of (a) the sample mixture sintered at different temperatures 1: kaolinite; 2: feldspar; 3: graphite 4: cellulose 5: xylitol; and (b) kaolinite powder 1: kaolinite (PDF-00-001-0527)

## 2.2.3 Permeation characterization of membrane screened through 44 B.S.S. mesh

### 2.2.3.1 Determination of porosity and pore diameter via gas permeation

Figure 2.14 illustrates the deviation in effective permeability factor with average pressure from 6 to 68 kPa for all the membranes. The determined gas permeance of the SM6 membrane sintered at 550, 700 and 850°C are  $1.02 \times 10^{-1}$ ,  $2.205 \times 10^{-1}$  and  $2.22 \times 10^{-1} \text{ m}^3 \text{ m}^{-2} \text{ min}^{-1} \text{ kPa}^{-1}$  at an average trans-membrane pressure drop of 2.442 kPa (calculated by deducing outlet pressure from inlet pressure shown by pressure gauge). Slope and intercept values are obtained from Figure 2.14.

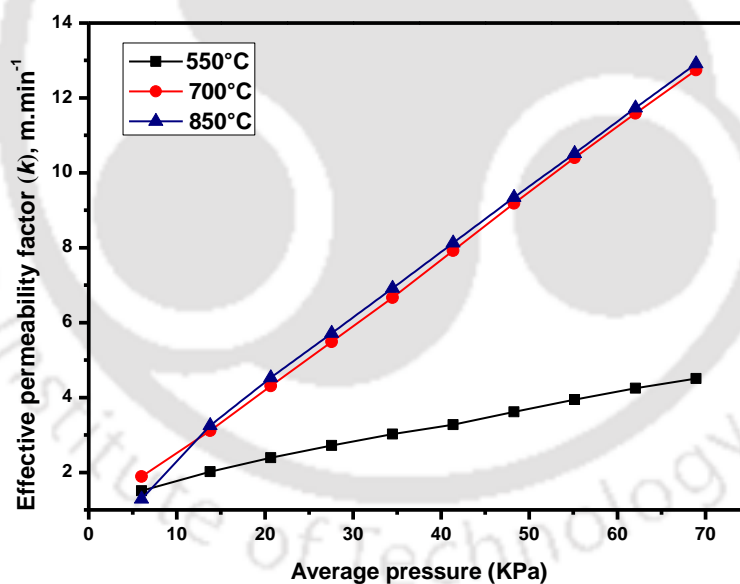


Figure 2.14 Effect of pressure on gas permeability for membranes sintered at different temperatures

Porosity values are calculated by equating the value of slope with the second term of Eq. 2.2. Average pore diameter is obtained from Eq. 2.4. All these parameters are tabulated in

**Table 2.7.** Porosity and pore size of SM6 are calculated assuming tortuosity factor one, in the range of 14 to 34% and 0.38 to 0.13  $\mu\text{m}$  with increasing sintering temperature, respectively, by using Eq. 2.2. It is quite close to the value (0.35 to 0.19  $\mu\text{m}$ ) obtained from FESEM analysis and uses appreciably for microfiltration range applications.

**Table 2.7** Parameters determined from the study of graph between nitrogen gas permeability and average pressure obtained from gas permeability data

Temperature (°C)	Intercept of Eq. (2.2) ( $\text{m}\cdot\text{min}^{-1}$ )	Slope of Eq. (2.2) ( $\text{m}\cdot\text{min}^{-1}\cdot\text{kPa} \times 10^{-6}$ )	Pore diameter ( $\mu\text{m}$ )	Porosity (%)
550	1.506	0.078	0.38	14
700	1.86	0.192	0.20	25
850	0.0215	0.192	0.13	34

### 2.2.4 Mechanical stability

The flexural strength of SM6 membranes is observed as 2 MPa at 850°C using ASTM standard test (ASTM D790) without any binder which is considerable and almost close to the reported value of kaolin based membrane having two different binder in their composition [115]. The number of contact between the particles as well as the specific surface is reduced due to higher particle size of SM6 membrane and absence of binder, thus decreasing the flexural strength of the solid ceramics.

### 2.2.5 Chemical stability

The fabricated SM6 membranes are verified for corrosion resistivity towards acid (concentrated HCl, pH 2) and alkali (NaOH, pH 12) media. The chemical resistance of the prepared membrane is measured by weighing the membranes after keeping it in contact with

the acid and base solution separately for a week at atmospheric conditions. To verify morphological change, porosity of the membrane is measured after acid and alkali test. An increase in porosity of SM6 membranes is observed during both alkali and acid tests. The porosity values are observed as 21%, 27%, 37% and 20%, 27%, 37% with increasing temperature during alkali and acid test, respectively. The residual hemicellulose and most part of the lignin are extracted and oxidized by alkali and acids, respectively, provides an increase in porosity. No significant compositional change is observed after acid and alkali test compared to that of SM6 membrane before acid-alkali test, indicated by EDX study (**Figure 2.15 and 2.16**). This result approves the suitability of the membrane in acid and base media.

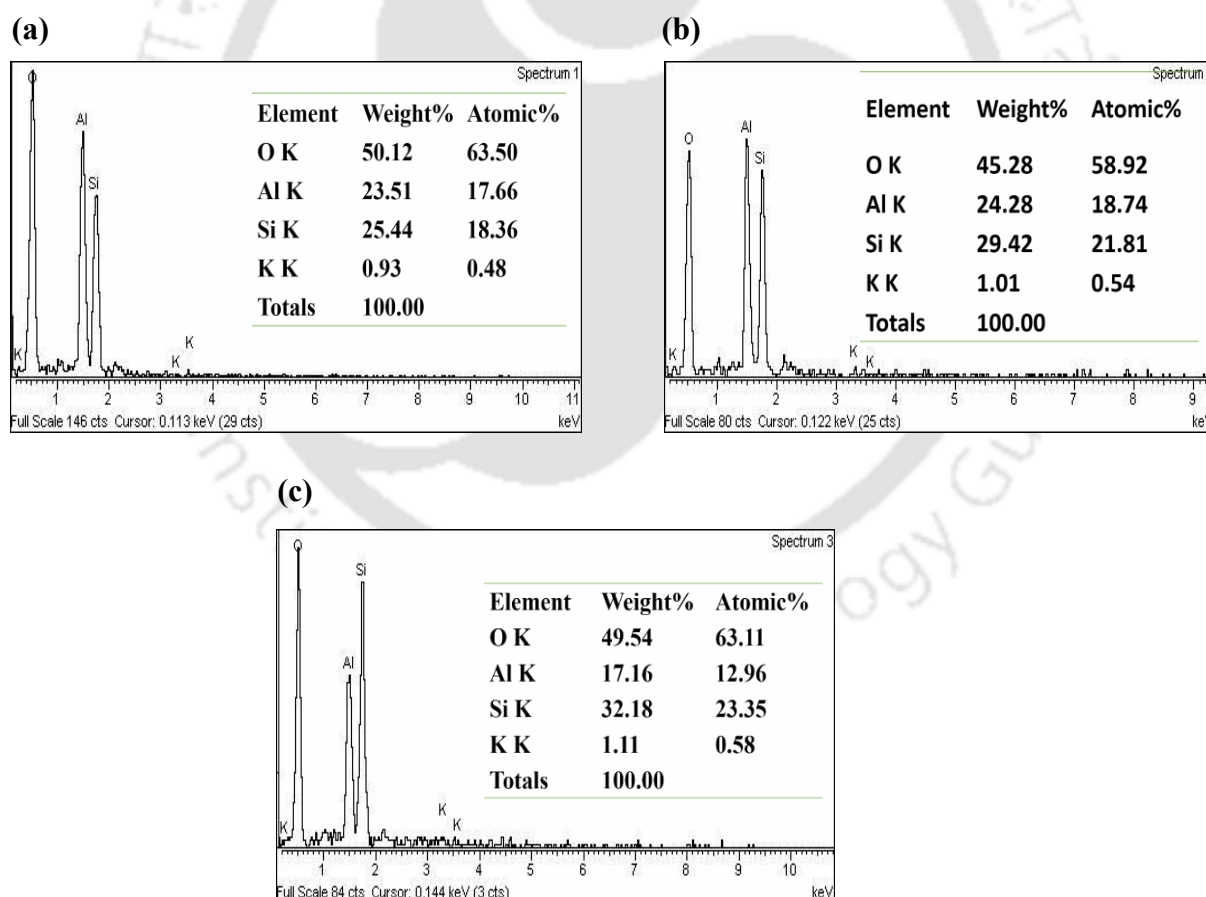


**Figure 2.15** EDX analysis of the fabricated tubular ceramic membrane (SM6) before acid-alkali test sintered at (a) 550, (b) 700 and (c) 850°C

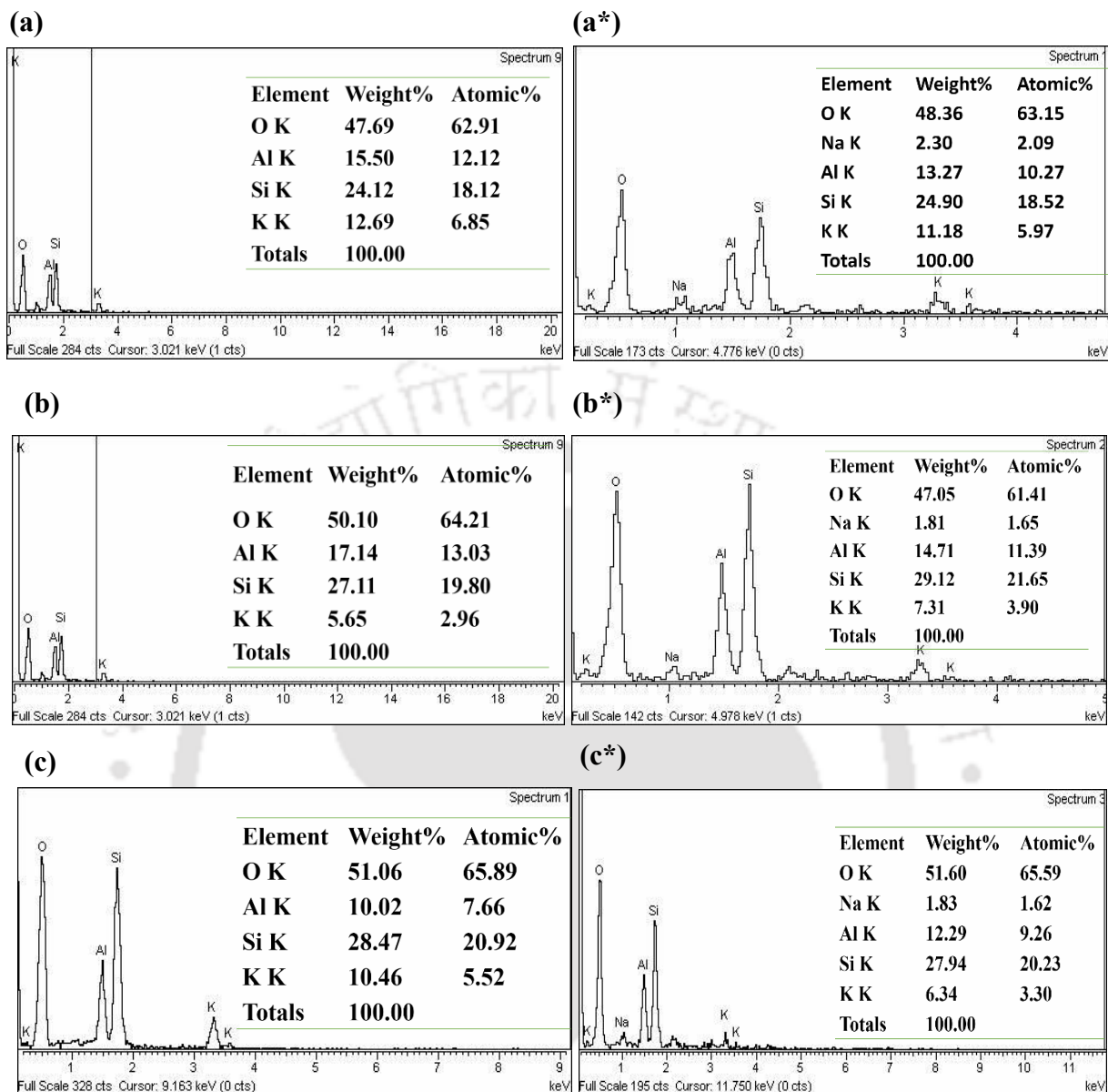


**Figure 2.16** EDX spectrum and data of SM6 membranes after acid (a, b, c) and alkali (a\*, b\*, c\*) test sintered at (a) 550, (b) 700 and (c) 850°C

## 2.2.6 Cost evaluation of the membrane sieved through 44 B.S.S. mesh screen

Ceramic membranes are becoming cost competitive in terms of industry, especially tubular membranes. Tubular ceramic membranes are higher in cost per square meter of filtration area than the other configurations due to the difficulty in homogeneous tubular mould

preparation. Ceramic support membranes mainly made of  $\alpha$ -alumina which costs in the range of \$500-5000/m<sup>2</sup>. Based on the unit cost of raw materials and energy cost for sintering process, the manufacturing cost of the fabricated membrane is evaluated and presented in **Table 2.8**.

**Table 2.8** Cost evaluation of fabricated membrane from the unit cost of raw materials

Combinations	Raw material used	Weight (Kg×10 <sup>-3</sup> )	Unit price (\$)	Energy consumption @ 0.075 \$/Kwh	Total price (\$/m <sup>2</sup> )
SM1	Kaolin	40	1.93	5.95	387.39
	Saw dust	30	0.0027		
	Quartz	20	2.74		
	Feldspar	10	0.782		
SM2	Kaolin	40	1.93	5.95	440.47
	Saw dust	10	0.0009		
	Quartz	30	4.12		
	Feldspar	20	0.156		
SM3	Kaolin	30	1.45	5.95	225.14
	Saw dust	20	0.0018		
	Quartz	10	1.37		
	Feldspar	40	0.3127		
SM4	Kaolin	40	1.93	5.95	394.50
	Saw dust	10	0.0009		
	Quartz	25	3.43		
	Feldspar	25	0.1954		
SM5	Kaolin	50	2.42	5.95	352.26
	Saw dust	25	0.0023		
	Quartz	25	2.53		
SM6	Kaolin	50	2.42	5.95	189.00
	Saw dust	25	0.0023		
	Feldspar	25	0.1954		

Among all the combinations, the cheapest membrane is SM6 and the estimated cost of that membrane is around \$250/m<sup>2</sup> (including membrane mould preparation charge). The evaluated cost is almost closer to the cost of polymeric membranes and higher than some disk shaped ceramic membranes made from low cost raw materials [115]. The fabricated low-cost tubular membrane is exceptional in comparison with the  $\alpha$ -alumina ceramic symmetric membranes available in the market cost approximately \$500/m<sup>2</sup> and symmetric stainless steel membrane costs approximately \$3000/m<sup>2</sup> [120]. SM6 is considered as the most suited support membrane for micro filtration range applications after performing all characterization methods. This study approves that the ceramic membrane prepared by kaolin, saw dust and feldspar would be attractive and useful in industrial arrangements. The cost of the membranes may vary with their performance and stability in different process applications.

### 2.3 Summary

The change in physical properties of sawdust while heated in presence of air and the way sawdust behaves while kept in contact with acid and alkali solution have been investigated thoroughly. Based on these characteristics, how sawdust performs during sintering in membrane fabrication is also studied. The effect of particle size of sawdust, controlling the porosity and pore size as well as the microstructure of the ceramic membrane made of sawdust is discussed. Tubular ceramic membrane has been prepared using sawdust of 44 B.S.S. (355  $\mu$ m) as the pore-formers as-well-as the effect of particle size on the microstructure before and after firing, and their thermal and chemical behaviour during membrane fabrication, have been investigated and the following results are:

- (a) Based on the nature of particle size distribution and average particle size of sawdust, 44 B.S.S. (355  $\mu$ m) screened sawdust has been selected for the fabrication of ceramic

membrane. Two important parameters i.e., porosity and pore size of fabricated membrane increases and decreases with increase in the amount of sawdust, respectively, due to the removal of the ligno-cellulosic material.

(b) The presence of hemicellulose, cellulose and lignin in the raw and acid-alkali treated sawdust (without heat treatment) are clearly visible in the finger print region between 1100 and 1800  $\text{cm}^{-1}$  (from FTIR analysis) but no peaks related to ligno-cellulosic compounds are observed in thermally and thermally-chemically modified sawdust which confirms that sawdust burns and decomposes fully with increase in temperature, attributes to the pore-forming ability of sawdust.

(c) The SEM images of sawdust show pore forming ability (micro-fibril like structure) with no significant change in composition (EDX analysis) after exposing in thermal and aggressive environment (acid and alkali media) with various temperatures and pH, respectively. Therefore, it is concluded that the thermal, chemical and morphological properties of sawdust has a vital effect in ceramic membrane fabrication.

(d) Formation of a new combination of porous tubular ceramic membrane (36%) using cheap raw materials, such as, kaolin, sawdust and feldspar fabricated by optimized sintering temperature of 850°C on the basis of TGA analysis of raw materials.

(e) The microstructures of the fabricated ceramic (from FESEM images) show an excellent surface structure of the fabricated membrane.

(f) Mechanical strength of the membranes is high but not appreciable.

(g) The estimated cost ( $\sim \$250/\text{m}^2$ ) of the prepared tubular membrane is less compared to the tubular shaped membrane available in market.



# Chapter 3

---

## Membrane Parameter Optimization using Response Surface Methodology (RSM)

## Chapter 3

# Membrane Parameter Optimization using Response Surface Methodology (RSM)

*Performance of a membrane and its durability greatly depends on its morphology and mechanical strength. Therefore, membrane morphological property, such as, porosity and mechanical property, like flexural strength are important parameters in ceramic processing. These parameters mainly depend on binder content, preparation pressure, and sintering temperature, etc. In second chapter of this thesis, we have addressed fabrication of a low-cost tubular ceramic support membrane without the addition of binder. It is necessary to add binders for enhancing the flexural strength of the support membrane. In this chapter, the effects of binders, such as, sodium metasilicate and boric acid on the mechanical (flexural) strength and porosity of the fabricated low-cost tubular ceramic support membrane on the basis of an empirical model using response surface methodology (RSM) via central compact design (CCD) are discussed. A comparison between experimental and predicted results obtained from mathematical model are presented to validate the model and to predict the optimum independent parameters (binder content and preparation pressure) in fabricating microfiltration range membrane with high durability. On the basis of the study, an optimized membrane is fabricated. The fabricated membrane is then characterized on the basis of morphology and mechanical (flexural) strength and the manufacturing cost is also evaluated.*

---

This work is published in the following journal:

S. Bose, C. Das, "Role of binder and preparation pressure in tubular ceramic membrane processing: Design and optimization study using response surface methodology (RSM)", *Industrial & Engineering Chemistry Research*, 53 (31) (2014) 12319-12329.

## 3.1 Materials and methods

### 3.1.1 Membrane fabrication

Twenty numbers tubular-shaped membranes are fabricated by thorough mixing and grinding of sodium metasilicate ( $\text{Na}_2\text{SiO}_3$ ) (Loba Chemie Pvt. Ltd, India) and boric acid ( $\text{H}_3\text{BO}_3$ ) (Merck India Pvt. Ltd., India) along with other raw materials such as kaolin ( $\text{Al}_2\text{O}_3 \cdot 2\text{SiO}_2 \cdot 2\text{H}_2\text{O}$ ) (Loba Chemie Pvt. Ltd, India), saw dust (mixture of teak, coco and sal wood taken from local sawmill) and feldspar ( $\text{KAlSiO}_3$ ) (National Chemicals, India) of different weight percentages (with respect to binder content) using mixer machine and ceramic mortar via a dry compaction method as it is described in **Chapter 2**. Sodium metasilicate (SM) and boric acid (BA) play the role of strength enhancer by forming silicate and metallic metaborates during sintering. According to the design expert, binders are varied from 4.21% to 10.79% of the total weight of the raw materials (total weight of sample mixture is 40 g) and the preparation pressure applied on the sample mixture is varied from 7.23 MPa to 12.39 MPa.

### 3.1.2 Membrane characterization

#### 3.1.2.1 Three-point bend test

Three-point bend test (ASTM D790) is performed to measure the flexural strength of all prepared membrane using a Universal Tensile Test Machine (Deepak polyplast Pvt. Ltd., India) applying 20 MPa load and maintaining a support span of 85 mm at a stroke rate of 0.5 mm.min<sup>-1</sup>. Rectangular bar-shaped specimens are prepared at thickness/length ratio of 1:16 for determining the flexural strength at room temperature ( $28 \pm 2^\circ\text{C}$ ).

### 3.1.2.2 Membrane porosity

Meanwhile, the porosity of the membrane is calculated using volumetric porosity determination technique based on Archimedes' principle (Eq. 2.1 in **Chapter 2**).

### 3.1.2.3 Surface morphology

The surface morphology and the phase identification of the optimized membrane are analysed by field emission scanning electron microscope (FESEM) ( $\Sigma$ igma, Zeiss, USA) and X-ray diffraction (XRD) analysis, respectively. A portion of the specimen is cut into a small piece and mounted on an aluminium stab with carbon tape. The sample then is coated with gold particles under vacuum and mounted on the FESEM plate. XRD study is performed using Bruker D8 Advanced series powder diffractometer with Cu K $\alpha$  radiation of 40kV and 40mA in the  $2\theta$  range of 15-80° with 0.05° steps at a rate of 1s per step to verify the change in phase with change in temperature.

### 3.1.2.4 Average pore diameter and porosity

An experimental setup is fabricated for gas permeation study, as shown in **Figure 2.2** in **Chapter 2**. The gas permeation data are utilized to estimate two vital membrane characteristics namely, average pore radius ( $r_g$ ) and effective porosity ( $\varepsilon/q^2$ ) according to Eq. 2.2-2.5 in **Chapter 2**.

### 3.1.2.5 Acid-alkali test

Chemical stability of the fabricated composite membrane is verified by immersing the composite into the acid (conc. HCl, pH 2) and alkali (NaOH, pH 12) solution. The entire step is mentioned in **Chapter 2**. EDX (LEO Model 1430VP, Oxford, U.K.) analysis of the

membranes before and after corrosion test is performed to verify the change in elemental composition.

### 3.1.3 Response surface methodology via design of expert

Nowadays, mathematical modeling and optimization techniques are frequently used in the field of membrane technology, especially, statistical tools are well-known in improving operating parameters and performances for membrane applications. In this study, design of expert software (Version 8.0.7.1, Stat-Ease, Inc., Minneapolis, MN, USA) has been used to develop central composite design (CCD) with a full polynomial. CCD procedure is an effective design tool that works for experimental design analysis with lack of fit testing which compares the variation around the model with “pure” variation within simulated observations and measures the adequacy of the quadratic response surface model, process optimization, development of second-order response models, estimating experimental error variance, etc. This tool follows three steps to conduct the experimental design and are (i) statistical design of experiments, (ii) assessment of coefficients through a mathematical model with the prediction of response, and (iii) analysis of the models applicability [121]. Design plan including three input factors i.e. preparation pressure, amount of sodium metasilicate and boric acid (in wt. %) and outputs (R1: flexural strength; R2: porosity) for each experiment is shown in **Table 3.1**. All the experimental response models are produced with respect to the input variables (experimental data). The experimental response models determine the flexural strength and porosity of membrane, thus indicating the role of binders in membrane fabrication.

**Table 3.1** Design arrangement and experimental responses for central composite design (CCD)

Run	Factor 1: A, Preparation Pressure (MPa)	Factor 2: B, Amount of sodium metasilicate (SM) (%)	Factor 3: C, Amount of boric acid (BA) (%)	Response 1: R1, Flexural strength (MPa)	Response 2: R2, Porosity (%)
1	7.84	5.00	10.00	10.54	15
2	9.81	7.50	4.21	8.35	24
3	11.77	5.00	5.00	9.72	26
4	9.81	7.50	7.50	11.68	21
5	9.81	4.21	7.50	11.53	22
6	9.81	7.50	7.50	11.68	21
7	11.77	10.00	5.00	11.82	18
8	9.81	7.50	7.50	11.68	21
9	12.39	7.50	7.50	11.99	16
10	7.84	10.00	10.00	11.29	13
11	7.23	7.50	7.50	5.32	24
12	9.81	7.50	10.79	12.33	11
13	9.81	7.50	7.50	11.68	21
14	7.84	10.00	5.00	5.01	25
15	9.81	10.79	7.50	11.85	13
16	9.81	7.50	7.50	11.68	21
17	9.81	7.50	7.50	11.68	21
18	7.84	5.00	5.00	4.46	28
19	11.77	10.00	10.00	12.82	10
20	11.77	5.00	10.00	13.78	13

The three input factors have been chosen for designing purpose and their values are selected based on preliminary study and are varied over five levels: the high value (+1), the centre points (0), the low level (-1) and two outer points ( $-\alpha$  and  $+\alpha$  value), details are outlined in **Table 3.2**. CCD contains design points and axial points that accompanied a total of 20 experimental runs are used to study the data obtained from the experimental runs. These data are then used to optimize the amount of binders and preparation pressure. The response variables (i.e., flexural strength and porosity of membrane) are measured using a mathematical modelling selected from the CCD with significant terms and the model is not aliased.

**Table 3.2** Design summary: Input variables and their coded and actual values used in the response surface study

Factors	Name	Coded levels				
		$\alpha$ (-)	-1	0	+1	$\alpha$ (+)
A	Preparation pressure (MPa)	7.23	7.84	9.81	11.77	12.39
B	Sodium metasilicate (%)	4.21	5	7.50	10.00	10.79
C	Boric acid (%)	4.21	5	7.50	10.00	10.79

### 3.1.4 Cost estimation

Manufacturing cost of the fabricated membrane is estimated in terms of raw materials cost, electricity consumption, mold preparation cost and other miscellaneous expenses. In this section, we specifically focus our attention on the issue of the manufacturing cost of the optimized tubular ceramic support membrane.

## 3.2 Results and discussion

This section aims to understand the interaction between binder content and preparation pressure with membrane porosity and membrane (flexural) strength using CCD of RSM. A comparison of this study with previously reported studies is also described.

### 3.2.1 Analysis of variance (ANOVA) and response surface

#### 3.2.1.1 Membrane flexural strength

The relationship between process factors (preparation pressures, SM content, and BA content) and desired responses (flexural strength and porosity) are plotted graphically, based on mathematical analysis of the experimental data. **Figure 3.1** presents three-dimensional response surface for membrane's flexural strength. It is observed from the figure that all factors applied in the membrane fabrication showed non-linear effects on the flexural strength of the membrane. High flexural strength is obtained at high preparation pressure with higher amount of binders (see **Figures 3.1a-c**). As SM and BA form silicate and metallic metaborates at higher temperature during sintering process, increases in particle-particle interconnectivity occur. On the other hand, among two binders, BA shows superior influence than SM to obtain high flexural strength (**Figure 3.1c**). Increase in particle-particle interconnection reduces the voids between membrane layers and thus, higher flexural strength is detected. Therefore, high pressure and high BA content are desirable condition for producing a membrane with high flexural strength.

All three fabricating factors have significant model terms (*A*, preparation pressure, *B*, SM content, *C*, BA content) and show quadratic model on both membrane flexural strength and

porosity. **Table 3.3** presents the analysis of variance and regression model for all three model terms where the model  $F$ -value of 41.10 implies that the model is significant.

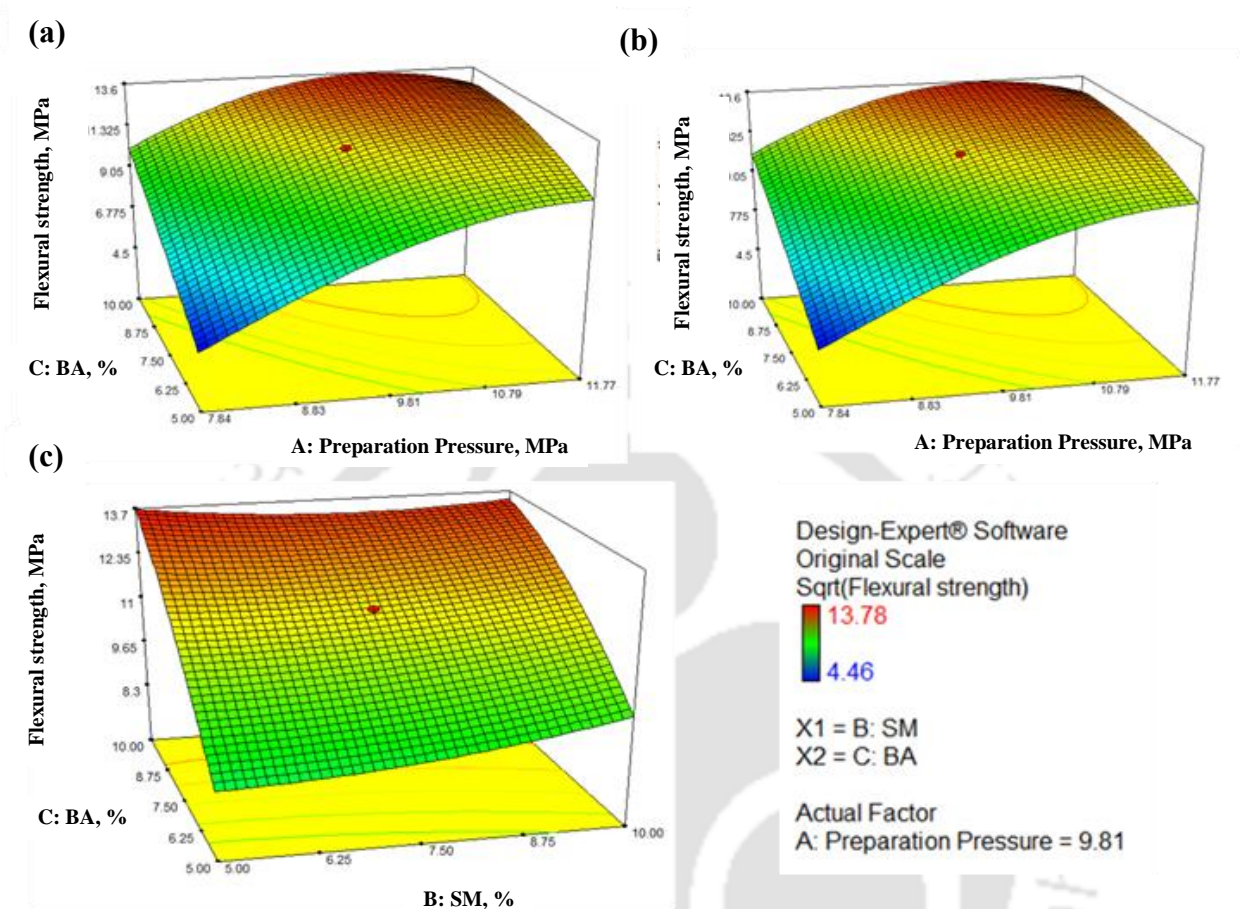


**Figure 3.1** Response surface plotted on (a) sodium metasilicate (SM) content and preparation pressure, (b) boric acid (BA) content and preparation pressure, and (c) sodium metasilicate (SM) content and boric acid (BA) content for membrane flexural strength

It has been observed from the results that the preparation pressure and BA content are significant model terms where  $\text{Prob} > F$  values are  $< 0.05$ . In **Table 3.3**, the  $F$ -value for SM content (1.97) is far lower compared to the  $F$ -values of BA content (119.07) and preparation pressure (159.61). It is confirmed that the effect of SM is less important in membrane flexural strength. The empirical model for membrane flexural strength in terms of actual factors obtained from ANOVA analysis is shown in Eq. 3.1.

Flexural strength model:

$$\begin{aligned}
 Sqrt(R1) = & -10.29102 + 1.87092(A) + 5.87759E - 003 (B) + 0.79157 (C) \\
 & - 1.30706E - 003 (A) (B) - 0.038743 (A) (C) - 9.29759E - 003 (B) (C) \\
 & - 0.070072(A^2) + 6.25176E - 003(B^2) - 0.013929(C^2)
 \end{aligned}
 \tag{3.1}$$

**Table 3.3** Analysis of variance (ANOVA) for respective response surface quadratic models

Responses	Model terms	Sum of squares (SS)	Degree of freedom (DF)	Mean square (MS)	F-value	Prob>F	Remarks
Flexural strength, MPa Quadratic model		3.94	9	0.44	41.10	<0.0001	In this case A, C, AC, A <sup>2</sup> are significant model terms
	A	1.70	1	1.70	159.61	<0.0001	
	B	0.021	1	0.021	1.97	0.1908	
	C	1.27	1	1.27	119.07	<0.0001	
	AB	0.0003285	1	0.0003285	0.031	0.8641	
	AC	0.29	1	0.29	27.11	0.0004	
	BC	0.027	1	0.027	2.54	0.1422	
	A <sup>2</sup>	0.51	1	0.51	47.53	< 0.0001	
	B <sup>2</sup>	0.011	1	0.011	1.00	0.3410	
	C <sup>2</sup>	0.053	1	0.053	4.96	0.0501	
Lack of fit		0.11	5	0.021	-	-	
Porosity, % Quadratic model		7.17	9	0.80	32.71	< 0.0001	In this case A, B, C, B <sup>2</sup> , C <sup>2</sup> are significant model terms
	A	0.71	1	0.71	28.96	0.0003	
	B	0.94	1	0.94	38.68	< 0.0001	
	C	4.87	1	4.87	199.81	< 0.0001	
	AB	0.069	1	0.069	2.82	0.1243	
	AC	0.007148	1	0.007148	0.29	0.5999	
	BC	0.024	1	0.024	0.98	0.3453	
	A <sup>2</sup>	0.0003971	1	0.0003971	0.016	0.9009	
	B <sup>2</sup>	0.19	1	0.19	7.93	0.0183	
	C <sup>2</sup>	0.25	1	0.25	10.30	0.0093	
Lack of fit		0.24	5	0.049	-	-	

The dependability of regression models for flexural strength of membrane is explained on the basis of high value of  $R^2$  (0.97),  $R_{Adj}^2$  (0.95) and  $R_{Pred}^2$  (0.76) which approves that this model is well-fitted to the experimental results shown in **Table 3.4**.

### 3.2.1.2 Membrane porosity

In **Figure 3.2**, the three-dimensional response surface plots demonstrate the influence of preparation pressure and binder content on membrane porosity. Maximum membrane porosity of 28% is obtained at preparation pressure of 7.84 MPa and 5% of binder content each, whereas the minimum porosity of 10% is attained at a preparation pressure of 11.77 MPa at high binder content (10% each), as shown in **Figures 3.2a-b**. This result infers that both preparation pressure and the binder content contribute to membrane porosity. However, the amount of BA seems to give a major effect on membrane porosity, compared to SM content (refer to **Figure 3.2c**). At high binder contents, particles have a tendency to remain close to each other, which causes a decrease in porosity. On the other hand, at maximum preparation pressure of 11.77 MPa (Run 3), it is observed that the porosity is high (26%), compared to the membranes made by applying less pressure (9.81 MPa) (Run 2), which is listed in **Table 3.1**. This phenomenon is due to the presence of less binder content in the former, although the forming pressure is high. Thus, binder seems to offer a greater effect on membrane porosity than that of preparation pressure.

Membrane porosity model:

$$\begin{aligned}
 Sqrt(R2) = & +5.12793 - 0.069077(A) + 0.40462(B) + 0.069356(C) \\
 & - 0.018886(A)(B) + 6.09732E-003(A)(C) + 8.74352E-003(B)(C) \\
 & + 1.96320E-003(A^2) - 0.026644(B^2) - 0.030356(C^2)
 \end{aligned} \tag{3.2}$$

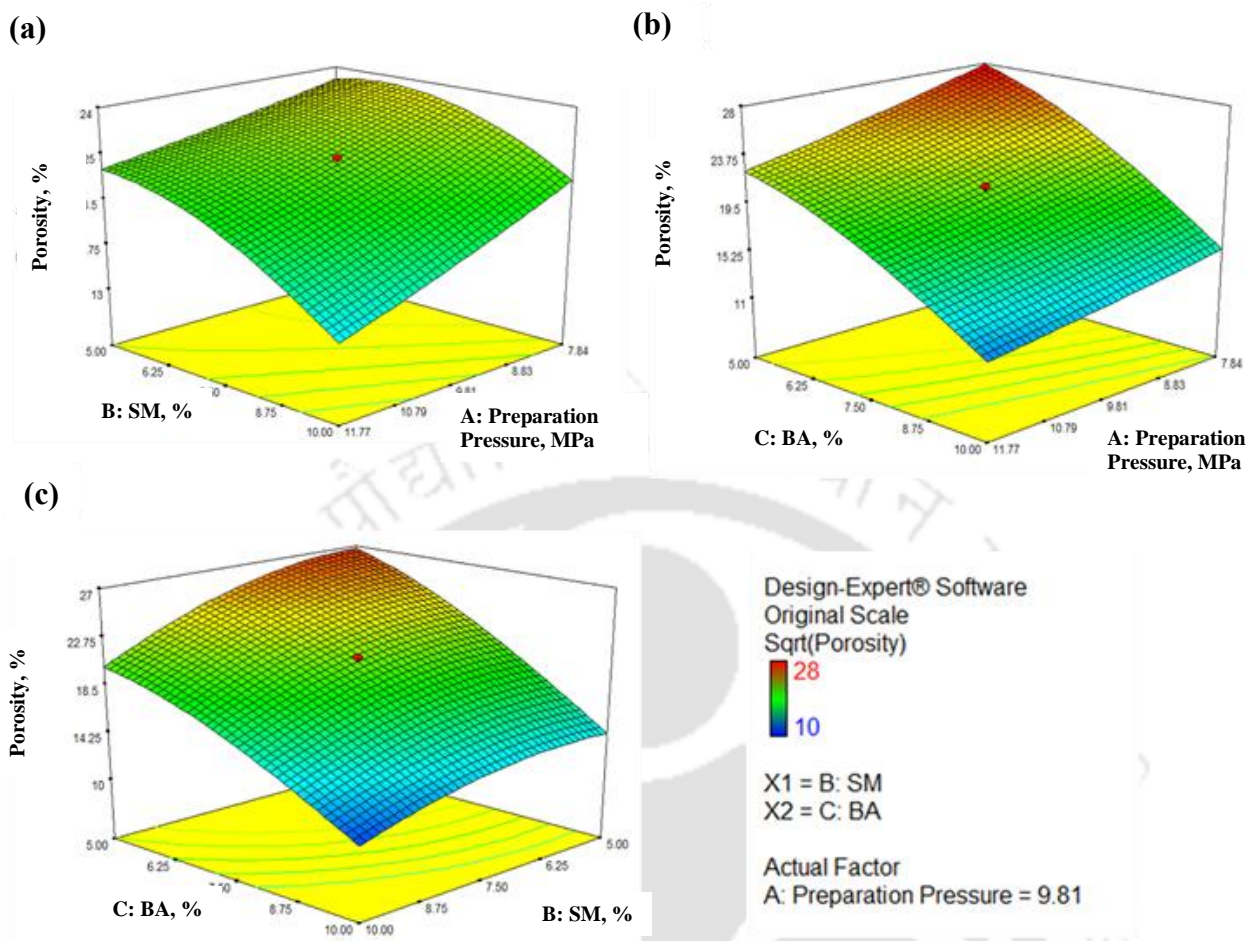


**Figure 3.2** Response surface plotted on (a) sodium metasilicate (SM) content and preparation pressure, (b) boric acid (BA) content and preparation pressure, and (c) sodium metasilicate (SM) content and boric acid (BA) content for membrane porosity

**Table 3.3** shows the effect of significant terms, i.e., preparation pressure (A), amount of SM (B) and BA content (C), second-order effects of SM content ( $B^2$ ) and second-order effects of BA content for membrane porosity with the Prob>F being <0.05. The F-value for BA content is quite higher (199.81) than that of preparation pressure (28.96) and SM content (38.68) which approves that BA content is more prominent in membrane porosity. A quadratic

empirical model for membrane porosity is expressed in Eq. 7 which provides high value of  $R^2$  (0.97),  $R^2_{Adj}$  (0.94) and  $R^2_{Pred}$  (0.75) as shown in **Table 3.4**.

**Table 3.4** ANOVA and regression analysis for flexural strength and porosity

Model	Significant model terms	Standard deviation	$R^2$	$R^2_{Adj}$	$R^2_{Pred}$	Adequate precision
Flexural strength,						
MPa	A, C, AC, $A^2$	0.10	0.97	0.95	0.76	22.19
Quadratic model						
Porosity, %						
Quadratic model	A, B, C, $B^2$ , $C^2$	0.16	0.97	0.94	0.75	21.50

### 3.2.2 Model verification on the basis of statistical analysis

Interaction effect among all the input parameters is investigated using response surface methodology (RSM) software. This model has the advantage of identifying the effects of binary combination of combining two independent input factors. **Figures 3.3** and **3.4** show the variable interaction for all responses. **Figure 3.3b** shows nonparallel curvatures, which suggest a strong interaction between the variables of BA content (C) and preparation pressure (A) for membrane flexural strength. As a result, AC seemed as one of the significant model terms and is mentioned in **Table 3.4**.  $R^2$ -predicted values are low for both R1 and R2 compare to the values of  $R^2$ .  $R^2$  is calculated on the basis of the entire equation involving all the values of significant and insignificant input parameters whereas  $R^2$ -predicted is considered on the basis of the reduced equation involving only the values of significant input parameters. ‘Adequate Precision’ measures the signal to noise ratio which is higher than 4 in both the cases, is desirable to

navigate the design space. In **Figure 3.4**, parallel curvatures indicate that there is no such significant interaction between the independent parameters with each other, but there is an obvious effect of individual parameters on the membrane porosity. The model predicts that the maximum flexural strength and maximum porosity are predicted around the region of middle preparation pressure, and SM and BA content (see **Table 3.5**).

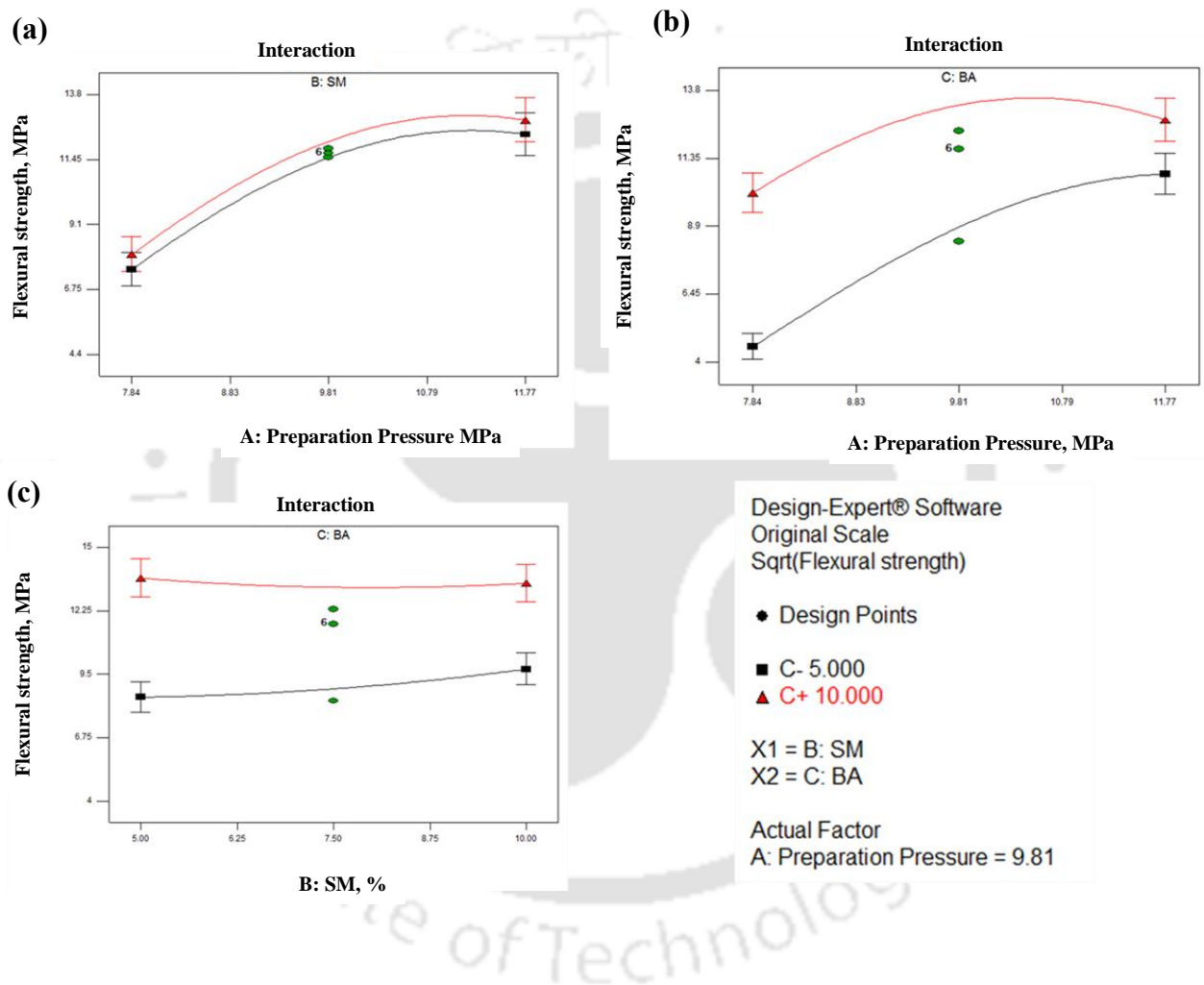


**Figure 3.3** Interaction via (a) sodium metasilicate (SM) content and preparation pressure, (b) boric acid (BA) content and preparation pressure, and (c) sodium metasilicate (SM) content and boric acid (BA) content for membrane flexural strength (circular dots (●) in figures represent design points

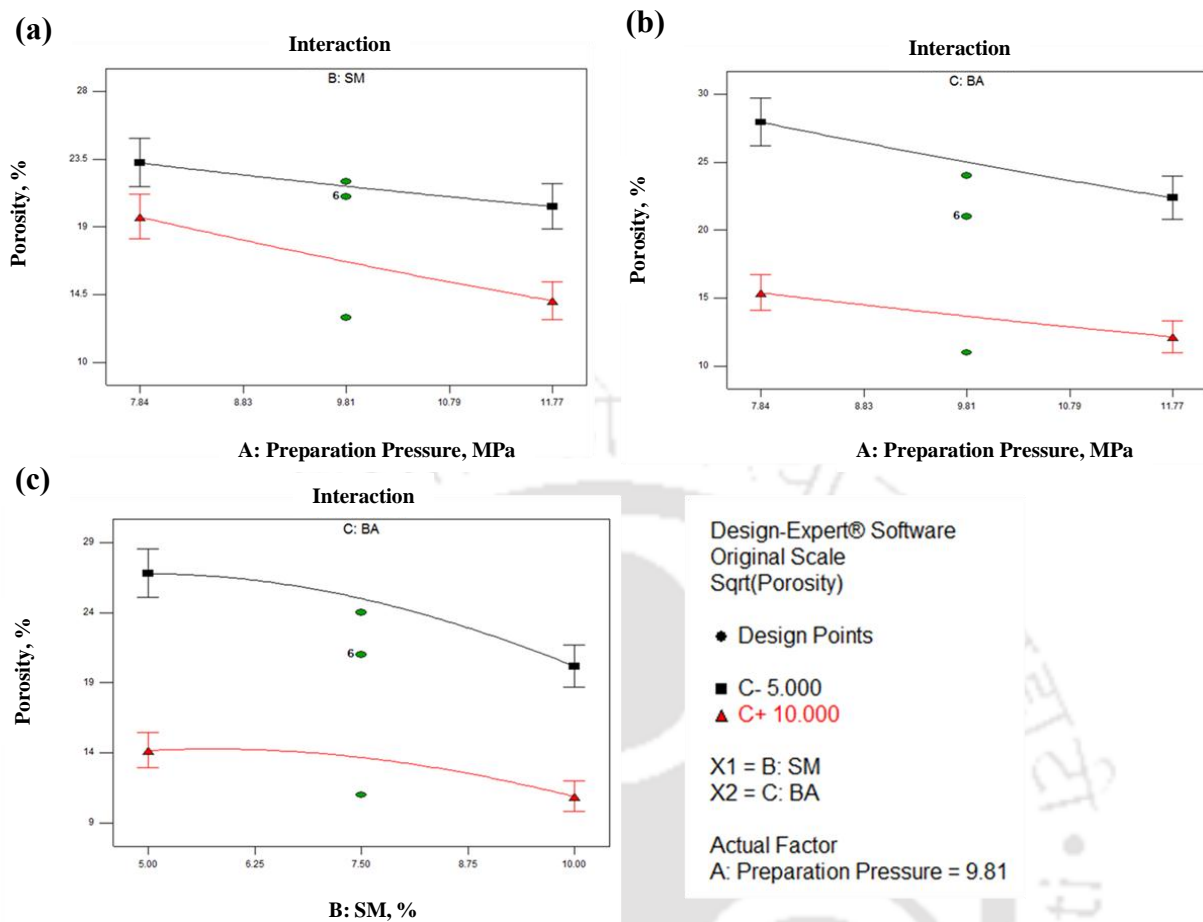


**Figure 3.4** Interaction via (a) sodium metasilicate (SM) content and preparation pressure, (b) boric acid (BA) content and preparation pressure, and (c) sodium metasilicate (SM) content and boric acid (BA) content for membrane porosity (circular dots (●) in figures represent design points

Residual analysis of response surface design is presented graphically in **Figures 3.5** and **3.6** to ensure the fitting of analysis data with the statistical assumptions and to verify whether the standard deviations (SD) between the actual and predicted responses follow the distribution in a normal way. **Figures 3.5a** and **b** ensure that there is no indication of non-normality of the experimental results as the residual points fall near to a straight line showing normal distribution of points.

Table 3.5 Optimized input variables calculated from CCD

No.	Factor 1: A Preparation Pressure (MPa)	Factor 2: B Sodium metasilicate (SM) (%)	Factor 3: C Boric acid (BA) (%)	Response 1: R1 Flexural strength (MPa)	Response 2: R2 Porosity (%)	Desirability	Remarks
1	9.81	6.96	9.25	12.88	16.24	0.97	
2	9.81	7.50	7.50	11.55	20.59	0.97	
3	9.81	6.50	7.76	11.69	20.70	0.96	Selected
4	9.81	9.44	8.43	12.60	15.68	0.96	
5	9.81	9.76	7.94	12.39	16.24	0.96	
6	9.81	5.66	9.72	13.32	15.13	0.96	

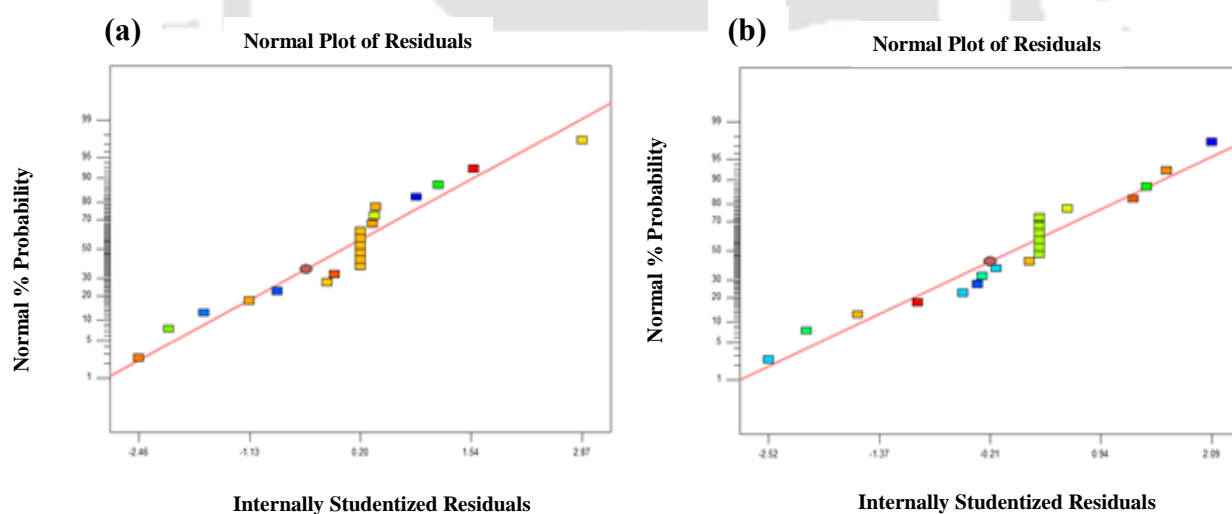
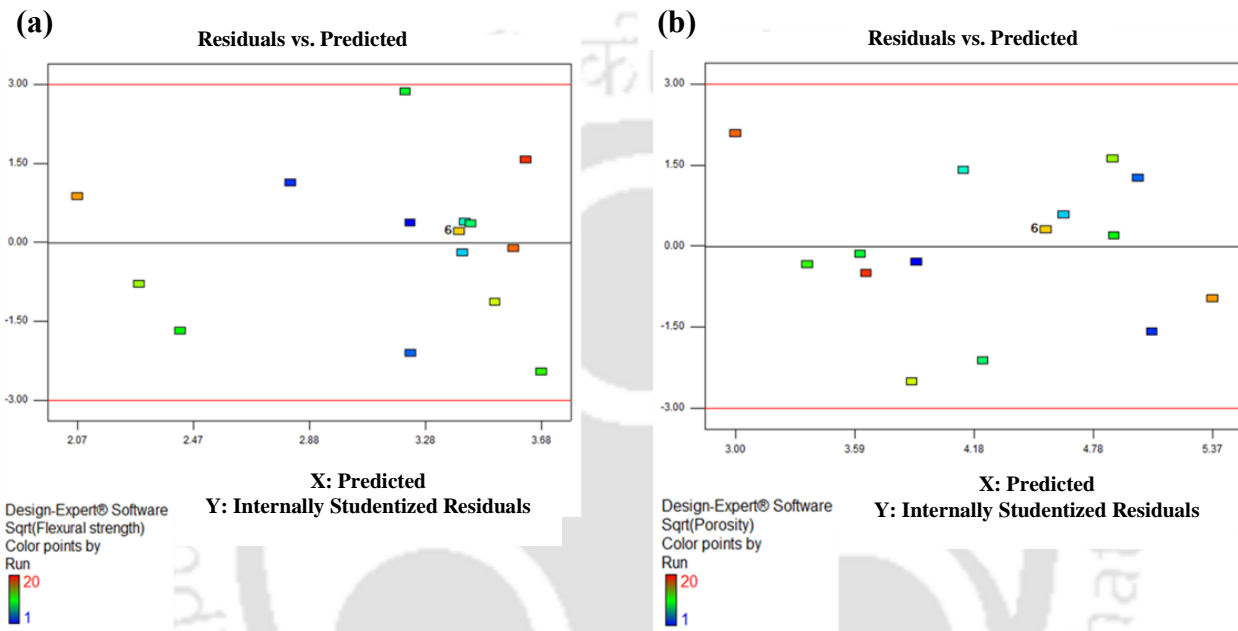


Figure 3.5 Normal probability plot of residual for (a) membrane flexural strength and (b) porosity

Figures 3.6a and b present the plots of the residuals versus predicted response for the membrane flexural strength and porosity, respectively. Figure 3.6 reveals a random scattering of all experimental data points across the horizontal line of residuals which suggests that the proposed models are adequate. The residuals between predicted and actual values are within the range of  $\pm 4\%$  and  $\pm 5\%$  for flexural strength and porosity, respectively.



**Figure 3.6** Plot between residual and predicted response for (a) membrane flexural strength and (b) porosity

The predicted values obtained from regression model are compared with the actual values from experimental studies to confirm the consistency and acceptability of empirical models from individual responses (Figure 3.7). Figures 3.7a and b show the comparison between actual values and predicted values for membrane flexural strength and porosity, respectively, and indicate that all design points are distributed along the diagonal line where, above the line, data are overestimated and below the line, data are underestimated. The overestimated and under-estimated data points for flexural strength are distributed along the diagonal line within a range of 5%. But the over- and under-estimated data points for porosity

lie along the diagonal line within a range of 7%. This comparative study indicates a negligible experimental error as the responses from the empirical model are well-fitted in acceptable variance range. According to the data, the empirical model obtained from CCD can be used as an analyst for the optimization of binder content and preparation pressure in order to achieve a porous ceramic membrane with high appreciable strength.

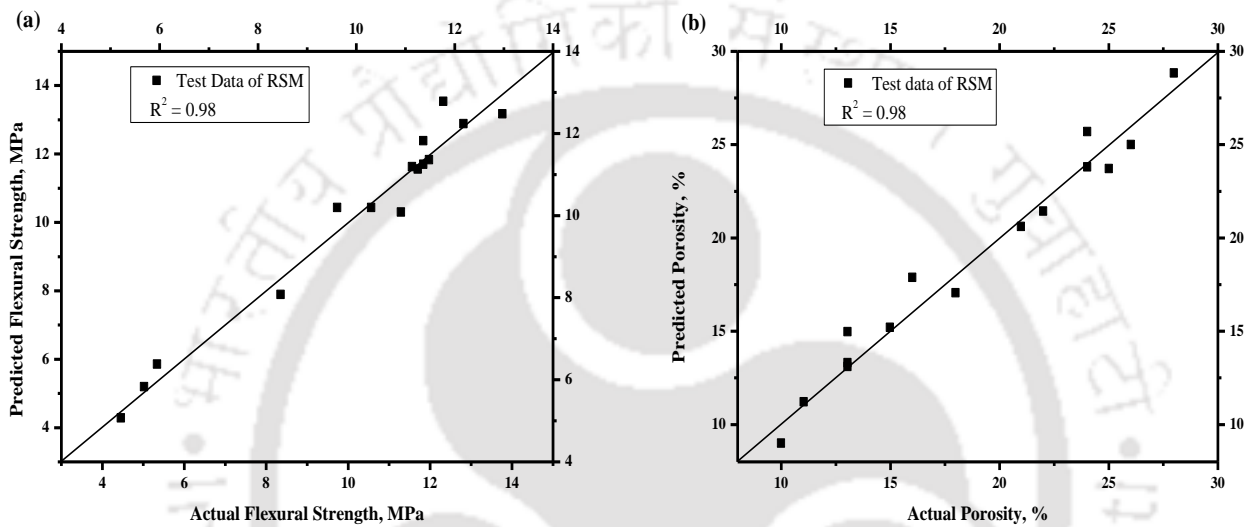


**Figure 3.7** Plot of predicted versus actual values for membrane (a) flexural strength ( $R^2 = 0.98$ ); (b) porosity ( $R^2 = 0.98$ )

### 3.2.3 Optimization study

An optimization study of all of the independent input variables is performed through a desirability function ( $D$ ) for two responses according to Eq. 3.3 [122]. The optimum preparation pressure and binder content for membrane fabrication predicted from all responses with high or low limit of inputs can be satisfied with desirability function ( $D$ ).

$$D = \left[ \prod_{i=1}^N d_i^{r_i} \right]^{1/\sum r_i} \tag{3.3}$$

where,  $D$  is the desirability function,  $N$  is the number of responses,  $r_i$  refers to the significance of a particular response and  $d_i$  signifies the partial desirability function for specific responses.

The common approach is to first transform each response into an individual desirability function  $d_i$  that lies in the range between 0 and 1. Depending on whether a particular response is to be maximized, minimized, or assigned to a target value, different individual desirability  $d_i$  functions can be used. Here, we assigned a particular target value which lies between the lower and upper range values provided during selection of input parameter range.

The individual or partial desirability function  $d_i$  will be as follows [123]:

$$d_i(\hat{y}_i) = \left\{ \left( \frac{\hat{y}_i(X) - L_i}{T_i - L_i} \right)^r \right\}_0^1 \quad (3.4)$$

if  $\hat{y}_i(X) \leq L_i$  and if  $L_i \leq \hat{y}_i(X) \leq T_i$

$$d_i(\hat{y}_i) = \left\{ \left( \frac{\hat{y}_i(X) - U_i}{T_i - U_i} \right)^r \right\}_0^1 \quad (3.5)$$

if  $T_i \leq \hat{y}_i(X) \leq U_i$  and if  $\hat{y}_i(X) > U_i$  and the objective is  $\min(\hat{y}_i(\hat{\theta}; X) - T_i)^2$ . Where,  $X$  is the factors,  $\hat{\theta}$  is parameter estimates of polynomial regression coefficients obtained by least square method,  $L_i$  and  $U_i$  are lower and upper acceptable values of  $\hat{y}_i$ , while  $T_i$  is target values desired for  $i$ -th response, where  $L_i \leq T_i \leq U_i$ . Here,  $r$  is the parameters that determine the shape of  $d_i(\hat{y}_i)$ . A value of  $r = 1$  means that the desirability function is linear,  $r > 1$  means that the desirability function is convex, more importance should be attached to close with the target value, and when the shape of the  $d_i(\hat{y}_i)$  is concave when the value is  $0 < r < 1$  which means

less importance to be attached. The individual desirability are then combined using the geometric mean, which gives the overall desirability  $D$ :

$$D = (d_1(\hat{y}_1) \times d_2(\hat{y}_2) \times \dots \times d_N(\hat{y}_N))^{1/N} \text{ Where, } N \text{ denotes the number of responses.}$$

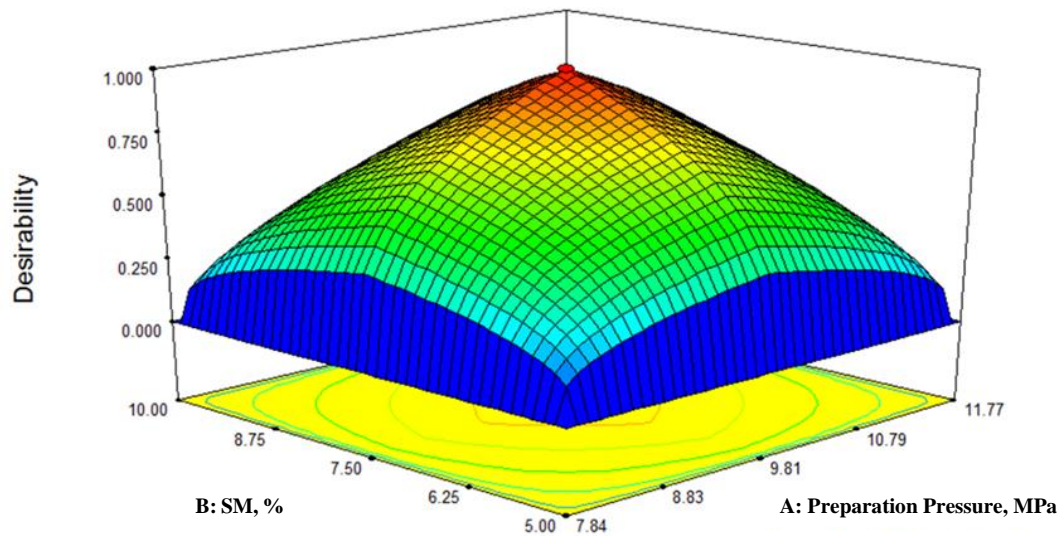


**Figure 3.8** Response surface plot of desirability operating region over SM:BA at preparation pressure set at 9.81 MPa

In **Figure 3.8**, the desirability plot ensures that the desirable preparation pressure is 9.81 MPa and the weight percentage of both SM and BA are 7.5% of total weight of the sample mixture which gives optimized porosity of 21% and flexural strength of 11.55 MPa, is in good agreement with the literature [117,109]. This prediction of desirable input variables is also confirmed with the optimized input variables calculated from central composite design (listed in **Table 3.5**). This optimization study shows that the desirability value of the model is  $D = 0.97$ . **Table 3.6** explains the errors between the experimental and predicted values, and the values are found to be under 2%, which is quite appreciable. This shows that, using response surface methodology, a formulation can be generated to obtain the role of binders and preparation pressures in ceramic membrane fabrication.

**Table 3.6** Error analysis between predicted and experimental value

Factor 1: A, preparation pressure (MPa)	Factor 2: B, Amount of sodium metasilicate (SM) (%)	Factor 3: C, Amount of boric acid (BA) (%)	Response 1: R1, Flexural strength (MPa)	Response 2: R2, Porosity (%)
Predicted value using central composite design				
9.81	7.50	7.50	11.55	20.59
Experimental value selected from Table 1 (Run 13)				
9.81	7.50	7.50	11.68	21.00
Error (%), (Actual value-Predicted value)/Actual value × 100%			1.10	2.0

### 3.2.4 Study of phase transformation and microstructure of the optimized membrane

The XRD patterns of the ceramic membrane using optimized binder contents obtained from RSM study, namely, C1 (SM content = 7.50% and BA content = 7.50%) along with C2 sintered at 550, 700 and 850°C are shown in **Figure 3.9**. The reason behind the selection of three different sintering temperatures is to verify the change in morphology of the optimized ceramic membrane and phase transformation with sintering temperature. The additional composition i.e., C2 (SM content = 5% and BA content = 5%) is introduced to verify the phase transformation with the change in binder contents, keeping the preparation pressure constant. The introduction of C2 is stated since it is difficult for the optimized membrane to identify any phase transformation with the variation in sintering temperature. A graphite-free sample is formed as the temperature rises to 850°C. The formation of crystalline inoyite and nephiline are

detected at diffraction patterns at  $2\theta = 29.455^\circ$  and  $29.757^\circ$ , respectively, because of the reaction between the binders and metakaolinite during heating. The XRD diffractogram clearly reveals that inoyite and nephiline are the predominant crystalline component in the membrane matrix, which signify membrane hardening with high crystallinity and is in good agreement with the literature [124].

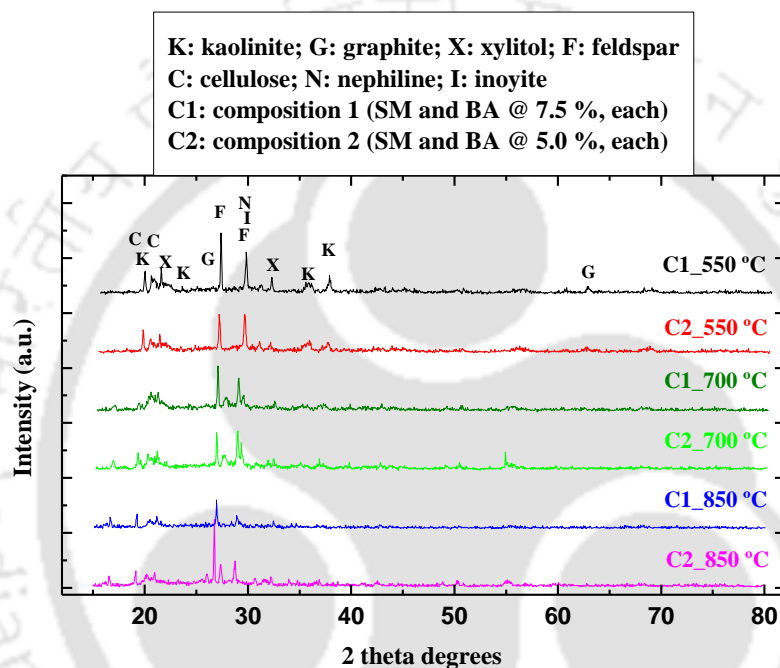


**Figure 3.9** XRD patterns of the ceramic membrane (C1: optimized composition, C2: composition for validation) sintered at 550, 750 and 850°C with the formation of inoyite (PDF-00-006-0361) and nephiline (00-019-1176)

The microstructure of the ceramic matrix using FESEM images are shown in **Figure 3.10**. The microstructure of the ceramic matrix mainly depends on two factors: one is sintering temperature and the other is binder content. At lower temperature (550°C), a muddy and patchy matrix (**Figure 3.10a**) is observed, which corresponds to an interfacial layer of partially decomposed raw materials (mainly hemicellulose, cellulose and lignin present in sawdust)

during heating. A rough and pellet-like surface texture (**Figure 3.10b**) is detected when the membrane sintered at 700°C, because of the increase in the rate of decomposition of ligno-cellulosic material with increasing temperature. On the other hand, at 850°C, the densification of ceramic matrix increases due to complete decomposition of raw materials and binder burnout. Hence, the image shows a highly consolidated and well-bonded matrix grains (**Figure 3.10c**). At 700°C or higher temperature, the occurrence of consolidated surface texture evidently discloses the densification of ceramic body by forming silicate/metaborates or borosilicate bonds and, hence, increases the bonding strength, resulting in a higher flexural strength.

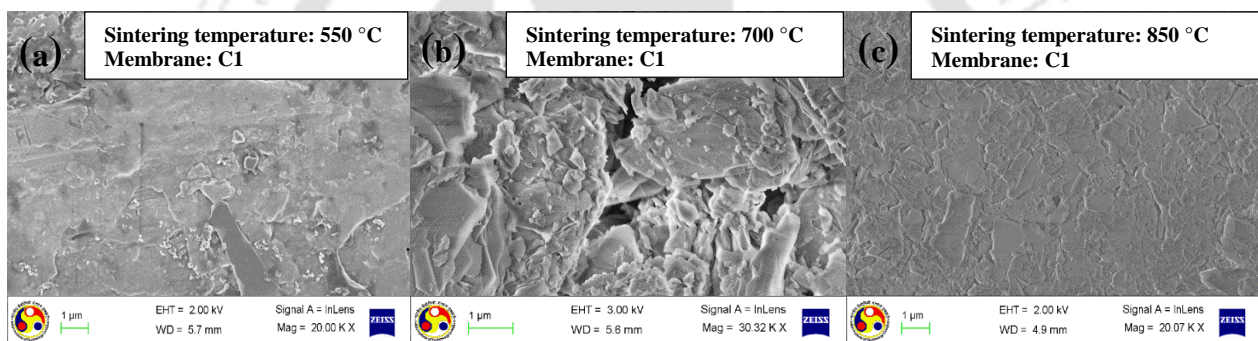


**Figure 3.10** FESEM images of the ceramic membrane surface sintered at (a) 550, (b) 700 and (c) 850°C using optimized composition from CCD analysis

### 3.2.5 Gas permeation test of the optimized membrane

The gas permeation experiment is implemented for the membrane prepared on the basis of optimized composition with three different sintering temperatures to determine the average pore diameter. **Figure 3.11** illustrates the variation of effective permeability factor with average pressure and determines the value of slope and intercept for the membranes. The determined gas permeance of the membranes sintered at 550, 700 and 850°C are  $2.27 \times 10^{-1}$ ,  $2.77 \times 10^{-1}$ ,

$1.18 \times 10^{-1} \text{ m}^3 \text{ m}^{-2} \text{ min}^{-1} \text{ kPa}^{-1}$ , respectively, and the average pore diameter of the membranes sintered at 550, 700 and 850°C are 0.13, 0.12 and 0.21  $\mu\text{m}$ , respectively. The porosity values (see **Table 3.7**) obtained from the volumetric porosity method (Eq. 2.1) are 0.34, 0.44, and 0.20 with increasing temperature, which is in good agreement with the literature [124].

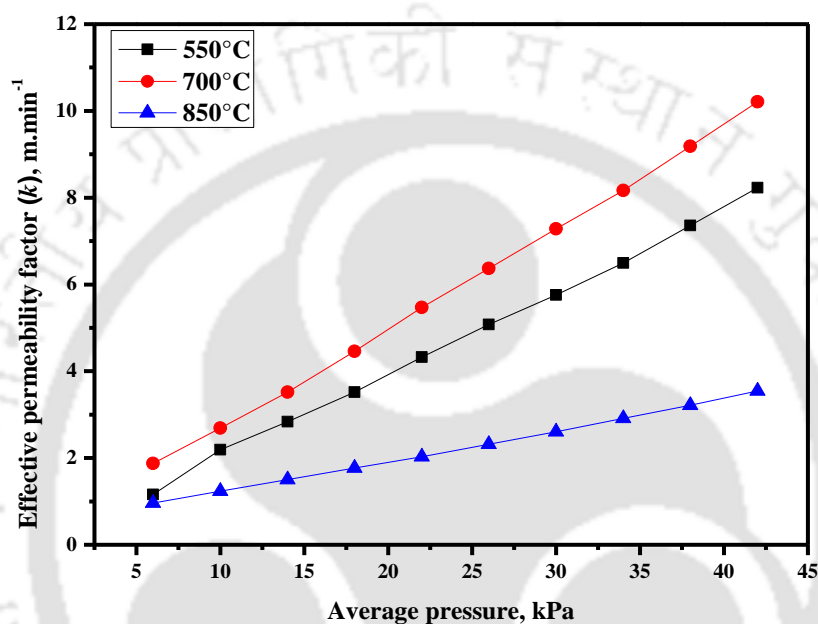


**Figure 3.11** Effective permeability factor vs. average pressure for the optimized membranes sintered at 550, 700 and 850°C temperatures

**Table 3.7** also defines the porosity values calculated from a gas permeation study (Eq. 2.2) and the values are 0.33, 0.41, and 0.15 with increasing sintering temperature. Because of the uneven surface structure, the permeation rate of the membrane sintered at 700°C is higher than that of sintered at 550°C, which is quite clear from FESEM images (**Figure 3.10**). This phenomena is due to partial construction of borosilicate and metaborates and partial decomposition of cellulose and lignin. The tortuosity factor is assumed to be one (straight cylindrical pores) during the calculation procedure. It is interesting to observe that the permeation rate of the membrane sintered at 850°C is reduced, compared to the membrane

sintered at 700°C. This behaviour is due to the complete decomposition of sawdust, along with the formation of borosilicate and metaborates with sintering temperature. This condition clearly confirm that the formation of borosilicate and metasilicate bonds is completed after 700°C, which controls the morphology of the membrane superiorly than the decomposition of sawdust.

Porosity values obtained from volumetric porosity method are slightly higher, compared to the values calculated from gas permeation tests as water remains intact in the pore interiors and pore walls, because of the swelling nature of kaolin-based membrane.

### 3.2.6 Chemical stability test of the optimized membrane

The porosity values of the ceramics during acid-alkali testing are also shown in **Table 3.7**. The weight loss of the membrane is under 6% during acid-alkali testing. However, an increase in membrane porosity in the range of 9%-10% is observed in both acid and alkali media for the optimized membranes sintered at 850°C. However, a 3% decrease in porosity is detected for the membrane sintered at 550 and 700°C during acid testing, because of the production of silicon dioxide while SM reacts with HCl, whereas a decrease in porosity in the range of 3%-8% is noted in alkali testing, because of the production of sodium metaborate while SM reacts with NaOH solution.

Energy-dispersive X-ray (EDX) studies of the membranes obtained from optimization study before and after chemical stability test are shown in **Table 3.8**. It is confirmed from the table that there is no significant change in elemental composition of the membrane in both acid-alkali media. Therefore, the observed trends in weight loss and EDX analysis during acid-alkali tests convey that there is no major change in elemental composition due to the presence of binders in ceramic processing.

**Table 3.7** Change in porosity of the optimized membrane in acid and alkali media as a function of temperature

Composition	Raw materials (wt. %)	Temperature (°C)	Volumetric porosity obtained from Eq. 2.1	Porosity obtained from Eq. 2.2 (Gas permeation)	Porosity in acid media (pH 2)	Porosity in alkali media (pH 12)
C1	Kaolin (50) Sawdust (10)	550	0.34	0.33	0.33	0.32
	Feldspar (25) Sodium metasilicate (7.5)	700	0.44	0.41	0.43	0.41
	Boric acid (7.5)	850	0.20	0.15	0.22	0.22
	Kaolin (50) Sawdust (10)	550	0.41	0.40	0.40	0.39
C2	Feldspar (30) Sodium metasilicate (5)	700	0.50	0.42	0.49	0.46
	Boric acid (5)	850	0.31	0.25	0.34	0.32

**Table 3.8** EDX analysis of the optimized membrane materials sintered at 850°C temperature before and after acid-alkali test

Components	Membrane (wt. %)	Membrane after acid test (wt. %)	Membrane after alkali test (wt. %)
Oxygen	40.68	39.87	40.82
Silicon	27.12	27.91	27.28
Aluminium	29.50	30.18	29.66
Potassium	1.69	1.26	0.85
Sodium	1.01	0.78	1.39

### 3.2.7 Cost analysis of the fabricated support membrane

In **Chapter 2**, the economic feasibility assessment of the membrane is carried out on the basis of few parameters, such as raw materials cost, energy consumption, and membrane mold manufacturing cost. In this work, the cost analysis is performed including cost of two

binders. The projected cost of the membrane is evaluated and presented in **Table 3.9**. The estimated cost of the prepared C1 membrane is approximately \$302/m<sup>2</sup>. The total cost including membrane mold preparation and other miscellaneous expenditures (50% of the estimated cost) is \$332/m<sup>2</sup>. The optimized membrane is slightly more expensive than the previously fabricated membrane without binder and less expensive than an  $\alpha$ -alumina-based ceramic tube costing \$500–1000/m<sup>2</sup> available in market. This study proves that the ceramic membrane prepared by kaolin, sawdust, and feldspar, along with binders, would be attractive and more useful than polymeric membranes as well as ceramic tubular membranes installed in industrial arrangements. The cost of the membranes may vary with their performance and stability in different process applications.

**Table 3.9** Cost assessment of the optimized membrane

Raw material used	Weight (%)	Unit price (\$)	Energy consumption @ \$ 0.08/kWh	Total price (\$/m <sup>2</sup> )
Kaolin	50	2.58		
Feldspar	25	1.13		
Saw dust	10	0	6.19	301.95
Sodium metasilicate	7.5	0.08		
Boric acid	7.5	0.08		

(US\$ 1 = ₹ 59.26 in the year 2012)

### 3.3 Comparison with formerly published work

The cost of the precursors such as  $\alpha$ -alumina,  $\gamma$ -alumina, zirconia, titania and silica generally used in ceramic processing are significantly high and therefore contributes to the high operating cost of membrane modules for industrial purposes. In recent past, to overcome the

issue of membrane cost, research in the fabrication of ceramic membranes is focused towards the utilization of cheaper raw materials like natural raw clay, fly ash, apatite powder, dolomite and kaolin along with pore-formers, such as, calcium carbonate and sodium carbonate [116, 125-138]. Manufacturing cost of the fabricated ceramic membranes (disc and tubular shaped) reported in the previously published literatures are given in **Table 3.10**.

**Table 3.10** Comparisons of manufacturing cost of various studies

Materials	Parameters considered	Configuration	Cost	Reference
Kaolin, quartz, and calcium carbonate, sodium carbonate, boric acid, sodium metasilicate, water		disc	\$130/m <sup>2</sup>	[115]
Kaolin, quartz, and calcium carbonate		Circular disc	\$81/m <sup>2</sup>	[135]
Kaolin, quartz, and calcium carbonate, sodium carbonate, boric acid, sodium metasilicate, polyvinyl alcohol	Only raw materials cost	Circular disc	\$78/ m <sup>2</sup>	[138]
Kaolin, quartz, and calcium carbonate, sodium carbonate, boric acid, sodium metasilicate, water		Tubular	\$110-135/m <sup>2</sup>	[139]

As the above discussion, so far, has indicated no energy consumption cost and other costs like, mould preparation cost are not considered during cost evaluation of the ceramic membranes. On the other hand, our study have already proven successful use of sawdust as a pore-former and its economic and strategic value to lower temperature which provides excellent membrane morphology, strength and chemical sustainability.

### 3.4 Summary

Based on the response surface designs, it is confirmed that all the factors have an appreciable effect on the membrane porosity and flexural strength.

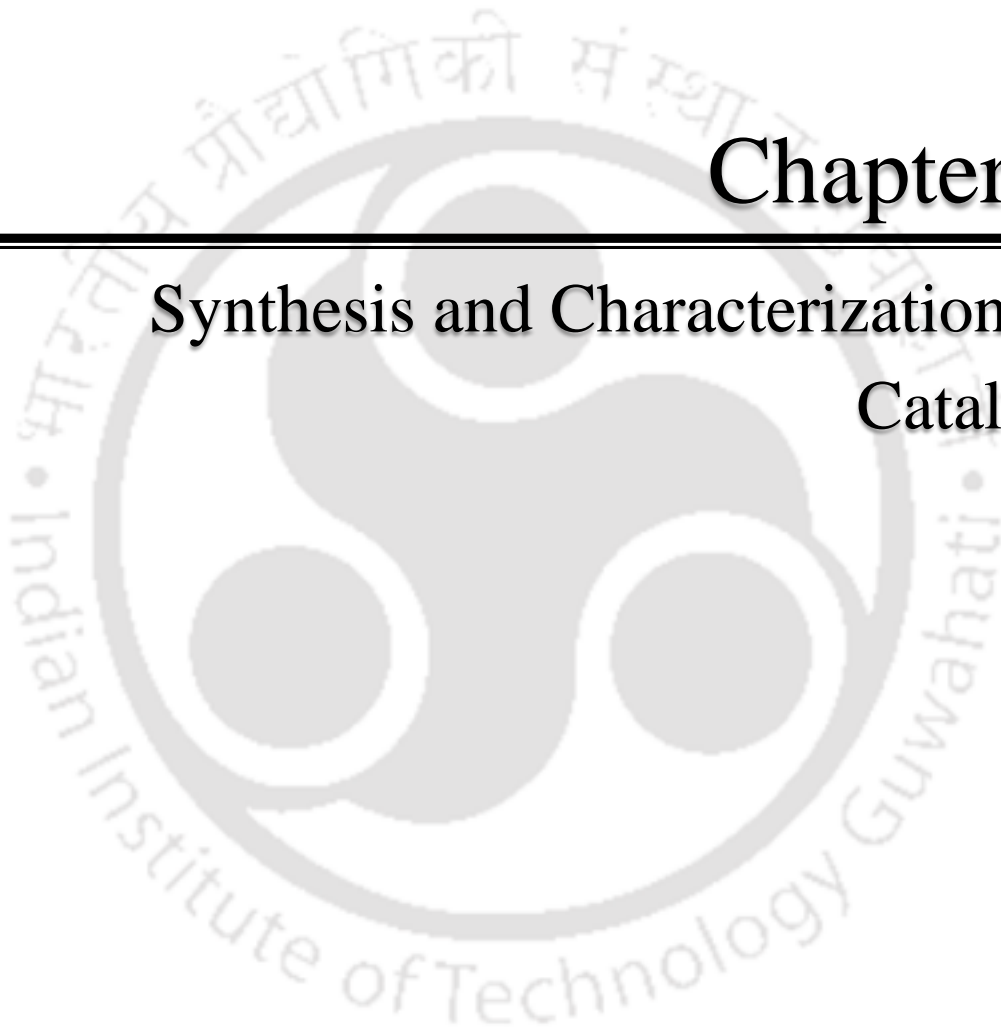
- Among the binders, boric acid (BA) is found to be the key factor in affecting the flexural strength of the membrane. However, the effects of both BA content and sodium metasilicate (SM) content are equally significant for the porosity of membrane, but the influence of preparation pressure is less significant.
- The optimum membrane fabricating condition is obtained at a preparation pressure of 9.81 MPa, 7.50% SM, and 7.5% BA each with the desirability function value of 0.97 for microfiltration range membrane fabrication.
- The predicted values of flexural strength and porosity are 11.55 MPa and 20.59%, respectively, which is in good agreement with the actual experimental data (flexural strength = 11.68 MPa, porosity = 21%).
- Error analysis between actual and predicted values from central composite design (CCD) confirms that the deviation fell within 2%.

This result indicates that the proposed model optimized through RSM on the basis of CCD is reliable and useful tool to understand the role of binder in the fabrication of membrane with desired morphological and mechanical behaviour. The morphological study of the optimized membrane shows appreciable range of average pore diameter along with good chemical stability. X-ray diffraction (XRD) patterns illustrates that the optimized membrane is free of graphite. These results suggest that the optimized membrane offers low manufacturing cost of the membrane (as little as \$332/m<sup>2</sup>), along with good mechanical strength, morphology, and chemical stability.

# Chapter 4

---

## Synthesis and Characterization of Catalyst



## Chapter 4

### Synthesis and Characterization of Catalyst

*In this chapter, we have discussed the synthesis and characterization of a suitable catalyst as one of the major segments of this present research pursued by our laboratory for the development of a catalytic membrane. A series of  $\gamma$ -alumina (high surface area) supported Mo/Co catalysts with different Mo loadings have been prepared through the impregnation by soaking metal precursors over the alumina support followed by drying and calcination for the fabrication of catalytic membrane. The novelty of this proposed method is to obtain high dispersion of metal over catalyst support material by means of well-distribution of metals. A comparative study on  $\gamma$ -Al<sub>2</sub>O<sub>3</sub> with high and low surface area is performed to understand the metal-support interaction and to select the suitable support in terms of metallic dispersion and metallic surface area for better catalytic activity. Several characterization techniques, such as, BET surface area, X-ray diffraction (XRD), Fourier transform infrared spectroscopy (FTIR), field-emission scanning electron microscopy (FESEM), electron spin resonance (ESR), temperature-programmed reduction (TPR), laser Raman spectroscopy (LRS), transmission electron micrograph (TEM), Energy dispersive X-ray (EDX) spectroscopy and CO chemisorption have been used to verify interaction between Mo and activated  $\gamma$ -alumina. The appropriate catalyst composition is finally selected in terms of high metallic surface area and metal dispersion.*

---

This work is communicated in the following journal:

S. Bose, C. Das, "Preparation, characterization, and activity of activated  $\gamma$ -alumina-supported molybdenum/cobalt catalyst for the removal of elemental sulfur", Applied Catalysis A. (Under review)

## 4.1 Materials and methods

### 4.1.1 Chemicals for catalyst preparation

Cobalt nitrate hexahydrate (as Co precursor) and ammonium molybdate tetrahydrate (as Mo precursor) are purchased from M/s Merck specialities private limited, India.  $\gamma$ -aluminium oxide (Alfa Aesar, USA) with high surface area ( $100 \text{ m}^2.\text{g}^{-1}$ ) and low surface area ( $60 \text{ m}^2.\text{g}^{-1}$ ) are used as catalyst support. Millipore water is used for slurry preparation.

### 4.1.2 Catalyst synthesis

Twenty four numbers of Mo-Co/ $\gamma$ -Al<sub>2</sub>O<sub>3</sub> samples (denoted by SC1, SC2, SC3 and SC4) have been prepared via impregnation by mixing Mo, Co precursors and water for both  $\gamma$ -alumina support with high and low surface area to find out the appropriate support material, optimum Mo content and calcination temperature. This method allows well controlled distribution of the species. Accurately weighed 20 g of catalyst (by maintaining the weight percentage) has been prepared for this study. The support material is mixed with precursors and Millipore water by maintaining 1:1 water/solid ratio to get a slurry solution, and kept at the ambient temperature ( $28 \pm 2^\circ\text{C}$ ) for 30 min to retain the homogeneity of the sample. The sample is then placed in a muffle furnace and temperature is increased and kept at  $120^\circ\text{C}$  for 9 h to remove excess water from the solution and calcined at three different calcination temperatures ( $350$ ,  $400$  and  $600^\circ\text{C}$ ) for 5 h at a heating rate of  $5^\circ\text{C}/\text{min}$ . The catalysts compositions of different loading of Mo and Co precursors with different synergistic ratio (0.18-0.50) are given in **Table 4.1**.

**Table 4.1** Catalyst compositions and surface area of support

Composition	Co-Mo supported catalysts			
	SC1	SC2	SC3	SC4
Support [Al <sub>2</sub> O <sub>3</sub> ] (Wt. %)	79.33	84	78.67	75
Mo (Wt. %)	8	12	16	20
Co (Wt. %)	12.67	4	5.33	5
[Co/(Co + Mo)] <sup>a</sup>	0.50	0.23	0.23	0.18
Texture properties of raw commercial $\gamma$ -alumina (low surface area)				
BET surface area = 59 m <sup>2</sup> .g <sup>-1</sup>				
Total pore volume = 0.25 mL.g <sup>-1</sup>				
Texture properties of raw commercial $\gamma$ -alumina (high surface area)				
BET surface area = 151.59 m <sup>2</sup> .g <sup>-1</sup>				
Total pore volume = 0.48 mL.g <sup>-1</sup>				

a – synergistic ratio by means of atomic% of metal precursors (elemental analysis)

## 4.2. Characterization techniques

### 4.2.1 BET surface area analysis

The specific surface area and pore size of the catalysts are characterized by a BET surface area analyser (Beckman Coulter, Switzerland) using N<sub>2</sub> adsorption at liquid nitrogen temperature. The sample is previously weighed (approx. 50 mg) and kept in a sample tube and then degassed for 1 h at 120°C before being exposed to the analysis conditions. The sample tube is then fixed at analysis port, the bottom part of which is merged into a Dewar containing

liquid nitrogen. Specific surface area is obtained by multi-point BET equation in the 0.05 to 1.0  $P_s/P_0$  range.

### 4.2.2 Particle size analysis

The catalyst particle diameter is measured by DLS in a particle size analyser [Beckman Coulter (Switzerland), Delsa Nano<sup>TM</sup> C] by sonication of samples into water as dispersing agent in a JEIOTECH UC-02 Ultrasonicator. The samples are irradiated with a He-Ne laser (wavelength = 632.8 nm), and the intensity fluctuations of the scattered light are analysed to obtain the correlation function, from which the size distribution is obtained by fitting a multiple exponential to it by non-negative least-squares method.

### 4.2.3 Fourier Transform Infrared Spectroscopy (FTIR)

FTIR spectra are recorded in transmission mode using a diffuse reflectance assembly (Shimadzu IR Affinity-1 FTIR spectrometer) over the range of 400 to 4000  $\text{cm}^{-1}$  to realize the formation of complex between cobalt-molybdenum precursor and alumina support. A background is first measured with dried potassium bromide (KBr) (Merck KGaA, Germany). Then the catalyst sample of 1 to 2 mg is grinded to fine powder and mixed with the KBr using ceramic porcelain mortar and then is loaded into a sample holder, mounted inside the instrument.

### 4.2.4 X-ray diffraction (XRD)

The change in phase of catalysts with the change in calcination temperature and dispersion of active phase are predicted by a Bruker, D8 Avance diffractometer with a Bragg/Brentano geometry equipped with a proportional detector using a Cu  $K\alpha$  radiation ( $\lambda =$

1.54060 Å) of 40 kV and 40 mA in the  $2\theta$  range from  $5^\circ$  to  $80^\circ$  with  $0.05^\circ$  steps at a rate of 1 s per step. The various phases are predicted on the basis of JCPDS powder diffraction file cards.

#### 4.2.5 Field-emission scanning electron microscopy (FESEM)

The surface texture of the catalysts is analysed by FESEM (Sigma, Zeiss, USA) operating at 3 kV. A small amount of the catalyst sample is mounted on an aluminium stab with carbon tape, coated with gold particles under vacuum and then is mounted on the FESEM sample holder.

#### 4.2.6 Electro spin resonance (ESR)

Electron spin resonance (ESR) spectroscopy is a very powerful and sensitive method for the characterization of the electronic structures of materials with unpaired electrons. The ESR spectra of the catalyst sample (~ 30 mg) are taken at room temperature with a JEOL, JES-FA200 spectrometer (USA) to verify the presence of metal complex during catalyst preparation.

#### 4.2.7 H<sub>2</sub> Temperature programmed reduction (TPR)

The prepared catalysts are heated overnight in hot air oven and cooled to room temperature. TPR in hydrogen atmosphere started until the baseline is stabilized. The flow rate of hydrogen is maintained at  $30 \text{ cm}^3 \text{ min}^{-1}$ . TPR has been performed up to  $900^\circ\text{C}$  for 1h, at  $10^\circ\text{C min}^{-1}$ , in  $30 \text{ mL min}^{-1}$  of 50% H<sub>2</sub>/N<sub>2</sub> mixture followed by degassing of sample (He purging) at  $120^\circ\text{C}$ , in  $30 \text{ mL min}^{-1}$  for half-an hour. The temperature has been recorded using ChemiSoft Tpx V1.02 software.

### 4.2.8 CO chemisorption

Metal dispersion, metallic surface area and active particle diameter of the catalysts are measured in micromeritics® Unit 1 (2720). The catalyst samples are first degassed at 150°C in helium atmosphere for 30 min at the degassing port using a sample tube. After cooling down to room temperature, the sample tube is transferred to the analysis port for the reduction analysis of the sample. The reduction procedure has been done upto 900°C for 1h at a heating rate of 10°C min<sup>-1</sup>. The chemisorption study is then analysed by injecting CO gas until the reduction temperature cooled down to room temperature under argon atmosphere. The formulae used for the calculation of metal dispersion and metallic surface area are as follows:

#### CO chemisorption on 0.5 wt. % Mo on Alumina

##### a. Volume of active gas injected from a syringe 10 %CO /He

$$V_{inj} = V_{syr} \times \frac{T_{std}}{T_{amb}} \times \frac{P_{std}}{P_{amb}} \times \frac{\%A}{100} \quad (4.1)$$

##### b. Calculating volume chemisorbed:

$$V_{ads} = \frac{V_{inj}}{m_s} \times \sum_{i=1}^n \left( 1 - \frac{A_i}{A_f} \right) \quad (4.2)$$

##### c. % Metal dispersion (MD):

$$\%D = S_f \times \frac{V_{ads}}{V_g} \times \frac{m.w}{\%M} \times 100 \times 100 \quad (4.3)$$

##### d. Active Metal surface area (per gram of sample) (MSA):

$$MS_{as} = S_f \times \frac{V_{ads}}{V_g} \times N_A \times \delta_m \times \frac{m_s^2}{10^{18} \text{ nm}^2} \quad (4.4)$$

### 4.2.9 Laser Raman spectroscopy (LRS)

The local structure of the oxidic precursors is studied by laser Raman spectroscopy using a Horiba Jobin Vyon (Labram HR) spectrometer with a 632.8 nm He-Ne, run in a back-scattered confocal arrangement. The samples are pressed in a microscope slide and the scanning time is set to 30 s. Raman spectra are recorded in air at room temperature with a resolution of  $2\text{ cm}^{-1}$  in the scanning range of 100 to  $1200\text{ cm}^{-1}$ .

### 4.2.10 Transmission electron microscope (TEM)

For the transmission electron microscope (TEM) analysis, a tiny amount of each sample is dispersed in ethanol, then sonicated for 30 min, and a drop of the suspension is placed on a holey carbon thin film that is supported by a copper TEM grid. TEM images, selected-area electron diffraction (SAED) patterns, and chemical analyses of the materials are obtained using a JEOL 2100 (200 KV) TEM equipped with an OXFORD energy-dispersive X-ray (EDX) spectrometer.

## 4.3 Results and discussion

This section discusses the result of the entire study considering the preparation and characterization of the alumina based Mo-Co catalyst. The effect of suitable support matrix, metal content, and calcination temperature on the metal dispersion and metallic surface area have been investigated. Based on the characterization studies, a suitable composition is selected for further study in the development of a catalytic membrane.

### 4.3.1 Effect of support, Mo content and calcination temperature on metal dispersion and metallic surface area

A number of simple mathematical equations are used to estimate an estimate of metal dispersion (MD) and metallic surface area (MSA). An assumption is made that all metal particles are half-sphere in shape which sit on the surface of the alumina support. The volume of a half-sphere is  $\frac{2}{3}\pi R_p^3$ , and the surface area is  $2\pi R_p^2$ . The number of atoms in the crystallite is calculated by dividing the volume of the crystallite with the volume of an individual molybdenum atom whereas the number of potential adsorption sites is determined by the surface area of the crystallite with the cross-sectional area of an atom, given as  $\pi r^2$ . The atomic radius of Mo is considered as 0.139 nm. According to this model, the active particle diameter  $d$  is calculated by the relation  $d=2R_p=1.11/D$  where,  $D$  is the metal dispersion. The active particle diameter of the deposited molybdenum particles as calculated using this formula is found to vary from 100 nm for the alumina (high surface area) supported catalyst at high Mo loading (20 wt. %) to as little as 1 nm for the most highly dispersed samples at 16 wt. % loading. Metal dispersion depends not only on the metal content but also on the support material and calcination temperature. **Table 4.2** displays data of metal dispersion and metallic surface area for both  $\gamma$ -Al<sub>2</sub>O<sub>3</sub> (high and low surface area) supported catalyst. It is observed that  $\gamma$ -alumina supported (high surface area) catalyst shows higher metal dispersion (MD) and metallic surface area (MSA) compared to the alumina (low surface area) supported catalyst. The catalyst with  $\gamma$ -alumina having low surface area (**Table 4.1**) reduces metal exposure on the support matrix.

However, it is interesting that the alumina (high surface area) supported catalysts containing 16 wt. % Mo calcined at 400°C show higher MD and MSA values compared to alumina (low surface area) supported catalysts calcined at the same temperature. This is due to

the dissimilar nature of active sites and some metal sites are blocked due to the sintering. Lower calcination temperature (350°C) causes a decrease in the number of surface metal atoms per unit mass of metal because of particle agglomeration and low metal dispersion. Even, higher calcination temperature (600°C) causes collapse in pore structures and reduction in metal dispersion. The metal dispersion and metallic surface area for the  $\gamma$ -alumina based catalyst decrease with increasing Mo content (20 wt. %), due to the formation of catalytically inactive  $\text{Al}_2(\text{MoO}_4)_3$  which inhibits dispersion capability of metal particles at higher Mo contents. Lower BET surface area of  $\gamma$ -alumina (low surface area) based catalyst reduces the possibility of metal trapping within the support which causes lower metal dispersion and metallic surface area compared to the  $\gamma$ -alumina (high surface area) supported catalyst. Based on this experimentation, samples calcined at 350°C containing 20 wt. % Mo are not considered for further characterization techniques.

**Table 4.2** Chemisorption analysis data

Composition	Calcination temperature (°C)	Alumina (low surface area)			Alumina (high surface area)		
		MD* (%)	MSA*(metal) (m <sup>2</sup> .g <sup>-1</sup> )	APD* (nm)	MD* (%)	MSA*(metal) (m <sup>2</sup> .g <sup>-1</sup> )	APD* (nm)
SC1	350	25.5	120.1	5.2	24.7	125.3	4.9
	400	18.8	96.4	6.4	57.6	341.1	1.9
	600	26.6	151.3	4.2	26.2	155.4	4.2
SC2	350	11.3	55.7	10.2	30.4	156.1	3.9
	400	9.7	49.8	11.5	85.7	439.6	1.3
	600	22.7	122.7	4.8	49.0	251.3	2.5
SC3	350	11.0	54.0	11.2	40.4	207.4	3.0
	400	9.5	48.7	12.7	93.7	480.5	1.1
	600	13.5	69.1	8.9	71.5	366.7	1.7
SC4	350	10.4	52.8	12.9	5.4	15.4	85.5
	400	9.4	47.5	13.3	1.2	6.2	98.7
	600	6.5	32.5	10.2	1.2	5.9	99.3

(MD\* = Metal dispersion in %, MSA\* = Metallic surface area in m<sup>2</sup>.g<sup>-1</sup> metal, APD\* = Active particle diameter in nm)

### 4.3.2 Identification of bimetallic oxide catalyst

The presence of MoO<sub>3</sub>, bimetallic oxide CoMoO<sub>4</sub> appears at 457.12, 478.34, 563.05, 605.20, 663.51 and 830-840 cm<sup>-1</sup> due to Mo-O-Mo and Mo=O bending and stretching vibrations, respectively (**Figure 4.1a**). The spectrum of  $\gamma$ -Al<sub>2</sub>O<sub>3</sub> (low surface area) supported SC1, SC2 and SC3 calcined at 600°C (**Figure 4.1a**) show the presence of MoO<sub>3</sub> at 663 cm<sup>-1</sup>, which is referred to asymmetric stretching mode of tetrahedral MoO<sub>4</sub><sup>2-</sup>.

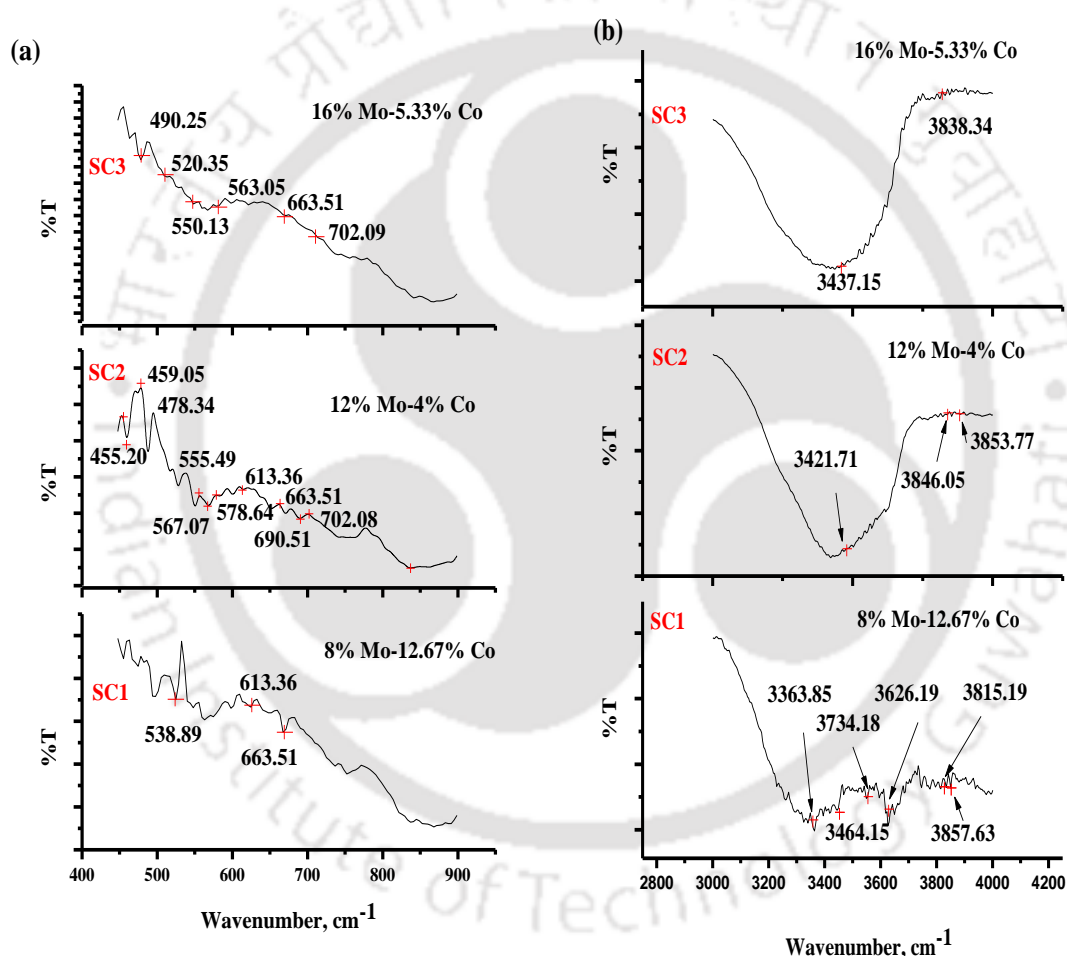


**Figure 4.1** FTIR spectra of the Co-Mo catalysts over  $\gamma$ -Al<sub>2</sub>O<sub>3</sub> with low surface area in the range of (a) 300-900 cm<sup>-1</sup> & (b) 3000 to 4000 cm<sup>-1</sup> calcined at 400°C

The spectra of hydroxyl stretching region (3300-3900 cm<sup>-1</sup>) establishes presence of well dispersed octahedral Co and Mo phase on  $\gamma$ -Al<sub>2</sub>O<sub>3</sub> (low surface area) with strongly perturbed

OH bonds (**Figure 4.1b**) for the catalysts calcined at 400°C, is in good agreement with literature [140]. In **Figure 4.2a**, the band of MoO<sub>3</sub> at 663 cm<sup>-1</sup> is vanished for the  $\gamma$ -Al<sub>2</sub>O<sub>3</sub> (low surface area) supported catalyst calcined at 400°C as the IR spectra of CoMoO<sub>4</sub> contains only the vibrations of MoO<sub>4</sub><sup>2-</sup> tetrahedral units, confirms the formation of CoMoO<sub>4</sub> for  $\gamma$ -Al<sub>2</sub>O<sub>3</sub> (low surface area) supported catalyst calcined at higher temperature. Presence of CoMoO<sub>4</sub> at higher temperature refers formation of  $\beta$ -CoMoO<sub>4</sub>. Figure 4.2b shows similar fact of presence of well dispersed octahedral Co and Mo phase on  $\gamma$ -Al<sub>2</sub>O<sub>3</sub> (low surface area) with strongly perturbed OH bonds. For  $\gamma$ -Al<sub>2</sub>O<sub>3</sub> (high surface area) supported catalyst, SC3 sintered at 400°C and all the catalysts (SC1, SC2 and SC3) calcined at 600°C show the presence of  $\beta$ -CoMoO<sub>4</sub> (see **Figure 4.3**) prove that  $\gamma$ -Al<sub>2</sub>O<sub>3</sub> (high surface area) can form bimetallic oxide with metal precursor at lower as well as high temperature.

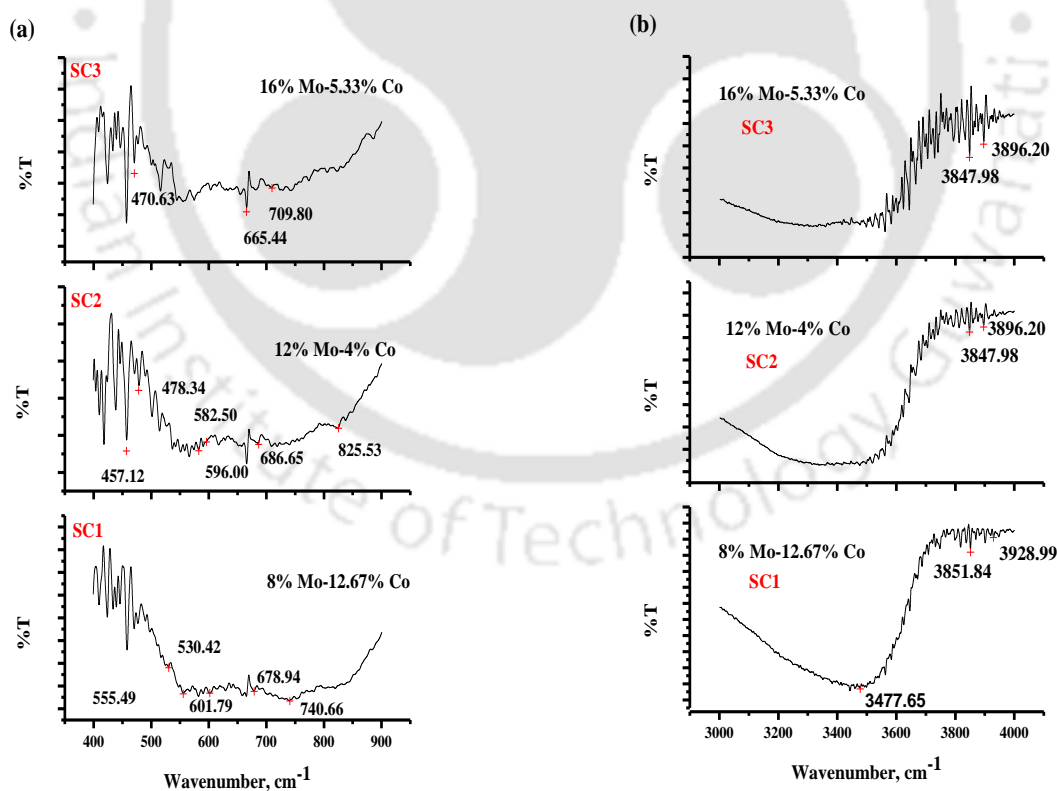


**Figure 4.2** FTIR spectra of the Co-Mo catalysts formed on  $\gamma$ -Al<sub>2</sub>O<sub>3</sub> (low surface area) at 600°C in the range of (a) 300-900 cm<sup>-1</sup> and (b) 3000-4000 cm<sup>-1</sup>

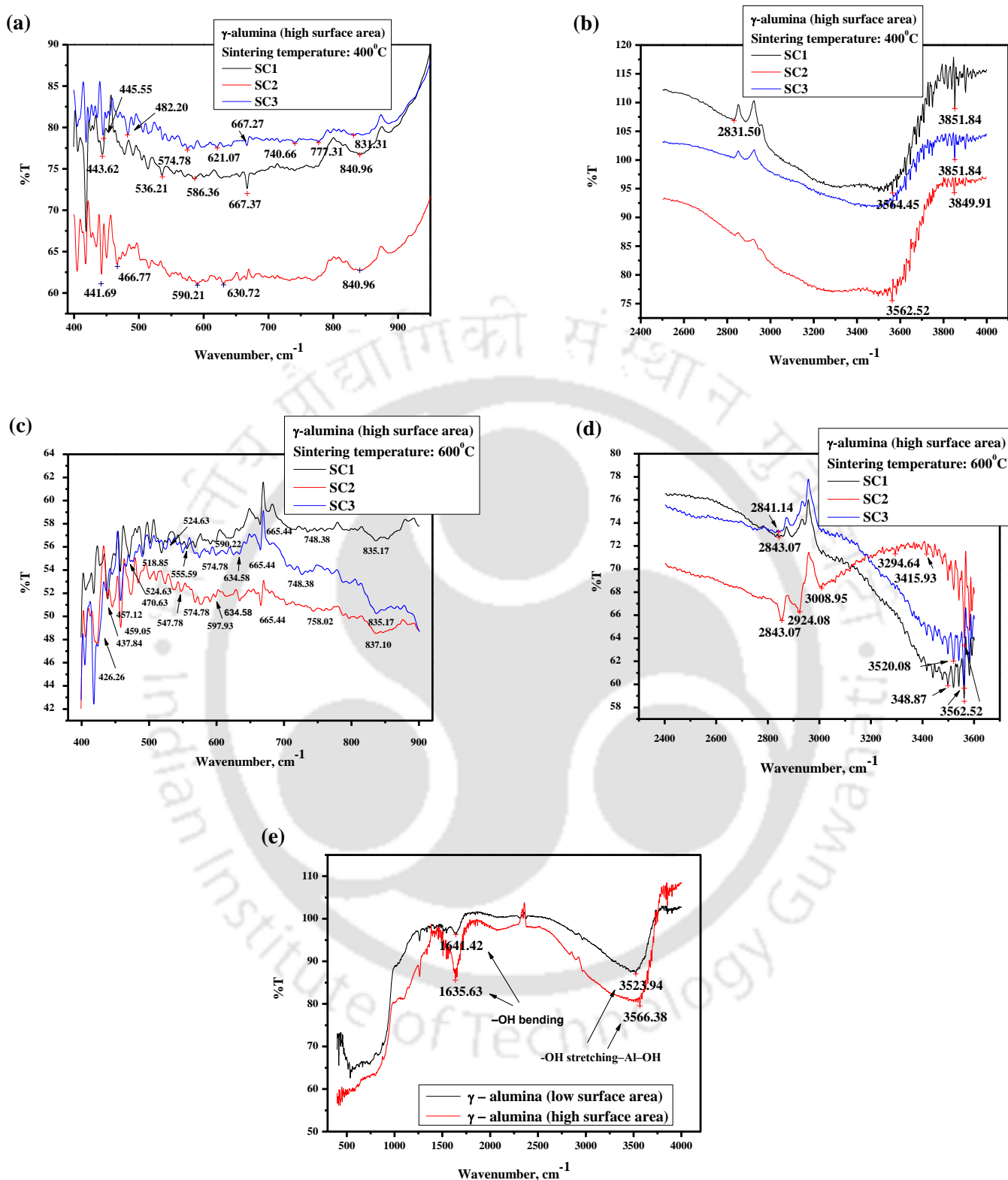


**Figure 4.3** FTIR spectra after impregnating Mo-Co precursor over  $\gamma$ -Al<sub>2</sub>O<sub>3</sub> (high surface area) calcined at (a-b) 400 °C and (c-d) 600 °C. (e) Comparison of IR spectra between  $\gamma$ -Al<sub>2</sub>O<sub>3</sub> with low and high surface area at room temperature

This trend of bimetallic oxide and crystalline  $\text{MoO}_3$  formation is similar with the results obtained for the  $\gamma\text{-Al}_2\text{O}_3$  (low surface area) catalysts calcined at  $600^\circ\text{C}$  (**Figures 4.2a and b**). The catalyst with minimum Mo loading (8%) shows absence of  $\text{MoO}_3$  band due to the higher Co content that strengthens tetrahedral  $\text{MoO}_4^{2-}$  and reduces the intensity of  $\text{MoO}_3$ . The band at  $709\text{ cm}^{-1}$  signifies the presence of  $\text{Co}_3\text{O}_4$  (**Figure 4.2a**).

XRD patterns of the prepared catalysts of different Mo loadings on both  $\gamma\text{-Al}_2\text{O}_3$  having high and low surface area are shown in **Figure 4.4**. Higher Mo content reduces the chance of forming the catalytically inactive cobalt aluminium oxide and confirms the presence of  $\text{CoMoO}_4$  (JCPDS 00-021-868), orthorhombic aluminium molybdenum oxide (JCPDS 000023-0764) and crystalline molybdenum oxide (JCPDS 01-072-0527) for alumina (low surface area) support calcined at both  $400$  and  $600^\circ\text{C}$  (**Figures 4.4a and b**). The attachment of cobalt and molybdenum oxide gives rise to X-ray diffraction peaks at  $2\theta$  values of  $26.6^\circ$  for both catalyst. This diffraction peak is assigned to monoclinic  $\beta\text{-CoMoO}_4$  which is more stable at high temperature. In the XRD patterns, the peaks of  $\beta\text{-CoMoO}_4$  become sharper while cobalt content increases, indicating more and more formation of cobalt molybdate. However, for alumina support (high surface area), an existence of catalytically inactive compound is found upto 12 % Mo content at calcining temperature of  $400^\circ\text{C}$  due to the absence of  $\text{MoO}_3$  compound (**Figures 4.4c and d**). Meanwhile, the diffraction peak of both  $\text{MoO}_3$  and  $\beta\text{-CoMoO}_4$  are seen when the Mo content is increased to 16 % for both the catalysts calcined at  $400$  and  $600^\circ\text{C}$ .

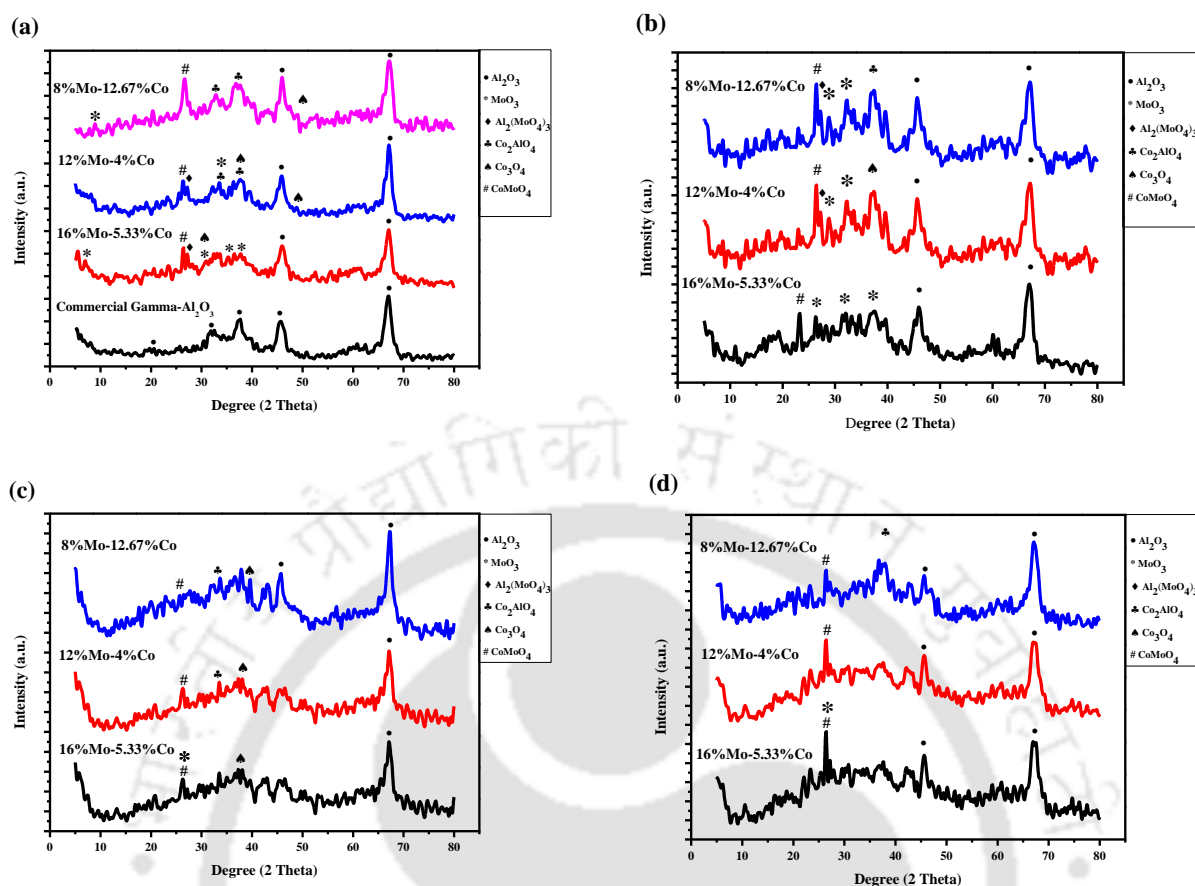


**Figure 4.4** Comparisons of the XRD spectra of Co-Mo/ $\gamma$ -Al<sub>2</sub>O<sub>3</sub> catalysts of different Mo and Co loadings calcined at (a) 400°C and (b) 600°C for 5 h using  $\gamma$ -Al<sub>2</sub>O<sub>3</sub> with low surface area and calcined at (c) 400°C and (d) 600°C for 5 h using  $\gamma$ -Al<sub>2</sub>O<sub>3</sub> with high surface area as support

**Figures 4.5(a-b)** show the N<sub>2</sub> adsorption/desorption isotherms for  $\gamma$ -alumina (low surface area) based catalysts, namely, SC1, SC2 and SC3 calcined at 400 and 600°C. The type IV adsorption isotherms show capillary condensation in mesopores and H2 type hysteresis loop, indicating inter-connected pore systems (**Figure 4.5a** and **b**) and random distribution of mesopores (20–80 nm) (**Figure 4.5c** and **d**). No such impact of calcination temperature and Mo content on the pore size distribution are found when the support is alumina (low surface area).

But, alumina (high surface area) based catalyst shows type IV isotherm which attributes to a range of meso and micropores diameter and H1 type hysteresis loop, indicates random distribution of cylindrical pores (6-80 nm) and spheroidal pore systems (**Figure 4.6a** and **b**), strongly confirmed by pore size distribution curve (refer **Figure 4.6c** and **d**). The quantity of nitrogen adsorption decreases with the increasing calcined temperature, resulting in a decrease in the pore volume of catalyst [**Figures 4.5** and **4.6 (a-b, inset)**].

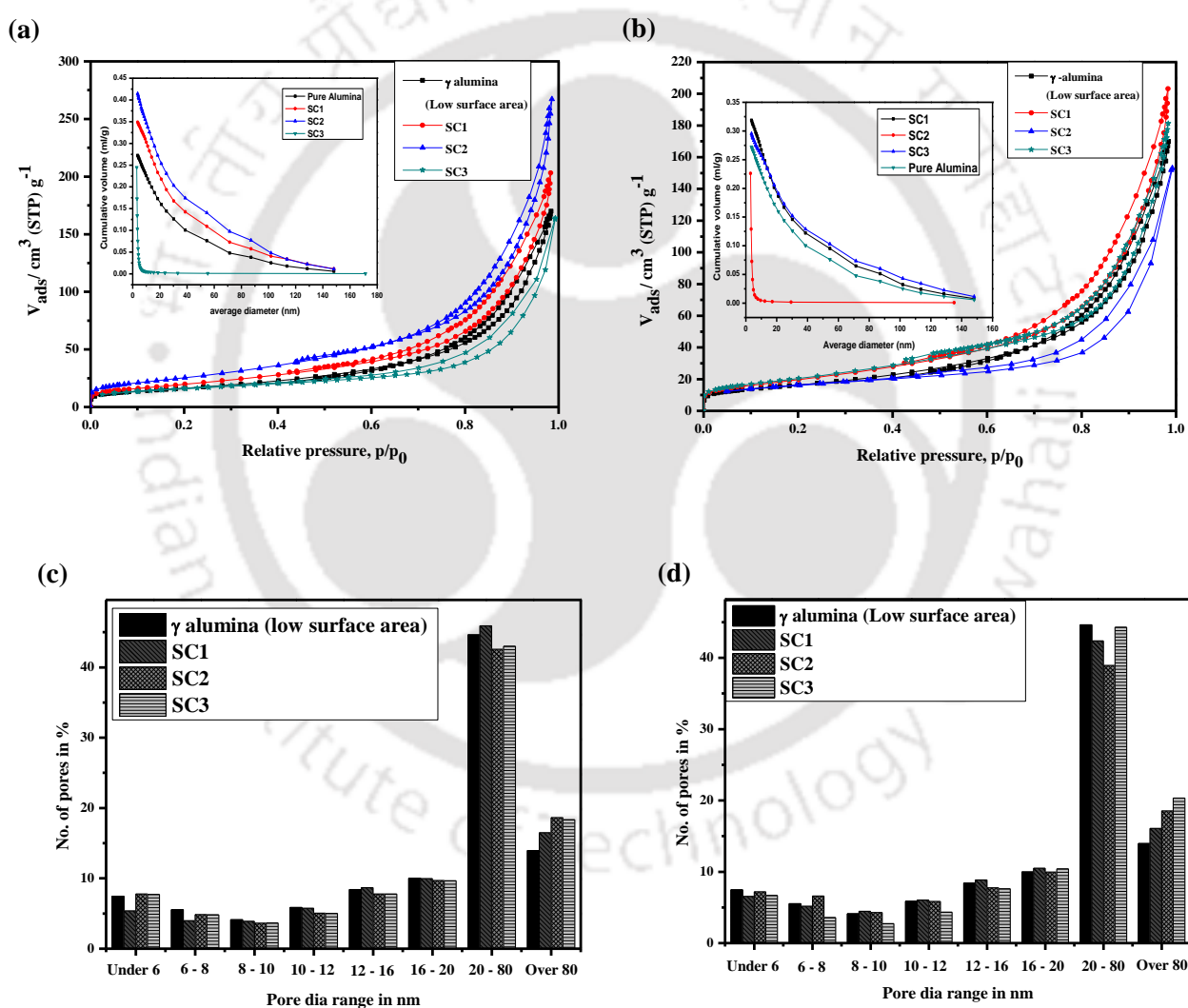


**Figure 4.5**  $N_2$  adsorption/desorption isotherms for  $\gamma$ -alumina (low surface area) based catalysts calcined at (a) 400°C and (b) 600°C with pore volume distribution (inset); (c-d) pore size distribution

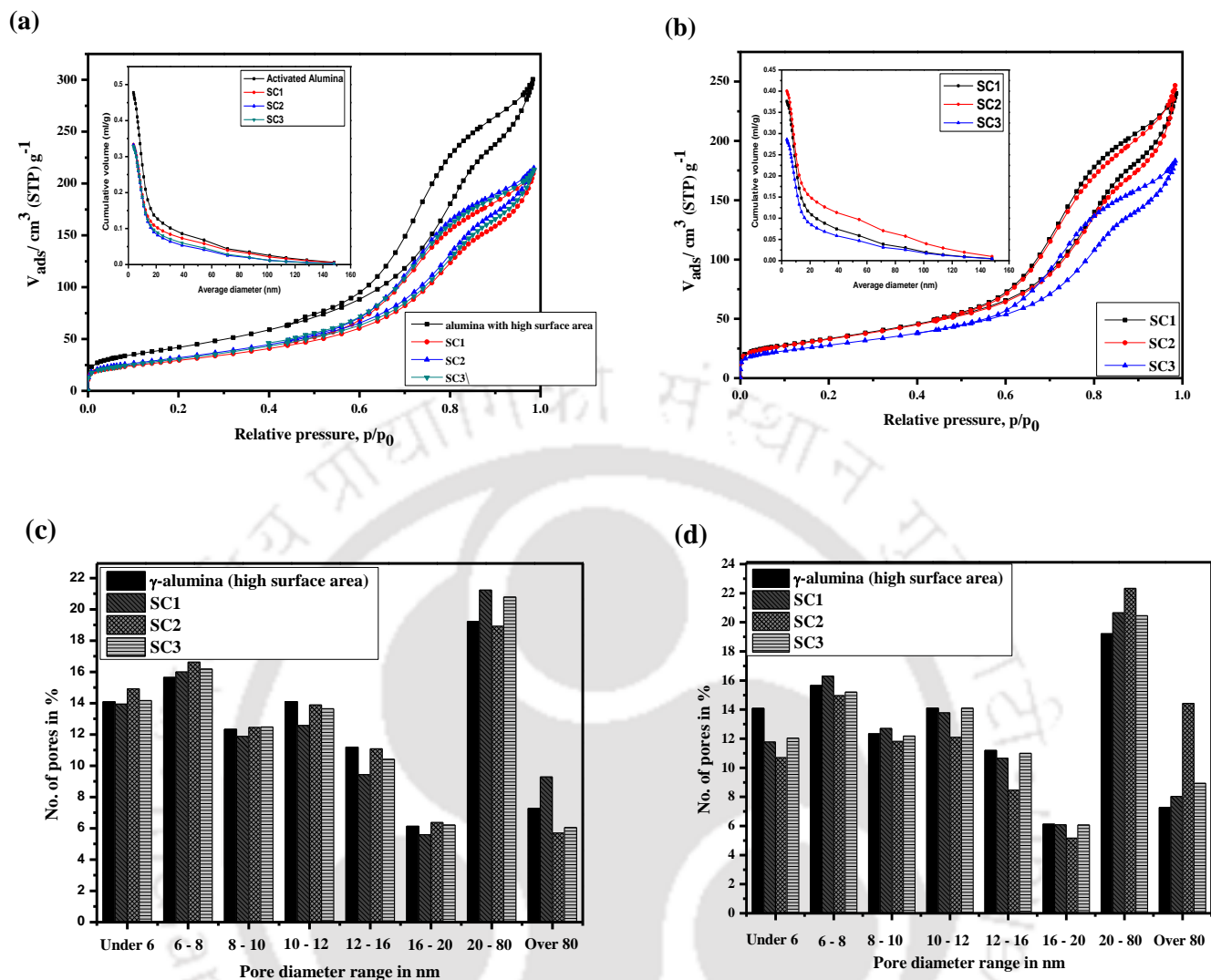


**Figure 4.6**  $N_2$  adsorption/desorption isotherms for  $\gamma$ -alumina (high surface area) supported catalysts calcined at (a) 400°C and (b) 600°C with pore volume distribution (inset); (c-d) pore size distribution

BET surface area and pore volume of the catalysts decrease (72 to 90  $m^2/g$ ) with increase in calcination temperature than that of the  $\gamma$ - $Al_2O_3$  support (low surface area) (**Table 4.3**) due to high particle agglomeration. For  $\gamma$ - $Al_2O_3$  support (high surface area), an opposite trend is observed due to its small particle size (0.267 micron). A decrease in surface area for  $\gamma$ - $Al_2O_3$  (high surface area) based samples (16 wt. % Mo) recommends maximum dispersion of metal ions within the support.

**Table 4.3** BET surface area, pore volume and maximum reduction temperature of catalysts

Composition	Calcination temperature (°C)	Alumina (low surface area)				Alumina (high surface area)			
		BET surface area (m <sup>2</sup> .g <sup>-1</sup> )	Pore Volume (mL.g <sup>-1</sup> )	H <sub>2</sub> uptake (mL.g <sup>-1</sup> STP)	Maximum reduction temperature (°C)	BET surface area (m <sup>2</sup> .g <sup>-1</sup> )	Pore Volume (mL.g <sup>-1</sup> )	H <sub>2</sub> uptake (mL.g <sup>-1</sup> STP)	Maximum reduction temperature (°C)
SC1		86	0.32	17.06	812	106	0.33	21.80	774
SC2	400	82	0.38	0.08	834	116	0.33	16.85	766
SC3		90	0.36	0.89	818	112	0.32	28.22	781
SC1		72	0.30	20.03	774	121	0.36	15.15	766
SC2	600	56	0.24	11.59	778	119	0.37	5.07	788
SC3		74	0.27	17.11	754	101	0.28	41.61	797

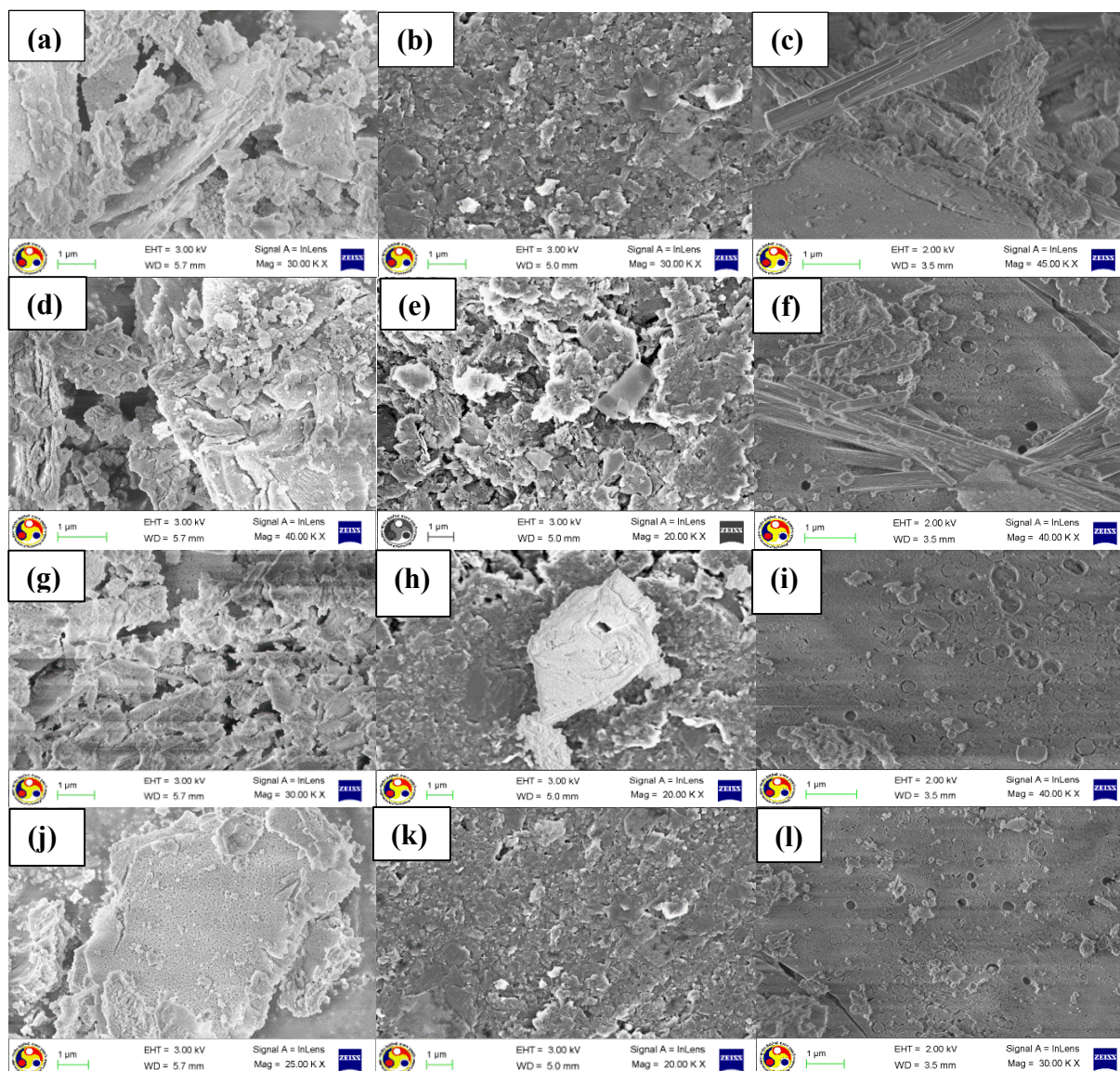
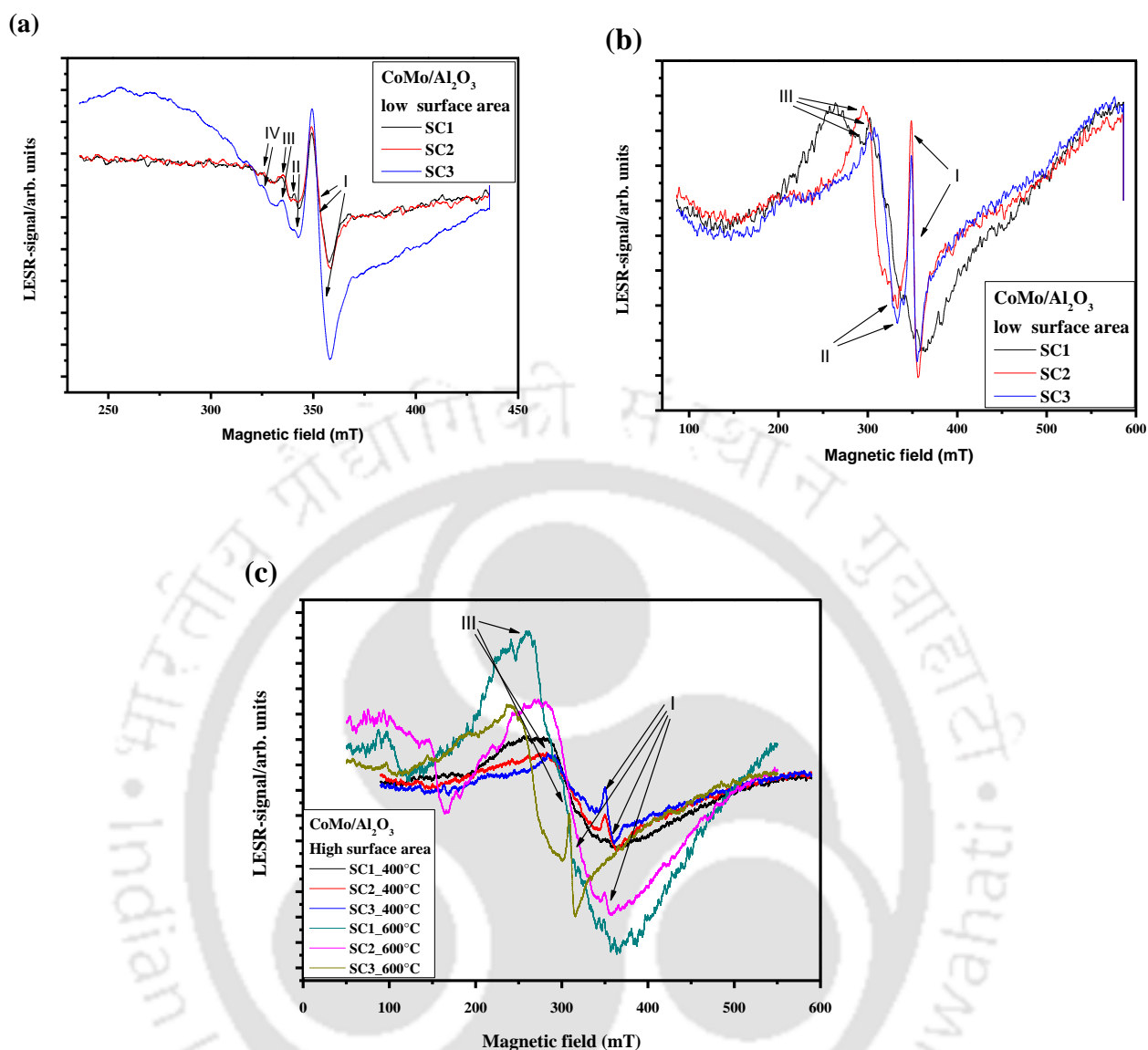


**Figure 4.7** FESEM micrographs of Mo-Co over  $\gamma$ -Al<sub>2</sub>O<sub>3</sub> (low surface area) containing (a) 8 % Mo, SC1, (b) 12 % Mo, SC2, (c) 16 % Mo, SC3 calcined at 400°C and (d) 8 % Mo, SC1, (e) 12 % Mo, SC2, (f) 16 % Mo, SC3 calcined at 600°C. FESEM micrographs of Co-Mo over  $\gamma$ -Al<sub>2</sub>O<sub>3</sub> (high surface area) containing (g) 8 % Mo, SC1, (h) 12 % Mo, SC2, (i) 16 % Mo, SC3 calcined at 400°C and (j) 8 % Mo, SC1, (k) 12 % Mo, SC2, (l) 16 % Mo, SC3 calcined at 600°C

**Figure 4.7** represents FESEM images of  $\gamma$ -Al<sub>2</sub>O<sub>3</sub> (both high and low surface area) based catalyst. FESEM images of all the catalysts show almost similar surface texture except the samples containing 16 wt. % of Mo for both alumina (high and low surface area) based catalyst (**Figures 4.7c, f, i and l**). Catalysts calcined at both 400 and 600°C show a more compact surface due to high Mo content which assure significant influence of calcination temperature and Mo content on catalyst surface texture.

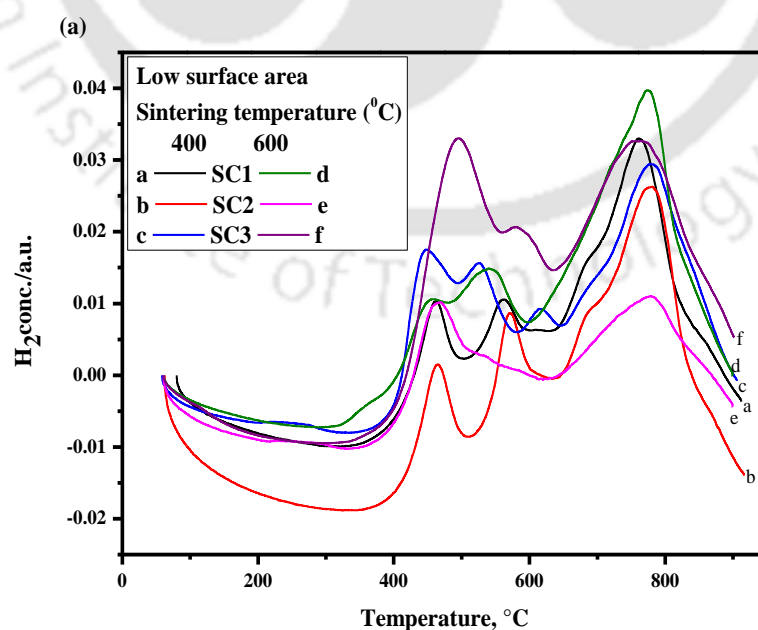
### 4.3.3 ESR-TPR of bimetallic oxide catalyst

**Figure 4.8a** describes ESR bands of alumina (low surface area) based catalyst calcined at 400°C. Band I ( $g$  value - 1.939) confirms an interaction between oxo-Mo<sup>5+</sup> and the alumina support. Intensity of band (I) increases with increasing Mo content. Weak band II ( $g$  value - 1.98) is assigned to Co<sup>3+</sup>/Co<sup>2+</sup> ions interacting either with Mo<sup>4+</sup> or Al<sup>3+</sup> ions. Band III ( $g$  value - 2.056) confirms the presence of Mo<sup>4+</sup> interacting with Co<sup>2+</sup> which attributes to the presence of CoMoO<sub>4</sub>. Band IV ( $g$  value - 2.09) denotes interaction between Mo<sup>3+</sup> and Co<sup>2+</sup> ions. With increasing calcination temperature, band IV disappears, as Mo<sup>5+</sup> species easily reduce to lower valence species and form catalytically inactive bimetallic compounds (**Figure 4.8b**). The alumina (high surface area) supported catalyst shows presence of band I (CoMoO<sub>4</sub>) and band III for all the samples, confirms reduction of Mo<sup>6+</sup> to oxo-Mo<sup>5+</sup> which depends on the support material and calcination temperature (see **Figure 4.8c**).



**Figure 4.8** ESR spectra of the Mo-Co catalysts of different Mo and Co loadings (SC1 – 8 % Mo & 12.67 % Co, SC2 – 12 % Mo & 4 % Co and SC3 – 16 % Mo & 5.33 % Co) calcined at (a) 400°C and (b) 600°C with  $\gamma$ -Al<sub>2</sub>O<sub>3</sub> having low surface area and (c)  $\gamma$ -Al<sub>2</sub>O<sub>3</sub> (high surface area)

The existence of bimetallic oxide is represented by TPR curves in **Figure 4.9**. **Table 4.3** displays the reduction temperature regime of the fabricated catalyst. Alumina (low surface area) based catalyst containing 8% Mo gives a single peak at higher temperature (**curve f** of **Figure 4.9a**) compared to the other metal supported catalyst due to the difficulty in the reduction of molybdenum. The absence of any reduction peak at 350°C attributes to bulk cobalt oxide, which strongly proves that the Co octahedral species are well dispersed onto the MoO<sub>3</sub> reduced surface oxides [141], in agreement with the FTIR curves mentioned above. Peaks at 570 and 790°C confirm the formation of CoMoO<sub>4</sub> as well as bimetallic-support (MoAl<sub>2</sub>O<sub>4</sub> and CoAl<sub>2</sub>O<sub>4</sub>) interactions for both alumina (high and low surface area) supported catalyst, is in good agreement with the literature [142]. But, no peak at 570°C (**Curves d** and **e** of **Figure 4.9b**) is observed for the alumina (high surface area) supported catalyst containing 12% Mo, calcined at 600°C. This is due to the presence of catalytically inactive compounds as CoAl<sub>2</sub>O<sub>4</sub> and Al<sub>2</sub>(MoO<sub>4</sub>)<sub>3</sub> which prevents to form CoMoO<sub>4</sub>. Therefore, the joint ESR-TPR technique suggests that higher Mo content increases the chance of bimetallic oxide formation.



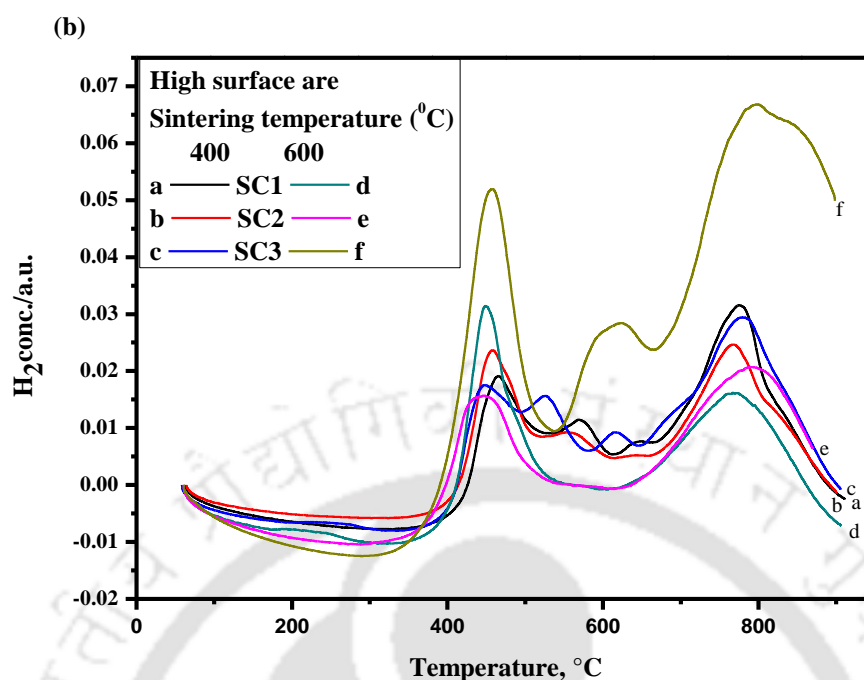


**Figure 4.9**  $\text{H}_2$  temperature-programmed reduction profile of the Mo-Co/ $\gamma$ - $\text{Al}_2\text{O}_3$  catalysts. Catalysts prepared with (a) alumina having low surface area and (b) alumina (high surface area) maintaining different calcination temperatures

Based on the aforesaid results, the catalyst having  $\text{CoMoO}_4$  and crystalline  $\text{MoO}_3$  with high value of MD and MSA (SC3\_400 $^{\circ}\text{C}$ ; average particle size of 267 nm) are optimized and selected for the activity test, will be discussed in **Chapter 6**. The activity result is compared with the activity of the catalyst having low MD and MSA (SC4\_600 $^{\circ}\text{C}$ ; average particle size of 1337 nm) to verify the influence of metal dispersion and metallic surface area on the catalytic activity of the catalyst. In addition to this, it is found that the catalyst with high MD and MSA values have low particle size with narrow particle size distribution (**Figure 4.10**) and vice-versa.

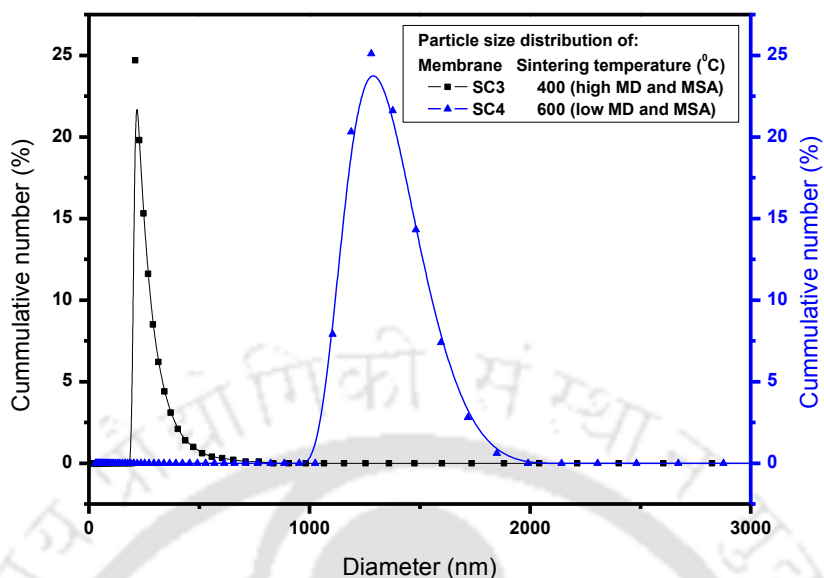


**Figure 4.10** Particle size distribution of the catalysts having high MD and MSA

#### 4.3.4 Verification of the presence of optimized crystalline catalyst

The Raman spectra for alumina (high surface area) supported catalyst (SC3) calcined at 350, 400 and 600°C (**Figure 4.11**) show that the main phases of the optimized catalyst are MoO<sub>3</sub> and CoMoO<sub>4</sub>. The significant Raman bands at 130, 152, 290, 820 and 996 cm<sup>-1</sup> (**Figure 4.11a**) correspond to the bending mode of Mo-O, the anti-symmetric stretching mode of Mo-O-Mo and the stretching mode of Mo-O, respectively [140].

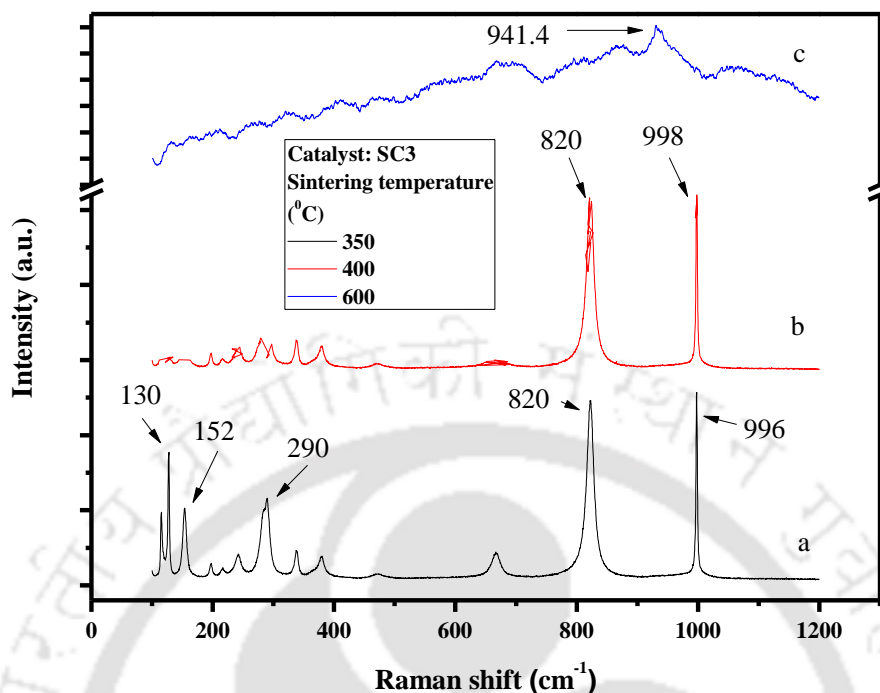


**Figure 4.11** Raman Spectra of  $\text{MoO}_3$  and  $\text{CoMoO}_4$  for alumina (high surface area) supported catalyst (SC3) calcined at 350, 400 and 600°C

The broad band at 820 and 998  $\text{cm}^{-1}$  (**Figure 4.11b**) is due to stretching mode of Mo-O in the  $\text{MoO}_4^{2-}$  tetrahedral units, which can be stretched into two peaks, representing the presence of  $\text{CoMoO}_4$ . The Raman results suggest that the main phase of the catalyst calcined at 350°C is crystalline  $\text{MoO}_3$ . When calcination is increased to 400 and 600°C, the  $\text{MoO}_3$  bands become weaker until these disappear, and the bands at 820, 884 and 941.4  $\text{cm}^{-1}$  are increased in magnitude which suggests the formation of  $\beta\text{-CoMoO}_4$ . These results are in agreement with the above discussed XRD and FTIR results.

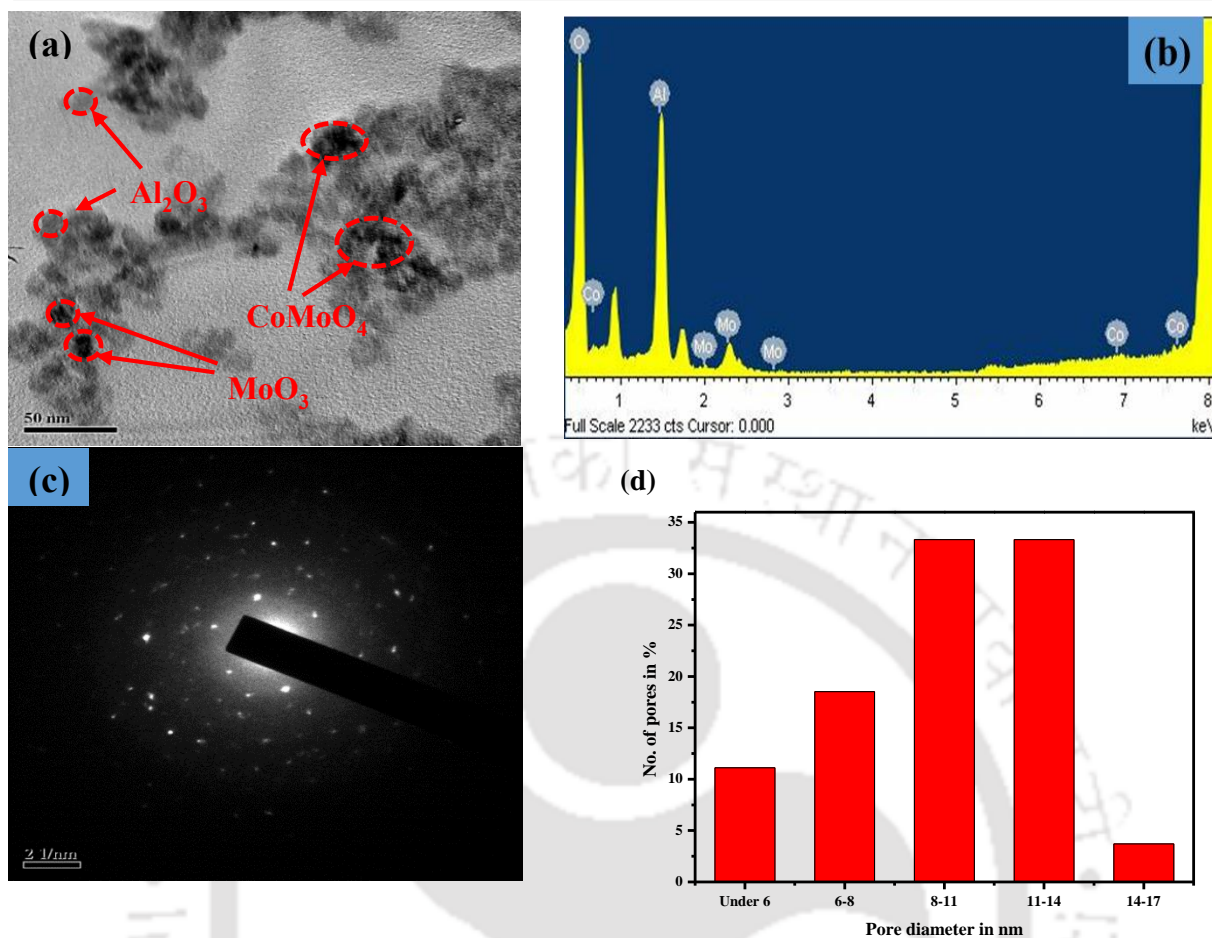


**Figure 4.12** (a) Transmission electron micrograph, (b) EDX study, (c) SAED analysis and (d) pore size distribution of the optimized catalyst with high MD and MSA

**Figure 4.12a** (TEM micrograph) clearly reveals that the core of support matrix is enriched with spherical metal precursors with a minor degree of agglomeration and forms highly crystalline  $\text{MoO}_3$  and  $\text{CoMoO}_4$  particles (black spots, **Figure 4.12b**) indicating high metal dispersion. **Figure 4.12c** suggests presence of highly crystalline  $\text{MoO}_3$  and  $\text{CoMoO}_4$  particles and **Figure 4.12d** shows a well distributed pore size (66%) of the optimized catalyst (SC3\_400°C) in the range of 8-14 nm.

## 4.4 Summary

The significant findings drawn from the present study are summarized as follows:

- (a) The catalyst prepared by depositing metal precursors via impregnation by soaking on  $\gamma$ -Al<sub>2</sub>O<sub>3</sub> (high surface area) surface is proved better than the  $\gamma$ -Al<sub>2</sub>O<sub>3</sub> (low surface area) based catalysts in terms of morphology, metal dispersion and metallic surface area. No such influence of support material on catalyst textural properties (from FTIR and XRD analysis) is observed except the physicochemical properties such as pore size, pore volume and specific surface area. Alumina (high surface area) based catalysts show wide range of pore sizes along with high MD and MSA due to negligible particle accumulation or pore restriction which may be useful for solid-catalysed reaction.
- (b) More compact and agglomerated surface structure are observed in the FESEM images of all the catalyst samples containing higher Mo content (16 wt. %). MD and MSA increase with increase in Mo content for the  $\gamma$ -alumina (high surface area) supported catalyst.
- (c) Higher calcination temperature initiates crack on the surface of the metal particles. As a result, MD and MSA decreases for the alumina (high surface area) based catalyst.
- (d) ESR technique confirms that the oxo-Mo<sup>5+</sup>, and Mo<sup>6+</sup> binds with alumina and Mo<sup>4+</sup> interacts with Co<sup>2+</sup>. ESR study also concludes that metal dispersion increases with increase in metal content. The presence of crystalline MoO<sub>3</sub> and CoMoO<sub>4</sub> are established also by SAED. TEM images show a well-distributed dispersion of metal precursors over support matrix.
- (e) The optimum Mo content on alumina and the optimum calcination temperature are 16 wt. % and 400°C, respectively as shown by textural and physico-chemical properties.



# Chapter 5

---

## Fabrication and Characterization of Low-cost Catalytic Membrane

## Chapter 5

### Fabrication and Characterization of Low-cost Catalytic Membrane

*Catalytic membranes and membrane reactors present numerous advantages in comparison with conventional separation processes. Nevertheless, its main drawbacks are the manufacturing process and manufacturing cost due to the use of overpriced raw materials. Hence, it is necessary to combine a low-cost ceramic support membrane and catalyst for the fabrication of catalytic membrane. The fabrication procedure includes the coating of catalyst over the membrane surface with a solid lubricant i.e. molybdenum disulfide, which can provide long life, no contamination and can sustain in the harsh environment. Paint coating, a novel technique, is introduced for simplicity, ease of methodology and minimization of cost. In this chapter, a complete description of experimentation involving in the fabrication and characterization of the CMR by coating of the catalyst over the outer surface of the low-cost tubular ceramic support membrane with a solid lubricant using paint coating is outlined. We have also discussed the viability and economic feasibility of the coating method and evaluated the morphological and structural behaviour of the coated ceramic surface when lubricated with catalyst to assess the influence of lubricant on such coatings. The manufacturing cost of the catalytic membrane reactor (CMR) is also evaluated.*

---

This work is communicated in the following journal:

S. Bose, C. Das, "Solid Lubricant-based Coating of Catalyst on the Surface of Tubular Ceramic Support for Catalytic Membrane Fabrication", International Journal of Applied Ceramic Technology. (Under Review)

## 5.1 Materials and methods

### 5.1.1 Materials used

Molybdenum disulphide pure ( $\text{MoS}_2$ ) and silica gel are purchased from M/s Sisco Research Laboratories Pvt. Ltd. (India). Sodium silicate powder (Meta) ( $\text{Na}_2\text{SiO}_3 \cdot 9\text{H}_2\text{O}$ ) is obtained from M/s Loba Chemie Pvt. Ltd. (India). These chemicals are used for the preparation of lubricant solution.

A tubular ceramic support membrane of size 45 mm height, 50 mm diameter and 10 mm thickness (**Figure 5.1a**), is used as test specimen to lubricate  $\text{MoS}_2$  and to verify the effect of lubricant on the physical properties (morphology and strength) of the membrane. The preparation procedure of the support membrane and catalyst is discussed earlier in **Chapter 2**, **Chapter 3** and **Chapter 4**, respectively.

Sodium metasilicate is used as binding material to perform  $\text{MoS}_2$  coating on the ceramic specimen. Four types of support membranes have been prepared on which three different catalyst compositions (SC1, SC2 and SC3) are coated, mentioned in **Table 5.1**, namely M1, M2, M3 and M4. Among the four support membranes, both M1 and M2 are made of using binder and M3, M4 are made of without binder. The lubricant solution containing additive is coated on the outer surface of M1 and M3 whereas the solution without additive in the lubricant mixture is coated over the outer surface of M2 and M4. Silica gel is used as an additive to verify the change in membrane morphology.

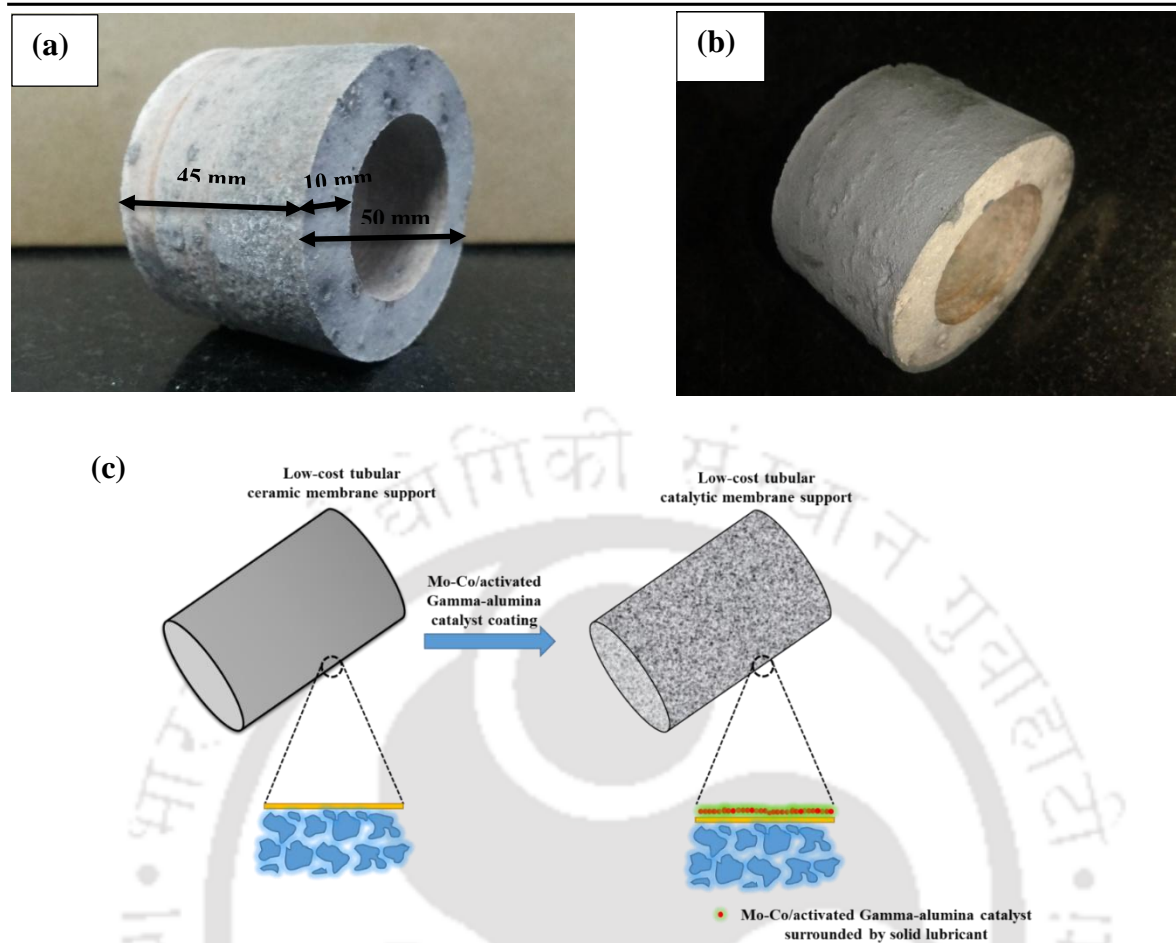


**Figure 5.1** (a) Eco-ceramic low-cost ceramic tubular membrane; height – 45 mm, diameter – 50 mm and thickness – 10 mm. (b) catalytic membrane after coating of catalyst using solid lubricant. (c) schematic diagram of the novel scheme

**Table 5.1** Different combinations used to prepare and characterize the coated membranes

Support Membranes	Coating on support membranes		Combinations			
	With additive (silica gel)	Without additive (silica gel)	Materials	SC1 (wt.%)	SC2 (wt.%)	SC3 (wt.%)
			Mo	8	12	16
With binder	M1	M2	Co	12.67	4	5.33
Without binder	M3	M4	$\gamma$ -Al <sub>2</sub> O <sub>3</sub>	79.33	84	78.67

**Table 5.2** displays different weight ratios of sodium metasilicate, Millipore water, MoS<sub>2</sub> and the catalyst. The weight of Na<sub>2</sub>SiO<sub>3</sub> and catalyst are taken as twice of weight of MoS<sub>2</sub> and the silica gel is added in the lubricant mixture by maintaining the ratio of 1:2:0.05 (MoS<sub>2</sub>: Na<sub>2</sub>SiO<sub>3</sub>: silica gel) [143].

### 5.1.2 Catalytic membrane fabrication method

An optimum proportion maintaining one part of MoS<sub>2</sub> and two parts of sodium silicate/catalyst are experimentally obtained via three steps for the preparation of lubricant mixture. Firstly, 4.6 g of sodium metasilicate is added to 100 mL of Millipore water and the solution is mixed thoroughly. Secondly, the prepared solution is heated to 80°C for 1 h to evaporate the moisture present in the solution. Thirdly, lubricant solution is applied 4 to 5 times on the support membrane by brush and then the specimen is heated in the hot air oven for 1h at 150°C. Finally, a soft brush is used to remove loose MoS<sub>2</sub> powder from the surface of the support membrane after heating (**Figure 5.1b**). The entire scheme is schematically shown in **Figure 5.1c**.

**Table 5.2** Weight of the lubricant, binder and additive used in preparing lubricant solution for coating over support membranes

Components	M1 (wt. in g)	M2 (wt. in g)	M3 (wt. in g)	M4 (wt. in g)
MoS <sub>2</sub>	2.3	2.3	2.3	2.3
Na <sub>2</sub> SiO <sub>3</sub>	4.6	4.6	0	0
Catalyst	4.6	4.6	4.6	4.6
Silica gel	0.12	0	0.12	0

## 5.2 Characterization techniques

The performance of a coating depends upon the paint layer thickness, dispersion and the distribution across the layer which have an impact on the membrane morphology and the surface texture. Therefore the characterization techniques are as follows:

### 5.2.1 Membrane surface morphology

The porosity, pore size and surface topography of the fabricated membrane are determined to verify the effects of coating of MoS<sub>2</sub> along with catalyst on the morphology of the support membrane. The porosity of the membrane is being determined by volumetric porosity method and is calculated based on Eq. 2.1. The volumetric porosity determination method is the gravimetric analysis of water entrapped into the pores of the membrane walls. The dry coated membrane is weighed first and then immersed in water (Millipore) for 24 h. The soaked membrane is then dried in atmospheric condition for 4-5 h and weighed. A portion of the specimen is cut into a small piece to observe the surface morphology of the specimen using field emission scanning electron microscope (FESEM) (Sigma, Zeiss, USA). to observe the surface morphology of the specimen. Several images are taken at different magnifications in the range between 20 to 130 KX under 30 kV acceleration voltage with a vacuum of 10<sup>-6</sup> Pa. EDX (LEO 1430VP<sup>®</sup>, Oxford) mapping analysis is carried out to confirm the presence and homogeneous distribution of S, Mo and Co into the prepared sample. The average membrane pore size of all the samples is determined by ImageJ software (Version 1.37).

### 5.2.2 Film thickness measurement

The MoS<sub>2</sub> film thickness on the support membrane is determined by measuring mass and area of the coated specimen which is called gravimetric coating determination technique

(ASTM standard – B767-88). The specimen is weighed before and after coating to determine mass of the MoS<sub>2</sub> coating. The thickness of the membrane is determined using the following equation:

$$T_c = V_c / A \quad (5.1)$$

where,  $T_c$  is the thickness in m,  $V_c \left( = \frac{m}{d_{sl}} \right)$  is the volume of the coated surface m<sup>3</sup>,  $m$  is the mass of the coating in g,  $d_{sl}$  is the density of solid-lubricant solution in g.m<sup>-3</sup> and  $A$  is the area in m<sup>2</sup>.

### 5.2.3 Phase transformation study

The X-Ray diffraction patterns of prepared samples are obtained on a Bruker (D8 Advance) X-ray diffractometer at 40kV and 40mA with Cu K $\alpha$  radiation. XRD is performed using a scan speed of 1°/min at an increment of 0.05° from 5° to 65° (2 $\theta$ ) for pure molybdenum sulfide and 10° to 80° (2 $\theta$ ) for prepared samples. All the phases are identified with reference to the database of the International Centre for Diffraction Data.

### 5.2.4 Spectrophotometric analysis

FTIR spectra are recorded in transmission mode using a diffuse reflectance assembly (Shimadzu IR Affinity-1 FTIR spectrometer) over the range of 400 to 4000 cm<sup>-1</sup> to realize the dispersion of catalyst using the solid lubricant solution over the membrane surface. A background is first measured with dried potassium bromide (KBr) (Merck KGaA, Germany). Then a small portion of the membrane surface (exterior) is rubbed with abrasive paper (~0.001 to 0.002 g) to obtain fine powder and mixed with the KBr using ceramic porcelain mortar and then is loaded into a sample holder and mounted inside the instrument.

### 5.2.5 Cost estimation

The overall manufacturing cost of the catalytic membrane is estimated in terms of support membrane fabrication, catalyst preparation and the coating solution preparation cost.

## 5.3 Results and discussion

### 5.3.1 Determination of porosity of the coated membrane and thickness of the coated layer

A complete picture of porosity values of the catalyst coated membrane with and without binder and additive is shown in **Figure 5.2**. Porosity is determined as a function of water entrapped into the pores of the membrane walls. The result declares that porosity of the binder assisted support membrane (M1) is decreased when the outer surface is coated with the lubricant solution containing additive. Conversely, the support membrane M2 shows slight higher porosity than that of M1. This is due to the absence of additive within the lubricant solution mixture coated over the outer surface of M1. An absence of additive ensures loose interaction between the surface of the support membrane and the coated surface which causes an increase in porosity. The support membrane M4 shows higher porosity. This phenomena is due to the absence of binder in support membrane. An absence of binder reduces the particle-particle interaction, creates higher voids which entraps water into the wall of the membrane, thus increasing the porosity.

The thickness of all the samples have been measured by gravimetric coating determination technique and are in the range of  $9 \times 10^{-8}$  to  $9.5 \times 10^{-8}$  m.

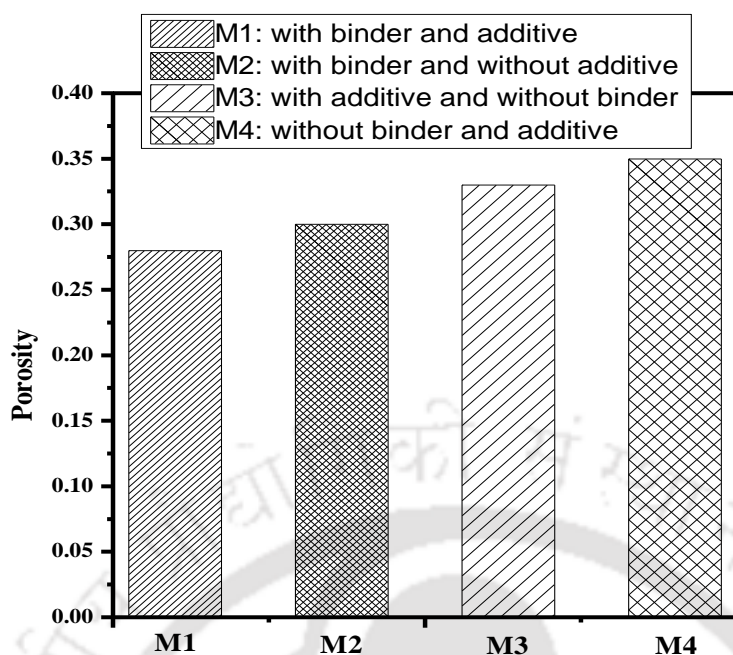


**Figure 5.2** Porosity of four different membranes coated with  $\text{MoS}_2$ , namely, M1 (binder & additive); M2 (binder & without additive); M3 (additive & without binder); M4 (without binder & additive)

### 5.3.2 Surface morphology of coated membrane using FESEM image analysis

Panel a-d of **Figure 5.3** display the FESEM images of catalytic membranes made with different loadings of additive. **Figure 5.3a** shows a dense surface of the membrane with the pore diameter of  $\sim 64$  nm prepared with binder and additive (M1) along with  $\text{MoS}_2$ . **Figure 5.3b** shows the presence of pores with nonhomogeneous structure, which is made in absence of additive. As the binder is absent at the time of support membrane fabrication, the particle-particle interaction become less and make the surface more porous (**Figure 5.3 c-d**). This hypothesis is in agreement with the increase in porosity values for M3 and M4 refer in **Figure 5.2**. From the FESEM images, the average pore size of M1, M2, M3 and M4 have been

determined as 0.047  $\mu\text{m}$ , 0.043  $\mu\text{m}$ , 1.5  $\mu\text{m}$  and 1.76  $\mu\text{m}$  using ImageJ software. The results convey that the binder assisted support membrane having additive mixed coating solution are less porous than the membranes prepared without binder and additive.

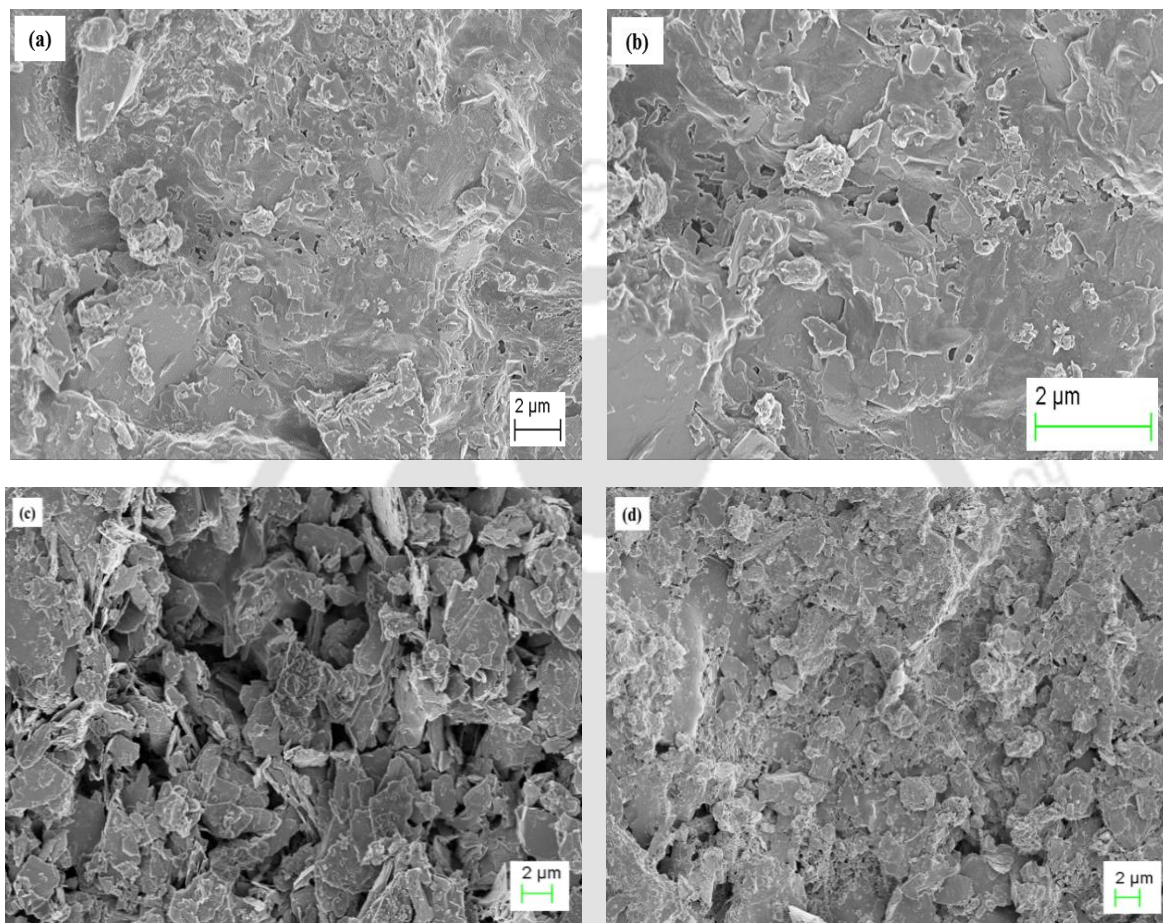


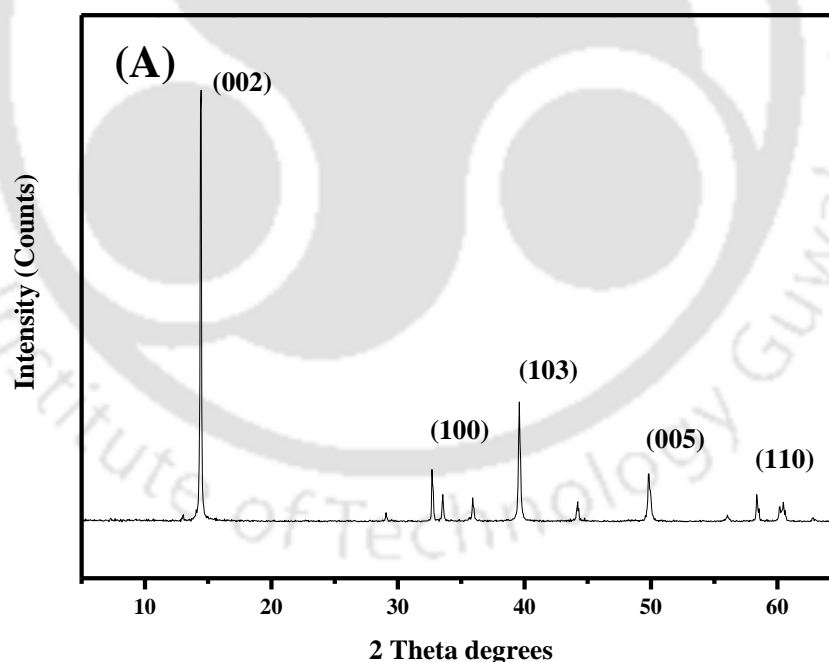
**Figure 5.3** FESEM images of the MoS<sub>2</sub> coated membrane: (a) binder & additive, M1; (b) binder & without additive, M2; (c) additive & without binder, M3; (d) without binder & additive, M4

### 5.3.3 XRD analysis

**Figure 5.4** A and B show X-Ray diffraction peaks of commercial MoS<sub>2</sub> and MoS<sub>2</sub> coated membranes. The high order diffraction peaks at  $2\theta = 14.5^\circ$  (002),  $32.75^\circ$  (100),  $39.61^\circ$  (103),  $49.8^\circ$  (005) and  $58.42^\circ$  (110) indicate that the commercial hexagonal MoS<sub>2</sub> (JCPDS:

077-1716) has a strong crystalline layered structure with an interatomic distance of 0.614 nm, as shown in **Figure 5.4 A**. The solid catalyst sample is very difficult to disperse and coat on the ceramic matrix without special procedures. However, the membrane made of catalyst/MoS<sub>2</sub> mixed lubricant in presence of binder and additive is amorphous, as shown by the lack of intensity or high-order basal peaks of the coated membrane (**Figure 5.4 B**).

An absence of the high-order basal peak at  $2\theta = 14.5^\circ$  and  $32.75^\circ$  in M1, M2 and M3 samples indicates a decrease in the extent of crystallinity, suggests destacking of the MoS<sub>2</sub> basal plane and a little dispersion on the membrane surface [144]. The XRD pattern of M4 sample shows two sharp peaks at  $26.65^\circ$  and  $68.24^\circ$  which indicate no destacking and split of MoS<sub>2</sub> basal plane due to the absence of binder and additive.



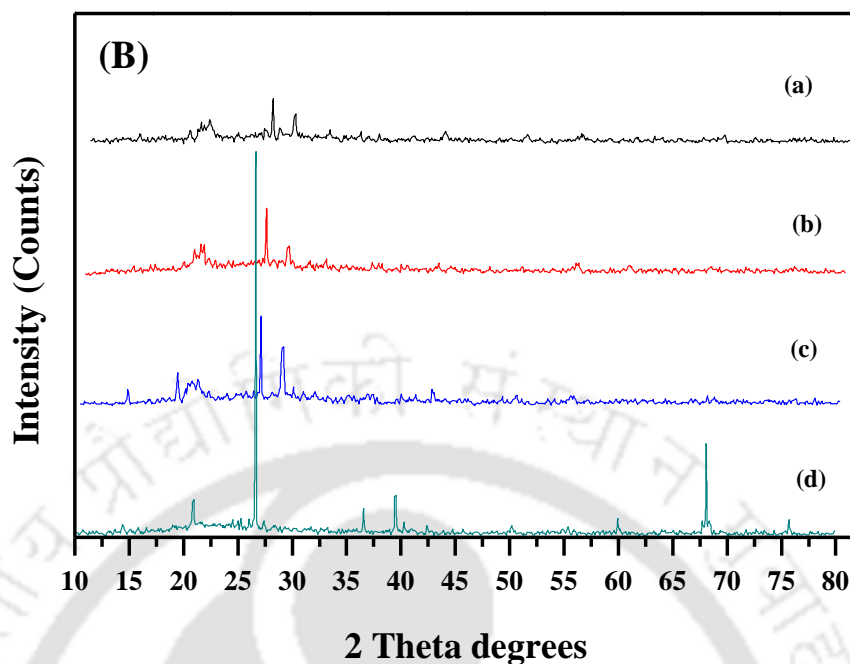


**Figure 5.4** XRD patterns of (A) commercial MoS<sub>2</sub> powder (B) MoS<sub>2</sub> coated membrane with four different compositions, namely, (a) M1, (b) M2, (c) M3 and (d) M4

### 5.3.4 FTIR analysis of coated membranes

The successful deposition of molybdenum disulfide solution on the surface of membrane support is confirmed by FTIR spectra, as shown in **Figure 5.5**. **Curve a of Figure 5.5** exhibits significant bands at 432, 732, 1045 and 1134 cm<sup>-1</sup> that are related to Si-O(Na) asymmetric stretching vibrations. The IR spectra in the fingerprint region displays the presence of Mo-S and S-S bands at 482 and 567 cm<sup>-1</sup> respectively. The highly intense 'O-Si-O' band at 1431 cm<sup>-1</sup> confirms the presence of silicate ions. FTIR spectra for the MoS<sub>2</sub> coated (without using additive) support membrane prepared by binders is presented in curve b of **Figure 5.5**.

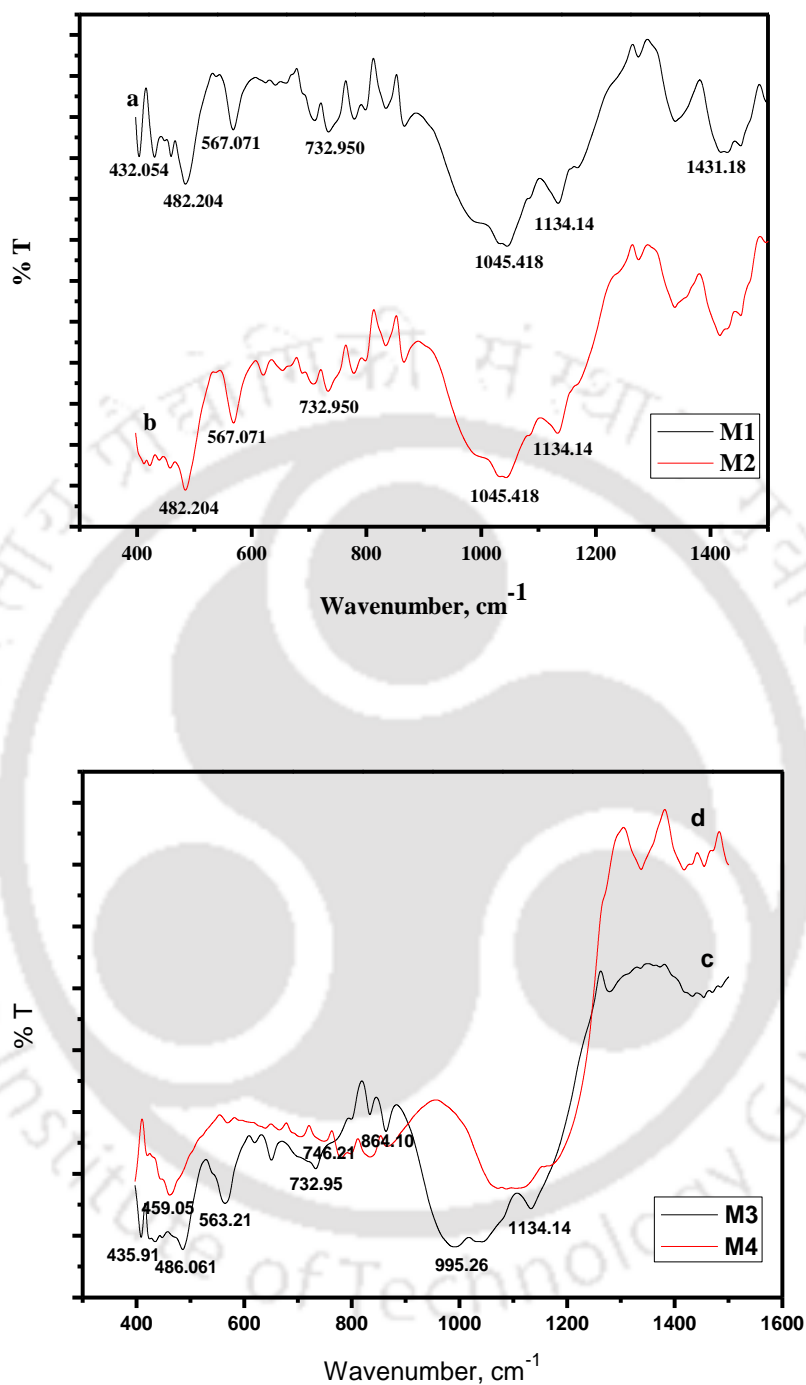


**Figure 5.5** FTIR spectra of  $\text{MoS}_2$  coated membrane prepared with binder & additive (curve a), M1; binder & without additive (curve b), M2; additive & without binder (curve c), M3; and without binder & additive (curve d), M4

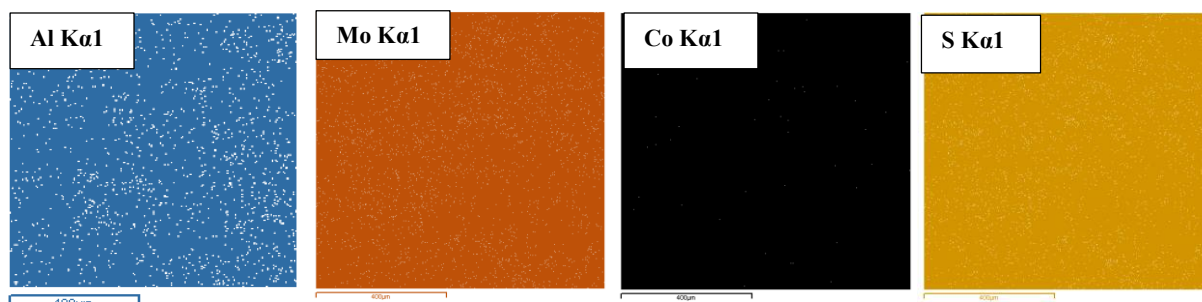
The characteristic vibrations of both M1 (curve a) and M2 (curve b) samples are not affected greatly except the absence of  $\text{O-Si-O}$  band in curve b. The FTIR spectra of M3 and M4 show absence of characteristic peaks due to vibration of silicates at  $1431\text{ cm}^{-1}$  compared to M1 and M2 which strongly agrees the effect of absence of binders during membrane fabrication. The characteristic band at  $563\text{ cm}^{-1}$  confirms the stretch vibrations of terminal and bridging S-S groups. The presence of Mo-S vibration in the FTIR spectra of curve c at  $486\text{ cm}^{-1}$  confirms well-dispersed  $\text{MoS}_2$  in the M3 sample. **Figure 5.5d** shows broad and weak FTIR signal of Mo-S and S-S vibrations at  $459$  and  $567\text{ cm}^{-1}$  and no Si-o(Na) vibration, thus, suggesting a smaller amount of dispersion of lubricant onto the membrane surface due to absence of both binder and additive in M4 sample.

### 5.3.5 EDX mapping analysis

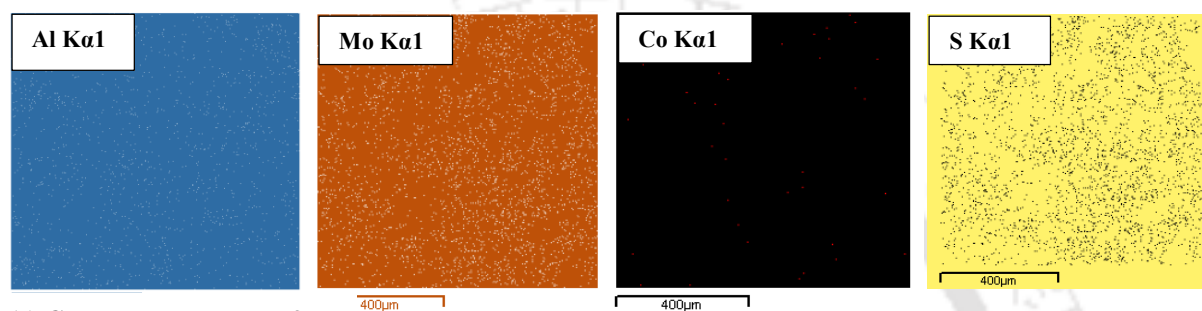
The homogeneity of the  $\text{MoS}_2$ , catalyst solution with and without binder and additive coated on membrane surface is verified by EDX microanalysis mapping (**Figure 5.6**) on a cross-section of the coated ceramic membrane.

EDX maps clearly demonstrate that all the elements are distributed throughout the membrane. The uniform distribution of all the elements in EDX maps explain that the elements dispersed in a well-manner into the membrane surface. **Figure 5.6a** shows better distribution of elements compared to other samples as the coating is finished in presence of binder and additive. Distribution of  $\text{Al}^{3+}$  strongly suggests that the catalyst is well mixed and highly dispersed in the  $\text{MoS}_2$  solution. The presence of Al, Mo and Co throughout the membrane surface of all the coated membrane approves the presence of catalyst over the exterior surface of the membrane.

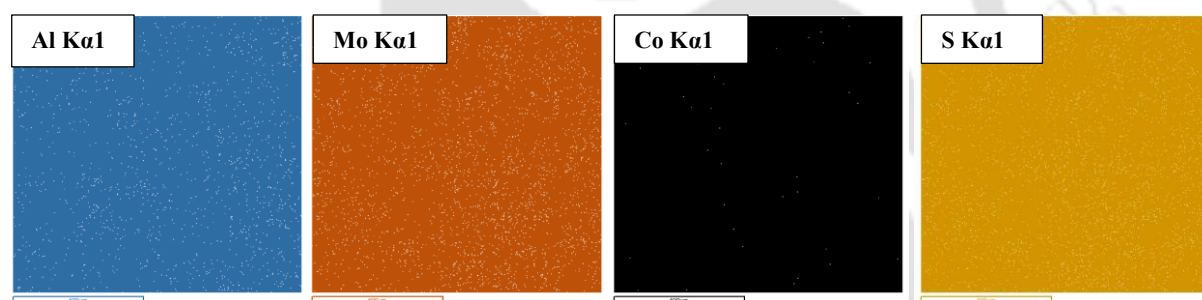
(a) Coated Membrane M1



(b) Coated Membrane M2



(c) Coated Membrane M3



(d) Coated Membrane M4

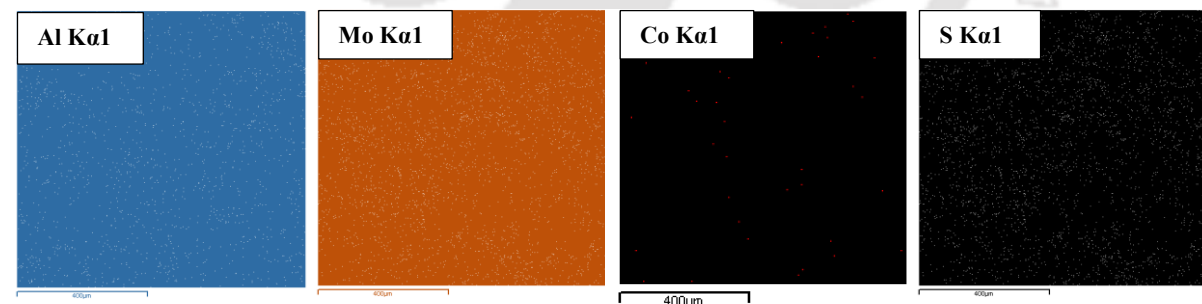


**Figure 5.6** EDX mapping micrographs: (a) Distribution and deposition of alumina, molybdenum and cobalt along with sulfur particles on (a) M1 (b) M2 (c) M3 (d) M4

### 5.3.6 Manufacturing cost evaluation

In **Chapter 2** and **Chapter 3**, the economic feasibility of the membrane is carried out on the basis of raw materials cost, energy consumption, and membrane mold manufacturing cost etc. The approximate manufacturing cost has been estimated as \$332/m<sup>2</sup> including membrane mold preparation and other miscellaneous expenditures (10% of the estimated cost). In this chapter, the cost analysis is performed including cost of catalyst preparation and coating solution (as per the weight ratios of the raw materials mentioned in **Table 5.2**). The probable cost of all the catalytic membranes along with the optimized one is evaluated as \$381/m<sup>2</sup> and presented in **Table 5.3**.

**Table 5.3** Estimated cost of the catalytic membranes

Combination for coating solution	Cost in INR	Cost in \$	Total in INR	Total in \$*
M1	2761.18	44.13	23708.58	380
			23744.07	381
M2	2761.05	44.13	23708.58	380
			23708.45	380
			23743.94	381
M3	2758.23	44.26	23720.06	380
			23705.63	380
			23741.12	381
M4	2758.10	44.26	23717.24	380
			23705.5	380
			23740.99	381
			23717.11	380
Combination of catalyst				
SC1	616.40	9.89		
SC2	651.89	10.46		
SC3	628.01	10.08		
Support membrane	20331.00	332.00		

\*1 USD = 62.31 INR

The projected cost is even far less expensive than an  $\alpha$ -alumina-based ceramic tube costing \$500-1000/m<sup>2</sup> available in market [120]. This study proves that the approach adopted to coat catalyst on the surface of a support membrane for the fabrication of CMR would be attractive and more useful than the conventional preparation processes. The cost of CMR may vary with their performance and stability in different process applications.

## 5.4 Summary

A catalytic membrane is fabricated on the basis of simple catalyst coating technique on a tubular support membrane using MoS<sub>2</sub> as solid lubricant. Firstly, the catalytic membrane is developed based on the surface coating of catalyst with the help of lubricant. After coating, catalytic membranes are verified by FESEM image analysis, XRD, FTIR and EDX mapping throughout the membrane surface. The conducted characterization techniques for the present study summarize few significant conclusions and are

- Fabricated catalytic membrane shows 28 to 35% porosity. This indicates that the addition of binder and additive have an obvious effect on the membrane morphology.
- The thickness of the coated layer is determined by the gravimetric coating determination technique which results a formation of the catalyst layer of  $9 \times 10^{-8}$  to  $9.5 \times 10^{-8}$  m.
- FESEM images show that for coated membranes, the surface changes accordingly with the addition of binders and additives along with the change in porosity values. The average pore diameters of M1, M2, M3 and M4 after coating are 0.047  $\mu$ m, 0.043  $\mu$ m, 1.5  $\mu$ m and 1.76  $\mu$ m respectively, as confirmed by FESEM image analysis using ImageJ software.

- The dispersion of the catalyst particles into the lubricant solution confirmed by XRD peaks.
- EDX mapping shows the distribution of catalyst particles on the membrane surface and the effect of binder and additive on the distribution which conclude that the coating of catalyst by paint coatings technique is appreciable. This result displays there is an increase in distribution of the catalyst particles with the presence of binder and additive into the solution mixture.
- M4 is optimized as the best combination in terms of morphology and the estimated cost of the optimized catalytic membrane is \$381/m<sup>2</sup>.

We believe that this membrane can be used as a catalytic membrane where the catalytic properties should be maintained during operation.



## Chapter 6

---

# Performance of Catalytic Membrane and Membrane Reactor

## Chapter 6

# Performance of Catalytic Membrane and Membrane Reactor

*In this chapter, the removal or recovery of elemental sulfur using the fabricated catalytic membrane reactor (CMR) as a function of catalytic activity and mass transport is studied. A batch experiment is carried out at room temperature to collect elemental sulfur in solid form, by reacting hydrogen sulfide and sulfur dioxide. The recovery of elemental sulfur is confirmed by means of the catalytic activity (conversion, yield and selectivity) and turnover frequency of the catalyst. The deposition of elemental sulfur on the catalytic layer of the membrane is recognized by FTIR and XRD study. The multi-reactant mass transfer behaviour of the CMR is studied on the basis of reaction conditions, membrane properties such as reaction equilibrium constant ( $K_{eq}$ ), membrane area and reactor volume, which claims that the fabricated reactor behaves like an ideal CMR by means of the mass transport.*

---

This work is communicated in the following journal:

S. Bose, C. Das, "Preparation, characterization, and activity of activated  $\gamma$ -alumina-supported molybdenum/cobalt catalyst for the removal of elemental sulfur", Applied Catalysis A. (Under Review)

S. Bose, R. Kundu, C. Das, "Mass transfer in a novel tubular catalytic membrane reactor (CMR) for the recovery of elemental sulfur", Chemical Engineering and Processing: Process Intensification. (Revision submitted)

## 6.1 Materials and methods

### 6.1.1 Chemicals and catalyst synthesis

Cobalt nitrate hexahydrate (as Co precursor) and ammonium molybdate tetrahydrate (as Mo precursor),  $\gamma$ -aluminium oxide (high surface area) are used to synthesize catalysts, details of the synthesis procedure is elaborated in **Chapter 4**.

### 6.1.2 Reactor configuration

To study the feasibility and mass transport inside the fabricated CMR, a model has been adopted very similar to the study for multi-component mass transfer at the bulk-fluid membrane interface in a CMR [145]. A novel reactor is fabricated as a tubular configuration and is illustrated in **Figure 6.1**.

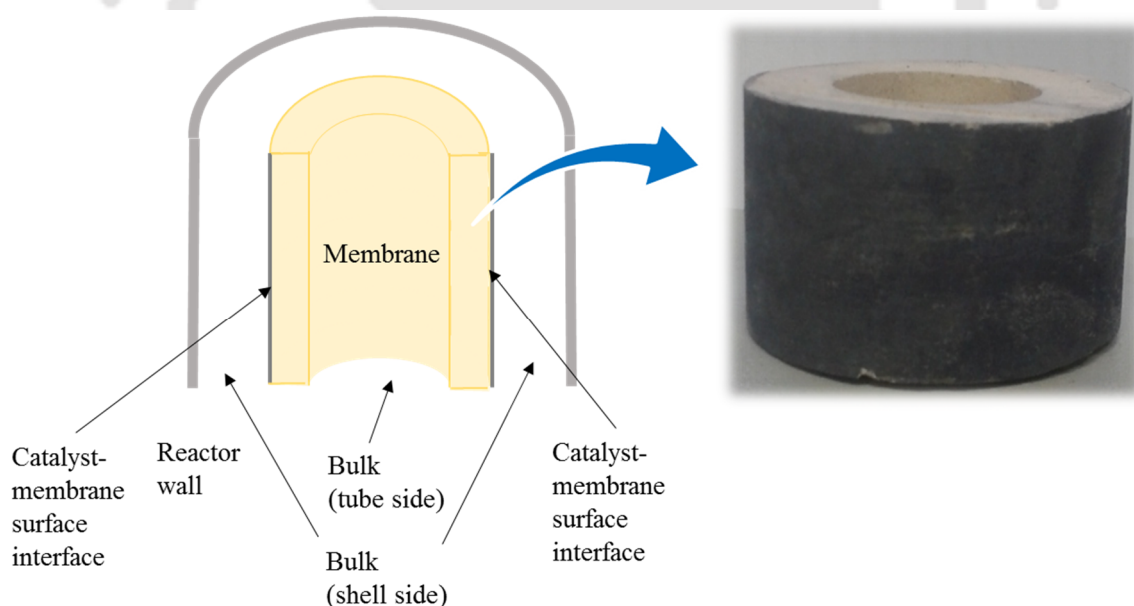


**Figure 6.1** CMR configuration for multi-component mass transport

A CMR must not simply combine a membrane separation unit with a chemical reactor, must also integrally couple them in such a way that a synergy is created between the two units

which potentially resulting in enhanced performance in terms of separation, selectivity and yield. This is the novelty of using membrane reactor instead of using traditional packed bed reactor where both reaction and separation occur simultaneously by eliminating undesired products, such as, water, CS<sub>2</sub> and COS and maintaining thermodynamic equilibrium. This CMR mainly consists of two compartments (e.g. shell-and-tube configuration). The H<sub>2</sub>S and SO<sub>2</sub> gas (centre of the reactor) are fed from same direction at the shell side and tube side of the membrane simultaneously, as schematically represented in **Figure 6.2**. The H<sub>2</sub>S gas is fed over the catalytic surface whereas the SO<sub>2</sub> gas is diffused through the membrane pores from tube side (no catalytic layer) to the shell side surface and reacts with H<sub>2</sub>S over the catalytic layer. The product deposits over the exterior surface of the membrane. The purpose of feeding H<sub>2</sub>S at the shell side is to maintain a minimum distance from catalytic layer (reaction region) and to retain as much as with the reaction place, resulting higher conversion, and negligible slip of the reactant to the tube side. During the operation, low pressure (0.19 MPa) is maintained at the shell side due to high diffusivity of H<sub>2</sub>S ( $4.2 \times 10^{-7} \text{ m}^2 \cdot \text{min}^{-1}$ ) and high pressure (0.39 MPa) is retained at the tube side owing to low diffusivity of SO<sub>2</sub> ( $1.34 \times 10^{-7} \text{ m}^2 \cdot \text{min}^{-1}$ ). The entire process is performed at room temperature in batch mode. To the best of our knowledge, there is no report on Claus reaction over activated  $\gamma$ -alumina (high surface area) based Mo-Co catalyst at room temperature. But, catalytic activity of catalysts at room temperature for different purposes has been reported over several noble metal catalysts, like, Pt/TiO<sub>2</sub>, Pt/Fe<sub>2</sub>O<sub>3</sub> etc. [146-148]. Furthermore, the fabricated catalytic membrane (thickness – 10 mm, diameter – 50 mm) of 45 mm height is considered with a membrane support (pore diameter range ~ 0.3 to 0.8  $\mu\text{m}$ ) with a micro-porous catalytic layer (pore diameter range ~ 20 to 84 nm) on the top surface of the membrane.

## 6.2 Characterization techniques

### 6.2.1 Catalytic test

The catalytic activity of the prepared and optimized catalysts by means of high metallic dispersion and metallic surface area is measured by Claus reaction. The catalytic experiments are carried out at atmospheric pressure, in the room temperature using a batch-mode tubular reactor (i.d.0.09 m, length 0.05 m and volume  $2.86 \times 10^{-4} \text{ m}^3$ ), which consists of a catalytic membrane (outside is coated with the catalyst) situated inside the reactor. The feed is consisted of a mixture of  $\text{H}_2\text{S}$ ,  $\text{SO}_2$  and  $\text{N}_2$  with a volume % of  $\text{H}_2\text{S}$  and  $\text{SO}_2$  varying from 0.3 to 1.9 and 0.2 to 1. The initial concentration of  $\text{H}_2\text{S}$  and  $\text{SO}_2$  are  $1.35 \times 10^{-3}$  and  $1.01 \times 10^{-3} \text{ g. lit}^{-1}$ , respectively. In the reaction procedure, both  $\text{H}_2\text{S}$  and  $\text{SO}_2$  are fed into the reactor at a constant pressure of  $3.45 \times 10^{-3} \text{ MPa}$  and react on the surface of the membrane where exactly 4.6 g catalyst is coated and elemental sulfur is deposited on the membrane surface. Pressure inside the membrane is maintained at  $6.8 \times 10^{-2} \text{ MPa}$ .  $\text{N}_2$  gas is used to keep the reactor environment inert. The permeate gas flux is taken from the bottom of the reactor at different time intervals. The catalytic activity of the prepared catalyst is measured by means of conversion of reactant, yield and selectivity of the product and the turnover frequency (TF) of the catalyst. Mathematical expressions of the parameters are as follows:

$$\text{Overall conversion (\%)} = 100 \times \frac{C_{R_{\text{inlet}}} - C_{R_{\text{outlet}}}}{C_{R_{\text{inlet}}}} \quad (6.1)$$

$$\text{Yield (\%)} = 100 \times \frac{\text{The amount of sulfur produced}}{\text{Total amount of reactant fed}} \quad (6.2)$$

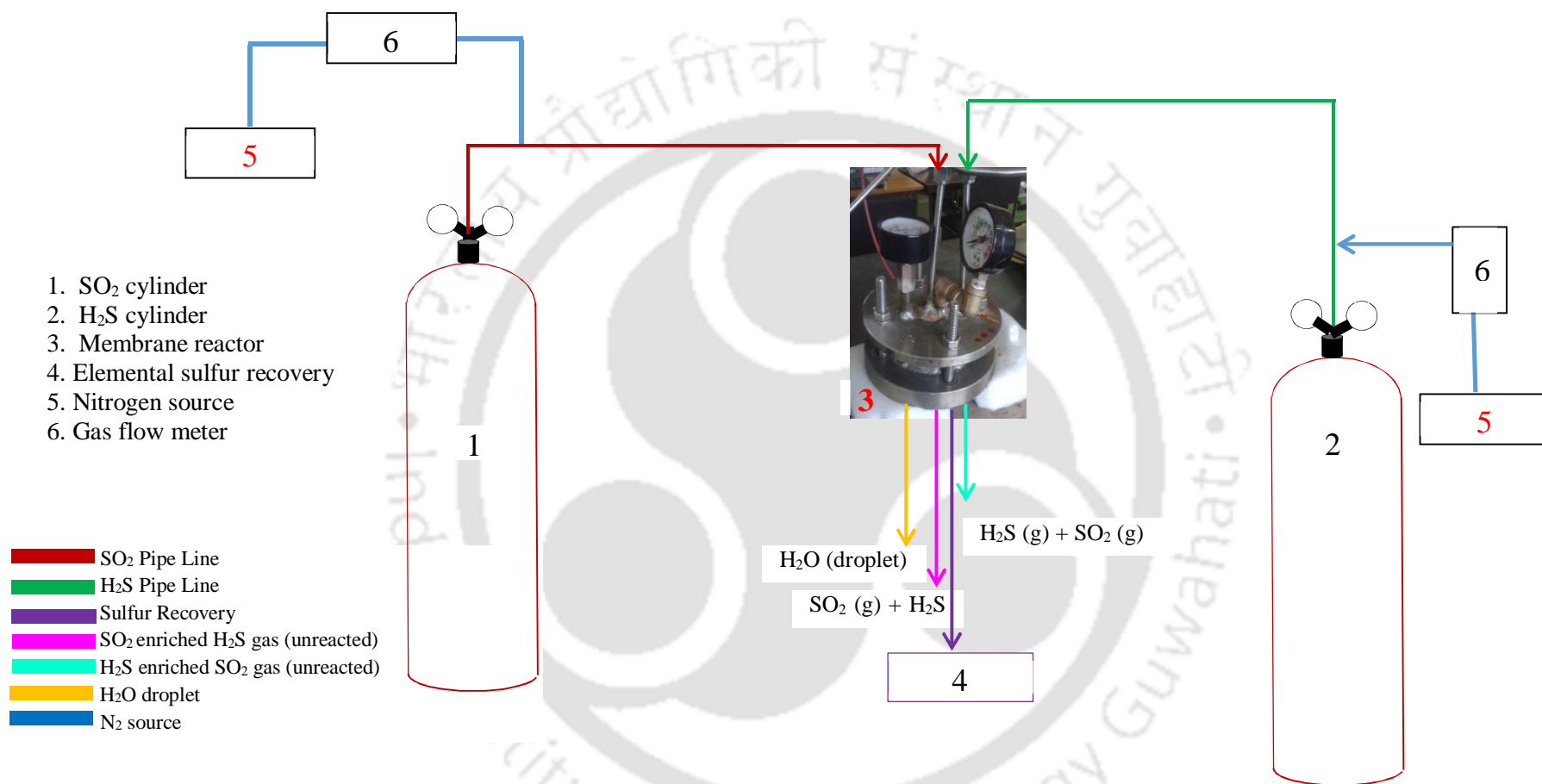


**Figure 6.2** Schematic diagram of the experimental set up [N.B. – (a) the study is under batch mode; (b) the purpose of showing inlet and outlet features is to assist audiences to better understand the process]

$$\text{Selectivity (\%)} = 100 \times (\text{Overall conversion} \times \text{Yield}) \quad (6.3)$$

$$\text{Turnover Frequency (TF)} = \frac{\text{Amount of product (mol)}}{\text{Amount of the catalyst active sites} \times \text{time}} \quad (6.4)$$

$$\text{Weisz-Prater criterion } (\phi_{W-P}) = \frac{r_a R_p^2}{C_s D_{ij}} \quad (6.5)$$

$$\text{Effective diffusivity } (D_{ij}) = \frac{1.0133 \times 10^{-7} T^{1.75}}{P \left[ (\sum v_A)^{1/3} + (\sum v_B)^{1/3} \right]^2 \left[ \frac{1}{M_A} + \frac{1}{M_B} \right]^{0.5}} \quad (6.6)$$

where,  $C_{R_{inlet}}$  is the initial concentration of reactant gases in the inlet of the reactor ( $\text{mol.m}^{-3}$ ) and  $C_{R_{outlet}}$  is the concentration of feed gases ( $\text{mol.m}^{-3}$ ) present in the permeate,  $D_{ij}$  is the effective diffusivity,  $82.8 \text{ m}^2.\text{min}^{-1}$ ,  $r_a$  is the reaction rate per volume of the catalyst,  $1.51 \times 10^{-4} \text{ mol.m}^{-3}.\text{min}^{-1}$ ,  $T$  is the temperature ( $^{\circ}\text{C/K}$ ),  $P$  is the total pressure (MPa),  $M_A$  and  $M_B$  are the molar mass of  $\text{H}_2\text{S}$  and  $\text{SO}_2$ , 34.08 and 64.06  $\text{g.mol}^{-1}$ , respectively,  $v_A$  and  $v_B$  are the volume terms of the reactant gases in  $\text{m}^3$ , 21.62 and 27.96, respectively,  $R_p$  is catalyst particle radius,  $0.133 \times 10^{-6} \text{ m}$  and  $C_s$  is the reactant concentration at the external surface of the catalyst,  $1.68 \times 10^{-3} \text{ mol.m}^{-3}$ . Individual conversion of the reactant gas is measured using Eq. 6.1 by considering individual concentration of the reactant gas.

## 6.2.2 Analytical instruments used

### 6.2.2.1 Gas chromatography

The analysis of the feed and product streams are performed in a Bruker 450 gas chromatograph using a carboxive S-II column ( $1.80 \text{ m}$  (length)  $\times$   $3.18 \times 10^{-2} \text{ m}$  (I.D.)  $\times$   $2.0 \text{ m}$  (O.D.)), equipped with PFP detector. 1 mL sample is injected for GC analysis to measure the initial concentrations of reactants with time by using a calibration curve (see **Appendix. 2**) for

each reactant. Operating conditions used for the gas chromatography (GC) and gas chromatography-mass (GC-Mass) are as follows:

### ***Gas Chromatography***

Injection port temperature: 250°C

PFPD (Pulsed flame photometric detector) detection temperature: 250°C

Column temperature: 150°C

Carrier gas: N<sub>2</sub> gas 30 mL.min<sup>-1</sup>

### ***Gas chromatography-mass***

Injection port temperature: 250°C

PFPD (Pulsed flame photometric detector) detection temperature: 250°C

Column temperature: 90°C

Carrier gas: He gas 1 mL.min<sup>-1</sup>

Injection volume: 20 µL

### ***6.2.2.2 Identification of the desired product***

Deposition of elemental sulfur (desired product) on the membrane surface after the reaction between H<sub>2</sub>S and SO<sub>2</sub> in presence of catalyst is verified by FTIR analysis. A small portion of the membrane surface is rubbed using abrasive paper. The collected particles after rubbing from the exterior surface of the membrane are then taken for the analysis.

## 6.3 Theory

This section delivers the reactor configuration, mathematical equations for mass transfer study and assumptions to simplify the calculations. Moreover, the reaction and membrane parameters are also given.

### 6.3.1 Motivation for batch reactors

Theoretically, an ideal batch membrane reactor maintains ideal conditions for reaction and selective-permeation, and after a desired amount of time, ejects the unwanted by-products. The reactor holds the reactant gases intimately over the catalytic layer of the membrane under atmospheric pressure to obtain the desired product (elemental sulfur) through the membrane by shifting the reaction equilibrium from reactant to the product side (higher conversion). As the partial pressure of both the reactant gases decrease, the rate of sulfur production slows down. As this occurs,  $\text{H}_2\text{S}$  and  $\text{SO}_2$  are fed in regular time interval (20 min) to keep continue the reaction. Once a sufficient amount of reactant gases react with each other, sulfur starts to deposit over the membrane surface as solid form along with unreacted reactant gases and trace amount of hydrogen disulfide. Due to high diffusivity of  $\text{H}_2\text{S}$ , a few amount of gas diffuses through the membrane without taking part in the reaction. The remaining unconverted mixture contains hydrogen disulfide due to oxidation of  $\text{H}_2\text{S}$  under mild conditions [149].

### 6.3.2 Assumptions considered

For reasons of simplicity following general assumptions are taken into account for the proposed reactor:

- Concentration gradient of sulfur dioxide from tube side to shell side (from the inner edge of the membrane wall to the exterior edge i.e., membrane-catalyst surface interface) is neglected as there is no reaction and separation. Therefore, the molar flux of sulfur dioxide through membrane from tube side (inner edge of the membrane wall) to the membrane-catalyst surface interface (shell side) remains constant.
- The reactions inside the pores of the membrane are ignored as the reaction predominantly takes place at the catalyst layer coated on the membrane surface.
- During the reaction, no fluid is entering and leaving as the reactor is operating in batch mode.
- Only bulk-catalyst surface interface is considered. All other resistances are neglected.
- Rate of reaction in bulk (shell side) is similar to the rate of reaction on the catalyst-membrane surface interface.
- Mass transfer coefficient ( $k_{ij}$ ) is assumed to be constant at the membrane-catalyst interface due to no mass transfer resistance offered by the membrane and no internal pore diffusion of the catalyst itself.

### 6.3.3 Reaction kinetics and mass balance equation

The Claus reaction on the catalytic membrane is described with the help of mathematical equations in which the mass transfer from the gas bulk to the catalyst-membrane surface is calculated according to the Maxwell-Stefan model [150]. The Claus reaction is considered as

the oxidation of H<sub>2</sub>S by SO<sub>2</sub> over the catalytic surface of the membrane which forms elemental sulfur by the reaction pathway given in **Table 6.1**, adopted from a literature [150].

The homogeneous Claus reaction is as follows:



where, x is 2 or 6 or 8,  $k_f$  and  $k_b$  are the forward and backward rate constants.

As the entire reaction occurs in presence of a heterogeneous catalyst, the scheme has to be considered as a heterogeneous process. But the process calculations, like, reaction kinetics is measured considering the system as a homogeneous system due to the consideration of mixed flow patterns of the reacting fluids [152]. In ideal contacting of heterogeneous system, each fluid is retained in the reactor as mixed flow. In this study, as one of the phase is discontinuous, as droplet, its macro fluid characteristics will have to be accounted as the material is in mixed flow. To avoid the difficulties during calculation, we have neglected, macro fluid characteristics of the product and calculated all the parameters of the system considering a homogeneous system.

A material balance for the batch reactor is executed to verify the change in rate of disappearance of reactant gases with time. It is assumed that no fluid enters or leaves the reaction mixture during reaction as it is operated in batch mode. Therefore, the material balance in the reactor is as follows:

$$-r_{\text{overall}} = C_{\text{overall}_0} \cdot \frac{dX_{\text{overall}}}{dt} \quad (6.8)$$

where,  $t$  is the time required to convert reactant gases into products (min),  $C_{\text{overall}_0}$  is the overall initial concentration of both the reactants (mol.m<sup>-3</sup>),  $-r_{\text{overall}}$  is the rate of disappearance

of the reactant gases ( $\text{mol.m}^{-3}.\text{min}^{-1}$ ),  $dX_{\text{overall}}$  is the change in conversion of the reactants into product with time.

The permeation rate via the membrane is calculated according to the dusty gas model [153] as the driving force is pressure difference across the membrane. For the reason of simplicity of the mathematical model, the outer surface of the membrane is considered to be the effective area of the membrane where both the reaction and separation occur simultaneously and the effective area of the membrane is thus determined by the height and the outer radii of the membrane.

$$\text{Effective membrane area } (A_{\text{eff}}) = 2\pi r_o h \quad (6.9)$$

where,  $A_{\text{eff}}$  is the effective membrane area where both the reaction and separation occur in  $\text{m}^2$ ,  $r_o$  is the outer radius of the membrane coated with catalyst in m and  $h$  is the height of the membrane in m.

The mass balance for each component across the membrane-catalyst interface (shell side) is given by [145]:

$$(v_\phi x_i c_t)_{\text{in}} - (v_\phi x_i c_t)_{\text{out}} + v_i V R_b - A_{\text{eff}} J_i = 0 \quad (6.10)$$

where,  $v_\phi$  is the volumetric flow rate [ $\text{m}^3.\text{min}^{-1}$ ],  $x_i$  is the molar fraction of the species  $i$  the interface,  $c_t$  is the total concentration of the reactant gases [ $\text{mol.m}^{-3}$ ],  $v_i$  is the stoichiometric coefficient of component  $i$ ,  $V$  is the reactor volume [ $\text{m}^3$ ],  $R_b$  is the rate of the reaction in the bulk [ $\text{mol.m}^{-3}.\text{min}^{-1}$ ], and  $J_i$  is the flux of  $i$ -th component gases [ $\text{mol.m}^{-2}.\text{min}^{-1}$ ].

**Table 6.1** Sulfur formation steps for the oxidation of H<sub>2</sub>S by SO<sub>2</sub> (Claus reaction) [150]

H <sub>2</sub> S + Z ↔ Z-SH <sub>2</sub>	(a)
SO <sub>2</sub> + Z ↔ Z-SO <sub>2</sub>	(b)
Z-SH <sub>2</sub> + Z → Z-SH + Z-H	(c)
Z-SO <sub>2</sub> + Z-H → Z-S: + Z-O <sub>2</sub> H	(d)
Z-SH + Z-O <sub>2</sub> H → Z-S: + Z-HO <sub>2</sub> H	(e)
Z-HO <sub>2</sub> H + Z → 2Z-OH	(f)
Z-SH + Z-OH → Z-S: + Z-OH <sub>2</sub>	(g)
Z-OH + Z-H → Z-OH <sub>2</sub> + Z	(h)
Z-OH <sub>2</sub> ↔ Z + H <sub>2</sub> O	(i)
2Z-S: ↔ Z-SS: + Z	(j)
2Z-SS: ↔ Z-SSSS: + Z	(k)
2Z-SSSS: ↔ Z-SSSSSSSS: + Z	(l)
Z-SSSSSSSS: ↔ Z + S <sub>8</sub>	(m)
Z – active site on the catalyst surface	

As the reactor is operated in batch mode thus no fluid is entering and leaving during reaction, therefore, Eq. 6.10 becomes,

$$v_i VR_b - A_{eff} J_i = 0 \quad (6.11)$$

In CMR, the reaction in the bulk is neglected as the reaction predominantly takes place at the catalytic layer on the membrane at the catalyst-membrane surface interface. Therefore, the relation for the reaction rate at the interface of the membrane is given by: [145]:

$$R_{int} = k_f \left( \prod_j^{\text{reactants}} (c_i x_i)^{|v_j|} - \frac{1}{K_{eq}} \prod_j^{\text{products}} (c_i x_i)^{v_j} \right) \quad (6.12)$$

Here,  $R_{int}$  is rate of the reaction at the interface [mol.m<sup>-3</sup>.min<sup>-1</sup>],  $k_f$  is the forward reaction rate constant [mol. L<sup>-1</sup>.min<sup>-1</sup>],  $K_{eq}$  is the equilibrium constant of the reaction which is assumed

to be valid through the entire membrane and  $v_j$  is the stoichiometric coefficient of component  $j$ .

The difference in mole fraction of H<sub>2</sub>S in the bulk and the catalyst-membrane surface interface through the boundary layer is calculated using Maxwell-Stefan equation [154]. The Maxwell-Stefan theory is also applied to verify the diffusion of reactant gases (H<sub>2</sub>S and SO<sub>2</sub>) along with undesired product (H<sub>2</sub>O) through the membrane. The importance of this equation is to verify any diffusion of water (undesired product), sulfur and unconverted reactant gas on the membrane wall during reaction by observing the change in mole fraction of H<sub>2</sub>S.

$$-c_i \Delta x_i = \sum_{j \neq i} \frac{\bar{x}_j J_i - \bar{x}_i J_j}{k_{ij}} \quad (6.13)$$

where  $\Delta x_i$  is the difference in mole fraction between the bulk and the catalyst-membrane surface interface,  $k_{ij}$  is the mass transfer coefficient for components  $i$  and  $j$  [m.min<sup>-1</sup>],  $\bar{x}$  is the average mole fraction between the bulk and the catalyst-membrane surface interface. Assuming the summation of molar fractions of SO<sub>2</sub> at the bulk ( $x_j$ ) and the interface ( $x_j^{\text{int}}$ ) are equal and is given by [145]:

$$\sum_{j=1}^{nc} x_j = \sum_{j=1}^{nc} x_j^{\text{int}} = 1 \quad (6.14)$$

Additional equations are provided to calculate  $K_{eq}$  and  $k_{ij}$ :

$$K_{eq} = \frac{x_{S_8}^{\frac{3}{8}} x_{H_2O}^2}{x_{H_2S}^2 x_{SO_2}} p^{\frac{-5}{8}} \quad (6.15)$$

where  $x_{S_8}$ ,  $x_{H_2O}$ ,  $x_{H_2S}$  and  $x_{SO_2}$  are the mole fractions of products and reactants, respectively.

$$k_{ij} = \frac{D_{ij}}{l_d} \quad (6.16)$$

where  $l_d$  is the distance between the reactor wall and the membrane surface where the diffusion occurs [in m],  $p$  is pressure at which reactant gases are entered into the reactor [in MPa] and  $D_{ij}$  is the effective diffusivity of the reactant gases [ $\text{m}^2 \cdot \text{min}^{-1}$ ], is determined through the Füller–Schettler–Giddings equation [155] i.e., Eq. 6.6.

Before solving Eqs. 6.11-6.16 simultaneously, the overall flux has to be determined. In this study, it is assumed that there are two mechanisms of transport, viscous flow and molecular diffusion according to Fick's law. Thus, flux through the boundary layer (catalytic layer) of the membrane is calculated by adding the flux of  $\text{H}_2\text{S}$  through the membrane wall (catalyst-membrane interface) and the viscous flux due to the flow of compressible fluid through a porous support membrane considering that they are independent.

$$J = J_{\text{membrane},i} + J_{\text{visc}} \quad (6.17)$$

The flux through the membrane is calculated from Eq. 6.18

$$J_{\text{membrane},i} = P_i x_i P_{\text{tot}} \quad (6.18)$$

where,  $P_i$  is the permeance [ $\text{mol} \cdot \text{m}^{-2} \cdot \text{min}^{-1} \cdot \text{MPa}$ ],  $x_i$  is the mole fraction of the species  $i$  at the interface,  $P_{\text{tot}}$  is the total pressure [MPa] for this multicomponent system. It is assumed that the partial pressure of the permeating components at the permeate side is negligible. This is close to reality as often a vacuum or a sweep gas is used at the permeate side, which removes all permeating species and keeps the partial pressure at the permeate side at the very low range. Pressure through the tube side to the shell side of the membrane is the driving force for this study. Therefore, depending on the rate of diffusion of reactant gases, pressure is chosen as one

of the significant factors for membrane flux calculation. As SO<sub>2</sub> (in the tube side) is less diffusive than H<sub>2</sub>S, more pressure is required to diffuse SO<sub>2</sub> through tube side to the shell side. Else, after feeding, due to high rate of diffusion of H<sub>2</sub>S, the gas immediately will diffuse through the membrane wall from shell side to the tube side and prevents product formation. Concentration in terms of mole fraction is considered as another important factor due to the dependency of membrane permeate flux on reaction equilibrium constant. It is assumed that viscous flux includes both Knudsen diffusion and viscous flow due to the distribution of wide ranges of pores and a strong affinity of the membrane surface for the reactant gas molecules to be transported through the core of the support membrane to the catalytic layer and vice-versa.

$$J_{visc} = -\frac{1}{RT} \left( D_{inert,k} + \frac{B_0 p}{\eta} \right) \frac{dp}{dx} \quad (6.19)$$

where  $J_{membrane,i}$  is the flux of the reactant gases through the membrane wall [mol.m<sup>-2</sup>.min<sup>-1</sup>],  $J_{visc}$  is the flux considering transport mechanism, viscous flow [mol.m<sup>-2</sup>.min<sup>-1</sup>],  $R$  is the universal gas constant [m<sup>3</sup>.MPa.K<sup>-1</sup>.mol<sup>-1</sup>],  $D_{inert,k}$  is the Knudsen diffusion coefficient [m<sup>2</sup>.min<sup>-1</sup>],  $\eta$  is the viscosity of the gas [MPa.min],  $t$  is the time [min]. The viscous flow is represented by the Eq. 6.19 for the flow of a compressible gas through a porous body and is solved by integrating over the thickness of the membrane ( $L = 0$  to  $0.001$  m) and the reaction time (0 to 460 min). The parameter  $B_0$  is a specific membrane parameter (m<sup>2</sup>), defined by Eq. 6.20.

$$B_0 = \frac{\varepsilon d_p^2}{\tau 32} \quad (6.20)$$

$$D_{inert,k} = \frac{4 d_p}{3} \frac{1}{3} \sqrt{\frac{4RT}{\pi M_{N_2}}} \quad (6.21)$$

where  $\varepsilon$  is the porosity,  $\tau$  is the tortuosity factor,  $d_p$  is the pore diameter [m] and  $M_{N_2}$  is the molecular weight of the inert gas [g.mol<sup>-1</sup>]. The above equations are solved simultaneously. A summary of all parameters used in Eqs. 6.10-6.21 [145,155,156] are given in **Table 6.2**.

**Table 6.2** Parameters (feed, reactor conditions) used to solve the equations in the study

Parameter	Value	Unit	Parameter	Value	Unit
$r$	0.025	m	$L$	0.001	m
$h$	0.045	m	$\eta$	$1.06 \times 10^{-7}$	MPa.min
$v_i$	2	-	$R$	8.314	m <sup>3</sup> .Pa.K <sup>-1</sup> .mol <sup>-1</sup>
$V$	$2.86 \times 10^{-4}$	m <sup>3</sup>	$M_A$	34.08	g.mol <sup>-1</sup>
$c_i$	$1.4 \times 10^{-4}$	mol.m <sup>-3</sup>	$M_B$	64.06	g.mol <sup>-1</sup>
$v_A$	21.62	m <sup>3</sup>	$P$	0.101325	MPa
$v_B$	27.96	m <sup>3</sup>	$\varepsilon$	30	%
$T$	303	K	$d_p$	$1.76 \times 10^{-6}$	m
$P$	0.01033	MPa	$\tau$	1	-
$M_{N_2}$	14	g.mol <sup>-1</sup>	$l$	0.04	m

## 6.4 Results and discussion

### 6.4.1 Catalytic activity

#### 6.4.1.1 Material balance

In order to determine the activity of the optimized catalysts (16 wt. % Mo loadings) calcined at 400°C having high metal dispersion (93.69%) and metallic surface area (480.51 m<sup>2</sup> g<sup>-1</sup>) coated on catalytic membrane, the Claus reaction is carried out inside a reactor in batch mode at room temperature ( $28 \pm 2^\circ\text{C}$ ) (below the dew point of sulfur) to obtain sulfur in solid form. A material balance for the batch reactor is performed to verify the change in rate of

disappearance of reactant gases with time. It is considered in the batch mode that no fluid enters or leaves the reaction mixture during reaction and the composition remains uniform throughout the process.

#### 6.4.1.2 Conversion of $H_2S$ into elemental sulfur

The changes in conversion of reactant gases, product yield and selectivity with time up to 460 min for an interval of 20 min are obtained for the catalyst sintered at 400 and 600°C (refer **Table 6.3**). MD and MSA are calculated on the basis of CO adsorption on both metallic Mo and Co. From **Table 6.3**, it is observed that the catalyst with a high MD and MSA value shows a gradual increase in conversion, yield and selectivity whereas the catalyst having minimum MD and MSA shows opposite trend (see **Figure 6.3**). In **Figure 6.3a**, a simultaneous increase in conversion for both reactant gases having high MD and MSA (SC3\_400°C) with reaction time up to 300 min is observed, after which a limiting value is reached and then reduced. In case of catalyst showing minimum MD and MSA (SC4\_600°C), the conversion of hydrogen sulfide and sulfur dioxide are maximum at the starting of the reaction but decreases gradually with time (**Figure 6.3b**) and has reached to a limiting value, opposite to the trend shown in **Figure 6.3a**. This phenomenon clearly indicates a beginning of catalyst deactivation as the number of active metal sites is less in the catalyst having minimum MD and MSA. It may be stated here that the MD and MSA are greatly influenced by preparation process and metal-support interaction and are responsible for the formation of desired product by means of higher catalytic activity. It is also further observed that, yield and selectivity of the elemental sulfur are increased with the increase in overall conversion of the reactant gases at a decreasing rate of disappearance of reactant gases with time (**Figure 6.3c**) and the maximum yield is obtained as 87%. Elemental sulfur is produced mainly from hydrogen sulfide species adsorbed on the metal (Mo) active sites which are responsible for the catalytic reaction.

**Table 6.3** Catalytic activity of the sample catalysts calcined at 400 and 600°C<sup>†</sup>

Composition	Calcination temperature (°C)	Catalytic activity					
		Alumina with low surface area			Alumina with high surface area		
		Maximum Conversion* (%)	Maximum Yield* (%)	Maximum Selectivity* (%)	Maximum Conversion* (%)	Maximum Yield* (%)	Maximum Selectivity* (%)
SC1	400	22	15	9	61	56	47
SC2		16	7	2	72	67	58
SC3		15	7	2	87	80	70
SC1	600	34	68	60	37	28	21
SC2		28	19	10	48	40	35
SC3		18	8	3	62	53	45

(\*calculated upto 300 min) <sup>†</sup>(Reaction conditions - reaction temperature: room temperature (28 ± 2°C); initial concentration of H<sub>2</sub>S and SO<sub>2</sub>: 1.35 × 10<sup>-3</sup> and 1.01 × 10<sup>-3</sup> g. lit<sup>-1</sup>; feed pressure: 3.45 × 10<sup>-3</sup> MPa; amount of catalyst used: 4.6 gm)

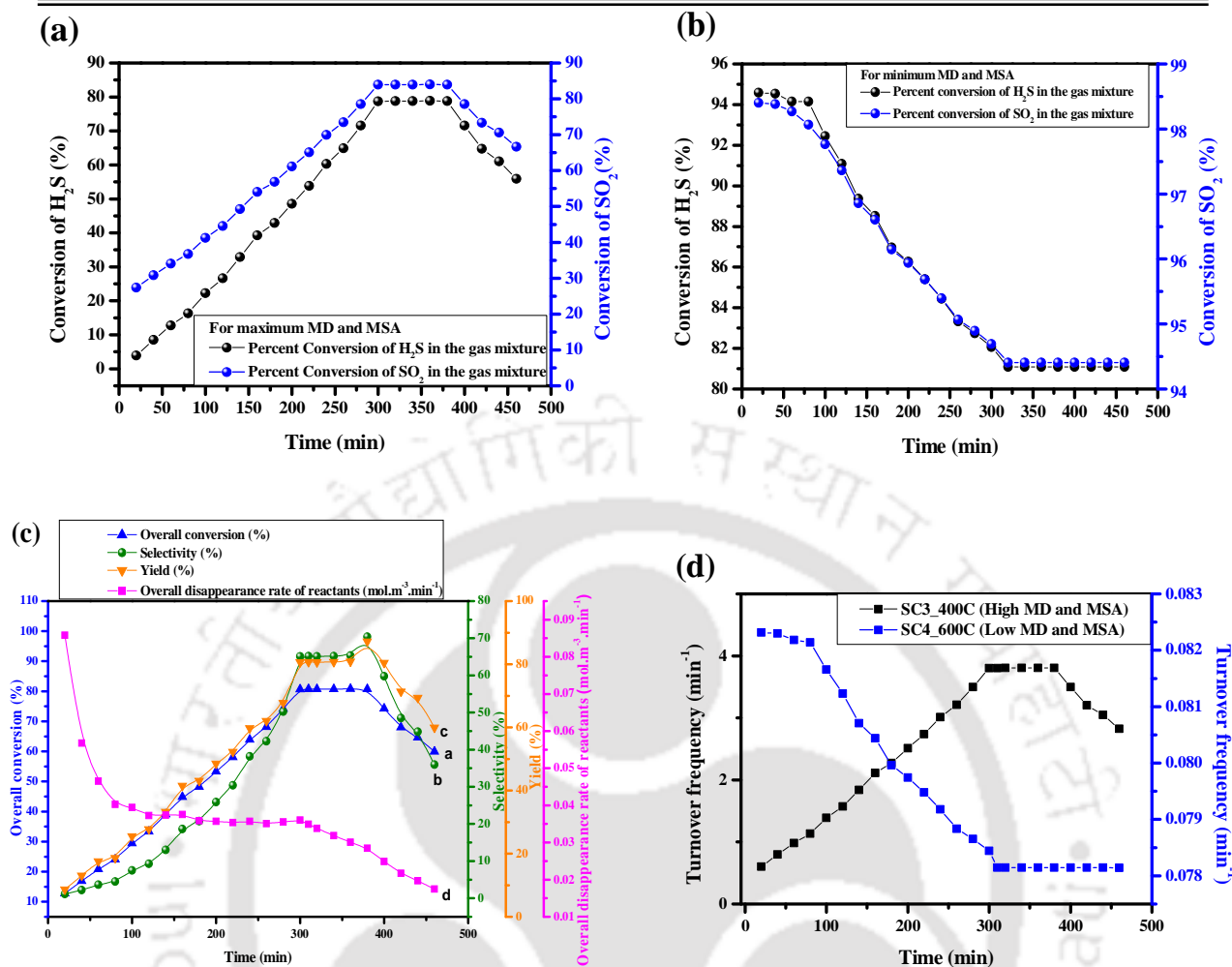


**Figure 6.3** Conversion of H<sub>2</sub>S into elemental sulfur as a function of time with the optimized catalyst: (a) SC3\_400°C having maximum MD (93.69%) and MSA (480.51 m<sup>2</sup> g<sup>-1</sup>), (b) SC4\_600°C having minimum MD (1.15%) and MSA (5.94 m<sup>2</sup> g<sup>-1</sup>), (c) relation between product concentration and overall conversion of reactant with time. (d) Variation of turnover frequency (TF) with time

In addition to this, a relationship between turnover frequency (TF) and metal dispersion is observed in **Figure 6.3d** which reports the highest TF (3.80 min<sup>-1</sup>) at 300 min for the catalyst SC3\_400°C. But the highest TF (0.08 min<sup>-1</sup>) at 20 min is observed for SC4\_600°C catalyst.

This result confirms that the catalyst having high MD and MSA (16 wt. % Mo) obtains high TF compared to the catalyst having low MD and MSA (20 wt. % Mo), causes higher activity.

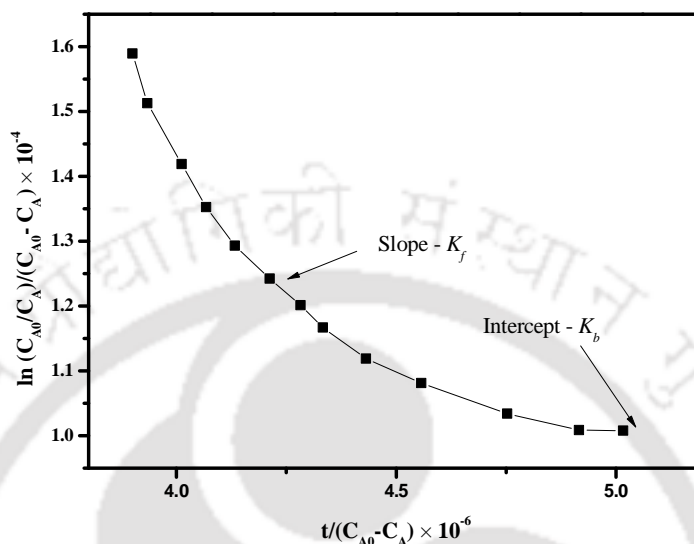


**Figure 6.4** Determination of rate constants by plotting  $\ln(C_{A0}/C_A)/(C_{A0}-C_A)$  vs  $t/(C_{A0}-C_A)$

**Figure 6.4**, a plot of  $\frac{\ln(C_{A0}/C_A)}{(C_{A0}-C_A)}$  versus  $t/(C_{A0}-C_A)$  demonstrates that the reaction rate

follows a pseudo 1<sup>st</sup> order kinetics for bimolecular type reaction with a rate equation

$$-r_A = \frac{k_f C_A}{1+k_b C_A}$$

time. The slope and the intercept of the linear fit of the data are  $k_f$  ( $4.84 \times 10^{-3} \text{ mol. L}^{-1} \cdot \text{min}^{-1}$ ) and  $k_b$  of Eq. 6.1.

$$\frac{\ln(C_{A0}/C_A)}{(C_{A0}-C_A)} = -k_b + \frac{k_f t}{(C_{A0}-C_A)} \quad (6.22)$$

It is clear from **Figure 6.3** that the catalyst having high MD and MSA achieves appreciable conversion, selectivity and yield of desired product by using only 4.6 g of catalyst.

However, it is remarkable to note that the catalytic activity remains constant even after several recycles experiments signifying that these catalysts can be employed effectively for the recovery of elemental sulfur. This experimental analysis is based on Mo only to obtain catalytically active highly crystalline components like  $\text{MoO}_3$  and  $\text{CoMoO}_4$ .

### 6.4.1.3 Mass transfer limitation

In case of a porous catalyst, diffusional limitations can change the overall kinetics of a reaction through internal and external resistances. There are established criteria and experimental methods to determine the presence or absence of internal mass transfer limitations. The objective here is to apply a realistically accurate analysis based on observed variable properties of reactant and physical properties of catalyst to determine the presence or absence of any significant internal mass transfer limitations. The most suitable approach is chosen as Weisz-Prater criterion ( $\phi_{w-p}$ ) as the reaction follows pseudo 1<sup>st</sup> order kinetics [157], which represents a ratio of the rate of the reaction to the rate of diffusion in the pores. This criterion is calculated using Eq. (6.5) and the value is obtained as 0.0019, which is less than 0.6. The reason behind yielding a smaller  $\phi_{w-p}$  value is the equimolar consumption of  $\text{H}_2\text{S}$  and  $\text{SO}_2$  by the reaction as there is no significant secondary reaction to form intermediate products like carbonyl sulfide and carbonyl disulphide within the first sampling time. Therefore, internal pore diffusion limitation is not responsible for the reduction in conversion of  $\text{H}_2\text{S}$  after 380 min of reaction and could be neglected for the kinetic study of Claus reaction.

### 6.4.2 IR transmittance spectra of elemental sulfur

The IR spectra of the sample collected after the Claus reaction from the outer surface of the membrane within the reactor are investigated and it is found that the collected sample is rhombic sulfur ( $\text{S}_8$ ), shown in **Figure 6.5a**. According to **Figure 6.5a**, the stretching vibrations

of the S-S bonds in crystalline S<sub>8</sub> are observed at 468 (s) and 434 (w) cm<sup>-1</sup> along with two other bands of the S-S band stretching vibrations at 524 and 538 cm<sup>-1</sup> that is in good agreement with literature [158]. At the same time, another four bands of the S-S band stretching vibrations are observed at 590, 621, 665, and 686 cm<sup>-1</sup> which correspond to the presence of elemental sulfur.

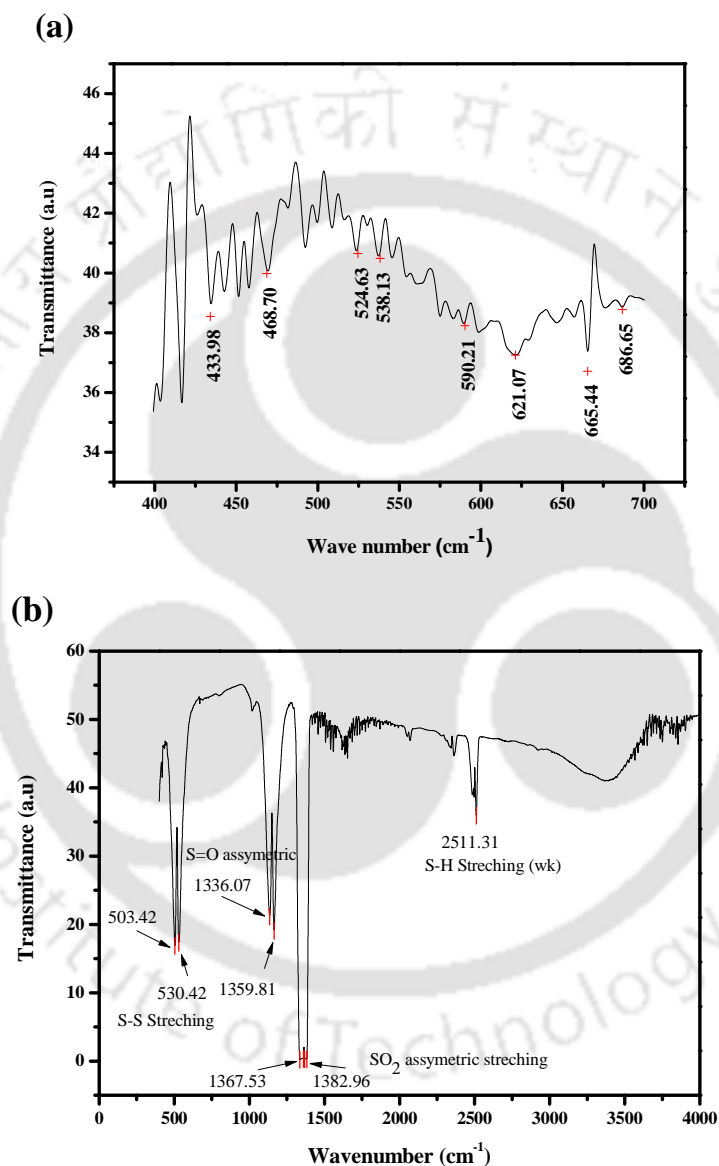


**Figure 6.5** FTIR spectra of (a) elemental sulfur (S<sub>8</sub>) deposited on the catalytic membrane surface, (b) unreacted reactants and hydrogen disulfide collected from permeate

In addition to this, in **Figure 6.5b**, S-S stretching vibrations at 503 and 530  $\text{cm}^{-1}$ , S=O asymmetric stretching in the range of 1336-1382  $\text{cm}^{-1}$  and a weak band of S-H stretching at 2511  $\text{cm}^{-1}$  are observed, confirm the presence of unconverted reactants ( $\text{H}_2\text{S}$  and  $\text{SO}_2$ ) and sulfur (gaseous form) collected from the permeate at different time interval during reaction time.

### 6.4.3 Influence of fixed pressure difference over the membrane on the flux and mole fraction of $\text{H}_2\text{S}$ and $\text{SO}_2$ changing with time

In order to study the variation of flux and mole fraction of  $\text{H}_2\text{S}$  and  $\text{SO}_2$  with time at a fixed pressure difference over the membrane, experiments are performed at  $3.45 \times 10^{-3}$  MPa at a temperature of 303 K and are presented in **Figure 6.6**. In **Figure 6.6a**, it can be seen that there is a decrease and a sudden increase in the total molar flux of  $\text{H}_2\text{S}$  into the membrane with time. In the beginning, the decrease in the total molar flux of  $\text{H}_2\text{S}$  is explained by asymptotic situation where high pressure is applied on  $\text{SO}_2$  side, causing high transport rate of  $\text{SO}_2$ . The overall flux is measured by viscous flow resulting in a high transport rate of reactants from the bulk to the catalyst-membrane surface interface, indicates no mass transfer limitation [156]. The substantial increase in the reactants flux over the membrane at a constant pressure difference also indicates a requirement of smaller effective membrane area for the reaction and separation.

In **Figure 6.6b**, it is found that due to pressure difference over the membrane and the presence of viscous flow from the  $\text{SO}_2$  side to the  $\text{H}_2\text{S}$  side, the reaction zone is shifted towards the low pressure side (shell side), the mole fraction profile of  $\text{H}_2\text{S}$  at the catalyst-membrane interface drops at 250 min, thus, increasing mole fraction profile of  $\text{SO}_2$  at that time. As the mole fraction at shell side decreases from the catalyst-membrane interface to the reaction region, the viscous contribution reduces.

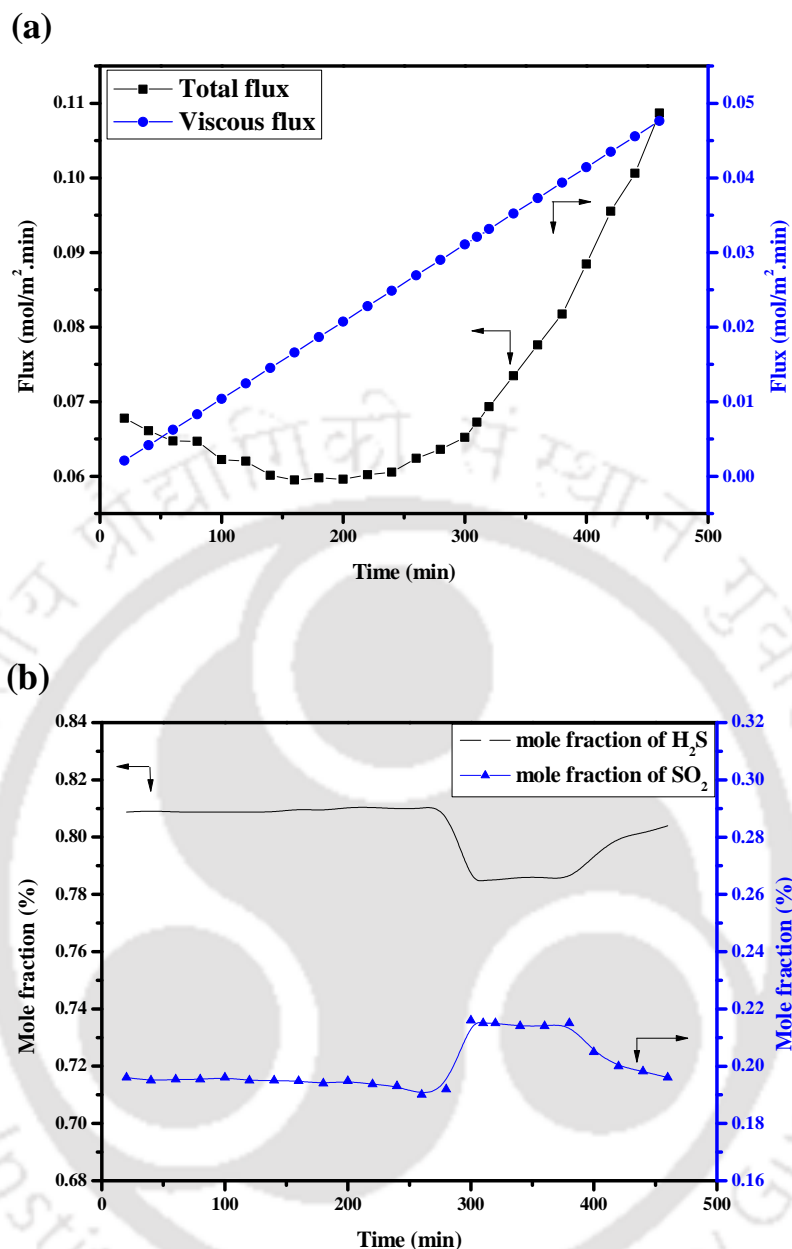


**Figure 6.6** (a) Molar flux of reactant into the membrane as a function of time; (b) change in mole fraction of the reactants with time

The mole fraction of H<sub>2</sub>S remains constant up to 300 min and starts to increase after 380 min of reaction time due to the increase in viscous contribution, as shown in **Figure 6.6a**. The lower mole fraction profile of SO<sub>2</sub> compared to H<sub>2</sub>S refers to shifting of reaction zone from bulk to the catalyst-membrane interface. Therefore, it is found that both the reaction and formation

of elemental sulfur occurs on the membrane surface and the performance of the reactor changes with time and at a fixed pressure difference.

#### 6.4.4 Reaction rate, equilibrium reaction constant ( $K_{eq}$ ) and mass transport coefficient at boundary layer of the membrane ( $k_{ij}$ )

The conversion of H<sub>2</sub>S into elemental sulfur depends on time, equilibrium reaction constant, mass transport coefficient and mostly the removal of water. In this study, the only resistance to transport for the membrane is removal of water. This section describes the asymptotic nature of conversion as a function of equilibrium reaction constant, mass transport coefficient and the removal of water.

**Figure 6.7** describes control of the conversion as a function of equilibrium constant and reaction rate as disappearance of H<sub>2</sub>S. The variation in equilibrium constant  $K_{eq}$  (from low to intermediate) over different ranges of time indicates formation of sulfur on the membrane surface. The asymptotic nature of the equilibrium constant value (curve a) has three distinct sections with reaction time and are labelled as PQ, QR and RS. In section PQ, a gradual increase of  $K_{eq}$  upto 320 min is observed due to high rate of reaction. The molecules of reactant gases adsorb onto the catalytic surface, attach to the active sites and react, indicating a reaction controlled zone. In section QR, the equilibrium constant value remains constant from 320 to 400 min because mass transfer effects are not important as reaction rate is limiting. The section RS represents a 'sharp equilibrium falling zone' which specifies fast rate of mass transfer compared to the reaction rate, corresponding to a pseudo-irreversible reaction.

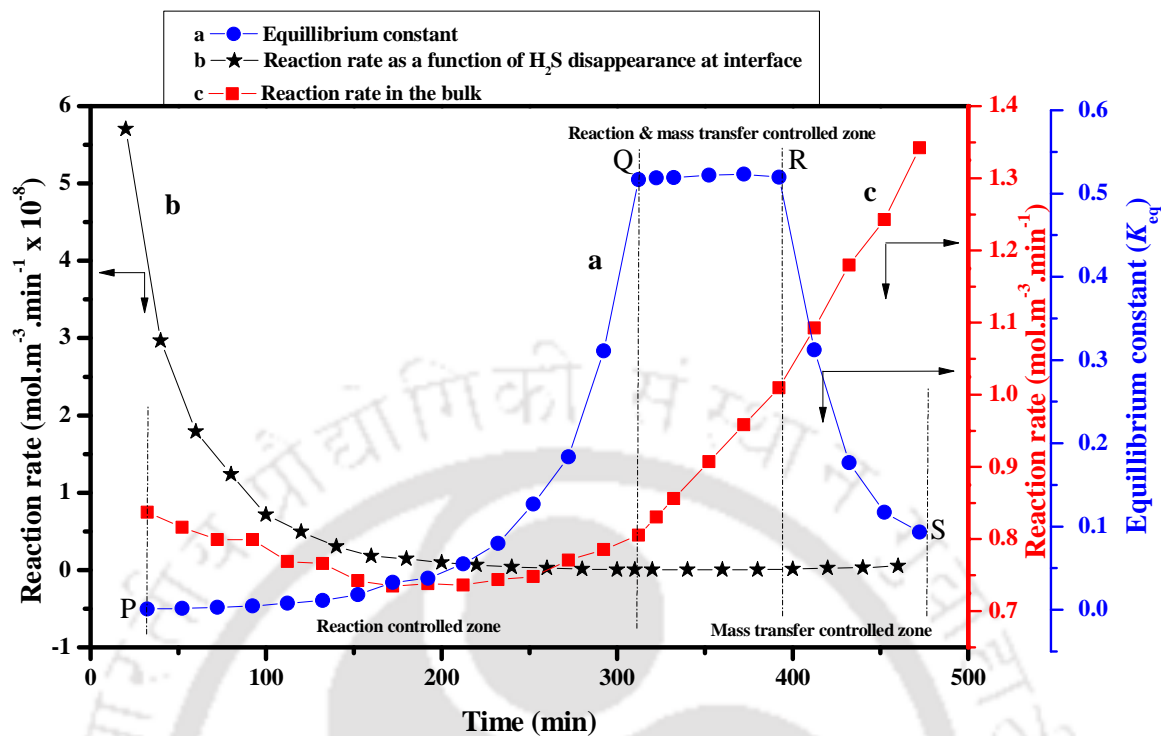


**Figure 6.7** Variation of equilibrium constant with time (curve a), reaction rate as a function of disappearance of  $H_2S$  evaluated using Eq. (6.12) (curve b) and overall reaction rate calculated on the basis of mass balance using Eq. (6.11) (curve c)

These results suggest that, conversion is not effected by the undesired product, i.e., the production of water but a significant effect of  $K_{eq}$  and  $k_{ij}$ . Though the performance of the CMR reduces after a certain period of time, but a higher conversion is achieved due to the shift of equilibrium from reactant to the product side for low and intermediate  $K_{eq}$  value. As reaction time increases, reactant particles come closer to each other and gets converted the reactants into desired product.

**Figure 6.7** (curves b and c) shows the variation in reaction rate in the bulk and at interface with time by means of mass balance equation and forward reaction rate constant  $K_f$  as

a function of equilibrium constant respectively. **Figure 6.7 (curve b)** indicates a decrease in reaction rate as a function of disappearance of  $H_2S$  with time at the interface of the membrane, suggesting occurrence of reaction at the catalytic surface of the membrane. The decline nature of the reaction rate can also be described by the increase in viscous flux, as is seen in the **Figure 6.6a**. **Figure 6.7 (curve c)** shows an increase in reaction rate with time and  $K_f$ , but the reaction kinetics is slow as  $K_f$  lies in the range of  $10^{-2} \text{ m.min}^{-1}$  causing small amount of water production. The nature of this increase resembles to the increase in equilibrium constant which is in the favour of CMR.

**Figure 6.8a** displays overall rate of loss of  $H_2S$  with time in terms of change in conversion with time. This graph provides almost a similar trend as shown in the **Figure 6.7 (curve b)** for the overall rate of disappearance of reactants, thus, signifying that the assumptions taken into account for the proposed batch reactor are well-acceptable. **Figure 6.8b** exhibits a sharp decrease in concentration of both the reactant gases with reaction time upto 300 min, after which a limiting value is reached and then increased again.

The sharp increase in concentration upto 300 min indicates dissociation of both  $H_2S$  and  $SO_2$  simultaneously due to the red-ox nature of the Claus reaction upto 300 min, confirms conversion of reactant gases into desired product (sulfur). The constant concentration value from 300 to 380 min specifies no reaction at all due to saturation of active metal sites. The sudden increase in concentration is due to the addition of  $H_2S$  and  $SO_2$  to maintain stoichiometric ratio (2:1) inside the reactor for further experimentation.

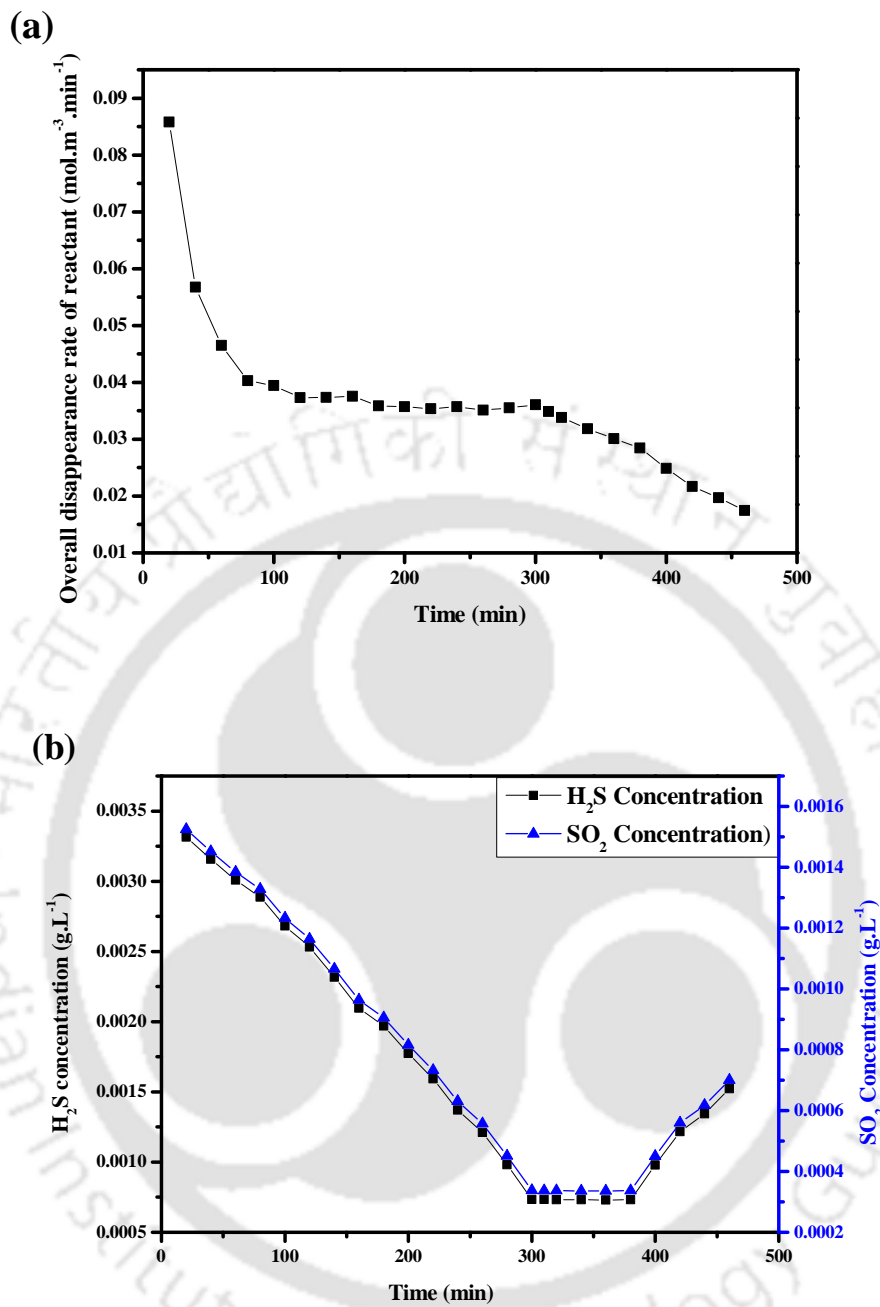


**Figure 6.8** (a) Overall rate of disappearance of H<sub>2</sub>S by means of material balance inside the reactor obtained from Eq. 6.8. (b) Change in concentration of both H<sub>2</sub>S and SO<sub>2</sub> with time

### 6.4.5 Comparison with formerly published work

The new experimental data from our study by means of newly proposed catalyst synthesis scheme and H<sub>2</sub>S conversion using Claus reaction are compared with the values obtained from the conventional methods reported in previously published literatures [156, 159, 160]. A CoMo/ $\gamma$ -Al<sub>2</sub>O<sub>3</sub> catalyst is prepared by EDF and dry impregnation, is compared with three CoMo/ $\gamma$ -Al<sub>2</sub>O<sub>3</sub> samples prepared using various conventional impregnation methods. The authors found 30-43% more conversion in HDS using the EDF-prepared catalyst than those prepared with the conventional impregnation techniques, is almost 60% lower than our experimental data [159]. Conversions of H<sub>2</sub>S and SO<sub>2</sub> at a temperature of 276°C and a pressure of 1.5 bar in absence of a pressure difference over the membrane using a  $\alpha$ -alumina based membrane of 41% porosity and 45 mm of thickness have been measured. Their aim had to present the basic fundamental of the membrane reactor not to present the parameter values [156]. The Claus H<sub>2</sub>S conversion (at room temperature) obtained from our study is numerous times greater than the conversion (at 850 and 1150°C) predicted by another study [161]. It is found that almost 63% and 82% H<sub>2</sub>S conversion with a different rate expression and reaction conditions at 850 and 1150°C, respectively. In a similar study with a different rate expression but at a same reaction temperature of 850 and 1150°C, 12% and 85% H<sub>2</sub>S conversion are observed, is lower than our experimental data [160].

In our study, we have also measured SO<sub>2</sub> conversion and these values follow almost similar trend with H<sub>2</sub>S conversion. We have shown consistent data and can suggest that the differences in results between our study and previous studies are due to a new proposed scheme and negligible mass transfer limitation.

### 6.4.6 Experimental versus Theoretical data

The relationship between output factors (overall conversion, selectivity and yield) with time obtained from the experimental data are compared with the predicted values on the basis of a polynomial fitting. A statistical analysis (ANOVA) is performed to validate the experimental values with the theoretical values.

**Table 6.4** Polynomial fitting of the catalytic activity (experimental data) of the CMR with the theoretical data

<b>Description</b>	Perform Polynomial Fitting
<b>Equation</b>	$Y = \text{Intercept} + B1 \times X^1 + B2 \times X^2$
<b>Weight</b>	No Weighting
<b>Multi-Data Fit Mode</b>	Independent Fit - Consolidated Report

**Table 6.5** Determination of catalytic activity of the CMR on the basis of polynomial fitting

		<b>Value</b>	<b>Standard Error</b>
<b>Overall conversion</b>	Intercept	9.97	1.15
	B1	0.19	0.02
	B2	$1.34 \times 10^{-4}$	$4.34 \times 10^{-5}$
<b>Selectivity</b>	Intercept	1.79	1.50
	B1	-0.02	0.02
	B2	$7.11 \times 10^{-4}$	$5.66 \times 10^{-5}$
<b>Yield</b>	Intercept	7.36	1.55
	B1	0.15	0.02
	B2	$2.75 \times 10^{-4}$	$5.89 \times 10^{-5}$

**Table 6.6** Statistical analysis of the predicted catalytic activity of the CMR

	Overall conversion	Selectivity	Yield
<b>Number of Points</b>	17	17	17
<b>Degrees of Freedom</b>	14	14	14
<b>Residual Sum of Squares</b>	32.10	54.47	58.88
<b>Adj. R-Square</b>	0.99	0.99	0.99

**Table 6.7** Summary of predicted catalytic activity based on statistical analysis

	Intercept		B1		B2		Statistics	
	Value	Standard Error	Value	Standard Error	Value	Standard Error	Value	Standard Error
<b>Overall conversion</b>	9.97	1.15	0.19	0.02	$1.34 \times 10^{-4}$	$4.35 \times 10^{-5}$	0.99	9.96
<b>Selectivity</b>	1.78	1.50	-0.020	0.02	$7.11 \times 10^{-4}$	$5.67 \times 10^{-5}$	0.99	1.78
<b>Yield</b>	7.36	1.55	0.15	0.022	$2.75 \times 10^{-4}$	$5.89 \times 10^{-5}$	0.99	7.35

**Table 6.8** ANOVA analysis for overall conversion, selectivity and yield

		DF	Sum of Squares	Mean Square	F Value	Prob>F
<b>Overall conversion</b>	Model	2	8808.26	4404.13	1920.68	0
	Error	14	32.10	2.30		
	Total	16	8840.36			
<b>Selectivity</b>	Model	2	8556.26	4278.13	1099.59	$4.44 \times 10^{-16}$
	Error	14	54.47	3.90		
	Total	16	8610.73			
<b>Yield</b>	Model	2	9472.45	4736.22	1126.19	$3.33 \times 10^{-16}$
	Error	14	58.88	4.20		
	Total	16	9531.32			

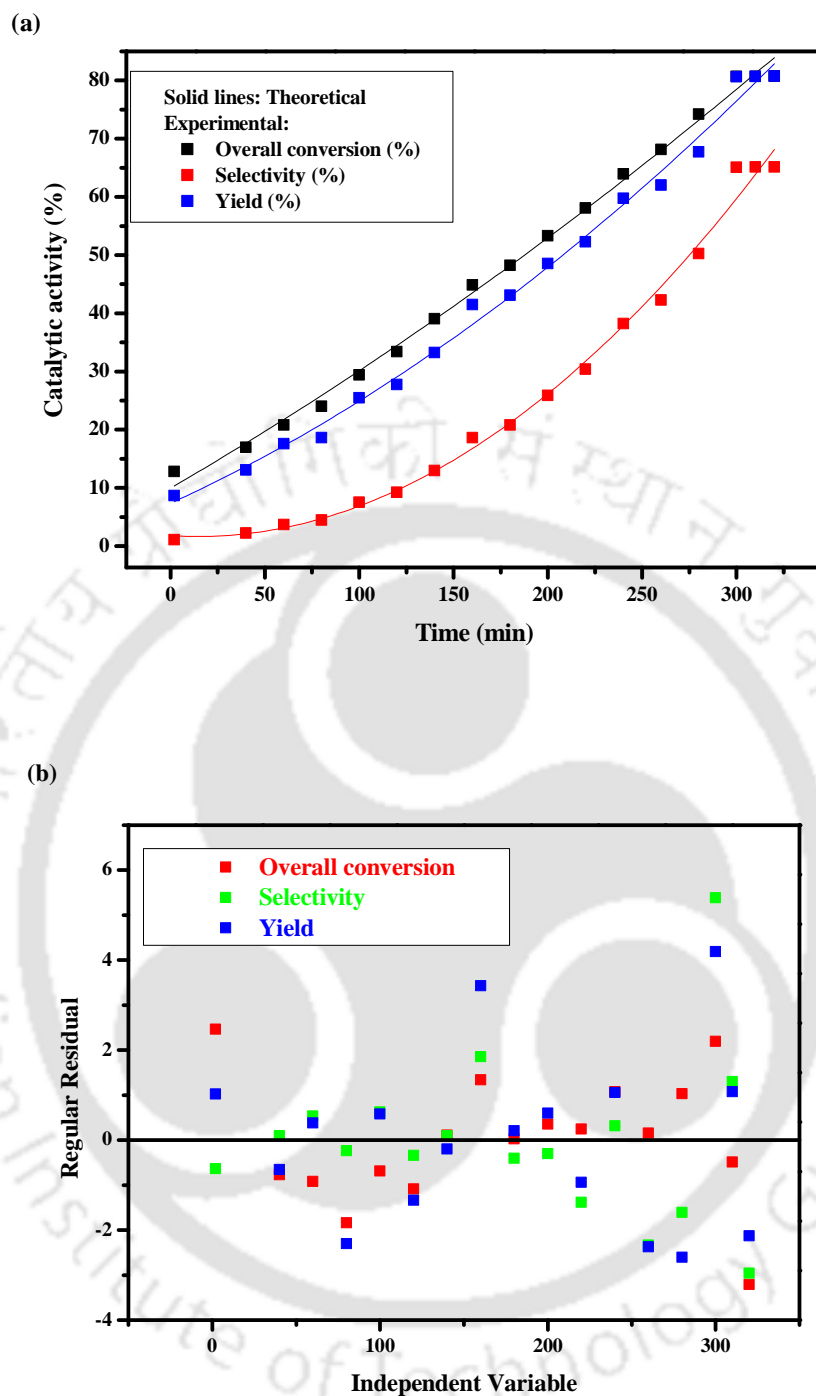


**Figure 6.9** (a) Plot of experimental and theoretical values for overall conversion, selectivity and yield, and (b) plot of regular residual for overall conversion, selectivity and yield

The predicted values obtained from the polynomial fitting (**Table 6.5**) are compared with the values obtained from experimental studies (actual values) to confirm the stability and

the feasibility of empirical model (**Figure 6.9**). **Figure 6.9a** depicts that the proposed model is well accepted and followed a polynomial fitting with an adjusted R-squared value 0.99 (**Table 6.6**) for overall conversion, selectivity and yield. The standard error for the output parameters lies within the range of  $\pm 6\%$  (**Table 6.7**). **Figure 6.9b** presents the plot of regular residuals for overall conversion, selectivity and yield which reveals a random scattering of all experimental data points across the horizontal line or residuals. This phenomenon suggests that the proposed model is adequate, is also confirmed by the ANOVA results, as shown in **Table 6.8**.

## 6.5 Summary

A novel membrane reactor with separated feed of reactants in co-current mode is presented to understand the mass transfer behaviour of Claus reaction with 2:1 stoichiometry. The mass transfer study of this membrane reactor is performed on the basis of mathematical equations to realize the effect of equilibrium constant and mass transfer coefficient on the reaction rate and conversion.

We can conclude the above study as follows:

- The results specify that the occurrence of sulfur over the membrane does not diminish the reactor performance.
- The performance of the reactor can be described, based on the value of equilibrium constant ( $K_{eq}$ ) and the mass transport coefficient at boundary layer of the membrane ( $k_{ij}$ ).
- A low to intermediate value (0.1 to 0.5) with asymptotic nature of  $K_{eq}$  with time specifies an appreciable performance of the fabricated CMR. A minimum value of  $k_{ij}$

( $2.07 \times 10^{-6} \text{ m} \cdot \text{min}^{-1}$ ) indicates a negligible effect on mass transfer by obtaining 80% yield and 87% conversion of reactants into elemental sulfur.

- A direct relationship between metal dispersion of  $\gamma$ -alumina (high surface area) supported molybdenum catalyst, TF and activity has been indicated.

In the last, we can conclude that the mass transfer study gives an excellent description of the performance of the fabricated CMR and a better modelling study can be done in the future work.



# Chapter 7

---

## Overall Conclusions and Scope of Future Work

## Chapter 7

### Overall Conclusions and Scope of Future Work

An attempt to fabricate a catalytic membrane and membrane reactor for the removal or recovery of elemental sulfur using Claus reaction has been completed successfully and vital conclusions have been drawn in four major segments of the entire work: (a) fabrication, characterization and optimization study of low-cost ceramic support membrane; (b) synthesis and characterization of catalyst; (c) fabrication and characterization of low-cost catalytic membrane; (d) performance of catalytic membrane and membrane reactor.

The findings on the various issues examined in the fabrication, characterization and application of catalytic membrane and membrane reactor are summarized as follows:

- For the commercial aspects, use of low-cost ceramic support for reducing the fabrication cost of catalytic membrane and membrane reactor has been considered as one of the key criteria. Incorporation of sawdust as a pore-former in the fabrication of low-cost ceramic support membrane, a scorching issue at the time, is done efficiently. With respect to morphology, thermal and chemical stability, mechanical strength and economic sustainability factors maintained for the ceramic support membrane, all the factors are given equal emphasis. The fabricated tubular ceramic support costs as \$332/m<sup>2</sup> including membrane mould preparation charge, is economic compared to the membranes available in the market and reported in the literatures.
- A novel Mo-Co/activated  $\gamma$ -Al<sub>2</sub>O<sub>3</sub> catalyst is simply and effectively synthesized for the fabrication of catalytic membrane and membrane reactor. An excellent metal-support

interaction is observed in terms of well-distributed dispersion of metal precursors over support matrix.

- Again, for the economic aspects, an inexpensive and innovative process i.e., ‘paint coating’ using solid lubricant over the fabricated low-cost ceramic support has been considered as one of the key criteria for minimizing the manufacturing cost of catalytic membrane and membrane reactor. The fabrication of catalytic membrane is fruitful in context of morphology and budget. The estimated cost of the fabricated catalytic membrane is \$381/m<sup>2</sup> which is still less compared to the catalytic membranes reported in the literature.
- For environmental aspects, the aim of this study is extremely effective. The fabricated reactor behaves like an ideal CMR by means of the mass transport where no internal pore diffusion mass transfer is observed during the reaction. Maximum of 87% yield and 80% conversion of the reactant into elemental sulfur are detected.

The results of this study confirm a productive fabrication of a best performing ceramic membrane reactor for environmental, commercial and economic aspects. We believe that this work has a large potential for future applications because it can minimize investment costs, intensify energy efficiency.

### **Future recommendations**

The discussion, so far, has focused on the fabrication, characterization of low-cost catalytic membrane reactor and its application. Precisely, this study has already established a process of minimizing manufacturing cost of a catalytic membrane which is novel and innovative.

This section delivers a number of future directions which would be valuable for further study of the fabrication and application of catalytic membrane reactor. Some essential areas of recommended research are suggested as an extension of the present study:

- Reactor performance study can be carried out by changing different parameters, like, membrane thickness and membrane effective area.
- Modification of present batch set-up (co-current) in other modes of operation like continuous counter-current to obtain more realistic idea upon the performance of the fabricated CMR in industrial applications.
- Modelling of reactor can be studied to get an accurate knowledge over the reactor performance.

Despite the progress recognized until now in this area, further advances must expect the development of more stable and affordable catalytic membrane and membrane reactors. The probable benefits of such advances in the field of catalytic membrane and membrane reactors are the significant factors for the possible large-scale applications in the oil and petrochemical industry. For this reason, we have carefully designed and analyzed catalytic membrane and membrane reactor to evaluate their potential advantages over the conventional process currently in operation. On account of high operating and manufacturing cost, our proposed scheme of using catalytic membrane reactor for sulfur recovery offers low capital investment, operating, manufacturing and maintenance cost.



**Appendix. 1****Table A1.** t-Test: Two-Sample Assuming Unequal Variances

	Variable 1	Variable 2
Mean	39.83	36.33
Variance	18.56	12.26
Observations	6	6
Hypothesized Mean Difference	0	
df	10	
t Stat	1.54	
P(T<=t) one-tail	0.07	
t Critical one-tail	1.81	
P(T<=t) two-tail	0.15	
t Critical two-tail	2.22	

N.B.: We have done a two-tail test (inequality). If the calculated statistical data satisfies the condition i.e.,  $t \text{ Stat} < -t \text{ Critical two-tail}$  or  $t \text{ Stat} > t \text{ Critical two-tail}$ , then we can reject the null hypothesis and can differentiate between two methods applied for the calculation of porosity. But, practically, this is not the case,  $-2.228 < 1.543 < 2.228$ . Therefore, we do not reject the null hypothesis and can conclude that the obtained porosities using volumetric porosity and gas permeation method differ marginally.

**Table A2.** Selection of porosity determination method using statistical analysis (Standard Deviation)

	Volumetric porosity determination method	Gas permeation method
Mean	39.83	36.33
Standard Error	1.75	1.42
Median	38	35
Mode	38	34
Standard Deviation	4.30	3.50
Sample Variance	18.56	12.26
Range	12	9
Minimum	36	34
Maximum	48	43
Sum	239	218
Count	6	6

Appendix. 2

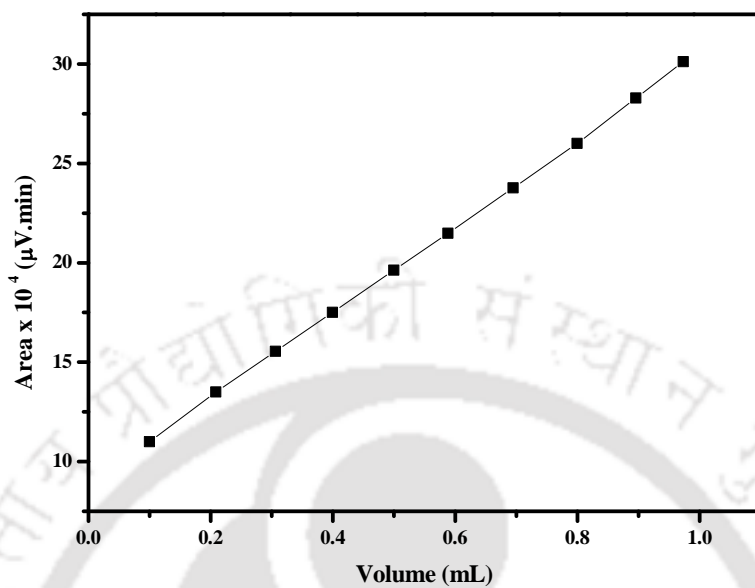


Figure A1. Calibration curve for H<sub>2</sub>S

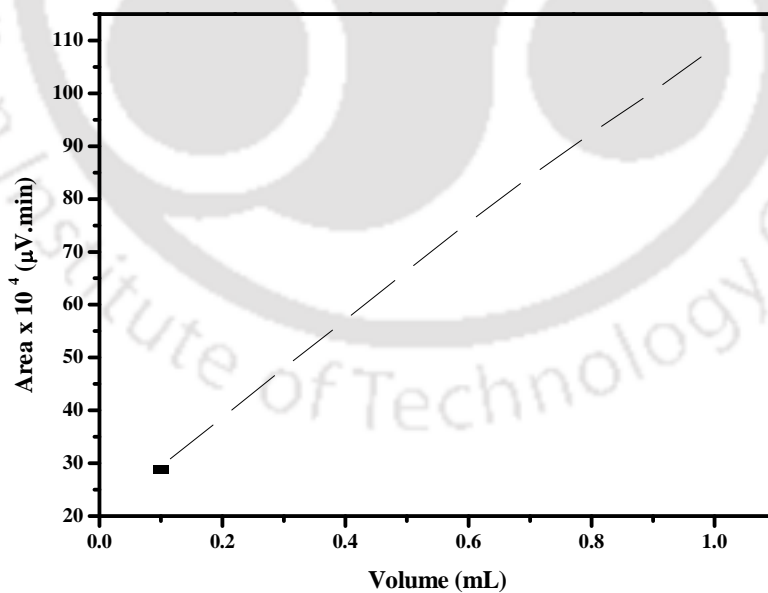


Figure A2. Calibration curve for SO<sub>2</sub>

## References

1. Vallero, D., *Fundamentals of Air Pollution*, Elsevier Academic Press, 5th Edition, (2014).
2. Lucking, A. J., Lundback, M., Mills, N. L., Faratian, D., Barath, S. L., Pourazar, J., Cassee, F. R., Donaldson, K., Boon, N. A., Badimon, J. J., Sandstrom, T., Blomberg, A., Newby, D. E., "Diesel exhaust inhalation increases thrombus formation in man, *Eur. Heart J.*," **29** 3043-3051 (2008).
3. Nielsen, O. R., Andersen, Z. J., Hvidberg, M., Jensen, S. S., Ketzel, M., Sorensen, M., Tjonneland, A., "Lung cancer incidence and long-term exposure to air pollution from traffic," *Environ. Health Persp.*, **119** (6) 860-865 (2011).
4. Oberdorster, G., and Utell, M. J., "Ultrafine particles in the urban air: to the respiratory tract-and beyond?," *Environ. Health Persp.*, **110** A440-A441 (2002).
5. Gary, J. H., and Handwerk, G. E., *Petroleum Refining Technology and Economics*, 2nd Edition, Marcel Dekker, ISBN 0-8247-7150-8 (1984).
6. Clark, P. D., Dowling, N. I., Huang, M., *Fundamental and Practical Aspects of the Claus Sulfur Recovery Process*, Alberta Sulfur Research Ltd., Calgary, Alberta, Canada, (2007).
7. Market Report, Global Membrane Technology Market, Acmite Market Intelligence, ca. 550 pages, (2013).
8. Sanchez Marcano, J. G., and Tsotsis, T. T., *Catalytic Membranes and Membrane Reactors*, Wiley-VCH Verlag GmbH, (2002).
9. Engasser, J. M., "Reacteurs a Enzymes et Cellules Immobilisees," in chapter 4.2, *Biotechnologie, Technique et documentation Lavoisier*, Paris, (1988).

10. Hanemaaijer, J. H., Stahouders, J., and Vissar, S., in *Proc. 4th Eur. Congr. in Biotechn.* (Edited by Neijssel, O. M., van der Meer R. R. and Luyben, K. Ch. M.,) vol. 1, pp. 119, Elsevier, Amsterdam, (1987).
11. Gobina, E., and Hughes, R., "Ethane dehydrogenation using a high-temperature catalytic membrane reactor." *J. Membr. Sci.*, **90** (1-2) 11-19 (1994).
12. Uemiya, S., Sato, N., Ando, H., Kikuchi, E., "The water gas shift reaction assisted by a palladium membrane reactor," *Ind. Eng. Chem. Res.*, **30** (3) 585-589 (1991).
13. Gokhale, Y. V., Noble, R. D., Falconer, J. L., "Effects of reactant loss and membrane selectivity on a dehydrogenation reaction in a membrane-enclosed catalytic reactor," *J. Membr. Sci.*, **103** (3) 235-242 (1995).
14. Tiscarño-Lechuga, F., Hill Jr., C. G., Anderson, M. A., "Effect of dilution in the experimental dehydrogenation of cyclohexane in hybrid membrane reactors," *J. Membr. Sci.*, **118** (1) 85-92 (1996).
15. Itoh N., "Simulation of a bifunctional palladium membrane reactor," *J. Chem. Eng. Jpn.*, **23** (1) 81-87 (1990).
16. Gobina, E., and Hughes, R., "Reaction coupling in catalytic membrane reactors," *Chem. Eng. Sci.*, **51** (11) 3045-3050 (1996).
17. Santos, A., Finol, C., Coronas, J., Menendez, M., Santamaria, J., "Reactor engineering studies of methane oxidative coupling on a Li/Mgo catalyst," *Stud. Surf. Sci. Catal.*, **81** (C) 171-176 (1994).
18. Lafarga, D., Santamaria, J., Menendez, M., "Methane oxidative coupling using porous ceramic membrane reactors - I. reactor development," *Chem. Eng. Sci.*, **49** (12) 2005-2013 (1994).
19. Mallada, R., Menendez, M., Santamaria, J., *Proceedings of the third international conference on catalysis in membrane reactors*, Copenhagen, 8-10 September (1998).

20. Xue, E., and Ross, J., *Proceedings of the third international conference on catalysis in membrane reactors*, Copenhagen, 8-10 September (1998).
21. Slood, H. J., "A non-permselective membrane reactor for catalytic gas phase reactions," Ph.D. Thesis, University of Twente, The Netherlands, (1991).
22. Veldsink, J. W., Versteeg, G. F., van Swaaij, W. P. M., *Proceedings of the first international workshop on catalytic membranes*, Lyon-Villeurbanne, France, 26-28 September, (1994).
23. Neomagus, H. W. J. P., van Swaaij, W. P. M., Versteeg, G. F., "The catalytic oxidation of H<sub>2</sub>S in a stainless steel membrane reactor with separate feed of reactants," *J. Membr. Sci.*, **148 (2)** 147-160 (1998).
24. Neomagus, H. W. J. P., Saracco, G., Wessel, H. F. W., Versteeg, G. F., "The catalytic combustion of natural gas in a membrane reactor with separate feed of reactants," *Chem. Eng. J.*, **77 (3)** 165-177 (2000).
25. Harold, M. P., Zaspalis, V. T., Keizer, K., Burgraaf, A. J., "Intermediate product yield enhancement with a catalytic inorganic membrane - I. Analytical model for the case of isothermal and differential operation," *Chem. Eng. Sci.*, **48 (15)** 2705-2725 (1993).
26. Herguido, J., Lafarga, D., Menendez, M., Santamaria, J., Guimon, C., "Characterization of porous ceramic membranes for their use in catalytic reactors for methane oxidative coupling," *Catal. Today*, **25 (3-4)** 263-269 (1995).
27. Coronas, J., and Santamaria, J., "Catalytic reactors based on porous ceramic membranes," *Catal. Today*, **51** 377-389 (1999).
28. Cini, P., and Harold, M. P., "Experimental study of the tubular multiphase catalyst," *AIChE J.*, **37 (7)** 997-1008 (1991).
29. Peureux, J., Torres, M., Mozzanega, H., Giroir-Fendler, A., Dalmon, J. A., "Nitrobenzene liquid-phase hydrogenation in a membrane reactor," *Catal. Today*, **25 (3-4)** 409-415 (1995).

30. Saracco, G., and Specchia, V., "Catalytic ceramic filters for flue gas cleaning. 2. Catalytic performance and modelling thereof," *Ind. Eng. Chem. Res.*, **34** (4) 1480-1487 (1995).
31. Saracco, G., Specchia, S., Specchia, V., "Catalytically modified fly-ash filters for NO<sub>x</sub> reduction with NH<sub>3</sub>," *Chem. Eng. Sci.*, **51** (24) 5289-5297 (1996).
32. Hsieh, H. P., *Inorganic Membranes for Separation and Reaction*, Elsevier Science B.V., (1996).
33. Julbe, A., Farrusseng, D., Guizard, C., "Porous ceramic membranes for catalytic reactors - overview and new ideas," *J. Membr. Sci.*, **181** 3-20 (2001).
34. Westermann, T., Melin, T., "Flow-through catalytic membrane reactors - principles and applications," *Chem. Eng. Process.*, **48** 17-28 (2009).
35. Dixon, A.G., "Innovations in catalytic inorganic membrane reactors," in *Catalysis* (Edited by Spivey J. J.), pp. 40-92 (Chapter 2), vol. 14 of Specialist Periodical Reports, RSC Publishing, (1999).
36. Pinnau, I., and Toy, L. G., "Solid polymer electrolyte composite membranes for olefin – paraffin separation," *J. Membr. Sci.*, **184** 39-48 (2001).
37. Weyten, H., Keizer, K., Kinoo, A., Luyten, J., Leysen, R., "Dehydrogenation of propane using a packed-bed catalytic membrane reactor," *AIChE J.*, **43** (7) 1819-1827 (1997).
38. Weyten, H., Luyten, J., Keizer, K., Willems, L., Leysen, R., "Membrane performance: the key issues for dehydrogenation reactions in a catalytic membrane reactor," *Catal. Today*, **56** (1-3) 3-11 (2000).
39. Tsai, C. Y., Ma, Y. H., Moser, W. R., Dixon, A. G., "Modelling and simulation of a nonisothermal catalytic membrane reactor," *Chem. Eng. Commun.*, **134** (1) 107-132 (1995).
40. Chanaud, P., Julbe, A., Larbot, A., Guizard, C., Cot, L., Borges, H., Fendler, A. G., Mirodatos C., "Catalytic membrane reactor for oxidative coupling of methane. Part 1:

- preparation and characterisation of LaOCl membrane,” *Catal. Today*, **25 (3-4)** 225-230 (1995).
41. Pina, M. P., Menendez, M., Santamaria, J., “The Knudsen-diffusion catalytic membrane reactor: An efficient contactor for the combustion of volatile organic compounds,” *Appl. Catal. B: Environ.*, **11 (1)** L19–27 (1996).
42. Binkerd, C. R., Ma, Y. H., Moser, W. R., Dixon, A. G., “An experimental study of the oxidative coupling of methane in porous ceramic radial-flow catalytic membrane reactors,” in *Proceedings of the fourth international congress on inorganic membranes*, Gatlinburg, TN, July 14-18 441 (1996).
43. Lambert, C. K., and Gonzalez, R.D., “Activity and selectivity of a Pd/ $\gamma$ -Al<sub>2</sub>O<sub>3</sub> catalytic membrane in the partial hydrogenation reactions of acetylene and 1,3-butadiene,” *Catal. Lett.*, **57 (1-2)** 1-7 (1991).
44. Jacoby, W. A., Maness, P. C., Blake, D. M., Wolfrum, E. J., *Proceedings of the third international conference on catalysis in membrane reactors*, Copenhagen, 8-10 September, Paper O13, (1998).
45. Maier, W. F., Lange, C., Tilgner, I., Tesche, B., “Effects of membrane catalyst on the activity and selectivity of hydrogenation reactions” in *Proceedings of the third international conference on catalysis in membrane reactors*, Edited by Hojlund, P. E., Haldor, N., Topsoe, A. S., pp. 22, Copenhagen, Denmark, September (1998).
46. Dong, X., Jin, W., Xua, N., Li, K., “Dense ceramic catalytic membranes and membrane reactors for energy and environmental applications,” *Chem. Comm.*, **47** 10886-10902 (2011).
47. Zaspalis, V. T., van Praag, W., Keizer, K., van Ommen, J. G., Ross, J. R. H., Burggraaf, A. J., “Reactor studies using vanadia modified titania and alumina catalytically active

- membranes for the reduction of nitrogen oxide with ammonia,” *Appl. Catal.*, **74** 249-260 (1991).
48. Dalmon, J. A., “Catalytic Membrane Reactors,” in *Handbook of heterogeneous catalysis*, edited by Ertl, G., Knözinger, H., Weitkamp, J., (Chapter 9.3) VCH Publishers, (1997).
49. Slood, H. J., Versteeg, G. F., van Swaaij, W. P. M., “A non-permselective membrane reactor for chemical processes normally requiring strict stoichiometric feed of reactants,” *Chem. Eng. Sci.*, **45** 2415-2421 (1990).
50. Mark, H. F., Othmer, D. F., Overberger, C. G., Seaborg, G. T., Othmer, K., *Encyclopedia of chemical technology*, vol. 22, John Wiley & Son, (1983).
51. Slood, H. J., Smolders, C. A., van Swaaij, W. P. M., Versteeg, G. F., “High-temperature membrane reactor for catalytic gas-solid reactions,” *AIChE J.*, **38** 887-900 (1992).
52. Saracco, G., Veldsink, J. W., Versteeg, G. F., van Swaaij, W. P. M., “Catalytic combustion of propane in a membrane reactor with separate feed of reactants - I. Operation in absence of trans-membrane pressure gradients,” *Chem. Eng. Sci.*, **50** (12) 2005-2015 (1995).
53. Saracco, G., Veldsink, J. W., Versteeg, G. F., van Swaaij, W. P. M., “Catalytic combustion of propane in a membrane reactor with separate feed of reactants - II. Operation in presence of trans-membrane pressure gradients,” *Chem. Eng. Sci.*, **50** (17) 2833-2841 (1995).
54. Gordon, L., Salutsky, M. L., Willard, H. H., *Precipitation from homogeneous solutions*, Chapman & Hall, (1959).
55. Saracco, G., Veldsink, J. W., Versteeg, G. F., van Swaaij, W. P. M., “Catalytic combustion of propane in a membrane reactor with separate feed of reactants - III. Role of catalyst load on reactor performance,” *Chem. Eng. Sci.*, **147** (1) 29-42 (1996).

56. Saracco, G., and Specchia, V., "Catalytic combustion of propane in a membrane reactor with separate feed of reactants - IV. Transition from the kinetics- to the transport-controlled regime," *Chem. Eng. Sci.*, **55** 3979-3989 (2000).
57. Capannelli, G., Carosini, E., Cavani, F., Monticelli, O., Trifiro, F., "Comparison of the catalytic performance of  $V_2O_5/\gamma-Al_2O_3$  in the oxi-dehydrogenation of propane to propylene in different reactor configurations: i) packed-bed reactor, ii) monolith-like reactor and iii) catalytic membrane reactor," *Chem. Eng. Sci.*, **51** (10) 1817-1826 (1996).
58. Alfonso, M. J., Julbe, A., Farrusseng, D., Menéndez, M., Santamaría, J., "Oxidative dehydrogenation of propane on  $V/Al_2O_3$  catalytic membranes. Effect of the type of membrane and reactant feed configuration," *Chem. Eng. Sci.*, **54** 1265-1272 (1999).
59. Murru, M., Gavriilidis, A., "Catalytic combustion of methane in non-permselective membrane reactors with separate reactant feeds," *Chem. Eng. J.*, **100** 23-32 (2004).
60. Basile, A., Tosti, S., Capannelli, G., Vitulli, G., Iulianelli, A., Gallucci, F., Drioli, E., "Co-current and counter-current modes for methanol steam reforming membrane reactor: Experimental study," *Catal. Today*, **118** 237-245 (2006).
61. Luyten, J., Buekenhoudt, A., Adriansens, W., Coymans, J., Weyten, H., Servaes, F., Leysen, R., "Preparation of  $LaSrCoFeO_{3-x}$  membranes," *Solid State Ionics*, **135** (1-4) 637-642 (2000).
62. Centri, G., Dittmeyer, R., Perathoner, S., Reif, M., "Tubular Inorganic catalytic membrane reactors: advantages and performance in multiphase hydrogenation reactions," *Catal. Today*, **79-80** 139-149 (2003).
63. Dalmon, J.-A., Cruz-Lo'pez, A., Farrusseng, D., Guilhaume, N., Iojoiu, E., Jalibert, J.-C., Miachon, S., Mirodatos, C., Pantazidis, A., Dassonneville, M. R., Schuurman, Y., van

- Veen, A. C., "Oxidation in catalytic membrane reactors," *Appl. Catal. A: Gen.*, **325** 198-204 (2007).
64. Ermilova, M. M., Morozov, L. S., Smith, N. V., Gryaznov, V. M., "Effect of catalytic hydrogenation on hydrogen transfer through the membrane of palladium-ruthenium alloy," *Nat. Chem.*, **68 (7C)** 1211-1214 (1994).
65. Gryaznov, V. M., Karavanov, A. N., "Hydrogenation and dehydrogenation of organic compounds on membrane catalysts (Review)," *Pharm. Chem. J.*, **7** S74-78 (1979).
66. Smirnov, V. S., Gryaznov, V. M., Lebedeva, V. I., Mishchenko, A. P., Polyakova, V. P., Savitskii, E. M., "Catalysts for dehydrogenation, dehydrocyclization, and dehydroalkylation of hydrocarbons," *German Öffentlichkeit*, DE 2015248 A 19710218, (1971).
67. Jackson, S. D., Glanville, B. M., Willis, J., McLellan, G. D., Webb, G., Moyes, R. B., Simpson, S., Wells, P. B., Whyman, R., "Supported metal catalysts: preparation, characterisation, and function III. The adsorption of hydrocarbons on platinum catalysts," *J. Catal.*, **139** 221-233 (1993).
68. Kotanjac, Ž. S., vanSint Annaland, M., Kuipers, J. A. M., "A packed bed membrane reactor for the oxidative dehydrogenation of propane on a Ga<sub>2</sub>O<sub>3</sub>/MoO<sub>3</sub> based catalyst," *Chem. Eng. Sci.*, **65** 441-445 (2010).
69. Yang, Z., Ding, W., Zhang, Y., Lu, X., Zhang, Y., Shen, P., "Catalytic partial oxidation of coke oven gas to syngas in an oxygen permeation membrane reactor combined with NiO/MgO catalyst," *Int. J. Hydrogen Energy*, **35** 6239-6247 (2010).
70. Iulianelli, A., Manzolini, G., De Falco, M., Campanari, S., Longo, T., Liguori, S., Basile, A., "H<sub>2</sub> production by low pressure methane steam reforming in a Pd/Ag membrane reactor over a Ni-based catalyst: Experimental and modelling," *Int. J. Hydrogen Energy*, **35** 11514-11524 (2010).

71. Rodriguez, M. L., Ardisson, D. E., Heracleous, E., Lemonidou, A. A., Lo'pez, E., Pedernera, M. N., Borio, D. O., "Oxidative dehydrogenation of ethane to ethylene in a membrane reactor: A theoretical study," *Catal. Today*, **157** 303-309 (2010).
72. Sa', S., Sousa, J. M., Mendes, A., "Steam reforming of methanol over a CuO/ZnO/Al<sub>2</sub>O<sub>3</sub> catalyst part II: A carbon membrane reactor," *Chem. Eng. Sci.*, **66** 5523-5530 (2011).
73. Vladov, Ch., Petrov, L., Ytua, B., "Structure and activity of a CoMo/Al<sub>2</sub>O<sub>3</sub> catalyst upon modification by Gamma irradiation," *Appl. Catal. A: Gen.*, **94** 205-213 (1993).
74. Jayaraman, V., Lin, Y. S., Pakala, M., Lin, R.Y., "Fabrication of ultrathin metallic membranes on ceramic supports by sputter de-position," *J. Membr. Sci.*, **99** 89-100 (1995).
75. Gobina, E., and Hughes, R., *Proceedings of the first international workshop on catalytic membranes*, Lyon-Villeurbanne, France, 26-28 September C17 (1994).
76. Linkov, V. M., Sanderson, R. D., Jacobs, E. P., Smith, S. P. J., *Proceedings of the first international workshop on catalytic membranes*, Lyon-Villeurbanne, France, 26-28 September C24 (1994).
77. Athayde, A. L., Baker, R.W., Nguyen, P., "Metal composite membranes for hydrogen separation," *J. Membr. Sci.*, **94** (1) 299-311 (1994).
78. Yan, S., Maeda, H., Kusakabe, K., Morooka, S., "Thin palladium membrane formed in support pores by metal-organic chemical vapor deposition method and application to hydrogen separation" *Ind. Eng. Chem. Res.*, **33** (3) 616-622 (1994).
79. Megris, C. E., Glezer, J. H. E., "Synthesis of hydrogen-permselective membranes by modified chemical vapor deposition. Microstructure and permselectivity of silica/carbon/Vycor membranes," *Ind. Eng. Chem. Res.*, **31** (5) 1293-1299 (1992).
80. Parvulescu, V., Julbe, A., Cot, L., Popescu, L., *Proceedings of the first international workshop on catalytic membranes*, Lyon-Villeurbanne, France, 26-28 September P6 (1994).

81. Kusakabe, K., Ichiki, K., Morooka, S., "Separation of CO<sub>2</sub> with BaTiO<sub>3</sub> membrane prepared by the sol-gel method," *J. Membr. Sci.*, **95** (2) 171-177 (1994).
82. Julbe, A., Guizard, C., Larbot, A., Cot, L., Giroir-Fendler, A., "The sol-gel approach to prepare candidate microporous inorganic membranes for membrane reactors," *J. Membr. Sci.*, **77** (2-3) 137-153 (1993).
83. Chou, M. L., Manning, N., Chen, H., "Deposition and characterization of thin electroless palladium films from newly developed baths," *Thin Solid Films*, **213** (1) 64-71 (1992).
84. Shu, J., Grandjean, B. P. A., Ghali, E., Kakiaguine, S., "Simultaneous deposition of Pd and Ag on porous stainless steel by electroless plating," *J. Membr. Sci.*, **77** (2-3) 181-195 (1993).
85. Kikuchi, E., *Proceedings of the first international workshop on catalytic membranes*, Lyon-Villeurbanne, France, 26-28 September, CI9 (1994).
86. Capannelli, G., Bottino, A., Gao, G., Grasso, A., Servida, A., Vitulli, G., Mastrantuono, A., Lazzaroni, R., Salvadori, P., "Porous Pt/ $\gamma$ -Al<sub>2</sub>O<sub>3</sub> catalytic membrane reactors prepared using mesitylene solvated Pt atoms," *Catal. Lett.*, **20** 287-297 (1993).
87. Li, Z. Y., Maeda, H., Kusakabe, K., Morooka, S., Anzai, H., Akiyama, S., "Preparation of palladium-silver alloy membranes for hydrogen separation by the spray pyrolysis method," *J. Membr. Sci.*, **78**(3) 247-254 (1993).
88. Basile, A., Drioli, E., Santella, F., Violante, V., Capannelli G., Vitulli, G., "A study on catalytic membrane reactors for water gas shift reaction," *Gas Sep. Purif.*, **10** (1) 53-61 (1996).
89. Li, Y. Y., Nomura, T., Sakoda, A., Suzuki, M., "Fabrication of carbon coated ceramic membranes by pyrolysis of methane using a modified chemical vapor deposition apparatus," *J. Membr. Sci.*, **197** (1-2) 23-35 (2002).

90. Xomeritakis, G., and Lin, Y. S., "Fabrication of a thin palladium membrane supported in a porous ceramic substrate by chemical vapor deposition," *J. Membr. Sci.*, **120** (2) 261-272 (1996).
91. Xomeritakis, G., and Lin, Y. S., "CVD synthesis and gas permeation properties of thin palladium/alumina membranes," *AIChE J.*, **44** 174-183 (1998).
92. Xomeritakis, G., and Lin, Y. S., "Fabrication of thin metallic membranes by MOCVD and sputtering," *J. Membr. Sci.*, **133** (2) 217-230 (1997).
93. Sea, B.K., Ando, K., Kusakabe, K., Morooka, S., "Separation of hydrogen from steam using a SiC-based membrane formed by chemical vapor deposition of tri-isopropylsilane," *J. Membr. Sci.*, **146** (1) 73-82 (1998).
94. Kuraoka, K., Shugen, Z., Okita, K., Kakitani, T., Yazawa, T., "Permeation of methanol vapor through silica membranes prepared by the CVD method with the aid of evacuation," *J. Membr. Sci.*, **160** (1) 31-39 (1999).
95. Lin, Y.S., "A theoretical analysis on pore size change of porous ceramic membranes after modification," *J. Membr. Sci.*, **79** (1) 55-64 (1993).
96. Tsapatsis, M., and Gavalas, G., "Modeling of SiO<sub>2</sub> deposition in porous Vycor: Effects of pore network connectivity," *AIChE J.*, **43** 1849-1860 (1997).
97. Lee, L. L., Hong, L. C., Hong, L. S., Tsai, D. S., "Pore Structure Modification by Chemical Vapor Deposition in Inorganic Membrane-Numerical Analysis," *J. Chin. Inst. Chem. Eng.*, **30** 105-115 (1999).
98. Takeda, Y., Shibata, N., Kubo, Y., "SiC Coating on Porous  $\gamma$ -Al<sub>2</sub>O<sub>3</sub> Using Alternative-Supply CVI Method," *J. Ceram. Soc. Jpn.*, **109** 305-309 (2001).
99. Schaeffer, J., and Gupta, B., *NASA Technical Brief*, Published Jointly by National Aeronautics and Space Administration (NASA) and Associated Business Publications Co, New York, (1999).

100. Viterna, L., *Advanced Materials & Processes*, pp. 20, ASM International, Materials Park, OH, (1999).
101. Rigney, D. J., Darolia, R., Walston, W. S., European Patent Application #EP-1,010,744-A1 10 July (1999).
102. Warnes, B. M., "Reactive element modified chemical vapor deposition low activity platinum aluminide coatings," *Surf. Coat. Technol.*, **146-147** 7-12 (2001).
103. Buxbaum, R. E., and Marker, T. L., "Hydrogen transport through non-porous membranes of palladium-coated niobium, tantalum and vanadium," *J. Membr. Sci.* **85 (1)** 29-38 (1993).
104. Mouton, D. W., Keuler, J. N., Lorenzen, L. L., *Proceedings of the sixth international congress on inorganic membranes*, Montpellier, France, 26-30 June 137 (2000).
105. Liu, B. S., Dai, W. L., Wu, G. H., Deng, J. F., "Amorphous alloy/ceramic composite membrane: preparation, characterization and reaction studies," *Catal. Lett.*, **49 (3-4)** 181-188 (1997).
106. Lefu, W., Hongbing, J., Lie, Z., *Proceedings of the fourth international conference on catalysis in membrane reactors*, pp. 63 (2000).
107. Jeon, J. H., Yeom, S. W., Oh, II-K., "Fabrication and actuation of ionic polymer metal composites patterned by combining electroplating with electroless plating," *Compos. Part A-Appl. S.*, **39** 588-596 (2008).
108. de Lange, R. S. A., Hekkink, J. H. A., Keizer, K., Burggraaf, A. J., "Formation and characterization of supported microporous ceramic membranes prepared by sol-gel modification techniques," *J. Membr. Sci.*, **99 (1)** 57-75 (1995).
109. Yeung, K.L., Aravind, R., Zawada, R. J. X., Szegner, J., Gao, G., Varma, A., "Nonuniform catalyst distribution for inorganic membrane reactors: Theoretical considerations and preparation techniques," *Chem. Eng. Sci.*, **49 (24)** Part A 4823-4838 (1994).

110. Michaels, A.S., Seventh ESMST Summer School, University of Twente, The Netherlands, (1989).
111. Farrusseng, D., Julbe, A., Cot, D., Guizard, C., Mota, S., Volta, J.C., *Proceedings of the third international conference on catalysis in membrane reactors*, Copenhagen, 8-10 September, (1998).
112. Watanabe, T., Miki, Y., Masuda, T., Deguchi, H., Kanai, H., Hosokawa, S., Wada, K., Inoue, M., "Synthesis of  $\gamma$ -Ga<sub>2</sub>O<sub>3</sub>-Al<sub>2</sub>O<sub>3</sub> solid solutions by spray pyrolysis method," *Ceram. Int.*, **37** 3183-3192 (2011).
113. Liu, J., Zhang, Y., Ionescu, M. I., Li, R., Sun, X., "Nitrogen-doped carbon nanotubes with tunable structure and high yield produced by ultrasonic spray pyrolysis," *Appl. Surf. Sci.*, **257(17)** 7837-7844 (2011).
114. Marchese, J. and Pagliero, C. L., "Characterization of assymmetric polysulphone membranes for gas separation," *Gas Sep. Purif.*, **5 (4)** 215-221 (1991).
115. Nandi, B. K., Uppaluri, R., Purkait, M. K., "Preparation and characterization of low cost ceramic membranes for micro-filtration applications," *Appl. Clay Sci.*, **42** 102-110 (2008).
116. Saffaj, N., Younssi, S.A., Albizan, A., Messouadi, A., Bouhria, M., Persin, M., Cretin, M., Larbot, A., "Preparation and characterization of ultrafiltration membranes for toxic removal from wastewater," *Desalination* **168** 259-263 (2004).
117. Yang, H., Yan, R., Chen, H., Lee, D. H., Zheng, C., "Characteristics of hemicellulose, cellulose and lignin pyrolysis," *Fuel* **86 (12-13)** 1781-1788 (2007).
118. Owen, N. L. and Thomas, D. W., "Infrared studies of hard and soft woods," *Appl. Spectrosc.*, **43** 451-455 (1989).
119. Hergert, H. L., "Infrared spectra", in *Lignins: Occurrence, Formation, Structure and Reactions* K.V. Sarkanen, (Edited by Ludwig, C. H.), pp. 267-297, Wiley-Interscience, New York (1971).

120. Mott Metallurgical Corporation, USA, (2007). (<http://www.mottcorp.com> ).
121. Guaracho, V. V., Kaminari, N. M. S., Ponte, M. J. J. S., Ponte, H. A., “Central Composite experimental design applied to removal of lead and nickel from sand,” *J. Hazard. Mater.*, **172 (2-3)** 1087-1092 (2009).
122. Montgomery, D.C., Design and Analysis of Experiments, John Wiley & Sons, USA, (2001).
123. Derringer, G., and Suich, R., “Simultaneous Optimization of Several Response Variables,” *J. Qual. Technol.*, **12 (4)** 214-219 (1980).
124. Jana, S., Purkait, M. K., Mohanty, K., “Preparation and Characterizations of Ceramic Microfiltration Membrane: Effect of Inorganic Precursors on Membrane Morphology,” *Sep. Sci. Technol.*, **46 (1)** 33-45 (2011).
125. Saffaj, N., Persin, M., Younssi, S. A., Albizane, A., Bouhria, M., Loukili, H., Dacha, H., Larbot, A., “Removal of salts and dyes by low  $ZnAl_2O_4$ - $TiO_2$  ultrafiltration membrane deposited on support made from raw clay,” *Sep. Purif. Technol.*, **47** 36-42 (2005).
126. Saffaj, N., Persin, M., Younssi, S. A., Albizane, A., Cretin, M., Larbot, A., “Elaboration and characterization of microfiltration and ultrafiltration membranes deposited on raw support prepared from natural Moroccan clay: Application to filtration of solution containing dyes and salts,” *Appl. Clay Sci.*, **31** 110-119 (2006).
127. Khemakhem, S., Larbot, A., Amar, R. B., “New ceramic microfiltration membranes from Tunisian natural materials: Application for the cuttlefish effluents treatment,” *Ceram. Int.*, **35** 55-61 (2009).
128. Jana, S., Purkait, M. K., Mohanty, K., “Preparation and characterization of low-cost ceramic microfiltration membranes for the removal of chromate from aqueous solutions,” *Appl. Clay Sci.*, **47** 317-324 (2010).
129. Mittal, P., Jana, S., Mohanty, K., “Synthesis of low-cost hydrophilic ceramic–polymeric composite membrane for treatment of oily wastewater,” *Desalination*, **282** 54-62 (2011).

130. Dong, Y., Liu, X., Ma, Q., Meng, G., "Preparation of cordierite-based porous ceramic micro-filtration membranes using waste fly ash as the main raw materials," *J. Membr. Sci.*, **285** 173-181 (2006).
131. Masmoudia, S., Larbot, A., Feki, H. E., Amara, R. B., "Elaboration and characterization of apatite based mineral supports for microfiltration and ultrafiltration membranes," *Ceram. Int.*, **33** 337-344 (2007).
132. Almandoz, M. C., Marchese, J., Prádanos, P., Palacio, L., Hernández, A., "Preparation and characterization of non-supported microfiltration membranes from aluminosilicates," *J. Membr. Sci.*, **241** 95-103 (2004).
133. Potdar, A., Sukla, A., Kumar, A., "Effect of gas phase modification of analcime zeolite composite membrane on separation of surfactant by ultra-filtration," *J. Membr. Sci.*, **210** 209-225 (2002).
134. Neelakandan, C., Pugazhenti, G., Kumar, A., "Preparation of NO<sub>x</sub> modified PMMA–EGDM composite membrane for the recovery of chromium (VI)," *Eur. Polym. J.*, **39** 2383-2391 (2003).
135. Vasanth, D., Pugazhenti, G., Uppaluri, R., "Fabrication and properties of low cost ceramic microfiltration membranes for separation of oil and bacteria from its solution," *J. Membr. Sci.*, **379** 154-163 (2011).
136. Singh, V., Purkait, M. K., Chandaliya, V. K., Biswas, P. P., Banerjee, P. K., Das, C., "Development of membrane based technology for the separation of coal from organic solvent," *Desalination*, **299** 123-128 (2012).
137. Agarwal, A., Pujari, M., Uppaluri, R., Verma, A., "Preparation, optimization and characterization of low cost ceramics for the fabrication of dense nickel composite membranes," *Ceram. Int.* **39** (7) 7709-7716 (2013).

138. Emani, S., Uppaluri, R., Purkait, M. K., "Preparation and characterization of low cost ceramic membranes for mosambi juice clarification," *Desalination*, **317** 32-40 (2013).
139. Ghosh, D., Sinha, M.K., Purkait, M.K., "A comparative analysis of low-cost ceramic membrane preparation for effective fluoride removal using hybrid technique", *Desalination*, **327** 2-13 (2013).
140. Al-Megren, H. A., Gonzalez-Corte's, S. L., Xiao, T., Green, M. L. H., "A comparative study of the catalytic performance of Co-Mo and Co(Ni)-W carbide catalysts in the hydrodenitrogenation (HDN) reaction of pyridine," *Appl. Catal. A*, **329** 36-45 (2007).
141. Wen, W., Calderon, J. E., Brito, J. L., Marinkovic, N., Hanson, J. C., Rodriguez, J. A., "In Situ Time-Resolved Characterization of Ni-MoO<sub>2</sub> Catalysts for the Water-Gas Shift Reaction," *J. Phys. Chem. C*, **112** 2121-2128 (2008).
142. Arnoldy, P., van den Heijkant, J. A. M., de Bok, G. D., Moulijn, J. A., "Temperature-programmed sulfiding of MoO<sub>3</sub>-Al<sub>2</sub>O<sub>3</sub> catalysts," *J. Catal.*, **92** (1) 35-55 (1985).
143. Shankara, A., Menezes, P. L., Simha, K. R. Y., Kailas, S. V., "Study of solid lubrication with MoS<sub>2</sub> coating in the presence of additives using reciprocating ball-on-flat scratch tester," *Sādhanā*, **33** 207-220 (2008).
144. Zhuravlev, T. S., Krinichnaya, E. P., Ivanova, O. P., Klimenko, I. V., Golub, A. S. Lenenko, N. D., Misurkin, I.A., Titov, S.V., "Synthesis of nanocrystalline molybdenum disulfide films and studies of their structure, spectral and photoelectrical properties," *Thin Solid Films*, **520** 3125-3130 (2012).
145. Mengers, H., Benes, N. E., Nijmeijer, K., "Multi-component mass transfer behavior in catalytic membrane reactors," *Chem. Eng. Sci.*, **117** 45-54 (2014).
146. Huang H., Leung D. Y. C., Ye D., "Effect of reduction treatment on structural properties of TiO<sub>2</sub> supported Pt nanoparticles and their catalytic activity for formaldehyde oxidation," *J. Mater. Chem.*, **21** 9647-9652 (2011).

147. An N., Yu Q., Liu G., Li S., Jia M., Zhang W., "Complete oxidation of formaldehyde at ambient temperature over supported Pt/Fe<sub>2</sub>O<sub>3</sub> catalysts prepared by colloid-deposition method," *J. Hazard. Mater.*, **186** (2-3) 1392-1397 (2011).
148. Chen B. -B., Shi C., Crocker M., Wang Y., Zhu A. -M., "Catalytic removal of formaldehyde at room temperature over supported gold catalyst," *Appl. Cat. B: Environ.*, **132-133** 245-255 (2013).
149. De, A.K., *A Text Book of Inorganic Chemistry*, ISBN 978-81-224-1384-7, (2001).
150. Taylor, R. and Krishna, R., *Multicomponent Mass Transfer*, Wiley Series in Chemical Engineering, New York, 1993.
151. Khanmamedov, T. K., and Weiland, R.H., "Catalytic oxidation of hydrogen sulfide," *Sulfur*, **345** 62-68 (2013).
152. Sendt, K., and Haynes, B. S., "Role of direct reaction H<sub>2</sub>S+SO<sub>2</sub> in the homogeneous Claus reaction," *J. Phys. Chem. A*, **109** 8180-8186 (2005).
153. Mason, E. A., and Malinauskas, A. P., *Gas Transport in Porous Media: The Dusty Gas Model*. Elsevier, Amsterdam, 1983.
154. Wesselingh, J. A., and Krishna, R., *Mass Transfer in Multicomponent Mixtures VSSD*, Delft 2000.
155. Fuller, E. N., Schettler, P. D., Giddings, J. C., "New method for prediction of binary gas-phase diffusion coefficients," *Ind. Eng. Chem.*, **58** (5) 18-27 (1966).
156. Slood, H. L., Versteeg, G. F., Van Swaaij, W. P. M., "A non-permselective membrane reactor for chemical processes normally requiring strict stoichiometric feed rates of reactants," *Chem. Eng. Sci.* **45** (8) 2415-2421 (1990).
157. Mukherjee, S., Vannice, M. A., "Solvent effects in liquid-phase reactions: I. Activity and selectivity during citral hydrogenation on Pt/SiO<sub>2</sub> and evaluation of mass transfer effects," *J. Catal.* **243** (1) 108-130 (2006).

158. Trofimov, B. A., Sinegovskaya, L. M., Gusarova, N. K., "Vibrations of the S–S bond in elemental sulfur and organic polysulfides: a structural guide," *J Sulfur Chem.*, **30 (5)** 518-554 (2009).
159. Papadopoulou, Ch., Vakros, J., Matralis, H. K., Voyiatzis, G. A., Kordulis, Ch., "Preparation, characterization, and catalytic activity of CoMo/gamma-Al<sub>2</sub>O<sub>3</sub> catalysts prepared by equilibrium deposition filtration and conventional impregnation techniques," *J. Colloid Interface Sci.*, **274 (1)** 159-166 (2004).
160. Monnery, W. D., Hawboldt, K. A., Pollock, A., Svrcek, W. Y., "New experimental data and kinetic rate expression for the Claus reaction," *Chem. Eng. Sci.*, **55 (21)** 5141-5148 (2000).
161. Tesner, P. A., Nemirovskii, M. S., Motyl D. N., "Kinetics of the thermal decomposition of hydrogen sulfide at 800-1200°C," *Kinetika I Kataliz*, **30 (5)** 889-892 (1990).

## **Curriculum Vitae** **Sujoy Bose, PhD**



### **CONTACT INFO:**

---

#### **Correspondence address**

Department of Chemical Engineering  
IIT Guwahati, Guwahati  
Assam -781039  
India

#### **Home address**

B-11A, Ashokenagar, Ichapur  
P.O. – Ichapur Nawabganj  
Dist. – 24 Parganas (North)  
Pin - 743144  
West Bengal, India

**Email:** [sujoybose83@gmail.com](mailto:sujoybose83@gmail.com)

[diatm\\_ch@yahoo.co.in](mailto:diatm_ch@yahoo.co.in);

[b.sujoy@iitg.ernet.in](mailto:b.sujoy@iitg.ernet.in)

**Mobile:** +919433214348; 918011215386; (033) 2561-7691 (R)

### **PERSONAL INFO:**

---

**Date of Birth:** May 01, 1983

**Sex:** Male

**Father's name:** Mr. Swapan Kumar Bose

**Mother's name:** Mrs. Swapna Bose

**Marital status:** Unmarried

**Nationality:** Indian

### **EDUCATION DETAILS:**

---

#### **Doctor of Philosophy**

Chemical Engineering

Indian Institute of Technology Guwahati, India

*Thesis:* Development of a Low-cost Catalytic Membrane Reactor for Sulfur Recovery

*Supervisor:* Dr. Chandan Das

**2015**

#### **Master of Technology**

Chemical Engineering

National Institute of Technology, Durgapur, India

Aggregate: 8.18 (CGPA)

*Thesis:* Modelling the microfiltration cell recycle bioreactor for continuous production of lactic acid

*Supervisor:* Dr. Jaya Sikder

**2011**

**Bachelor of Technology**

2008

Chemical Engineering

Durgapur Institute of Advanced Technology and Management, Durgapur, India

Aggregate: 8.39 (DGPA)

*Thesis:* Modelling of rotating disc ultrafiltration membrane module based on dimensional approach

*Supervisor:* Dr. Projjwal Sarkar

**Higher secondary in science (10+2 Standard)**

2001

Nawabganj Sridhar Bansidhar High School, Ichapur, 24 Parganas (N), West Bengal, India

Percentage: 56.90%

**Secondary education (10<sup>th</sup> standard)**

1999

Ichapur Northland High School, Ichapur, 24 Parganas (N), West Bengal, India

Percentage: 60.87%

**FELLOWSHIP:**

---

National scholarship

2011-2015

Ministry of Human Resource Development

Govt. of India

**RESEARCH EXPERIENCE:**

---

***Doctoral Training***

**Synopsis:** This work mainly deals with the fabrication and characterization of catalytic membrane reactor and its application to recover/remove different value-added products from petroleum industries. The main objectives of this study are:

- (a) Selection of suitable materials for support membrane fabrication.
- (b) Parametric optimization (sintering temperature, applied pressure) of membrane preparation methods using trial and error approach in experimentation.
- (c) Evaluation of the best membrane module (tubular, hollow fibre, flat) and mode of application (dead-end, cross-flow etc.)
- (d) Characterization of the fabricated membrane.
- (e) Selection of suitable catalysts for different purposes.
- (f) Evaluation of optimal operating conditions (preparation technique, calcination temperature) that enables to offer higher yield.
- (g) Choosing of suitable catalysts coating techniques (PVD, CVD, Vacuum coating etc.) on the surface of the membrane in terms of cost.
- (h) Evaluation of the best membrane reactor configurations and mode of applications (extractor, distributor and contactor).
- (i) Modelling and simulation for CMRs design purpose.
- (j) Cost and economic analysis.

### ***Masters Training***

**Synopsis:** In this study, an attempt has been made to obtain an empirical model of the microfiltration cell recycle bioreactor for continuous production of Lactic acid by FORTRAN. Cell concentration, substrate concentration, product concentration and permeate flux as a function of time was evaluated considering resistance-in-series model in which the membrane resistance and cake resistance are taken into account.

### ***Bachelors Training***

**Synopsis:** The project mainly dealing with the modeling of a rotating disc ultrafiltration membrane by using buckingham-pi theorem to get a correlation between permeates flux and rejection.

### **TEACHING EXPERIENCE:**

---

#### **Doctoral Teaching Assistant, IIT Guwahati, India**

- Trained 35 undergraduate students in Engineering design
- Trained 30 undergraduate students in basic and advanced techniques (mass transfer laboratory)
- Assisted undergraduate and postgraduate students in research work
- Evaluated exam papers of undergraduates and postgraduates

### **PROFESSIONAL MEMBERSHIP:**

---

- Executive committee member, IICHE Guwahati Regional Centre, IICHE-GRC, 2013-2014

### **PEER-REVIEWED JOURNAL PUBLICATIONS:**

---

1. **Sujoy Bose** and Chandan Das, "Preparation and characterization of low cost tubular ceramic support membranes using sawdust as a pore-former", **Materials Letters**, 110, (2013), 152-155. (Impact factor: 2.489)
2. **Sujoy Bose** and Chandan Das, "Role of binder and preparation pressure in tubular ceramic membrane processing: Design and optimization study using response surface methodology (RSM)", **Industrial & Engineering Chemistry Research**, 53, (2014), 12319-12329. (Impact factor: 2.587)
3. **Sujoy Bose** and Chandan Das, "Sawdust: From Wood Waste to Pore-former in the Fabrication of Ceramic Membrane", **Ceramics International**, 41, (2015), 4070-4079. (Impact factor: 2.605)
4. **Sujoy Bose** and Chandan Das, "Preparation, characterization, and activity of activated  $\gamma$ -alumina-supported molybdenum/cobalt catalyst for the removal of elemental sulfur", **Applied Catalysis A: General**. (Under review)
5. **Sujoy Bose** and Chandan Das, "Solid Lubricant-based Coating of Catalyst on the Surface of Tubular Ceramic Support for Catalytic Membrane Fabrication", **International Journal of Applied Ceramic Technology**. (Under review)
6. **Sujoy Bose**, Rishiket Kundu, Chandan Das, "Mass transfer in a novel tubular catalytic membrane reactor (CMR) for the recovery of elemental sulfur", **Chemical Engineering and Processing: Process Intensification**. (Revision Submitted)

7. **Sujoy Bose**, Chandan Das, “Fabrication of Catalytic Membrane and Membrane reactor: an Economic and Innovative Route”, *Materials Today: Proceedings* (Under review)

#### **JOURNALS UNDER PREPARATION:**

---

1. **Sujoy Bose** and Chandan Das, “Catalytic reactions and separations using catalytic membrane reactors with separate feed of reactants: A review”.
2. **Sujoy Bose** and Chandan Das, “A continuous catalytic membrane reactor for the recovery of sulfur: An approach via response surface methodology (RSM)”.

#### **ACADEMIC CONFERENCE PRESENTATIONS:**

---

##### National Conferences:

1. **S. Bose** and C. Das, “**A morphological and mechanical study of an eco-ceramic membrane influenced by parameters**”, Innovative approaches for food security and health care for better tomorrow, 66th Annual Session of Indian Institute of Chemical Engineers, 27-30 Dec, 2013, ICT Mumbai (**CHEMCON-2013**), 2013.
2. R. Kundu, **S. Bose** and C. Das, “**Catalytic membranes and membrane reactors: A novel separation scheme,**” **REFLUX 2.0**, Annual Chemical Engineering symposium, 29<sup>th</sup> – 30<sup>th</sup> March 2014, IIT Guwahati, Assam, India.

##### International Conferences:

1. **S. Bose** and C. Das, “**Catalytic membranes and membrane reactors to achieve a green environment: A review**”, 12<sup>th</sup> International Conference on Inorganic Membranes (**ICIM – 2012**), 9 -13 July 2012, University of Twente, Enschede, The Netherlands.
2. **S. Bose** and C. Das, “**Fabrication of low cost ceramic membrane from organo-polymeric wood precursors**”, Processing and fabrication of Advanced Materials XXI (**PFAM - 21**), 10-13 December 2012, Indian Institute of Technology, Guwahati, Assam, India.
3. **S. Bose** and C. Das, “**Utilities and basic functions of ceramic membranes in catalytic membrane and membrane reactors**”, International conference on Sustainable Technologies for Energy and Environment in Process Industries, 65th Annual Session of Indian Institute of Chemical Engineers, 27-30 Dec, 2012, NIT Jalandhar (**CHEMCON-2012**), India.
4. **S. Bose** and C. Das, “**Study of microstructures of ceramic-wood composites**”, Fourth International Conference on Recent Advances in Composite Materials (**ICRACM-2013**), IIT BHU, 18-21 February, 2013, Goa, India.
5. **S. Bose** and C. Das, “**Influence of Porosity on Flexural Strength and Flexural Modulus of an Eco-Ceramic Membrane**”, International Conference on Mechanical, Industrial and Materials Engineering, (**ICMIME-2013**), RUET, 1-3 November, 2013, Rajshahi, Bangladesh.
6. **S. Bose**, S. Saha, C. Das, “**Investigation of morphological and mechanical behaviour of a ceramic membrane based on different parameters**”, International Conference on Membranes and Applications, (**ICMA-2013**), CSIR-CGCRI, 22-23 November, 2013, Kolkata, India.

## **WORKSHOP ATTENDED**

---

1. Workshop on "**Engineering optimization using Matlab and Excel**", February 29- March 2, 2012, IIT Guwahati (Organized by Department of Civil and Mechanical Engineering, IIT Guwahati).
2. National course on "**Membrane Technology and Application**", December 9-10, 2014, IIT Guwahati conducted under the Technical Education quality Improvement programme sponsored by MHRD, Govt. of India. (Organized by Centre for Educational Technology, IIT Guwahati).

## **RESEARCH INTEREST:**

---

The long term research goal is to discover novel and inexpensive raw materials that could be used for ceramic membrane fabrication and manufacturing of light-weight ceramics.

## **SUBJECT INTEREST:**

---

Membrane Technology; Process Heat Transfer, Mass Transfer

## **VOCATIONAL TRAINING:**

---

- Undergone 15 days in plant training at Durgapur projects Ltd.
- Undergone 1 month in plant training at Essel Kitchenware Pvt.Ltd.

## **HOBBIES & EXTRACURRICULAR ACTIVITIES**

---

- Playing cricket
- Listening to music
- Active member of local puja organizing committee

Sujoy Bose

